1. Award Information

Award Number: DE-FG36-08GO18162

Project Title: Dual Layer Monolith ATR of Pyrolysis Oil for Distributed Synthesis Gas Production

Project Period: 09/30/08 – 09/29/12 ***(No-cost Extension till 09/29/12)***

Recipient:
Stevens Institute of Technology
Castle Point on Hudson
Hoboken, NJ 07030
13th Congressional District

Project Location: Stevens Institute of Technology

Technical Contact: Adeniyi Lawal (PI, Stevens), (201) 216-8241, alawal@stevens.edu

Partner:
BASF Catalysts LLC
25 Middlesex-Essex Turnpike
PO Box 770
Iselin, NJ 08830
Robert Farrauto (Co-PI)
(732) 205-5306
7th Congressional District

2. No distribution limitations

3. Executive Summary

We have successfully demonstrated a novel reactor technology, based on BASF dual layer monolith catalyst, for miniaturizing the autothermal reforming of pyrolysis oil to syngas, the second and most critical of the three steps for thermochemically converting biomass waste to liquid transportation fuel. The technology was applied to aged as well as fresh samples of pyrolysis oil derived from five different biomass feedstocks, namely switch-grass, sawdust, hardwood/softwood, golden rod and maple. Optimization of process conditions in conjunction with innovative reactor system design enabled the minimization of carbon deposit and control of the H_2/CO ratio of the product gas. A comprehensive techno-economic analysis of the integrated process using in part, experimental data from the project, indicates (1) net energy recovery of 49% accounting for all losses and external energy input, (2) weight of diesel oil produced as a percent of the biomass to be ~14%, and (3) for a 'demonstration' size biomass to Fischer-Tropsch liquid plant of ~ 2000 daily barrels of diesel, the price of the diesel produced is ~$3.30 per gallon, ex. tax. However, the extension of catalyst life is critical to the realization of the projected economics.

Catalyst deactivation was observed and the modes of deactivation, both reversible and irreversible were identified. An effective catalyst regeneration strategy was successfully demonstrated for reversible catalyst deactivation while a catalyst preservation strategy was proposed for preventing irreversible catalyst deactivation. Future work should therefore be focused on extending the catalyst life, and a successful demonstration of an extended (> 500 on-stream hours) catalyst life would affirm the commercial viability of the process.

4. Project Accomplishments

The following are the major accomplishments of this project:

- Performed successfully the Auto-thermal Reforming (ATR) of aged as well as fresh samples of whole pyrolysis oil (PO) using the BASF dual layer monolith catalyst.
- Designed and developed an effective in-house PO injection and re-vaporization system with low (~3%) carbon deposit for whole PO.
- Developed a combination of analytical methods for chemical characterization of PO, a complex mixture of oxygenates, derived from five different feedstocks (switch-grass, sawdust, hardwood/softwood, maple and golden rod).
- Produced syngas with tunable H_2/CO ratio in the range of 1.8 – 4.0.
- Determined the optimum process parameters (H_2O/C, O_2/C, temperature, and GHSV) for the production of syngas.
- Both O_2/C and H_2O/C ratios are lower than those typically used for ATR of hydrocarbons
- BASF dual layer monolith catalyst appears to be effective in suppressing methanation reaction thereby enhancing H_2 yield
- Experimental data were in good agreement with Aspen equilibrium calculations for some process conditions.
- Performed the kinetic study of a model compound, glycerol, which provides useful insight into the ATR of oxygenates using the dual layer monolith catalyst.
- Rate equations were successfully developed based on the Langmuir-Hinshelwood approach
- Identified the modes of catalyst deactivation, both reversible and irreversible for the dual layer monolith catalyst.
- Developed an effective catalyst regeneration procedure for mitigating reversible deactivation and proposed approaches for preventing irreversible catalyst deactivation.
- Performed a comprehensive techno-economic analysis of the integrated process which indicates (1) net energy recovery of 49% accounting for all losses and external energy input, (2) weight of diesel oil produced as a percent of the biomass to be ~14%, and (3) for a 'demonstration' size biomass to FT liquid plant of ~ 2000 daily barrels of diesel, the price of the diesel produced is ~$3.30 per gallon, ex. tax.

5. Project Activities

Task 1: Physical and Chemical Characterization of Pyrolysis Oil & ATR Product Gas

I. Summary

Lignocellulose comprises mainly cellulose, hemicellulose and lignin. Rapid pyrolysis of this feedstock produces pyrolysis oil (PO), a complex mixture of over 400 oxygenated compounds. Development of a rational approach to the upgrading of PO requires an informed understanding of its composition and properties. The chemical composition of the pyrolysis oil depends on the feedstock, the pyrolysis conditions, and the product collection method. However, generally PO is a mixture of oxygenated organics including carboxylic acids, aldehydes, ketones, alcohols, esters, ethers, and phenols along with 20-30 wt.% water. The oxygen content varies between 35 to 40 wt.%, and is responsible for the low heating value and other undesirable features such as chemical instability, immiscibility, acidity, and the tendency to phase-separate.

PO samples derived from switch-grass, sawdust, maple and Golden-Rod grass were analyzed during this study via wet-chemical methods using a combination of Varian 3900 GC/MS (Varian Factor Four Capillary Column VF-5ms – 30m x 0.25mm ID, 0.25 μm film thickness, CP-1177 injector, and Varian 8410 autosampler, and Saturn 2100T detector) and Shimadzu LC-10AT HPLC. We followed procedures similar to those developed by Mullen and Boateng (Mullen and Boateng, 2008).The water content of two of these four samples and another PO produced from hard/softwood was determined using the Karl Fisher titration (ASTM D-1744). The CHN elemental composition analysis was performed on these three PO samples using the services of Robertson Microlit Laboratories, a provider of analytical services. The amount of oxygen was determined by difference. ATR product gas composition was analyzed using the Shimadzu GC-14B with appropriate columns.

II. Chemical Characterization of Pyrolysis Oil

Complete and accurate characterization of all the chemical species in pyrolysis oil is not feasible as this will require a combination of many analytical methods. Besides, some of the components are present in quantities that are so small that they are hardly detectable even by the most sensitive analytical equipment. Chromatographic techniques are commonly used for the chemical characterization of pyrolysis oil, and a combination of GC and LC is adequate to quantify the most important components. In order to understand the chemical analysis results of PO made from lignocellulosic biomass, we need to identify the main pyrolysis products that are formed from the three major components of biomass, namely cellulose, hemicellulose and lignin. A lot of different species are expected in the liquid products of fast pyrolysis, and Table 1.1 presents the range of compositions of the most predominant groups of compounds in pyrolysis oil (Diebold, 2000). Water is typically the main component, ranging between 15 and 30 wt. %, and at higher fractions, the pyrolysis liquids tend to phase-separate. Water is generally quantified by Karl Fischer-titration. After that, the highest fraction of products is made up of the light organic compounds that are the products of cellulose and hemicellulose fragmentation, such as anhydrosugars (particularly levoglucosan) and furfural. Lignin pyrolysis yields monomers and oligomeric species (the latter often termed “pyrolytic lignin”). A lot of different monomers are found, but none typically accounts for more than 1 wt. % of the liquid product. As a matter of fact, most lignin-derivatives are typically found in the form of oligomers.

Table 1.1: Composition of Major Groups of Oxygenates in Pyrolysis Oil (Diebold, 2000)

Hemicellulose	
Species	wt. %
Acids	5.0 - 10.0
Formic	0.3-
Acetic	0.5 -
Propanoic	0.1 - 1.8
Esters	
Angelicalactone	0.1 - 1.2
Methyl formate	0.1 - 0.9
2(5H)-Furanone, 5-methyl	
Alcohols	
Methanol	0.4 -
Ethanol	0.6 - 1.4
Ethylene glycol	0.7 - 2
Ketones & Hydroxyketones	0 - 10
Acetone	2.8
Hydroxyacetone	0.7 - 7.4
Aldehydes & Hydroxyaldehydes	5.0 - 20.0
Formaldehyde	0.1 - 3.3
Acetaldehyde	0.1 - 8.5
Ethanedial	0.9 - 4.6
Hydroxyacetaldehyde	0.9 -
Sugars	
D-Xylose	0.1 - 3.2
Cellulose	
Species	wt. %
Sugars	
Levoglucosan	0.4 - 1.4
Glucose	0.4 - 1.3
Fructose	0.7 -
Cellubiosan	0.6 - 3.2
1,6 anhydroglucofuranose	3.1

Lignin	
Species	wt. %
Phenolics	20.0 -
Phenol	0.1 - 3.8
2-Ethyl phenone	0.1 - 1.3
1,4 DiOH benzene	0.1 - 1.9
Guaiacols	
2-Methoxy phenol	0.1 - 1.1
4-Methyl guaiacol	0.1 - 1.9
Isoeugenol	0.1 - 7.2
Eugenol	0.1 - 2.3
Syringols	
2,6 DiOMe phenol	0.7 - 4.8
Propyl syringol	0.1 - 1.5
Syringaldehyde	0.1 - 1.5
Furans	
Furanone	0.1 - 1.1
Furfural	0.1 - 1.1
Furfural alcohol	0.1 - 5.2
5-OH-Methyl-2-furfural	0.3 - 2.2
Others	
Methyl cyclopentenolone	0.1 - 1.9
4-OH-3-methoxybenzaldehyde	0.1 - 1.1
Water	15 - 30

The analysis should identify as many of the components as possible, but also it should quantify the main components. Gas chromatography alone cannot yield this information since it is limited to substances that are volatile and have a boiling point high enough to have sufficient retention time in the chromatographic column. Therefore, GC is well suited to identify the monomeric lignin depolymerization products (the phenolic compounds), and also the furanes (mainly furfural) from (hemi-) cellulose decomposition. Gas chromatography will yield good results with these moderately-heavy compounds and other aromatic derivatives, but those requirements rule out many of the main constituents of the PO, including water and light organic compounds such as acetic acid, hydroxyacetone (“acetol”), hydroxyacetaldehyde (“glycolaldehyde”), and heavy or non-volatile compounds, such as sugars or sugar-derivatives (*e.g.* anhydrosugars (levoglucosan), which is a particularly often-reported component of PO). Water content is quantifiable precisely by use of Karl-Fischer titration.

The light organic components (acetic acid, formic acid, formaldehyde, hydroxyacetone and acetaldehyde, among others) usually pass the GC columns too quickly to be resolved, unless a special technique is used for their purpose. Carbohydrate compounds such as anhydrosugars also cannot be analyzed in a GC. Instead, liquid chromatography is used for the identification and quantification of those two compound classes. The combination of GC and LC techniques is capable of resolving, identifying and quantifying most of the monomeric components of pyrolysis oil. The oligomeric components (of pyrolytic lignin), however, are usually not accessible with these techniques. They do not evaporate in the GC column – if anything, they decompose in the hot evaporator –, and have a high retention time on the reversed phase (unpolar) HPLC column, and do not resolve on this column. This high molecular weight fraction is nearly inaccessible by analytical techniques, and only a few studies exist on detailed analysis of this water-insoluble fraction, with Gel Permeation Chromatography (GPC) being the most successful approach.

It became clear during our work that the combination of these three analysis techniques (GC/MS, HPLC, Karl-Fischer Titration) will yield a very complex data set, which needs to be processed and documented in a suitable way for it to be easily accessible, and to leverage the information contained in the data so that it will actually serve as a valuable support for the goal of designing and optimizing the process parameters.

The procedure for chemical analysis of pyrolysis oil in this project comprised:

1. Elemental composition analysis
2. Karl-Fischer titration for water content
3. GC/MS analysis for moderately-heavy components and aromatic derivatives, and
4. HPLC as an additional technique for qualitative and quantitative analyses of light organic components, and carbohydrate compounds.

Pyrolysis oils produced from five different types of feedstocks, namely sawdust (Dynamotive Corporation), hardwood/softwood (Ensyn Corporation), switchgrass (ARS/USDA), maple (PNNL) and Golden-Rod (Innovative Biofuels Solutions) were characterized in our lab.

II.1. Elemental Composition Analysis & Karl-Fischer Titration of PO

Elemental composition analysis of three different types of whole pyrolysis oil, derived from sawdust, switch-grass, and hardwood/softwood was performed using the services of Robertson Microlit Laboratories, Ledgewood NJ. All the samples contained small amounts of nitrogen, negligible amounts of ash, and non-detectable quantities of sulfur. The sawdust-derived pyrolysis oil contained on average 43% C, 7.5% H and the rest oxygen while the switch-grass pyrolysis oil contained 49% C, and 7.5% H. The switch-grass PO has slightly more nitrogen, 0.57% vs. 0.25% but less ash than the sawdust PO. Compositional analysis of the water-soluble fraction of each sample of PO was also carried out. The carbon content reduced considerably for all samples (~ 10%) while the oxygen content increased as expected (~ 80%).

.

Water content in the PO samples was determined using the Karl Fischer (KF) titration. Since the PO was not homogeneous (as it contained particulate matter), it was vacuum-filtered using 1 μm filtration unit. KF titration was accomplished using Model 375 Volumetric Karl-Fischer Titration Workstation (Denver Instrument) with the use of hydranal reagents obtained from Sigma-Aldrich. Water content in the bio-oil was reported as the weight % of filtered PO (and not whole PO). The water content of the sawdust PO averaged 30% while that of switch-grass is 15%, with the latter value in close agreement with independent analysis performed by the provider of the PO, ERRC of USDA, PA. The water content of the hardwood/softwood-derived

PO was, as expected, closer to that of sawdust-derived PO. CHN analysis and water content of the three different samples of PO are reported in Table 1.2.

Table 1.2: CHN Analysis and Water Content of Pyrolysis Oil

All values in wt. %	C	H	N	O	Ash	Sulfur	Water Content
Sawdust (Dynamotive)	43.39	7.72	0.26	48.64	0.17	<0.05	29.8
Switchgrass (ARS/USDA)	49.12	7.50	0.57	42.81	<0.10	<0.05	15.1
Hardwood/Softwood (Ensyn Corp.)	45.03	6.98	<0.02	47.99	NA	NA	27.0

II.2. Chemical Analysis of PO by Chromatography Techniques

Based on an exhaustive literature review, we identified fourteen target compounds for quantification using either GC/MS or HPLC (in addition to water, which we quantified using Karl-Fischer titration, see Section II.1. above):

1. Acetic acid (by HPLC) CAS: 64-19-7
2. Hydroxyacetaldehyde (by HPLC) CAS: 141-46-8
3. Hydroxyacetone (by HPLC) CAS: 116-09-6
4. Furfural (by GC/MS) CAS: 98-01-1
5. Furfuryl alcohol (by GC/MS) CAS: 98-00-0
6. Phenol (by GC/MS) CAS: 108-95-2
7. 2-Methoxy-Phenol (Guaiacol) (by GC/MS) CAS: 90-05-1
8. *p*-Cresol (by GC/MS) CAS: 106-44-5
9. 4-Methyl-Guaiacol (by GC/MS) CAS: 93-51-6
10. Isoeugenol (by GC/MS) CAS: 97-54-1
11. Pyrocatechol (*i.e.*, 1,2-Benzenediol) (by GC/MS) CAS: 120-80-9
12. Syringol (2,6-Dimethoxy Phenol) (by GC/MS) CAS: 91-10-1
13. Methylsyringol (1,2,3-Trimethoxybenzene) (by GC/MS) CAS: 634-36-6
14. Levoglucosan (by HPLC) CAS: 498-07-7

To test our analysis techniques, samples of four different pyrolysis oils produced from different types of feedstock and supplied to us by different suppliers were analyzed:

1. sawdust-derived pyrolysis oil from Dynamotive (produced 06/06/09),

2. switchgrass-derived pyrolysis oil from ARS/U.S.D.A. (produced 05/01/07),

3. maple-derived pyrolysis oil from P.N.N.L. (produced 08/28/09), and

4. Golden-Rod grass-derived pyrolysis oil from Innovative Biofuels Solutions (produced 06/15/10). This sample – unlike the other three – was produced by a specific slow pyrolysis process, which was aimed at the production of biochar with pyrolysis oil produced only as a by-product. Due to some problems with the process conditions in the setup, this pyrolysis oil contained a high amount of water (far more than 30 wt.%), and was received phase-separated. It was very hard to obtain a well-defined solution from this sample using the standard techniques (which apply syringes as volumetric devices for the preparation of defined solutions). For the most part, the far less viscous aqueous phase was sucked into the syringes. The results, however, will be discussed to demonstrate the applicability of our

analysis techniques to samples resulting from such “beginner’s mistakes” in the production of pyrolysis oils.

II.3. Gas Chromatography/Mass Spectrometry

Characterization of pyrolysis oil was accomplished using GC-MS (Varian, Saturn 2100T). This gas chromatography was equipped with a fused silica capillary column (Varian, factorFOUR^{TM}, CP5887, VF-5ms, 30m x 0.25mm, df 0.15mm) while the isolated peaks were analyzed in the MS using an ion trap mass selective detector. Helium was used as the carrier gas.

It was important to develop and validate a method for analysis of pyrolysis oil with GC-MS. An appropriate method would separate majority of the components with adequate resolution. A gas chromatograph with a split ratio of 1:100 was used for separation. The injector temperature was 250^{o}C while the ion trap detector was maintained at 150^{o}C. The column flow was 0.6 ml/min. The heating profile began at 40^{o}C held for 2 min, and then the temperature was raised to 300^{o}C at a ramp rate of 1.8^{o}C/min. Such a low ramp rate was used to ensure maximum separation of pyrolysis oil components. The MS was auto-tuned for mass calibration and air/water leak test conducted every other day. Also, only m/z values ranging from 45 to 350 were analyzed. The data was obtained and processed using Varian MS Workstation System Control ver. 6.9. To identify the peaks using their m/z values, NIST library in conjunction with its software was used.

Sample preparation was a critical step in GC-MS characterization. It was ensured that all the pyrolysis oil components dissolved in the solvent selected. Pyrolysis oil was initially vacuum-filtered to 1 µm. For analysis, a 6% solution of pyrolysis oil was prepared in methanol (GC-MS grade). Other solvents including acetone, ethanol, n-hexane, and toluene were also tried but methanol was shown to dissolve all of the pyrolysis oil components and form a clear solution. This 6% pyrolysis oil/MeOH solution was stored in a refrigerator at 4^{o}C for further use. Prior to injection, the sample was further filtered to 0.2 µm using PTFE syringe filter.

The following graph (fig. 1.1) shows the gas chromatogram of sawdust-derived pyrolysis oil, with the major peaks assigned. This plot confirms that the main species identified by our GC method are the phenol monomers that derive from lignin pyrolysis, and the furanes from xylose dehydration (furfural and furfuryl alcohol). The light organic compounds do not separate in the column, and appear in the chromatogram as a large peak at the beginning of the data. Additionally, a broad peak of carbohydrates appears in the plot, approximately between 25 and 28 min. About 40 individual species were positively identified in our gas chromatogram of sawdust-derived pyrolysis oil based on the mass spectra, and some additional ones in other PO samples.

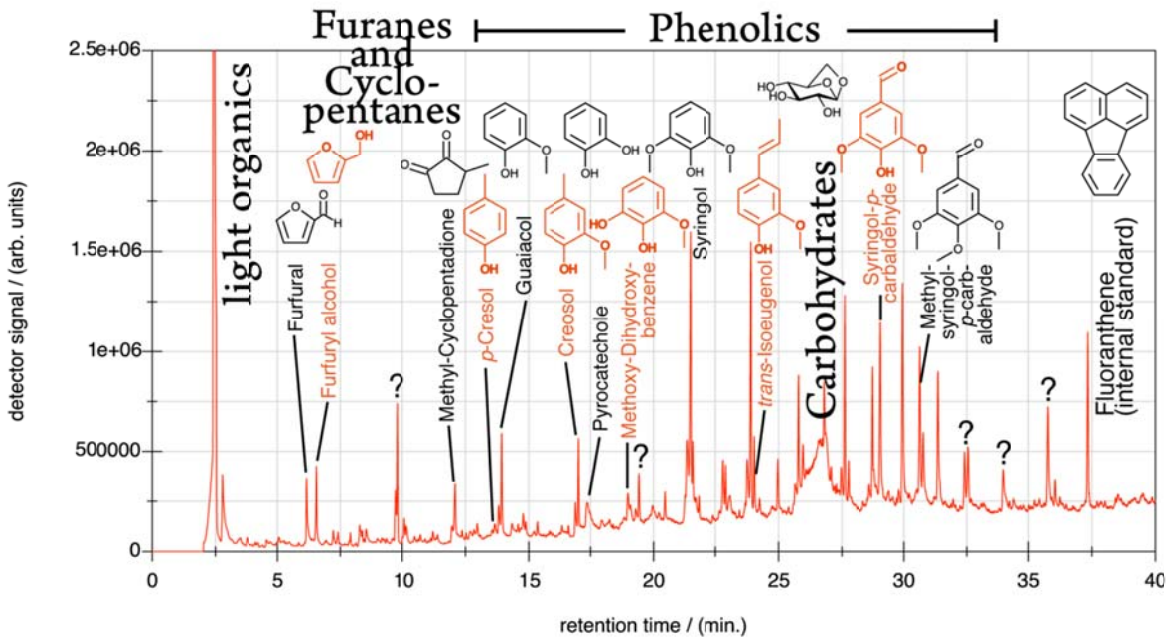

Figure 1.1: A few of the main peaks and their assignment in the gas chromatogram of sawdust-derived pyrolysis oil.

II.3.1. Quantification of Target Compounds in Pyrolysis Oil

As stated in Section II.2., ten target species were chosen for the quantification of the GC-accessible fraction of pyrolysis oils based on a literature survey. Those species, together with the chromatograms used for the calibration of the mass spectrometer's response factor ("sensitivity"), are shown in fig. 1.2.

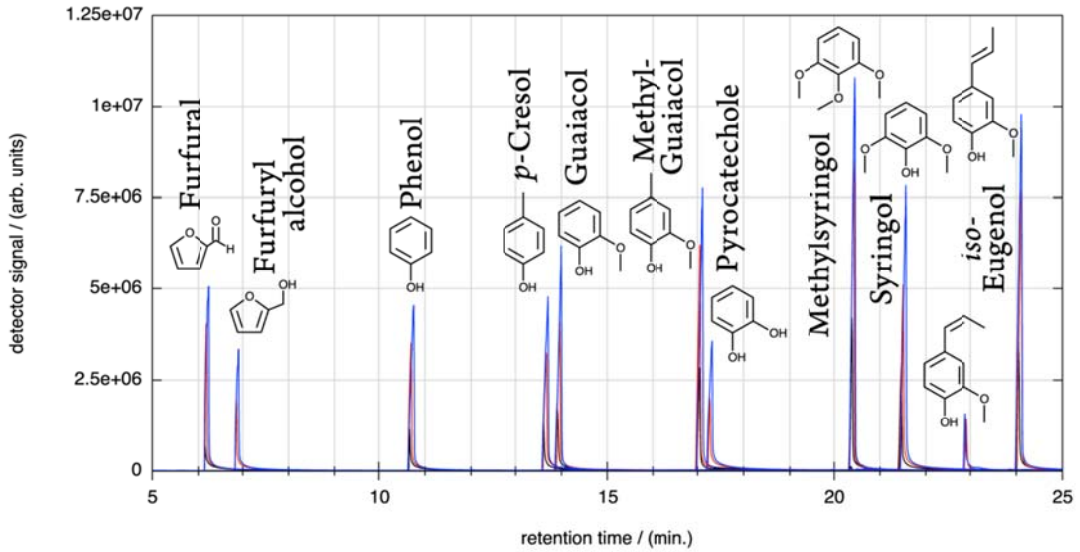

Figure 1.2: Target Molecules for Calibration of the GC-detector's Signal Response Factor ("Sensitivity") with the resultant TIC-chromatograms; concentrations: 1.0, 2.16 and 3.33 g/100 mL (dissolved to 6 vol.% solutions).

Here we present the results obtained from the four samples used as test cases. Figure 1.3 shows the "reconstructed" gas chromatograms (*i.e.*, the GCs based on the MS total ion current) of those four pyrolysis oils. Qualitative differences between the oils are obvious from this comparative plot, even without quantitative evaluation: the sawdust-derived pyrolysis oil contains the most intense peaks of all samples, the highest peak being the peak for syringol. However, it contains fewer peaks than other samples – for example, the switchgrass-derived pyrolysis oil shows significantly more peaks, though each of them with a lower absolute intensity than the sawdust-derived sample. The maple-derived pyrolysis oil shows the highest peaks of all the samples for the light organics fraction (which is in agreement with the HPLC results, where those species are resolved and quantified). Also, it shows a fairly large carbohydrate peak (also in agreement with HPLC), but relatively low peaks for the phenols; Douglas Elliott from P.N.N.L., the provider of that sample, told us that maple wood is relatively low in lignin – and consequently the low amount of phenols (which are lignin pyrolysis products) can be explained. Finally, the Golden Rod grass-derived PO shows very low peaks; as discussed for HPLC, the reason for this observation is likely that the fraction analyzed is mainly the aqueous phase of this phase-separated sample. The target species for GC-analysis would be expected to partition mainly into the organic phase.

These qualitative differences are reflected in the result presented in Table 1.3 which presents the quantification results for the target species. Furfuryl alcohol and methyl syringol were left out of that table because no peaks for those species were found in any of the pyrolysis oils (note that those species were chosen based on a literature survey of the most-observed peaks, not necessarily only on observations we made in our own experiments). Furfuryl alcohol was labeled in the chromatogram shown in fig. 1.3 which was obtained from an older solution (approx. two months old) of that respective sample. A fresh solution of the same sample did not show the peak of furfuryl alcohol – see the red curve in fig. 1.3; furfuryl alcohol does not seem to be a component of the pyrolysis oil itself, but a species that forms by reduction of furfural in the analysis solution in methanol, probably by a reaction of the Cannizarro-type – *i.e.,* the solvent methanol reacts with the analyte over time).

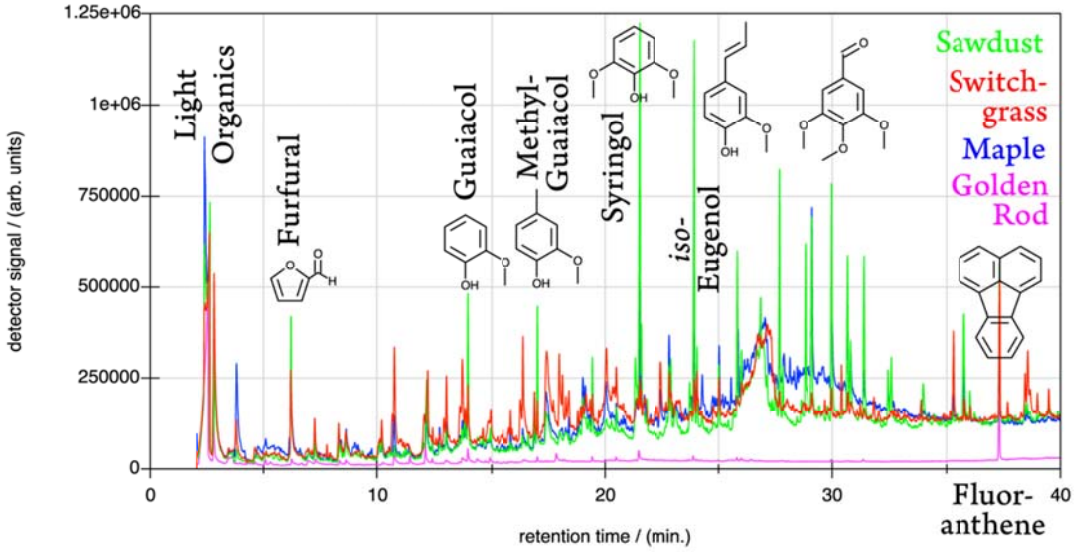

Figure 1.3: Gas Chromatograms (based on MS-TIC = "reconstructed gas chromatogram") of Different Pyrolysis Oils (6 vol.-% solutions in Methanol) - see color legend on the right.

Table 1.3 lists the results for sawdust- and switchgrass- and maple-derived pyrolysis oils, based on chromatograms obtained on different days from fresh solutions with the maple sample characterized much later than others. Golden Rod, due to the phase separation and thus ill-defined peak heights, was left out of the analysis. The results listed in the table demonstrate that the GC/MS-analysis can be well reproduced in between days, and even with longer time intervals (months) between the measurements.

One important observation has to be stressed: in order to obtain this good reproducibility, the signal of the internal standard (fluoranthene, retention time of 37.5 min. is added in identical amount to each calibration standard, and each solution of the pyrolysis oils) must be accounted for in the evaluation. Sometimes, signals of identical samples at different evaluation days were found to vary by more than a factor of two due to varying instrument response factors (not shown). In order to correct for these differences, each integral – for both the calibration standards, and analyte signals – was normalized to the integral of the internal standard (ion 202) of the respective chromatogram.

Table 1.3: GC Analysis of Three Samples of Pyrolysis Oil for Target Species

All values in wt.-%	Ion (Da.)	**Sawdust**			**Switch-grass**				**Maple**
		05/12	05/13	06/30	05/12	05/13	06/30	Ref.	06/30
Furfural	95	0.26	0.31	0.32	0.18	0.18	0.19	0.62	0.24
Phenol	94	0.04	0.04	0.04	0.28	0.28	0.31	n.a.	0.05
p-Cresol	107	0.04	0.04	0.04	0.21	0.21	0.23	0.27	0.06
Guaiacol	124	0.17	0.19	0.19	0.08	0.08	0.09	0.18	0.11
Methyl-guaiacol	138	0.13	0.11	0.12	0.04	0.04	0.04	0.07	0.09
Pyro-catechol	110	0.31	0.32	0.30	0.77	0.79	0.87	n.a.	0.47
Syringol	154	0.43	0.48	0.54	0.04	0.04	0.06	0.20	0.18
iso-Eugenol	164	0.07	0.08	0.07	0.03	0.03	0.04	0.45	0.05

Although the results are reproducible, some of the results differ from the literature data (only data for the switchgrass-derived sample are available, (Mullen & Boateng, 2008). The observed differences are likely due to, the age of the sample (more than 3 years), and the variations between sample preparations on different days (our analyzed sample, and the sample on which the reference analysis was based, were produced on different days). Phenols are quite reactive species, and their reactive consumption can be expected to explain the differences in GC values to some extent.

Nevertheless, it should also be noted that a Round Robin-test for pyrolysis oils has shown much higher deviations between different labs than the ones discussed here (Oasmaa and Meier, 2005). At the current stage, we cannot comment further on the issue of accuracy, since the data basis is small. It would be desirable to participate in a Round Robin-test ourselves – but such tests are rare.

II.4. HPLC Analysis of Pyrolysis Oil

As stated in section II.2 above, it is not possible to separate and quantify the very volatile compounds using the GC/MS. Also, heavy, non-volatile compounds such as carbohydrates usually do not cross the GC without big losses (and injector and column contamination). Since those two compound classes make up a considerable amount of PO, an HPLC method is needed. HPLC is used in the analysis of PO to quantify the products of cellulose and hemicellulose pyrolysis. These products are mainly the light organic compounds from the fragmentation of carbohydrate polymers, such as acetic acid, hydroxyacetone ("acetol"), hydroxyacetaldehyde ("glycolaldehyde") – and, some of the non-volatile carbohydrates and derivatives (most notably, the anhydro sugars levoglucosan, *i.e.* anhydro-β-D-Glucose, and cellobiosan, and the wood-sugar xylose).

Initial analysis was performed with the HPLC, and the associated chromatographic column (a reversed-phase column originally obtained for the analysis of organic acids, particularly acetic acid – Agilent Zorbax SB-Aq, see figures 1.4 and 1.5 below). Acetic acid is the most abundant of the compounds in the PO quantifiable by HPLC, and it turned out that it could be quantified quite reliably with the existing HPLC setup (its abundance is close to 10% based on preliminary experiments). Note that the biggest peak in the HPLC chromatogram is due to methanol, which was used as a solvent for the PO. However, the initial experiments showed that the separation of the other components was poor, and the supplier of the original column (Agilent) suggested the use of a different column (Bio Rad Aminex HPX-87H) from one of their competitors (Bio Rad Laboratories) in order to obtain a good separation of the broad range of compounds in the PO that were of interest to us.

Figure 1.4

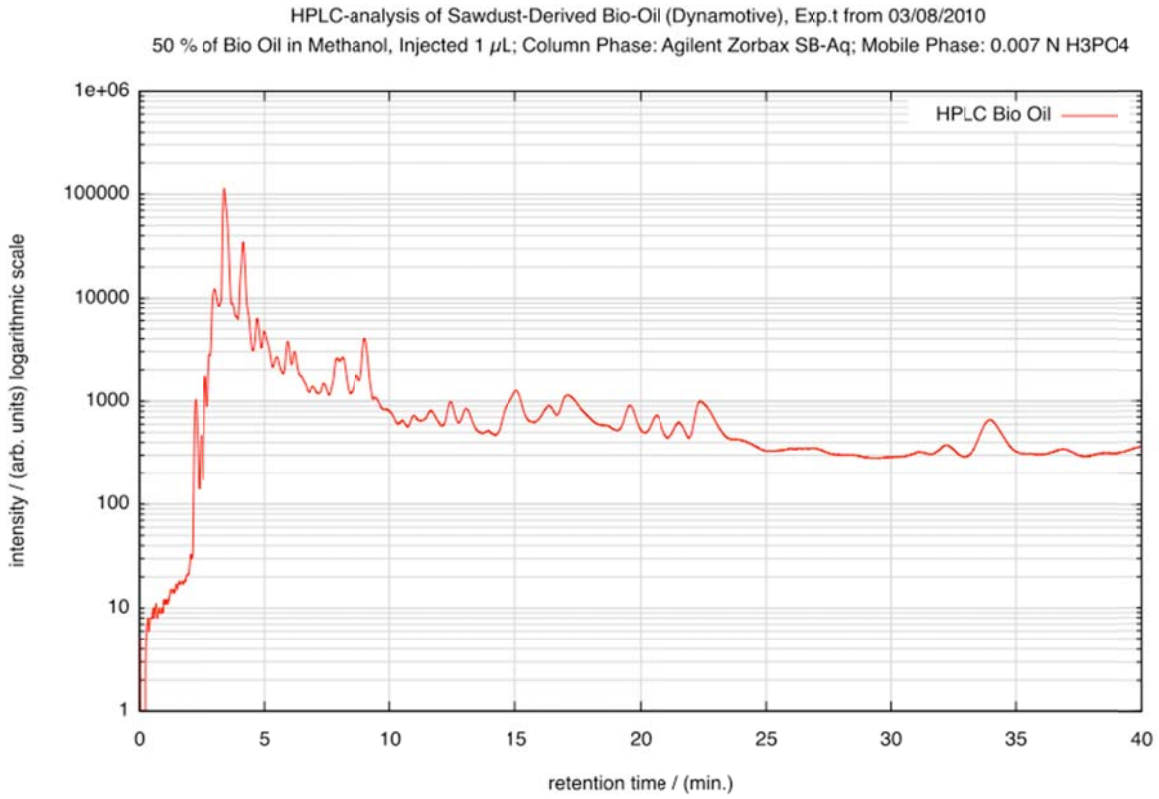

Figure 1.5

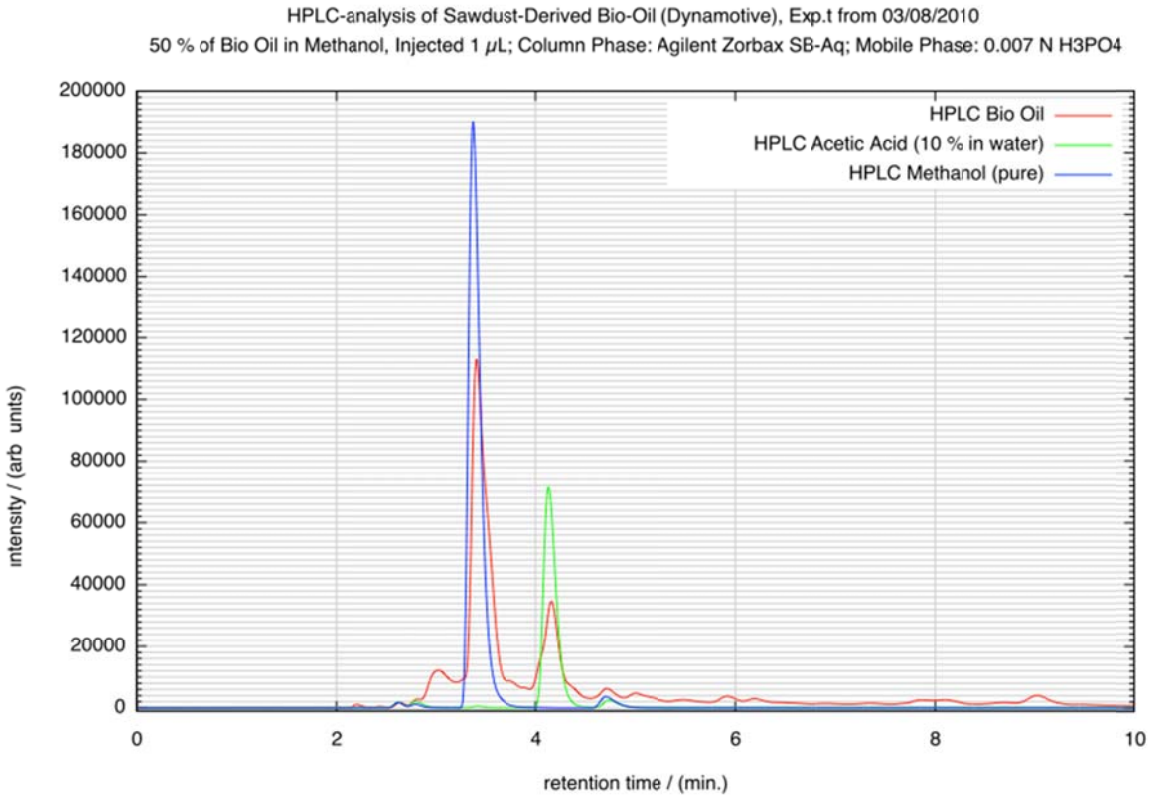

Using the new column, we developed an HPLC method based largely on other studies reported in the literature (Oasmaa and Meier, 2005). Figure 1.6 shows the main assignments for the sawdust-derived pyrolysis oil from Dynamotive's West Lorne Plant, produced on 06/06/09 while Figure 1.7 compares chromatograms obtained from our setup for all the PO samples studied.

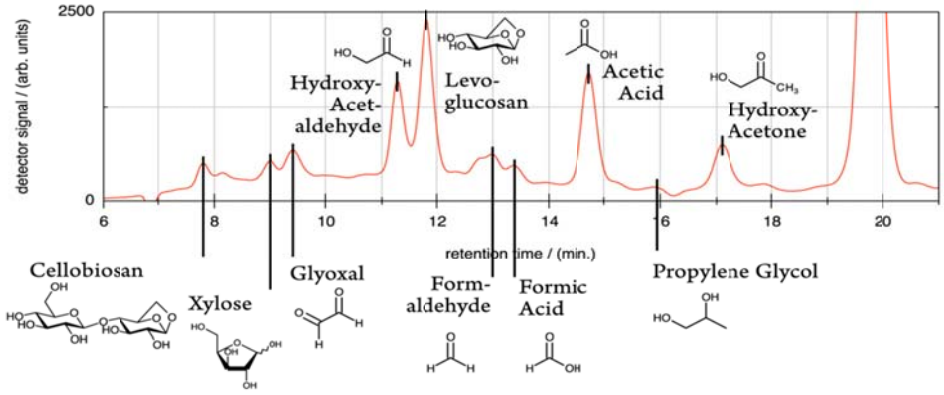

Figure 1.6: Assignment of peaks in the HPLC-chromatogram (sample: sawdust-oil).

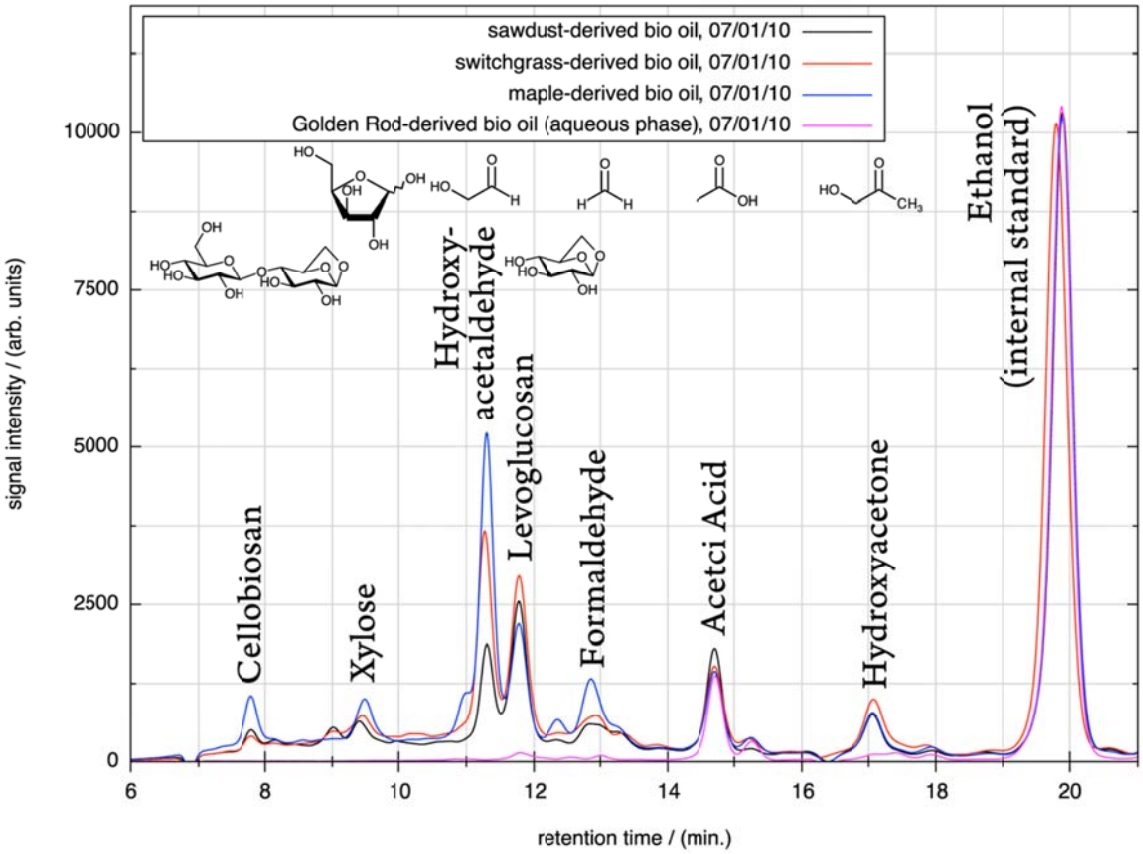

Figure 1.7: The HPLC-chromatograms of the four different pyrolysis oils used as test cases (for legend: see top left).

To allow quantification based on these results, calibration solutions were prepared and measured to obtain the necessary response factors ("sensitivity") of the system's RID detector towards the target analyte species (defined in Section II.2.). Based on these calibrations, the concentration of each of the target species in the four pyrolysis oils studied as test samples was evaluated (see Table 1.4 below); the sawdust- and switchgrass-derived samples were evaluated a few times (at least three times each) in two different months, and standard deviations between the evaluation results of these runs are included in the table. The maple- and Golden Rod grass-derived samples were evaluated only once in the HPLC.

Some of the standard deviations are relatively high, despite the good linearity and seemingly good precision of HPLC integration. The biggest source of that uncertainty reflected in the high standard deviations, derives not from the signal calibration, but from the non-zero baseline in the chromatograms of the pyrolysis oils, which is due to their being complex samples. Unlike the case of GC/MS, where the evaluation of ion chromatograms helps to circumvent treatments of non-zero base-lines, the HPLC only gives one detector signal, and thus the peaks have to be manually isolated from the baseline for integration as long as no analytical fits can be done. Since this process leaves room for interpretation, it is expected to be the main cause for deviations.

Table 1.4: HPLC Analysis of Different Samples of Pyrolysis Oils for Target Species

Absolute value in wt.-% Std.-Dev. in %		Sawdust		Switchgrass			Maple	Golden Rod
	Retention time (min.)	Avg.	Std.-dev.	Avg.	Std.-dev.	Mullen & Boateng, 2008		
Acetic Acid	14.75	6.03	19 %	5.09	6 %	2.94	4.12	4.74
Hydroxy-acetaldehyde	11.23	2.35	17 %	5.58	13 %	2.40	7.65	n.a.
Hydroxy-acetone	17.14	2.22	14 %	3.91	23 %	2.75	2.13	n.a.
Levoglucosan	11.83	3.85	15 %	4.54	19 %	6.38	3.22	n.a.

II.4.1. Discussion of the accuracy of HPLC Analysis

We believe that the data compiled in the table above are compelling proof that our HPLC analysis works with precision (*i.e.*, we are able to reproduce the results in our lab sufficiently). It is usually much harder to evaluate how accurate the results of the analysis of these highly complex pyrolysis oil samples are. Note also that matrix effects are expected to play an important role in such complex samples as those of pyrolysis oils, so that evaluation of the accuracy of results with such samples, based for example on evaluations of simple, defined solutions of the analytes, cannot fully predict the accuracy of the analysis results with the complex samples. For the purpose of the evaluation of accuracy for such complex samples, it is usually best to participate in Round-Robin tests (inter-laboratory comparisons) – which have not been available for pyrolysis oils recently. We were, however, evaluating that option (Douglas Elliott from P.N.N.L. recently gave a hint that a new Round Robin test was being planned).

The values obtained for the switchgrass-derived pyrolysis oil can, however, be compared with the values obtained by Mullen and Boateng (Mullen and Boateng, 2008). These reference data are also compiled in the table above). Our sample of switchgrass-derived pyrolysis oil comes from the same lab. However, the sample we analyze was produced on a date different from the one that they based their report on – and some deviations between the two samples should be expected. While some of the values are in good agreement, some of our analysis results differ considerably from the values obtained by the group at the U.S.D.A. – and they differ in both directions: for example, we found a lower value for levoglucosan than this group, whereas for acetic acid we found a significantly higher value.

A final explanation of these deviations cannot be given as of yet. It might either be an accuracy problem (*i.e.*, our data, although precise and reproducible, might be lacking in accuracy). Moreover, the deviations might as well be due to the deviations between the samples Mullen and Boateng analyzed, and our analysis sample – a possibility that was confirmed to us by Charles Mullen. Finally, those deviations can simply be due to the age of our sample compared to the age at which the ARS/U.S.D.A. analyzed their pyrolysis oil for the data in the reference (our sample was more than three years after preparation, dated 05/01/2007). Most likely, of course, the deviations are a consequence of all three reasons combined in various degrees.

From descriptions of similar analyses reported in Oasmaa and Meier (Oasmaa and Meier, 2005), we can at least conclude that the analysis results of different labs for some of the target species have deviated far more than the deviations discussed here, and, based on the small

amount of data currently available, we seem to be not too far from a desirable level of precision and accuracy.

III. Analytical Procedure for ATR Product

The ATR vapor product leaving the condenser (Task 3 below) was sent to a moisture trap to remove residual water. The water-free vapor product was analyzed in a gas chromatograph, a Shimadzu GC-14B equipped with two columns, HP Plot Q and HP Mole Sieve, manufactured by Agilent Technologies Inc., and a TCD detector for separation and quantification of the component species H_2, CO, CO_2, CH_4, N_2 and O_2. The carrier gas was Argon and an internal normalization method (Grob, 1977) was used to calculate the composition of the vapor product.

IV. References

Diebold, J. P. *A review of the Chemical and Physical Mechanisms of the Storage Stability of Fast Pyrolysis Bio-Oils* NREL/SR-570-27613; NREL: Golden, Colorado, January, 2000; pp 1-59.

Grob, R. L., ed. (1977) Modern Practice in Gas Chromatography, John Wiley and Sons, 181-184.

Mullen, C. A., and A. A. Boateng, "Chemical Composition of Bio-Oils Produced by Fast Pyrolysis of Two Energy Crops", *Energy & Fuels*, 2008, 22, 2104-2109.

Oasmaa, A. and D. Meier, p. 39 in "Fast Pyrolysis of Biomass: A Handbook", Volume 3 (CPL press, 2005)

Task 2: Pyrolysis Oil Atomization System Design & Evaluation

I. Summary

The objective of this task was to design, evaluate and optimize a low-maintenance atomization system that would aid the re-volatilization of the PO and deliver it to the entrance of the dual layer monolith ATR without appreciable char formation. The successful implementation of our process heavily depended on the re-volatilization step because of PO's tendency, even at moderate temperatures (~100^{o}C), to polymerize or form carbonaceous materials, which may be deposited as residues on the atomization system and downstream processing equipment, eventually clogging them, forcing process termination. There are several approaches to atomization of liquid fuels including mechanical, low and compressed air, low and high-pressure gas, steam atomization, and ultrasonic atomization. Mechanical atomization is used in applications where fine atomization is not required. Steam atomization is the most economical and commonly used atomization method but will be unsuitable for PO since the high temperature steam will increase the likelihood of polymerization and char formation. In addition, steam-atomized guns have small orifices, which may be blocked by the char fines in PO, especially if the PO is not hot-vapor filtered. Compressed air or high-pressure gas atomization will affect the production cost negatively as it may not be readily supported by the available infrastructure at the processing site.

In this study, we evaluated three different atomization systems, two of which are variants of mechanical atomization while the third one is based on ultrasonic atomization.

II. Atomization Systems

II.1. Mechanical (turbo-) Atomizer

We explored the use of a device that combines a mechanical (turbo-) atomizer with a vaporizer (AV), which was manufactured and supplied to us for evaluation by MSP Corporation, MN, USA. The atomizer shears the liquid into extremely tiny droplets, which are next sent through the vaporization section for vaporization. For proprietary reasons, the internal design of the AV, including the nozzle diameter, was not provided. In the first set of experiments, the AV was used without modification while in the second set of experiments, the vaporizer was removed and only the atomizer part was used. The AV had two separate nozzles, one for the atomizing gas and the other for the liquid. In the first part of the study, the atomizing gas used was N_2 while in the second case, a mixture of N_2 and steam was used. The whole purpose of using a mixture of gas and steam was to simulate actual conditions present during ATR of PO. Moreover, the amount of gas (or steam and gas) and PO used was close to that required during reforming. Clear tubing was connected to the exit of the AV for viewing the atomization pattern. After atomization (and vaporization), the liquid was collected in the line while the vapor was sent to the vent. The experiments were initially performed with water, and later model compounds – acetic acid, and methanol.

For the model compounds, the experiments were performed only with gas (without the use of steam). For the range of mass ratios and temperatures studied, a very fine mist, very close to vapor, was observed with each one of the model compounds even at the highest process liquid flow rate. The vapors did not condense on a sheet of cold paper suggesting that this was actually vapor and not mist. We next switched to PO using similar operating conditions as before. Initially, a fine vapor was seen at the exit of the AV suggesting adequate atomization but

after about 2 hours, we began to observe intermittently a thick brown liquid dripping from the exit of the vaporizer. The vaporizer part of the AV was then taken apart, and a thick highly viscous liquid was seen throughout the internals of the vaporizer. It was concluded that the PO was fractionated in the vaporizer, leaving behind the heavy components.

In order to avoid PO fractionation, the vaporizer section was removed and AV was operated only with the atomizer. The objective was to examine how effective the AV was as an atomizer by observing the spray pattern and evaluating the effect of flow rate of PO on the spray pattern and droplet size. Although the PO was finely atomized, the expanding cone of the spray would impose an operational constraint. It would require locating the AV as close as possible to the monolith reactor. Also, from the process point of view, a vaporizer can be viewed as a part of the tubular reactor for carrying out the ATR reaction. Thus, vaporization cannot be actually avoided but rather it has to be dealt with. One option is to re-design the atomizer/vaporizer to suit our application. MSP has agreed to work with Stevens to develop such a system that will address the problems we encountered, but as of the completion date of the project, no progress had been made on this collaborative effort.

II.2. Ultrasonic Atomizer

An arrangement was made with Sonotek Corporation, manufacturer of ultrasonic nozzle atomizers, to conduct a demonstration test of the atomization of our sawdust-derived pyrolysis oil. The objective was to establish the feasibility of atomization and generate a column of atomized liquid that could be fed into a glass tube in which a replica of our monolith catalyst was placed, approximately 12 – 16” away. On September 30, 2009, we visited Sonotek Corporation facility where exhaustive atomization tests were performed on the vacuum-filtered PO. Different atomizer systems were tested. We were able to atomize the PO at flow rates in the range of 0.1 to 3ml/min. The atomized spray maintained a plume of less than 1” for a distance of about 6 - 8”, and although we were not able to maintain a plume width of less than 1” for the entire length of the glass tube, we were able to demonstrate good atomization and spray control.

Based on this apparently successful demonstration, we came up with a design for the nozzle system in collaboration with Sono-Tek that we thought would best meet our requirements. This ultrasonic nozzle system, with a dual-bore nozzle configuration was fabricated and delivered to us. Initial cold-flow experiments were conducted, and the system performed remarkably well in producing fine atomization at all desired pyrolysis oil flow rates. We then explored various options to improve on the performance of the system as measured by the quality of atomization, including varying the flow rates of the different fluids and the system temperature. The viscosity and interfacial tension of the pyrolysis oil, both of which play an important role in liquid atomization, are greatly affected by temperature.

Although these cold-flow experiments were promising, the ultimate test of the atomization system would require the integration of the system with the ATR reactor system. Getting the reactants to go through the honeycomb structure at the bottom of the reactor quartz tube was recognized as a challenge, so also the shielding of the nozzle from the high temperature of the ATR reactor. In the end, the ultrasonic nozzle worked well to atomize the liquid under cold-flow conditions, leaving the matter of better controlling the plume width as well as nozzle system temperature as major obstacles to overcome.

To overcome these technical challenges, we designed and fabricated an adapter for the nozzle system. The modified experimental section consisted of the nozzle, 1” tee and an ***adapter*** connecting the nozzle with the tee. All these components were made of SS316 except as stated

below. One of the limitations of the ultrasonic nozzle, as stated above, was its inability to convey the atomized stream of liquid through the process equipment as the ultrasonic system did not require air (or gas) assistance for atomization. In our application, it was of utmost importance to convey the stream of atomized pyrolysis oil down to the monolith catalyst bed, which could be located far away from the nozzle. For this purpose, a high velocity atomizing gas would be needed. The atomizing gas served two purposes. It further sheared the liquid droplets, thereby reducing the final droplet size. More importantly, it played a significant role in conveying the droplets through the monolith. In addition to a port on the nozzle for atomizing gas, provision was made on the adapter for four other ports. The gas flowing through these ports were intended primarily for conveying the atomized oil into the monolith. For the testing of the set-up, a see-through acrylic ***adapter*** was used. The acrylic unit would later be replaced with SS316 adapter with slight modifications.

Pyrolysis oil derived from sawdust was vacuum filtered and the resulting oil was atomized using the nozzle. The experiments were started by flowing gas through the ports of the adapter, and the atomizing gas through the nozzle. The pyrolysis oil was then flowed using the HPLC pump before turning on the ultrasonic nozzle. For shut-down, the nozzle was turned off followed by the liquid flow. The gas flow was the last stream to be shut. It should be mentioned that the flow rate of gas through the ports was maintained between 1-5 SLPM.

II.2.1. Results

The tests were performed using acrylic unit. Some of the important results are summarized below:

- In the absence of any atomizing and conveying gas, a cloud of droplets was seen around the tip of the nozzle. There was slight backflow of the atomized stream thereby causing coalescence of droplets at the upper portion of the nozzle. It should be emphasized that this atomizing gas was important from the perspective of breaking the droplets further down.
- With the introduction of atomizing gas through the inbuilt port in the nozzle, the intensity of backflow increased tremendously and caused extensive coalescence at the top of nozzle. An increase in the flow rate of atomizing gas caused an increase in the turbulence and led to a more effective atomization. This also meant that there would be more backflow, which disappeared with the removal of atomizing gas.
- In order to get rid of the backflow, gas was flowed through the other ports of the adapter. It was observed that the ports were very effective in conveying the atomized liquid.

Atomization of pyrolysis oil was effectively done using Sono-Tek Ultrasonic nozzle. Although the droplet size was not measured, it was believed to be in the range of 20-60 microns as per the results obtained using other liquids. A cloud of atomized liquid droplets was seen to form around the nozzle tip in addition to some backflow. High velocity gas flow through specially designed ports was used to get rid of this backflow and convey it down to the monolith catalyst bed.

The acrylic adapter would not be able to withstand the high temperatures to which it would be exposed in the ATR reactor system; hence, it was replaced with the SS adapter and connected to the Sono-Tek ultrasonic nozzle. A transparent quartz tube was then attached downstream of the atomization device to allow for flow visualization. The ports on both the nozzle and the adapter were hooked up as previously described. The testing procedure implemented for the acrylic adapter last quarter was followed and the outcome, as expected was not different. Subsequently, the atomization system was incorporated into the reactor system as described below in Task 3 but the extremely high temperature environment of the ATR reactor system

prevented the use of this atomization system, hence we sought another option, an in-house nozzle system.

II.3. In-house Mechanical Atomizer

The Sono-Tek ultrasonic atomizer with the SS adapter was suitable for obtaining adequately fine mist of PO under cold-flow conditions. However, it was limited in application because of the built-in electronics that could not withstand high operating temperature. To achieve high heating rate needed to bring about the thermal cracking of atomized PO with minimum char formation, the nozzle tip had to be positioned close to a relatively high temperature zone (say, 400-700 ^{0}C) without polymerizing the PO around the nozzle tip (at this high temperature). In-house mechanical atomizers were therefore designed to overcome the operational issues associated with the ultrasonic atomizer. Mechanical atomizers, unlike most ultrasonic atomizers, are not constrained to low operating temperature, are relatively inexpensive, and operationally flexible. Our mechanical atomizer design was very simple and it featured fine-bore microchannel tubing into which both the PO and the atomizing gas were fed through a tee junction. At moderate gas flow rates, the flow in the tubing was the classical Taylor flow with alternating gas and liquid slugs. The high gas velocity shears the liquid into small slugs, which upon exiting the tubing are dispersed as fine droplets. As the diameter of the tubing decreases, the slug length also decreases but at the expense of increased pressure drop. At high gas rates, the flow regime became mist flow with the characteristic small size droplets, but with increase in pressure drop. Optimum values for the tubing diameter and flow rate of atomizing gas are obtained through a balance between the pumping requirements and the size of the atomized droplets of PO. Our in-house mechanical atomizer was able to achieve this balance.

Task 3: Experimental Dual Layer Monolith ATR Reactor System Design & Evaluation

I. Summary

An experimental laboratory dual layer monolith ATR reactor system was designed, and constructed. Performance and optimization studies on the ATR of whole pyrolysis oil involving varying the reactor temperature (500 – 800^{o}C), PO composition, residence time, H_2O/C ratio, and O_2/C ratio were carried out to determine their effects on the PO conversion, product gas composition, catalyst deactivation, and formation of carbon deposit. Initial performance studies were carried out for acetic acid (as a model compound of PO), and methanol-stabilized pyrolysis oil. Equilibrium calculations using the Aspen Plus© process simulator in conjunction with experimental data provided insight on reactor performance as well as guidance on the selection of the optimum process conditions.

II. Initial Experimental Planning and Design of the ATR Reactor System

A significant effort was directed at this task right from the beginning of the project since it represented perhaps the most important of all the tasks. A process diagram was prepared and Aspen Plus simulations were performed to aid in the selection of the optimum process conditions. Mixtures of model compounds (acetic acid, phenol, hydroxyacetaldehyde, and water) were used to simulate pyrolysis oil. Process conditions that maximize synthesis gas production and minimize coke formation were selected for the sizing of the process equipment. Next, a detailed Piping and Instrumentation Diagram (P&ID) for ATR reactor system was developed. In April 2009, about a month after contract negotiation with DOE-OBP was concluded, we held a meeting at BASF where we, amongst others: (1) Reviewed and commented on the P&ID, discussed materials of construction for ATR unit and identified acceptable vendors for supply of equipment (2) Discussed the use of model compounds in ATR first, before attempting to use viscous pyrolysis oil (3) Discussed molecular weight distribution of compounds from C1-compounds to Molecular-Wt of 1200, expected or known within the PO, and focused on model compounds such as acetic acid, crotonic acid, hydroxyl-acetaldehyde and phenol as starting compounds (4) Discussed some suggestions made by BASF for atomization of compounds in conjunction with fabrication of the upper heating zone of the ATR unit to facilitate vaporization of the atomized PO droplets while minimizing coke formation.

Based on the P&ID and process diagram, we prepared detailed parts list for equipment fabrication of entire unit. The reactor system should be capable of accepting the following feeds – hot or cold gas feeds, superheated steam, PO and solvents. Some char and/or ash deposits were expected and provisions were included in the design of the ATR chamber effluent system to handle these particles if present. Thermal stresses were a consideration in the design and selection of the ATR outlet cooling scheme along with special considerations for ATR catalyst poisoning and loss of conversion of the PO.

In May 2009, Stevens hosted a visit by BASF (Dr. Robert Farrauto, Lucas Dorazio) to observe the laboratory location and deliver cut catalyst cores for ATR unit. Catalyst support monoliths were both washed (dual layer treated) and unwashed blank (no catalyst material, just only support) catalysts.

While procuring and preparing orders for the main ATR reactor system, it was decided to use existing laboratory equipment to begin testing model compounds that would not require atomization, such as acetic acid. Several reactor system components were ordered including a simplified reactor tube of 316L Stainless Steel pipe and fittings, and several thermocouples, to

assemble this temporary test reactor. The unit was assembled and tested to operating temperatures without a catalyst monolith using de-ionized water and acetic acid, and the temporary unit was made ready for operation. The expectation was that data from this temporary system would provide guidance on the modifications that would be needed for the main ATR unit.

We received 4 gallons of sawdust-derived pyrolysis oil from Dynamotive to compare with existing samples (from switch-grass) previously provided to us by ERRC/USDA. We therefore had two samples of pyrolysis oil from two different biomass feedstocks as indicated in our proposal. There appeared to be a significant difference in the physical properties of the two samples of PO which might be related to the feedstock and shelf age.

In summary:

i) The process design of the main ATR reactor system was carried out including the preparation of the process diagram and the selection of the process conditions.
ii) The preparation of the Process & Instrumentation Diagram (PI&D) for the ATR reactor system was undertaken as well as the associated materials and equipment list.
iii) All the major pieces of equipment were sized, and quotes were received from vendors.
iv) A temporary ATR reactor system which could be used for model compounds that would not require atomization was designed and constructed from a previous experimental reaction system in the lab.
v) Pyrolysis oil from two different biomass feedstocks were supplied to us and intended for processing in the ATR reactor system.

III. ATR Experimental Studies of Acetic Acid

III.1. First Stage Experimental Study of ATR of Acetic Acid

The ATR of acetic acid (as a model compound for PO) was carried out in the temporary reactor system using the BASF dual layer monolith catalyst. One of the objectives of the initial study was to investigate the performance of the catalyst for production of synthesis gas (i.e. H_2/CO mixture) from oxygenates. The experimental setup comprised a feed section, a reactor unit, and an outlet/compositional analysis section. Temperatures were measured at the exit of the vaporizer, the inlet to the reactor system, and the outlet of the monolith. A furnace (MELLEN Microtherm MT 11) was used for heating the reactor system via a glass tube. The monolith was kept-in-place at the center of a stainless steel reactor pipe with a thermal blanket material wrapped around it. A re-circulating water bath maintained at 20^0C was used to condense the unreacted acetic acid (with freezing point of 17^0C), excess water, and other condensables before sending the non-condensable effluent stream to a GC (Shimadzu GC 14-B) for analysis. The GC which was purchased with a thermal conductivity detector (TCD) was equipped with a packed column (molesieve 5A) from a previous project in the lab, and was hence only suitable for analyzing for H_2, O_2, and N_2 in the exit gas mixture. While the preliminary experiments would provide some useful reactor performance data, a search was begun for GC columns and associated configurations that would effectively separate and analyze product gases containing CO, CO_2, CH_4, water, acetic acid, and acetone.

The optimum values of the operating variables such as steam-to-carbon (H_2O/C) ratio, oxygen-to-carbon (O_2/C) ratio, and feed and/or outlet temperature (to and/or from the monolith reactor) would provide information needed for the evaluation of the economic feasibility of the process. A water/acetic acid mixture (50% vol/vol) was fed from the HPLC pump into the ATR system at a total liquid flow rate of 2 mL/min, which corresponded to a H_2O/C ratio of 1.6. Other base

operating conditions used were O_2/C ratio of 0.4 (equivalent to air feed flow rate of 1.6 SL/min), gas feed temperature of 250^{0}C, and furnace temperature of 400^{0}C. Based on the "superficial" volume of the monolith catalyst used and the estimated monolith outlet gas flow rate (at STP, Q_{STP}), the gas hourly space velocity (GHSV = Q_{STP}/ V) was calculated to be between 21,450 and 29,254 hr^{-1} for the studied flow conditions. The duration of each experimental run was about 2 hours, after the furnace temperature (and thus the reactor system) had reached the set temperature. Using the GC, the mole fractions of H_2, O_2, and N_2 in the cooled effluent gas stream were determined.

Figure 3.1 shows the mole percent of H_2 in the product stream (without analyzing for other product gases except O_2 and N_2) obtained as a function of experimental run time at two O_2/C ratios. The yield of H_2 (per mole of the acetic fed) as a function of experimental run time was obtained at two O_2/C ratios (Fig. 3.2). At O_2/C ratios of 0.2 and 0.1, moderately high mol % H_2 (on average) of 36.3 % and 30.0% were obtained, respectively. Average yields of H_2 obtained at O_2/C ratios of 0.2 and 0.1 were 4.3 and 3.2, respectively. It was observed from the monitoring of temperature at the monolith outlet that the lower the O_2/C ratio, the more attenuated the temperature spikes at the monolith outlet; about 30 ^{0}C for O_2/C ratio of 0.1 but about 50 ^{0}C and 160 ^{0}C for ratios of 0.2 and 0.4, respectively. This result implied that there was an optimum amount of O_2 needed to achieve near-adiabatic ATR process.

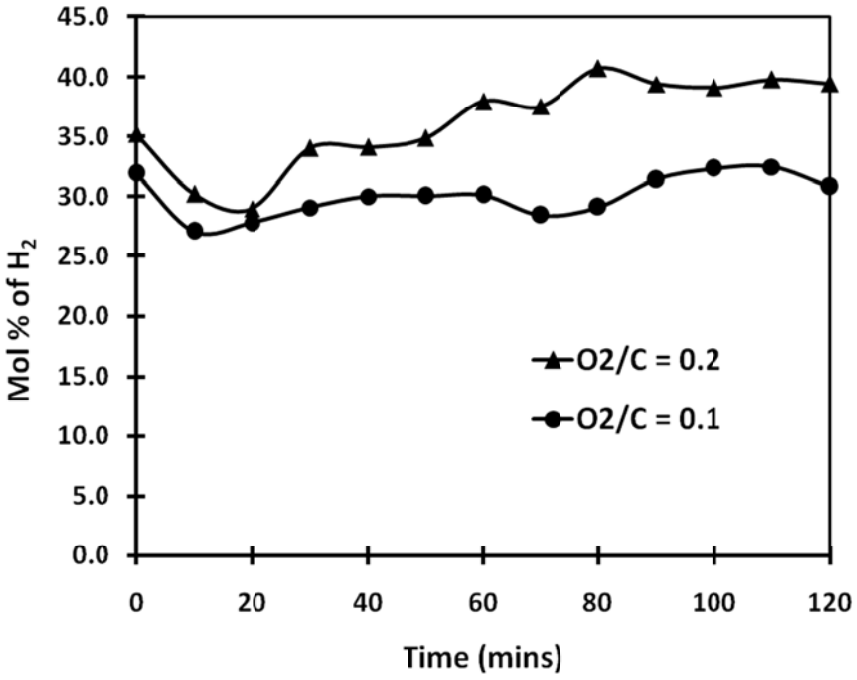

Figure 3.1: The plot of mol % of H_2 against run time at O_2/C ratios of 0.2 and 0.1.

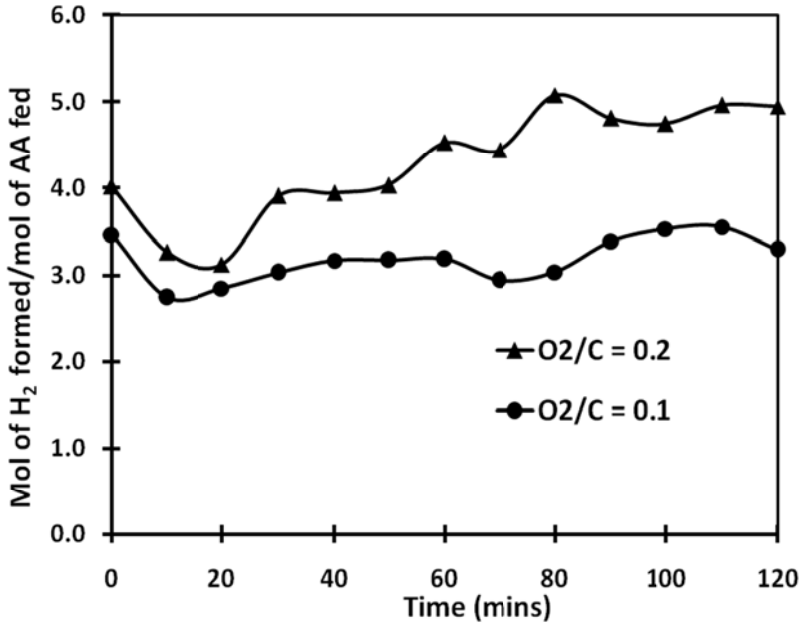

Figure 3.2: The plot of the yield of H_2 against run time at O_2/C ratios of 0.2 and 0.1.

III.2. Second Stage Experimental Study of ATR of acetic acid

In the second stage of the ATR of acetic acid, the GC (Shimadzu GC-14B) was reconfigured to accommodate two new capillary columns (Carboxen-1010 PLOT and HP-PLOT U) suitable for separating most of the components in the ATR effluent gas stream. These two columns were later replaced with Molesieve 5A and Plot Q because of the overlap of O_2 and N_2. Also, unlike in the experimental ATR results reported in Section III.1 where non-passivated stainless steel (SS) tubing was used to house the monolith catalyst, passivated SS tubing was used for most of the experiments in this section. A blank monolith was first used in the passivated tubing with experiments performed at 400 and 600 ^{0}C. The first set of experiments performed was to show that surface reaction was virtually absent. During the experimental run of about 2 hours (for each run), practically no H_2 was formed at a temperature of 400 ^{0}C while an average yield (mole of product per mole of the acetic acid fed) of about 0.024 was obtained at a temperature of 600 ^{0}C. The low H_2 yield at this moderately high temperature can be attributed to the non-catalytic, decomposition reaction occurring in the gas phase and not to the surface reaction. This result implied that the passivated SS reactor system should be used at high temperatures since unwarranted surface reactions are inevitable in the non-passivated SS tubing. It should be noted that in the preliminary experiments performed using non-passivated SS pipe, up to an average yield of 0.39 was obtained at a temperature of 600 ^{0}C.

Using the wash-coated monolith catalyst, the ATR reactor system was operated at 400 and 600 ^{0}C and two O_2/C ratios of 0.2 and 0.1. Each experiment was run for about 3 hours after the furnace temperature (and thus the reactor system) had reached the set temperature. At the base operating flow conditions of O_2/C ratios of 0.2 and 0.1, the gas hourly space velocities (GHSV) of 26,612 and 23733 hr^{-1} were calculated for the catalyst, respectively. These moderately low GHSV values imply high conversion of acetic acid to products. The result of the four experimental runs performed shows that the yields of H_2 and CO increase with increasing operating temperature, particularly at lower O_2/C ratio. Figure 3.3 shows the plot of mole % of the major components (H_2, CO, CH_4, and CO_2) observed in the GC analysis as a function of

O_2/C ratio for the reaction temperature of ~ 600 ^{0}C. The result shows that formation of most of these effluent components is highly favored at lower O_2/C ratio of 0.1. It also shows that more CO is formed with decreasing O_2/C ratio. This is expected since lower O_2/C represents incomplete combustion or partial oxidation of the acetic acid to CO and other products. The H_2/CO ratios at the two values of O_2/C ratio for the two operating temperatures are shown in Fig. 3.4. Numerically, H_2/CO ratios of 4.20 and 1.33 were obtained at 400 ^{0}C and O_2/C ratios of 0.2 and 0.1, respectively, while H_2/CO ratios of 4.64 and 2.71 were obtained at 600 ^{0}C and O_2/C ratios of 0.2 and 0.1, respectively. One of the objectives of our experiment was to investigate the performance of the catalyst for syngas (i.e. H_2 and CO) production with a desired H_2/CO ratio of ~ 2.0. A syngas with a H_2/CO ratio of ~ 2.0 is ultimately required since the syngas would be used later for Fischer-Tropsch synthesis to produce the desired transportation biofuel. It was important therefore to seek for the optimal processing conditions to achieve this goal. To complement the experiment, ASPEN process simulation runs were also performed to provide guidance in the selection and optimization of process conditions. Simulation runs were carried out initially for steam reforming of ethanol using one of BASF's catalysts since complete experimental data were available in the open literature (Simson, 2009). The ***equilibrium*** experimental data were in excellent agreement with ASPEN simulation results for the major components of the effluent gas stream, namely H_2, CO, CO_2, and CH_4. Simulation runs were also performed for the acetic acid-water mixture, and although the experimental data and the simulation results were in qualitative agreement, further improvement in the simulation was warranted as it appeared that the complete reaction pathways were not known for the ATR unlike simple steam reforming.

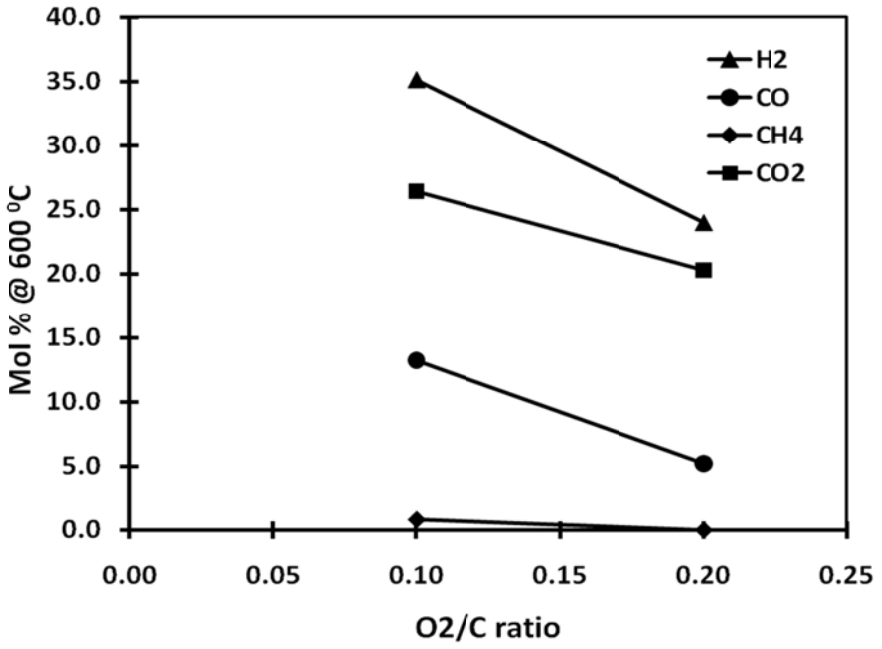

Fig. 3.3: The plot of mol % of H_2, CO, CH_4, and CO_2 at O_2/C ratios of 0.2 and 0.1.

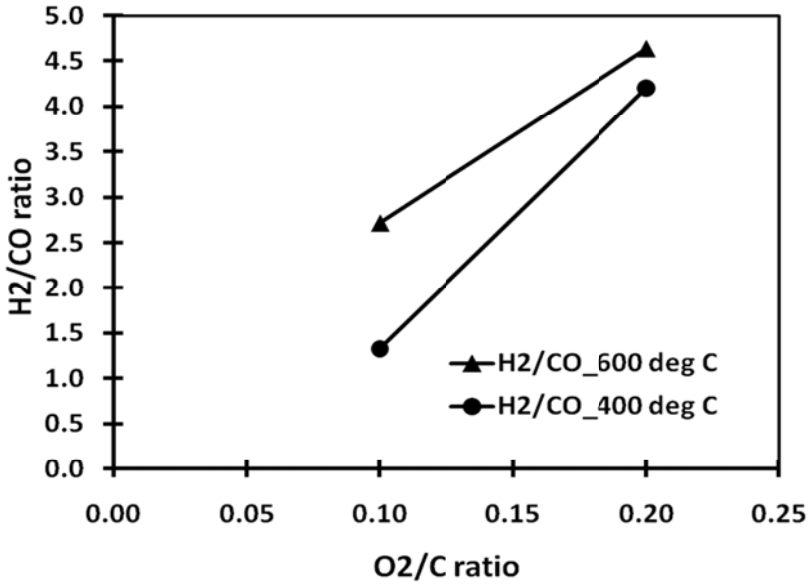

Fig. 3.4: The plot of H_2/CO ratio at O_2/C ratios of 0.2 and 0.1 (at T = 400 & 600 ^{0}C).

III.3. Final Stage Experimental Study of ATR of Acetic Acid

In the final stage of the ATR of acetic acid, the major objective was to conduct a systematic performance study that would cover a broader range of the process variables already studied, and other relevant variables. Also, through the first two stages, it was realized that more work would need to be done on the ATR setup and the GC configurations to allow for effective closing of the material balance of the ATR process. Therefore as a first step in this final stage, we resolved most of the operational issues with the ATR setup which then made it possible to obtain consistent experimental results. Reasonable material balance closure was subsequently achieved for the ATR process. Analyzing and quantifying almost all of the expected and/or likely components in both the reactor effluent dry-gas and condensate streams was critical to this effort. Although a significant amount of time was devoted to this effort, it was justified by the fact that the knowledge and experience gained in the ATR of acetic acid would be leveraged when we commenced the study on pyrolysis oil.

III.3.1. Equilibrium Studies of ATR of Acetic Acid

The first set of experimental runs was made at S/C = 1.6 and O_2/C = 0.10 while varying $T_{r,inlet}$ from 400 - 700 ^{0}C. The monolith catalyst used for these runs was 0.732 inch in diameter and 1.32 inches in length. Based on the catalyst used, and depending on the reactor exit gas flow rate, the calculated GHSV values varied from 17,000 to 21,000 hr^{-1}. This operating GHSV range was low for these experimental runs to be considered to be at or close to equilibrium. After reducing the catalyst in a stream of H_2/N_2 mixture, the ATR process was then run for about 2 hours (to reach steady state) before starting to acquire (for at least the next 3 hours) the effluent gas and liquid composition data. The result from the first set of runs showing the mole % (on water-free basis) of the effluent gas stream is presented in Table 3.1 below.

Table 3.1: The mole % of the dry effluent gas stream as a function of $T_{r,inlet}$

$T_{r,inlet}$	Mole % (of effluent gas stream (water-free basis)					
(^{0}C)	H_2	O_2	N_2	CH_4	CO	CO_2
400	29.55	0.00	30.77	1.02	5.44	33.23
500	36.22	0.00	25.49	1.71	5.43	31.16
600	41.02	0.00	24.55	0.82	7.82	25.79
700	44.17	0.00	17.42	2.20	11.68	24.53

As expected, both the compositions of H_2 and CO increase with $T_{r,inlet}$ while the CO_2 mol % decreases with $T_{r,inlet}$. In essence, the formation of H_2 and CO is favored by high operating reactor temperatures for the ATR of acetic acid while lower temperatures favor the formation of CO_2. This implies that the ATR process needs to be operated at a high temperature to achieve the desired H_2/CO ratio. At the low operating O_2/C of 0.10, the O_2 in the air was completely consumed, as expected. Using Aspen Plus software (a versatile process simulator), thermodynamic equilibrium calculations can be made to understand the ATR process conditions and better predict what can be expected experimentally. Figure 3.5 shows the plot of the composition of the effluent gas mixture (H_2, CO_2, CO, and CH_4) as a function of $T_{r,inlet}$ for both the numerical prediction and experimental data. It can be observed that the results of the Aspen Plus simulation and the experiment data compare reasonably well (see Fig. 3.5). Although it is possible that thermodynamic equilibrium was not attained, other reason(s) for the difference between the simulation results and experimental data, especially for CH_4 at lower $T_{r,inlet}$ (and for H_2 to some extent) needed further investigation.

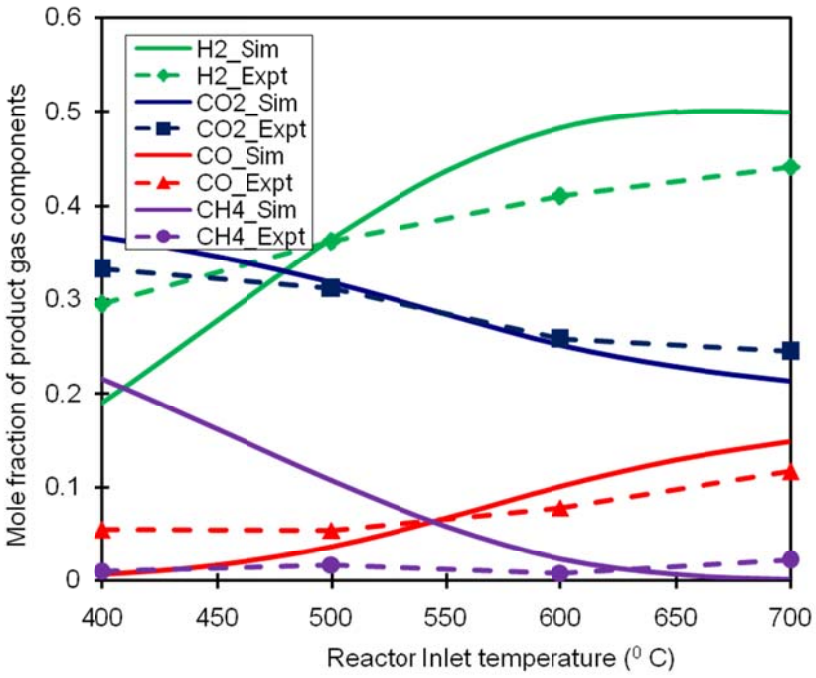

Fig. 3.5: The plot of the mole fraction of product gas components as a function of $T_{r,inlet}$ (for both the simulation and experiment).

III.3.2. Performance and Optimization Studies of ATR of Acetic Acid

Upon the completion of the initial equilibrium studies, the performance study on the autothermal reforming of acetic acid to synthesis gas mixture was begun. During the course of performing the experimental runs, the fresh catalyst used started losing its activity after about total on-stream time of 50 hours (over a period of a few weeks). However, the monolith catalyst was regenerated by passing O_2 (from air flowing at 0.250 L/min at a reactor temperature of 500 ^{0}C) over it for about 30 minutes before making subsequent runs. Prior to each experimental run, the flow of O_2 over the catalyst was performed as part of the catalyst regeneration step (see Task 5 below) before the catalyst reduction step which was usually carried out with a stream of 10% H_2/N_2 mixture flowing at 0.250 L/min for about 45-60 minutes at a reactor temperature of 500 ^{0}C.

The performance study involved carrying out experimental runs to evaluate the performance of the catalyst under different flow and reaction parameters such as the temperature of the gas stream entering the monolith reactor ($T_{r,inlet}$), steam-to-carbon ratio (H_2O/C), oxygen-to-carbon ratio (O_2/C), and the gas hourly space velocity (GHSV). The relevant operating ranges investigated for the parameters above were: $T_{r,inlet}$ from 400 - 700 ^{0}C, H_2O/C from 1.6 to 3.0, O_2/C from 0.00 to 0.25, and GHSV from ~ 8,500 to 12,500 hr^{-1}.

Depending on the process conditions, a combination of possible reactions for ATR of acetic acid given by Eqns. (3.1) – (3.6) below can occur.

$C_2H_4O_2 + 2H_2O \Rightarrow 2CO_2 + 4H_2$	(steam reforming, ΔH^0_{298} = 131.4 kJ/mol)	(3.1)
$C_2H_4O_2 + O_2 \Rightarrow 2CO + 2H_2O$	(partial oxidation, ΔH^0_{298} = -266.6 kJ/mol)	(3.2)
$CO + H_2O \Leftrightarrow CO_2 + H_2$	(water-gas shift, ΔH^0_{298} = -41.1 kJ/mol)	(3.3)
$C_2H_4O_2 + 2O_2 \Rightarrow 2CO_2 + 2H_2O$	(complete oxidation)	(3.4)
$C_2H_4O_2 \Rightarrow 2CO + 2H_2$	(decomposition)	(3.5)
$C_2H_4O_2 \Rightarrow CH_4 + CO_2$	(decomposition)	(3.6)

Based on stoichiometry for the complete steam reforming reaction of acetic acid (given by Eqn. 3.1), 2 moles of H_2O will be required per 1 mole of acetic acid. It should be noted that this H_2O/acetic acid ratio corresponds to H_2O/C molar ratio of 1.0, which was the optimum H_2O/C ratio used in our experimental runs. In order to investigate the effects of $T_{r,inlet}$ as well as H_2O/C ratio on the product gas distribution, two sets of experimental runs were conducted at O_2/C = 0.10 with $T_{r,inlet}$ ranging from 400 - 700 ^{0}C for H_2O/C of 1.6 and 1.0. The results of these two sets of runs are plotted and shown in Figs. 3.6 and 3.7. Figure 3.6 shows the plot of the mole % (on a water-free basis) of the main effluent gas components (H_2, CH_4, CO, and CO_2) as a function of $T_{r,inlet}$ at a H_2O/C ratio of 1.6. As expected, increasing temperature favors the endothermic steam reforming (see Eq. 3.1) of acetic acid to produce higher yields of H_2 as seen in both Figs. 3.6 and 3.7. Since the ATR is generally a combination of exothermic partial oxidation and endothermic steam reforming, CO formation is also favored at higher temperatures (as shown in Figs. 3.6 and 3.7) due to the acetic acid partial oxidation and/or reverse water-gas shift reactions (see Eqns. 3.2 & 3.3). At the same values of $T_{r,inlet}$, it can be seen in Figs. 3.6 and 3.7 that at the lower H_2O/C ratio of 1.0 (compared to 1.6) lower mol% of H_2 but higher mol% of CO were obtained. Therefore the H_2O/C of 1.0 compared to 1.6 better favors the desired H_2/CO ratio. For instance at $T_{r,inlet}$ = 600^{0}C, H_2/CO ratios of 2.91 and 4.40 were obtained for the H_2O/C ratios of 1.0 and 1.6, respectively.

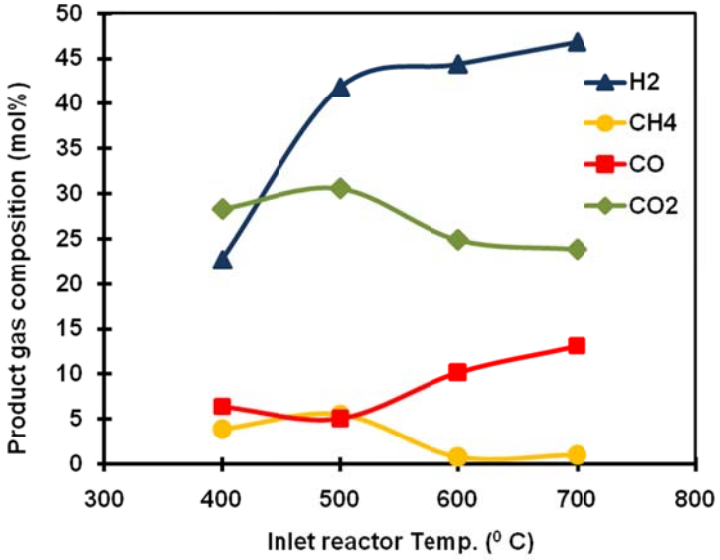

Figure 3.6: The plot of the mole % of main product gas components as a function of $T_{r,inlet}$ for H_2O/C = 1.6.

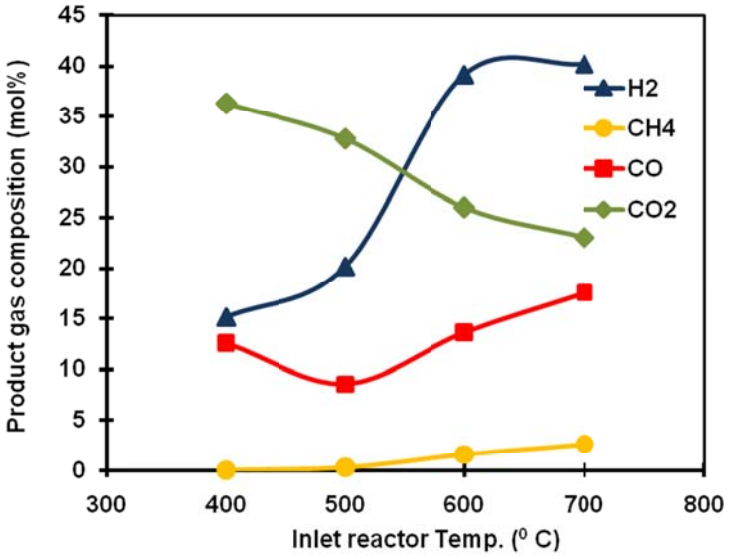

Figure 3.7: The plot of the mole % of main product gas components as a function of $T_{r,inlet}$ for H_2O/C = 1.0.

The effect of H_2O/C ratio on the product gas distribution was further investigated at a constant $T_{r,inlet}$ of 600 ^{0}C and O_2/C = 0.10. Figure 3.8 shows the plot of the mole % (on a water-free basis) of the main effluent gas components versus H_2O/C ratio (ranging from 1.0 to 3.0). The plot shows that increasing H_2O/C ratio generally leads to increase in H_2 formation but decrease in CO formation and vice versa. In essence, the lowest H_2O/C ratio required for minimization of

coke formation is desired to obtain the required H_2/CO ratio. The effect of O_2/C ratio on the product gas distribution was also studied at a constant $T_{r,inlet}$ of 700 ^{0}C and H_2O/C = 1.0. The obtained result is plotted as Fig. 3.9, showing that there is a slight increase in mol% of H_2 as O_2/C ratio decreases from 0.25 to 0.05. This observation is expected since at low O_2/C ratio less acetic acid is partially oxidized so that more acetic acid is available for steam reforming to give higher yield of H_2. Therefore, lower O_2/C ratio generally favors a H_2/CO ratio of around 2.0 (suited for producing Fischer-Tropsch fuels). Since the objective of this subtask is to use the ATR system to produce an effluent gas stream with the desired H_2/CO ratio of about 2.0, this ratio was calculated for the experimental runs made. The lowest value of H_2/CO ratio of 2.25 was obtained at O_2/C = 0.05 when $T_{r,inlet}$ = 700 ^{0}C and H_2O/C = 1.0. Figure 3.10 shows the plot of H_2/CO molar ratio versus O_2/C ratio (for H_2O/C = 1.0 and $T_{r,inlet}$ = 700 ^{0}C). At the same conditions as in Figure 3.10 except an inlet temperature of 600 ^{0}C, for an O_2/C ratio of 0.1, the H_2/CO is 2.9 in comparison to the value of 2.3 for 700 ^{0}C. We expect the trend at 600 ^{0}C to be similar to that of 700 ^{0}C.

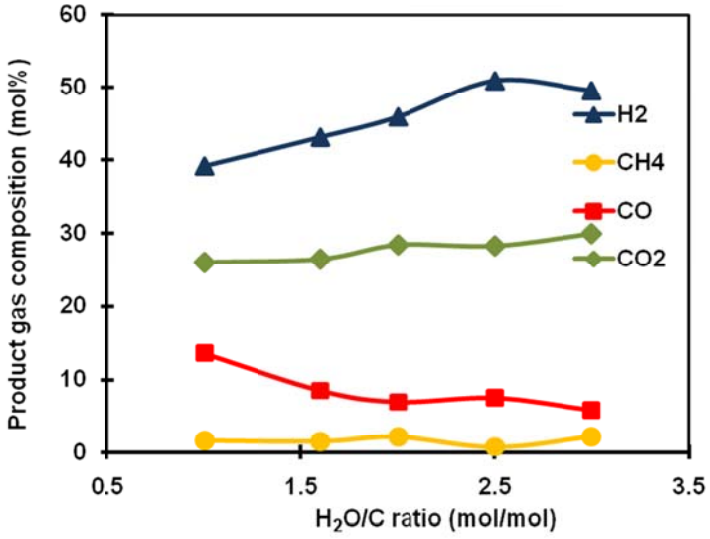

Figure 3.8: The plot of the mole % of main product gas components as a function of H_2O/C ratio (at O_2/C = 0.10 and $T_{r,inlet}$ = 600 ^{0}C).

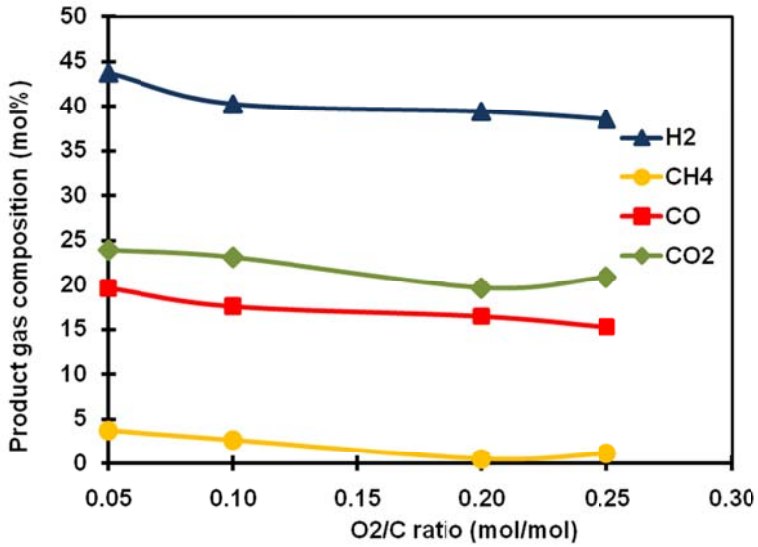

Figure 3.9: The plot of the mole % of main product gas components as a function of O_2/C ratio (at H_2O/C = 1.0 and $T_{r,inlet}$ = 700 ^{0}C).

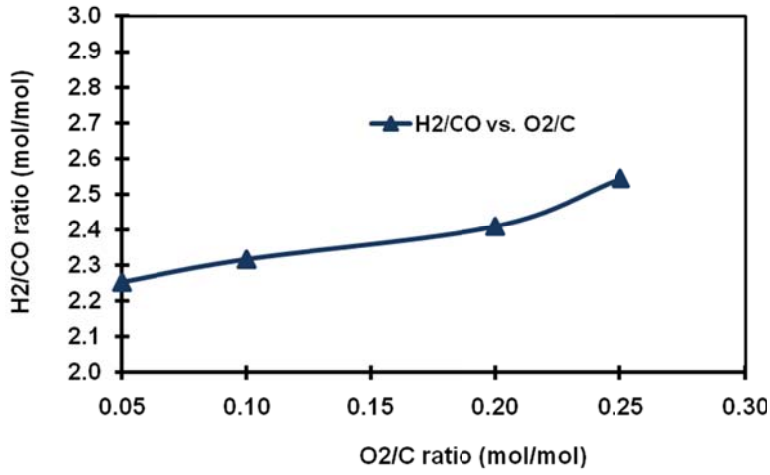

Figure 3.10: The plot of H_2/CO molar ratio as a function of O_2/C (for H_2O/C = 1.0, $T_{r,inlet}$ = 700 ^{0}C).

IV. ATR Experimental Studies of Pyrolysis Oil

After the completion of the relevant experimental runs with acetic acid as a model compound for pyrolysis oil (PO), our focus was then shifted to the autothermal reforming (ATR) of PO using

the same catalyst. The experimental setup, procedure used and results obtained from the ATR of acetic acid thus served as a good foundation for processing the more complex PO. Although some operational and technical issues associated with the ATR of the sawdust-derived PO were encountered at the beginning, the results obtained from the initial experimental runs were promising.

IV.1. Incorporation of Atomization System into the ATR Reactor System

Although the acetic acid/water mixture did not seem to require atomization for effective processing in the ATR reactor system, it was decided to incorporate the Sono-Tek atomizing ultrasonic nozzle (Task 2 refers) into the experimental set-up in preparation for the difficult-to-process pyrolysis oil. The Sono-Tek atomizing ultrasonic nozzle was designed to fit into a straight thread adapter shroud typically also supplied by Sono-Tek. The ATR reactor was made of 1" O.D. tubing and used 1" Compression fittings to interface all tubings. The ATR top fitting used a Tubing TEE arrangement of 1" Swagelok x 1" Swagelok x 1" FNPT. The 1" FNPT was on the TEE run and should be used for threading the male threaded Sono-Tek nozzle. However the thread types and sizes of the 1" FNPT of the Tubing TEE and the 1.437" x 28 UN straight thread of the Sono-Tek nozzle did not match. In order to mount the Sono-Tek nozzle on the Tubing TEE at the FNPT threaded end, a decision was made to fabricate an adapter bushing fitting that would accept the Sono-Tek Nozzle and also attach into the Tubing TEE FNPT threads without modifying either the nozzle or the TEE. This added device then presented other opportunities for controlling the processing conditions. Detailed mechanical drawings of the mounting device were prepared and submitted to a machine shop for fabrication.

IV.2. First Stage Experimental Study of ATR of Pyrolysis Oil

Upon the fabrication of the adapter for the Sono-Tek ultrasonic nozzle, the experimental setup was redesigned principally to accommodate the atomization nozzle. The adapter also provided additional liquid and gas feed lines. The effective atomization of the PO to small droplets is crucial to its thermal cracking before catalytic reforming to the desired products. Besides modifying the reactor system configuration for the nozzle, a few changes were made to the previous experimental procedure in order to process the PO through the reactor system. Methanol was usually passed through the ATR reactor system for about 30 minutes to stabilize the system at the beginning and for cleaning at the end of each experimental run. The temperature of the electronics controlling the nozzle system was maintained usually between 70 and 90 ^{0}C; though the manufacturer's recommended maximum temperature is 150 ^{0}C. Maintaining the nozzle electronics at this temperature range was important to obtaining unrestricted atomization of PO since PO flows well and is thermally stable at temperatures below about 80 ^{0}C. For the first run, the temperature of the steam was maintained at 350 ^{0}C before contacting/mixing with the atomized PO/air mixture, while the PO and air were at ambient temperatures before reaching the nozzle section. Other base operating conditions used were: $T_{r,outlet}$ (the temperature of the monolith catalyst bed close to the gas stream exiting the bed) of 700 ^{0}C; O_2/C ratio of 0.4 (equivalent to air feed flow rate of 1.26 L/min); and H_2O/C ratio of 3.0 (corresponding to water flow rate of 1.35 mL/min and PO flow rate of 0.68 mL/min). It is worth noting that the estimated amount of 30 wt% of water in the sawdust-derived PO was accounted for in the calculation of the H_2O /C ratio of 3.0 used in the experimental runs.

Using the GC (Shimadzu GC-14-B), the composition of the product gas stream (containing H_2, O_2, N_2, CO, CO_2, and CH_4), was determined. The average values of the component species over the run duration are given in Table 3.2 below.

Table 3.2: The mole % of the dry effluent gas stream for ATR of PO at $T_{r,outlet}$ = 700 ^{0}C

Mole % (of dry effluent gas stream)					
H_2	O_2	N_2	CH_4	CO	CO_2
21.20	0.00	50.87	1.44	3.66	22.83

The ATR setup had to be shut down after running the system for about 1 hour 45 minutes because of the high pressure that started building up within the system over time. Upon taking apart the reactor system, it was found that the pressure build-up was as a result of clogging caused by deposition of tar-like material (char) in the section between the atomizer and the top of the monolith catalyst bed. This observation was not unconnected with the axial heat conduction from heating the reactor tubing (using the furnace), thus making it difficult to control the temperature of the upper part of the reactor system. Therefore in the subsequent runs, changes were made to the feed concentration and the experimental reactor configuration used. The pure PO liquid feed was changed to a mixture (a 50 wt% PO in methanol) to see whether subsequent runs could be made for a longer time before the system clogged up. The reactor system configuration was also modified. In order to control the temperature of the section where the undesirable char formed, external water cooling was provided for that section. Although the situation improved considerably, char deposition persisted and still prevented the experiment from being run for a long duration. It should be noted that all the modifications made did not lead to appreciable change in the main product gas yields, they only made the duration of the experiment (before clogging) longer or shorter for similar runs. Table 3.3 shows for three runs, the composition data for the ATR of 50 wt% PO in methanol at $T_{r,outlet}$ = 700 ^{0}C.

Table 3.3: The mole % of the dry effluent gas stream for ATR of 50 wt% PO in methanol at $T_{r,outlet}$ = 700 ^{0}C

RUN	Mole % (of dry effluent gas stream)						
	H_2	O_2	N_2	CH_4	CO	CO_2	H_2/CO
1	26.99	0.00	47.08	0.55	13.85	11.53	1.96
2	27.09	0.00	46.40	0.90	12.80	12.81	2.37
3	26.50	0.00	46.46	0.86	14.40	11.77	1.85

The complex PO components are generally thermally stable, especially at the typical operating temperature of the ATR system, therefore the thermal cracking of PO usually led to the formation of lignin components instead of the desired smaller PO molecules and vapor. Therefore, immediately after the PO atomization, it is important to thermally crack the PO as quickly as possible into smaller molecules before catalytic reforming process to synthesis gas. The main challenge was to maintain the temperature of the atomized PO around the nozzle section low enough (ideally around 80 ^{0}C) while keeping the temperature of the atomized PO vapors entering the catalyst bed high enough (say, between 550 – 650 ^{0}C) without char formation in the transitional heating zone between the cold and hot zones.

In the next stage, we decided to replace the one-zone furnace with a new three-zone furnace for the performance study on the ATR of PO. With this three-zone furnace and the advanced control systems, more effective control of the reactor system temperature, especially the critical transition zone between the atomizer and the top of the monolith catalyst bed, would be possible. Calculations and tests would be made to achieve high heating rate within this zone so that the atomized PO was thermally cracked quickly without the heavier lignin component depositing inside and on the walls of the reactor tubing, blocking the flow of the vaporized PO components. Addressing the above-mentioned technical issues would allow the ATR system to be run effectively and for a longer duration.

IV.2. Second Stage Experimental Study of ATR of Pyrolysis Oil

In this stage, the autothermal reforming (ATR) of pyrolysis oil (PO) to synthesis gas was studied as a two-step process, namely thermal (non-catalytic) cracking and catalytic reforming. Studying and optimizing separately each of these two process steps was very important to the overall success of the ATR process. Experiments were thus carried out to first study and optimize the thermal cracking of PO. Various process conditions and configurations were tested and optimized for the ATR setup in order to achieve the desired goal of minimizing char formation while thermally cracking the sawdust-derived PO into smaller PO molecules in the form of oxygenated vapors, hydrocarbons, and permanent gases. It is worth mentioning that the suitable distribution of the products from thermal cracking of the PO would be crucial to the success of the subsequent catalytic reforming to syngas using the BASF dual-layer monolith catalyst.

The thermal cracking of the PO was first performed inside a semi-batch reactor (25 mL Parr Compact Reactor) equipped with an agitator (0-1500 rpm) for achieving good mixing and thus minimization of hot spots. This reactor was partially filled with sand, which acted as an inert porous material that aided in the minimization of the polymerization of the PO inside the reactor. Using the ultrasonic nozzle (acquired from Sono-Tek) earlier reported, PO droplets were generated and fed into the reactor in the presence of N_2 or air. The results of the experiments performed inside the semi-batch reactor show that some thermal cracking of the PO was achieved despite the fact that the maximum temperature achievable inside the reactor was only about 350 ^{0}C. Ring-shaped carbonaceous deposits were formed inside the reactor and were found above the sand bed where the temperature was relatively low and mixing was inadequate.

This experiment, as well as the earlier experiments on the ATR of PO showed that effective atomization of PO, and extremely rapid heating of the atomized PO were critical to the successful catalytic reforming of the resulting oxygenated vapors to the desired syngas with minimal char formation. In order to achieve effective atomization and thermal cracking, different nozzle/atomizing systems were tested with relevant process configurations and conditions. The Sono-Tek ultrasonic atomizer used in earlier experimental runs was suitable for obtaining adequately fine mist of PO. However, it was limited in application because of the built-in electronics that cannot withstand high operating temperature. To achieve high heating rate needed to bring about the thermal cracking of atomized PO with less char formation, the nozzle tip had to be positioned close to a relatively high temperature zone (say, 400-600 ^{0}C) without polymerizing the PO around the nozzle tip (at this high temperature). In-house mechanical atomizers were therefore designed to overcome the operational issues associated with the ultrasonic atomizer. Mechanical atomizers, unlike most ultrasonic atomizers, are not constrained by low operating temperature, are relatively inexpensive, and operationally flexible.

The desired thermal cracking process should involve a continuous feed of well-atomized PO into a heated reactor in the presence of air and/or steam (in form of water). The new three-zone furnace would provide for more effective thermal control. The optimization of the proximity of nozzle tip to the furnace heating zone was also a critical factor in achieving high heating rate. In order to determine the optimum position for the nozzle tip, temperature profile experiments were conducted to measure the temperature along the inner wall, and at the center of the reactor at positions close to the nozzle tip.

Performance studies on the thermal cracking of PO were then carried out using the ATR setup similar to previous experimental setups except for the new atomizing system (in-house

mechanical atomizer), and the three-zone furnace. In the experimental runs reported here, 50 wt% PO in methanol (MeOH) was the feed to the ATR system to ensure operational stability. The base flow rate of PO-MeOH was 1.0 mL/min. Other operating conditions used include: $T_{rxtor-wall}$ (the temperature of the reactor wall at the middle of the furnace's first heating zone) of 650 - 725 ^{0}C; O_2/C molar ratio of 0.3 - 0.6; and H_2O/C molar ratio of 1.98 – 2.20. At the beginning and end of each run, pure methanol was usually run for about 30 minutes through the ATR system for stabilizing and cleaning the system, respectively. A series of experimental runs was made with the aim of determining the optimum process conditions for PO thermal cracking that would lead to minimization of char formation and maximization of oxygenated vapors. The temperature of the cracked PO vapor/gas mixture stream, monitored with a thermocouple at the center of the reactor tubing approximately 4 cm below the nozzle tip, was usually between ~ 710 and 790 ^{0}C. The components in the product gas stream such as H_2, O_2, N_2, CO, CO_2, and CH_4, were analyzed using a GC (Shimadzu GC-14-B). Some of the hot effluent oxygenated PO vapors were condensed while those that remained in the gas phase along with some hydrocarbons, which the GC was not calibrated for, were observed as unidentified peaks in the GC chromatographs. The amount of the solid carbon (C_{solid}) or char residue recovered inside the reactor after each run was also determined. Although we performed many experimental runs, for the purpose of illustrating the effect of O_2/C ratio and the position of the nozzle tip on the product distribution, the results of only three of the experimental runs are shown in Table 3.4. The total run time for each experiment was approximately 3 hours and the H_2O/C molar ratio was ~ 2 (including the water already present in pyrolysis oil).

Table 3.4: Product distribution from PO-MeOH thermal cracking: GC and char residue analysis (Sample Results)

RUN	Run Time (mins)	Nozzle tip position relative to the beginning of the heating zone	H_2/CO molar ratio	CO_2/H_2 molar ratio	Wt % Char (on PO basis)	% Yield of Char, on Carbon basis)	% Yield of $C_{gaseous}$ (i.e. CO+CO_2+ CH_4)	~ % $C_{balance}$ (i.e. HCs, HCOs)
1	180	Outside the heating zone with $T_{rxtor-wall}$ = 650 ^{0}C and O_2/C = 0.30	1.38	0.15	11.7	**27.0**	**45.8**	**27.2**
2	180	Inside the heating zone with $T_{rxtor-wall}$ = 725 ^{0}C and O_2/C = 0.30	1.74	0.30	7.6	**17.6**	**43.7**	**38.7**
3	180	Inside the heating zone with $T_{rxtor-wall}$ = 700 ^{0}C and O_2/C = 0.45	1.22	0.43	6.8	**15.7**	**62.7**	**21.6**

The results show that having the nozzle tip inside the heating zone led to smaller char residue compared to run 1 where the nozzle was outside of the heating zone. The reason was that with the tip of the nozzle in the heating zone, the atomized PO/air mixture experienced a high temperature gradient (high heating rate) leading to the minimization of the polymerization of PO, the main source of char formation. Although the atomized mixture was injected at different locations of the furnace, the effect of $T_{rxtor-wall}$ on runs 1 and 2 can be assessed on the basis of

the same O_2/C ratio. It is obvious that run 2 with higher $T_{rxtor\text{-}wall}$ yielded higher H_2/CO (that is closer to 2) and expectedly higher CO_2/H_2, compared to run 1. The effect of the operating O_2/C ratio on the wt. % of char (produced from the fed PO) for runs 2 and 3 (with similar $T_{rxtor\text{-}wall}$) is that run 3 with higher O_2/C ratio (= 0.45) produced smaller amount of char residue but higher CO_2/H_2 ratio and lower H_2/CO ratio, both of which are undesirable. Apart from the minimization of char residue, the thermal cracking should also lead to a low yield of CO_2 and more of the oxygenated vapors that can be easily reformed catalytically to syngas. In terms of product distribution, run 3 produced the highest % yield of "gaseous C" (based on the total % yield of CO, CO_2, and CH_4) and expectedly lowest % carbon balance (in terms of oxygenated vapors and hydrocarbon compounds) from the thermal cracking. In essence, if the reactor wall ($T_{rxtor\text{-}wall}$) was between 700 and 725^0C, an optimum O_2/C ratio should be sought that minimized PO gasification but maximized production of oxygenated vapor. The results above compare very favorably with data from similar experiments that have been reported in the literature (van Rossum, 2009; Rennard, 2009) although we intended to pursue further optimization of the system. It is worth mentioning that in some experiments that were run for shorter duration of time (~60 minutes), we obtained as low as ~3 wt% char (on PO basis) and (~7% on Carbon basis).

For the next stage of the ATR of pyrolysis oil, we planned to improve upon the design of our in-house atomizer with the objective of producing better atomization of the PO, and thus minimize further char formation. After conducting a few more experimental runs on the PO thermal cracking to cover other relevant process conditions, the catalytic reforming of the ATR process would be integrated into our performance studies. Processing pure PO instead of 50 wt. % PO-MeOH mixture in the ATR setup was also planned for the next stage of the work.

IV.3. Third Stage Experimental Study of ATR of Pyrolysis Oil

The work described in the second stage of the experimental study of ATR of pyrolysis oil focused on reactor performance and process optimization of ATR of methanol-stabilized pyrolysis oil. Methanol was added to pyrolysis oil in different proportions as a stabilizing agent and ATR of the mixture was conducted to evaluate its performance. After successfully accomplishing the parametric sensitivity studies (O_2/C ratio, H_2O/C ratio and reactor temperature) of ATR of the pyrolysis oil-methanol mixture, the next objective was to extend a similar approach to the ATR of whole PO. However, before embarking upon the parametric studies of ATR of whole PO, it was important that we first tested reactor performance with the highly viscous and harsh whole PO. The work in this stage therefore, focused on process design optimization, aimed at maximizing synthesis gas yield while minimizing solid carbonaceous deposit. In addition, the effects of reactor temperature, steam temperature and steam to carbon ratio were also studied. Once this task was accomplished successfully, in the final phase of ATR of PO, we will continue the parametric sensitivity study for whole PO with the new and optimized reactor and process design.

Effect of reactor temperature was investigated using our previous reactor configuration. However, in order to study the effect of steam temperature, two important modifications were made to the reactor. These modifications were implemented primarily for ease of operation, and also to accommodate superheated steam. The experiments were conducted with pyrolysis oil produced from a mixture of hardwood and softwood, and was supplied to us courtesy of Ensyn Corporation, Ontario, Canada. The elemental composition which was obtained using proximate analysis was performed by Robertson Microlit Laboratories, Ledgewood, NJ. The results are shown below, Table 3.5:

Table 3.5: CHN Analysis of Hardwood/Softwood-derived Pyrolysis Oil (from Ensyn Corporation)

C	H	O	N	Ash
40.59	7.49	51.92	<0.02	<0.10

The base conditions used for the ATR of pyrolysis oil were temperature of 750^{o}C, total steam (including the water in the pyrolysis oil) to carbon ratio of 0.84 and oxygen to carbon ratio of 0.38. For the study of the temperature effect, the steam to carbon ratio and the oxygen to carbon ratio were 0.93 and 0.62 respectively. The results are reported in terms of H_2 yield, CO yield, H_2/CO ratio and % solid carbon deposit. These performance parameters were defined in previous reports.

IV.3.1. Effect of reactor temperature

Figure 3.11 shows the effect of temperature on H_2/CO ratio, solid carbon deposition, CO yield and H_2 yield. It must be emphasized that water was vaporized *in-situ* inside the reactor for these tests. No external steam generator was used. Increasing the reactor temperature did not produce any significant change in the amount of solid carbon deposition. Moreover, there was a significant decrease in the amount of H_2 and CO formed. This was mainly due to the reduction of the extent of steam reforming.

IV.3.2. Process design modifications

From the studies on the effect of temperature, we observed that a significant amount of carbon dioxide was produced compared to carbon monoxide, the desired product. Therefore, we sought to investigate the feasibility of minimizing the amount of carbon dioxide, thereby producing higher carbon monoxide yields, but without significantly increasing the amount of solid carbon deposition. In order to accomplish this objective, the experimental set-up and conditions were modified. Some of the results are summarized below.

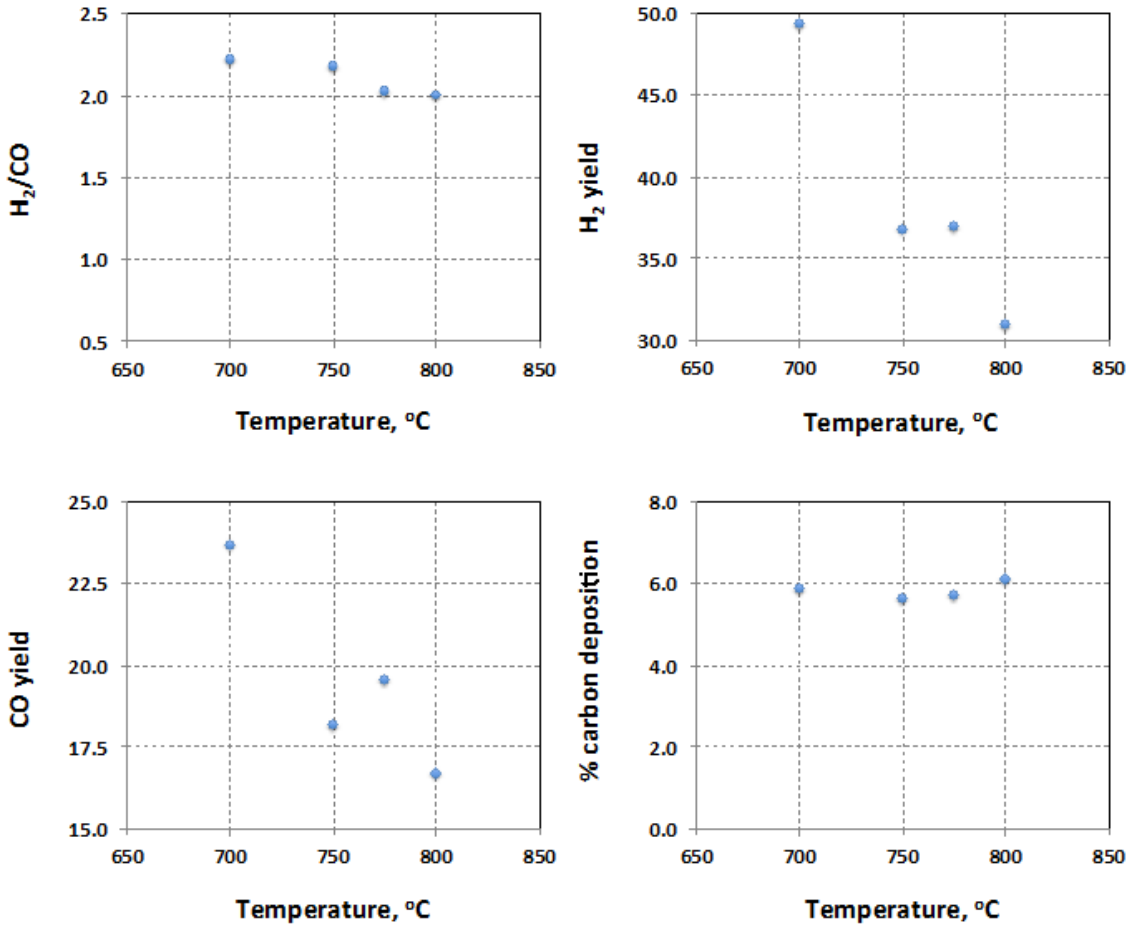

Figure 3.11: The effect of reactor temperature on product distribution for ATR of whole pyrolysis oil

IV.3.2.1. N_2 as atomizing gas

In this study, N_2 was used to atomize pyrolysis oil while reactant air was fed close to the top of the monolith catalyst. Water was sent through a separate 1/16" tubing, without vaporization. Figure 3.12 compares the results of ATR of N_2-atomized pyrolysis oil with the results obtained when air was used as the atomizing gas. It can be seen that using air as atomizing gas gave better results in terms of higher CO yield while minimizing the amount of solid carbon deposition. This can be attributed to better mixing of molecular O_2 with pyrolysis oil, which was unlikely in case of atomization with N_2 due to extremely short residence time in the reactor.

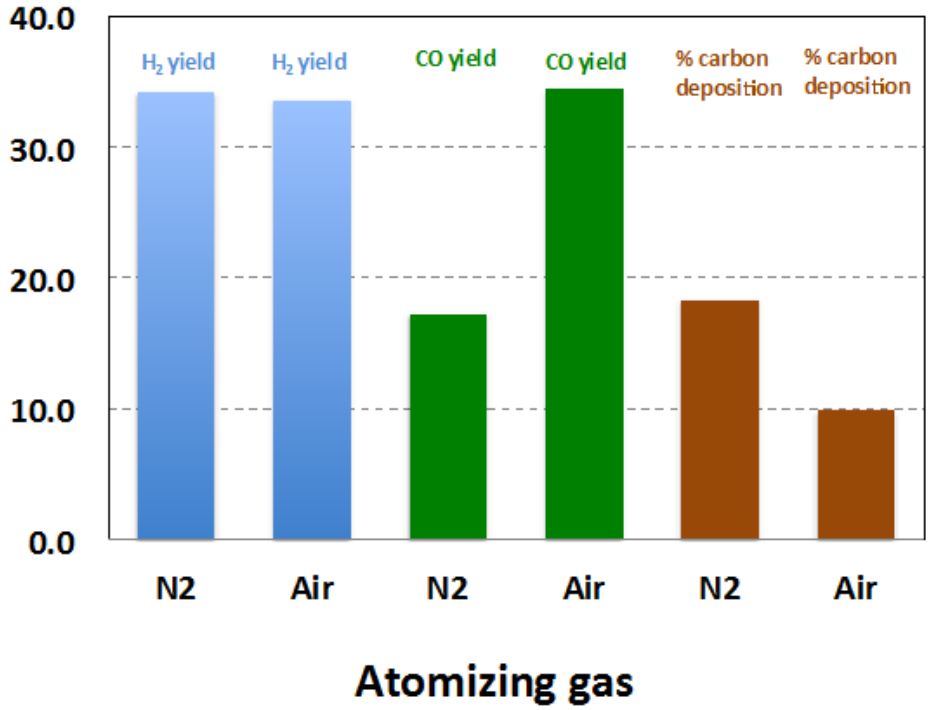

Figure 3.12: The effect of atomizing gas on product distribution for ATR of whole pyrolysis oil

IV.3.2.2. Location of release of air with respect to catalyst location

To increase the concentration of molecular O_2 reaching the monolith catalyst, one of the process design parameters that was studied was the distance between the catalyst and the location at which air was released in the reactor. In the earlier runs, air was sent through the water line, primarily to aid water atomization, the tip of which was located at the same height as that of the pyrolysis oil atomizer. In this study, this was modified such that air was fed separately and was released right on top of the monolith catalyst. The results are shown in Figure 3.13 and are compared with the earlier configuration where air was released at the same height as the PO. The steam to carbon ratio and the oxygen to carbon ratio were 0.93 and 0.54 respectively. With air fed right on top of the catalyst, an increased H_2 production was observed, however, CO yield was reduced which was probably caused by reduced oxidative cracking.

IV.3.2.3. Catalyst positioned right below atomizer tip

In an attempt to ensure molecular O_2 reaching the monolith catalyst, it was proposed to move the monolith catalyst right below the atomizer. In all previous experimental runs, the catalyst was placed in a heating zone separate from the oxidative cracking zone, approximately 215 mm below the atomizer. Two additional positions were experimentally studied: catalyst positioned 12 mm and 5 mm below the pyrolysis atomizer tip. One of the other reasons for this modification was to limit the residence time of atomized pyrolysis oil in the headspace above the monolith catalyst, with the idea that pyrolysis oil oxidative cracking is relatively fast. The results for the three cases are shown below in Figure 3.14:

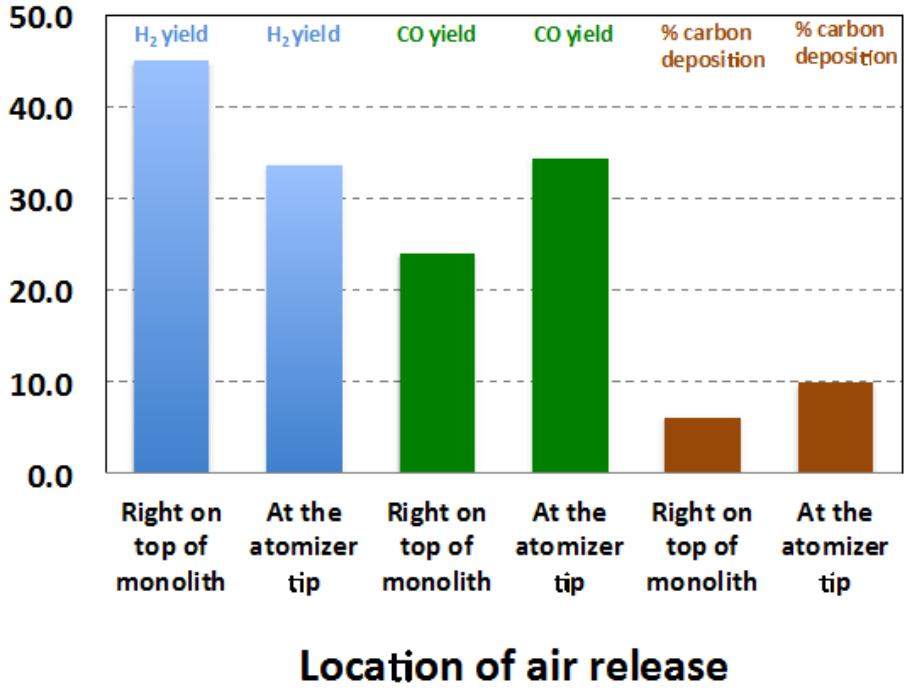

Figure 3.13: The effect of location of release of air on product distribution for ATR of whole pyrolysis oil

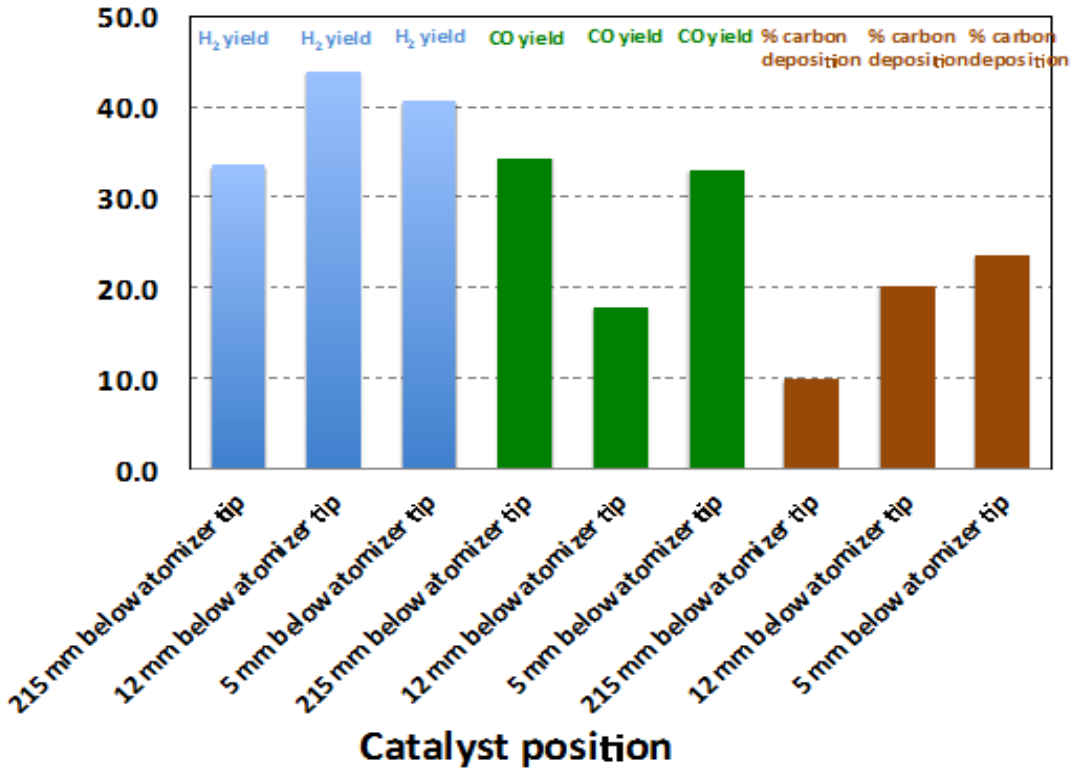

Figure 3.14: The effect of location of catalyst relative to atomizer on product distribution for ATR of whole pyrolysis oil

Moving the catalyst closer to the monolith catalyst helped in terms of higher hydrogen production but also led to increased carbon loss in the form of solid carbon deposited between the atomizer and the catalyst. In the same study, while keeping the catalyst location at 5 mm below the atomizer tip, the atomizing medium was changed from air to N_2. The comparison is shown below in Figure 3.15. Clearly, using air as the atomizing stream gave better results when compared to that using N_2.

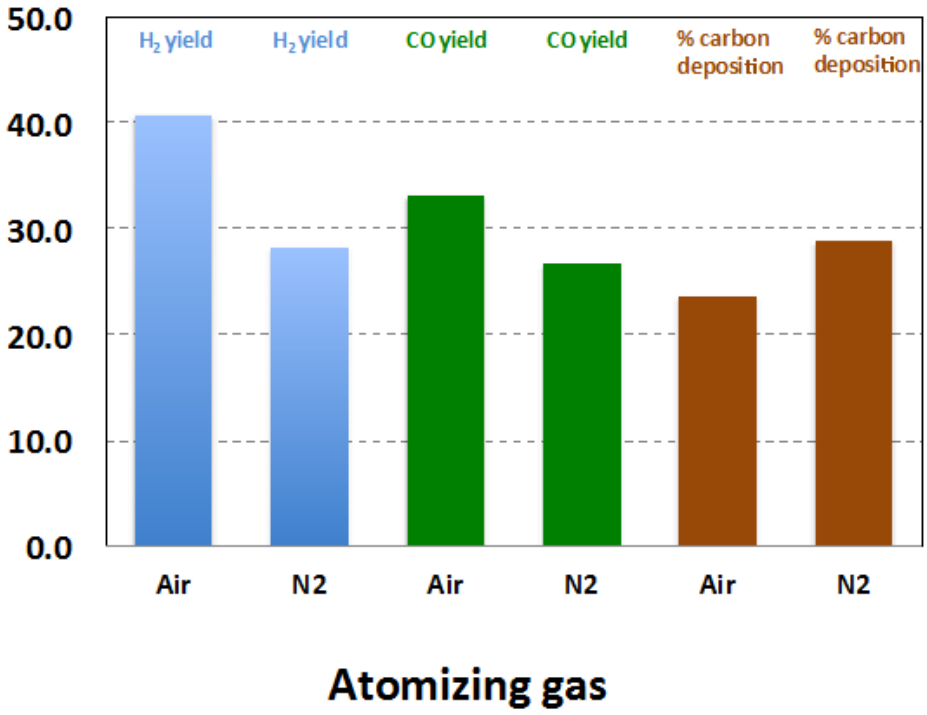

Figure 3.15: The effect of atomizing gas on product distribution for ATR of whole pyrolysis oil with the distance of 5 mm between catalyst and atomizer tip

IV.3.3. Effect of steam temperature

With the new reactor design, it became possible to study the effect of the temperature of injected steam. In the earlier runs, steam was generated in-situ inside the reactor, thereby having an indirect cooling effect on top of the monolith catalyst. To avoid such a cooling effect, the reactor was modified to accommodate superheated steam. Keeping the distance between the monolith catalyst and atomizer tip at 5 mm, the temperature of the steam was varied between 200^{o}C to 450^{o}C. The results are shown in Figure 3.16. Increasing the temperature of steam gave higher H_2 yields while causing a reduction in the amount of CO produced. However, as the steam temperature increased, so did the amount of solid carbon deposited.

IV.3.4. Effect of steam to carbon ratio

Keeping the distance between the atomizer tip and monolith catalyst at 5 mm, the effect of steam to carbon ratio on the ATR of pyrolysis oil was experimentally studied. Two values of steam to carbon ratios were studied while keeping the oxygen to carbon ratio fixed at 0.38 and reactor temperature at 750°C. The temperature of superheated steam was constant at 450°C. Figure 3.17 shows the effect of steam on H_2 yield, CO yield and the amount of solid carbon deposited during ATR of pyrolysis oil. Using higher steam to carbon ratio led to lower H_2 and CO production. While a reduction in CO yield could be explained by increased water-gas shift reaction, one would expect the H_2 yield to increase rather than decrease. Further experimental runs at different values of steam/carbon ration will be carried out in the next phase to confirm these results.

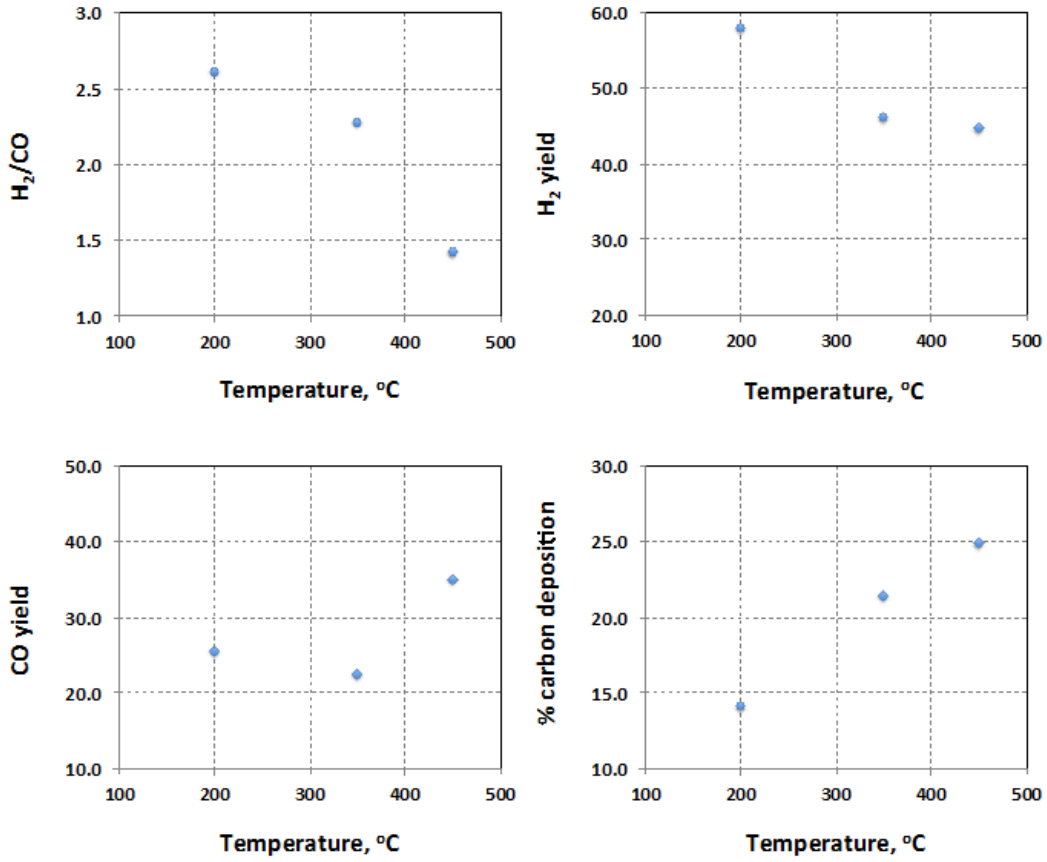

Figure 3.16: The effect of reactor temperature on product distribution for ATR of whole pyrolysis oil with the distance of 5 mm between catalyst and atomizer tip

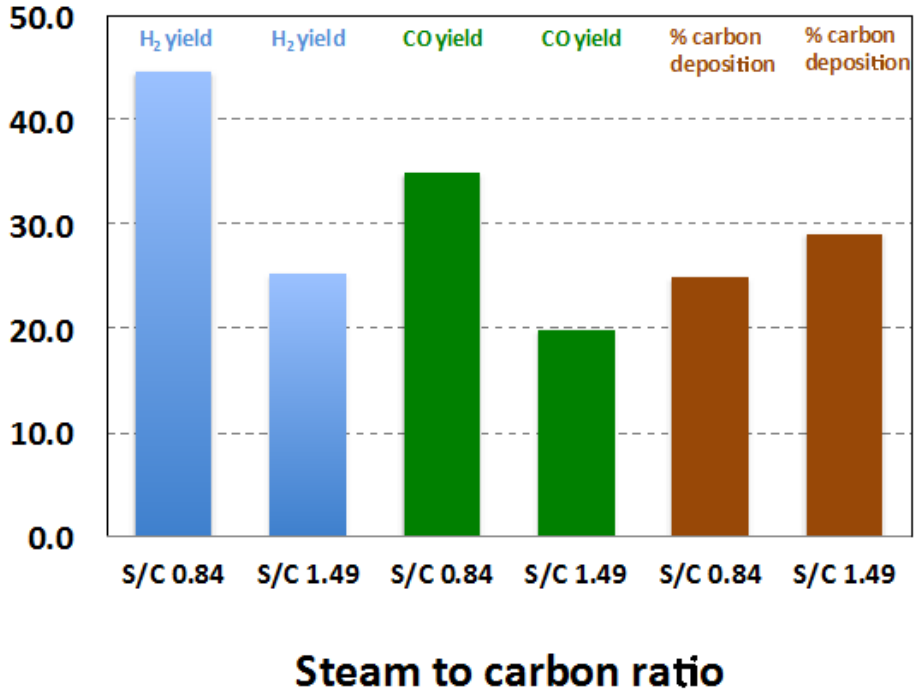

Figure 3.17: The effect of steam to carbon ratio on product distribution for ATR of whole pyrolysis oil

As a summary, at the end of the third-stage experimental study of ATR of pyrolysis oil, we had demonstrated steam reforming of whole pyrolysis oil without methanol addition. The in-house nozzle was shown to be capable of atomizing the seemingly viscous and harsh whole pyrolysis oil and the experimental results were very promising. Also at this third stage, modifications were made to the reactor configuration in preparation for the parametric study, and the study was systematically carried out using the best reactor configuration. The effects of temperature, Steam/C ratio and O_2/C ratio on Carbon Deposit, H_2 yield, CO yield and gas composition were studied. All the experimental runs for the parametric study were carried out with experimental run-time of 1 hour. Optimal reaction conditions were determined from the data, and during the next and final stage, longer duration runs would be conducted but in conjunction with catalyst deactivation and regeneration.

IV.4. Final Stage Parametric Study of ATR of Pyrolysis Oil

IV.4.1. Effect of Temperature

The temperature was varied from 600 to 800°C to examine its effect on CO yield, H_2 yield, and H_2/CO ratio with the yields as defined in previous sections. The data are presented in Fig. 3.18. As we increase the temperature from 600 to 700°C, both the CO and H_2 yields decrease, but suddenly increase at 750°C but decrease thereafter. Based on these yields, the optimum temperature appears to be 750°C, in agreement with our earlier experimental data on methanol-stabilized pyrolysis oil. However, if the amount of carbon deposit is used as the principal criterion for evaluating the reactor performance, the optimum temperature will be 800°C for the temperature range considered in our study. When these two measures are taken together, a temperature within the range of 750 to 800 °C will be acceptable for practical operation with the developed ATR system. Also, the H_2/CO ratio ranges between 2.3 and 2.9 which encompasses

the desired H_2/CO ratio for gas-to-liquid synthesis process. A reverse water-gas shift catalyst can be located at the exit of the reactor to fine-tune the H_2/CO ratio if needed, or the other process parameters can be used to adjust the ratio as demonstrated below.

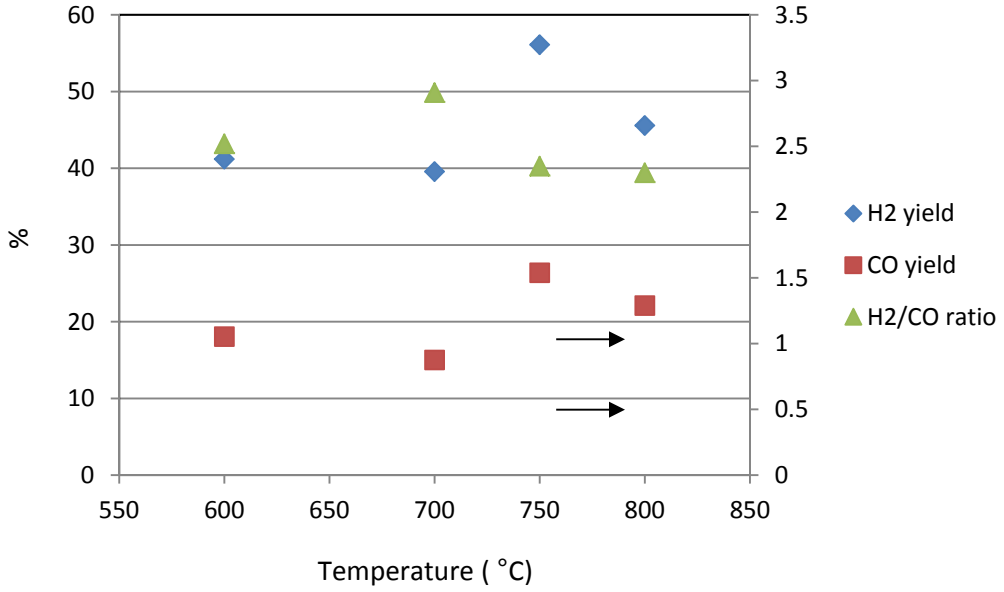

Figure 3.18: Effect of temperature on H_2 yield, CO yield and H_2/CO ratio. (Steam/C=1.1, O_2/C=0.37, GHSV=8102 (1/h))

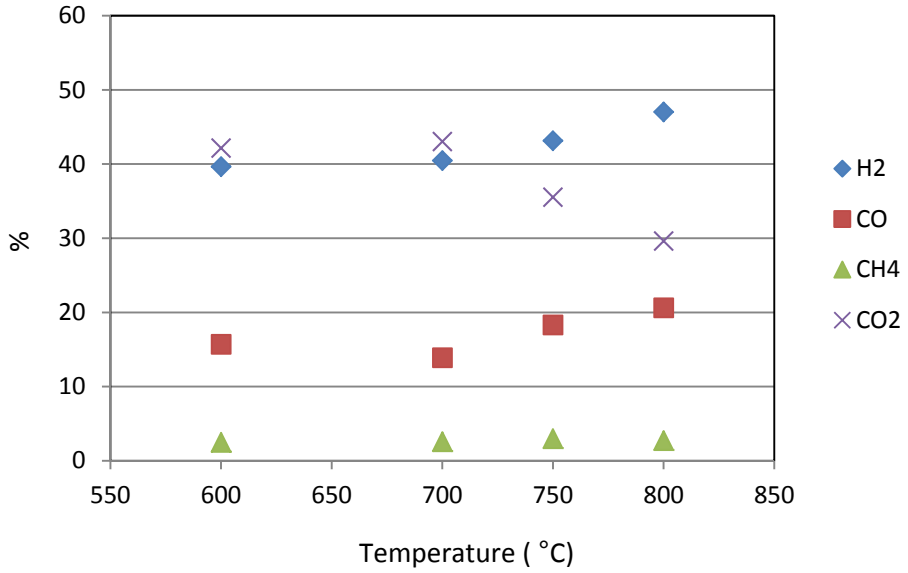

Figure 3.19: Effect of temperature on product gas composition on N_2-free dry basis. (Steam/C=1.1, O_2/C=0.37, GHSV=8102 (1/h))

The gas composition, on an N_2-free and dry basis is shown in Fig. 3.19 where it can be seen that both the compositions of H_2 and CO increase with temperature for the temperature range considered. In contrast, the composition of CO_2 decreases with temperature which implies that the carbon efficiency also increases with temperature. Although operating the reactor at a higher temperature will translate to a higher utility cost, this may be outweighed by the cost benefit of increased carbon efficiency. It's worth noting that even at a temperature as high as

800 °C, there is still a significant amount of CH_4 in the product stream, indicating incomplete reforming. However, an increase in the catalyst length or a slight decrease in the GHSV should reduce the level of CH_4 in product gas to a tolerable level in practice.

IV.4.2. Effect of O_2/C ratio

Even though atomic oxygen is present in a significant quantity in pyrolysis oil, externally added molecular oxygen is required, in part to initiate light-off after which its amount may be reduced. The amount of added O_2 is expected to affect not only the equilibrium product gas composition but also the amount of carbonaceous deposit. The O_2 is used for the CPO reaction which provides the heat required for the highly endothermic steam reforming reaction. By adjusting the O_2/C ratio, one could in principle, tune the product gas composition and hence H_2/CO ratio.

Figure 3.20 shows the effect of O_2/C ratio on H_2 yield, CO yield, and H_2/CO ratio in the O_2/C range of 0.1 to 0.5, which encompasses the range typically used for demonstration of methane auto-thermal reforming. As expected, within experimental error, the CO yield is observed to decrease generally as the O_2/C ratio increases. The H_2 yield also decreases as O_2/C ratio increases except at a value of 0.3 where a sharp jump is observed but subsequently decreases again. If the data at O_2/C ratio of 0.3 is ignored, the H_2/CO ratio appears to be constant while both the H_2 and CO yield decrease with increase in O_2/C ratio.

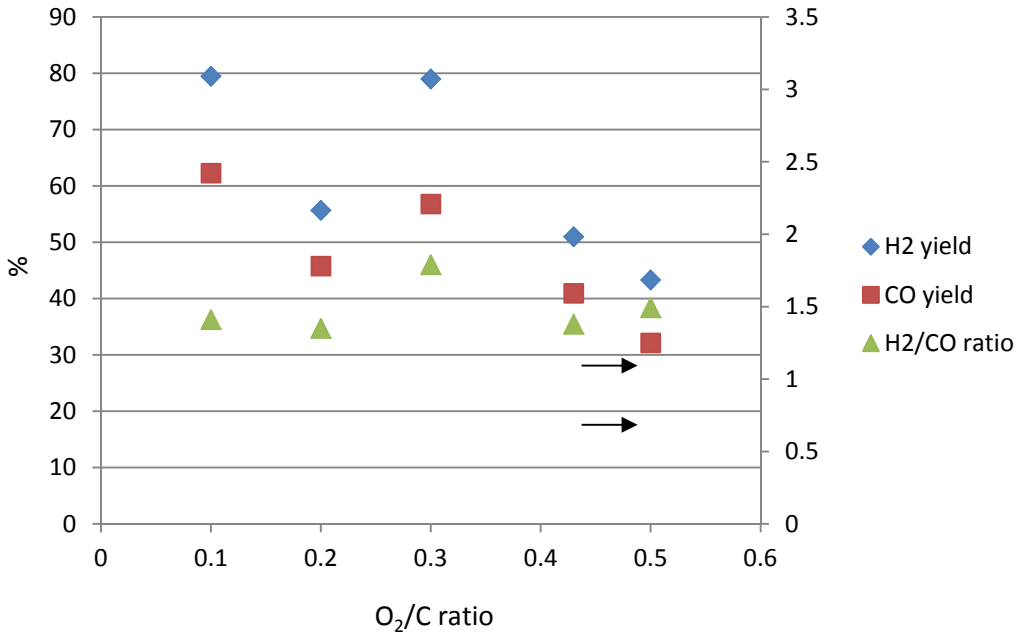

Figure 3.20: Effect of O_2/C ratio on H_2 yield, CO yield and H_2/CO ratio. (Temperature=800°C, Steam/C=1.1, GHSV=8102 (1/h))

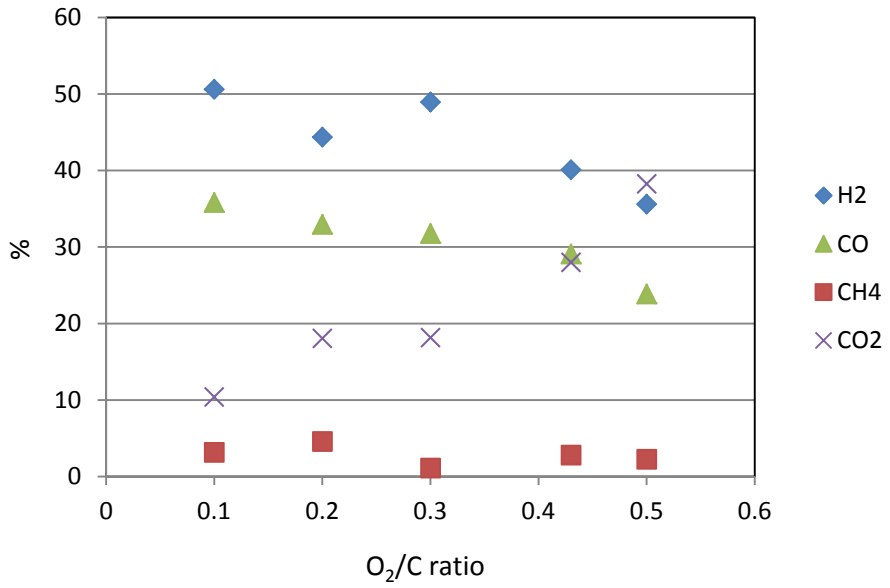

Figure 3.21: Effect of O_2/C ratio on product gas composition on N_2-free dry basis. (Temperature=800°C, Steam/C=1.1, GHSV=8102 (1/h))

The data on the gas composition, shown in Fig. 3.21 seem to be more consistent. The mole fractions of both H_2 and CO decrease as O_2/C ratio increases while that of CO_2 increases, displaying expected trends. As more O_2 is added, increased oxidation of H_2 to H_2O and CO to CO_2 will reduce the compositions of H_2 and CO respectively while increasing that of CO_2.

IV.4.3. Effect of Steam/C ratio

The literature on steam reforming of pyrolysis oil indicates that steam plays a very important role in the reduction of carbon deposit. However, the amount of steam cannot be increased without limit as higher steam flow rate demands higher energy requirement which is not preferred as it adversely impacts the economics of the process. For our experimental study, we selected a Steam/C ratio in the range of 0.46 to 1.8, and the experimental data indicate that a value between 1.1 and 1.5 would make continuous operation feasible. In practice, a Steam/C ratio of 1.3 is used for steam reforming of methane.

Figure 3.22 shows the effect of Steam/C ratio on H_2 yield, CO yield, and H_2/CO ratio. Water is present in significant amounts in pyrolysis oil, and the sample we used for all our experimental runs contained about 27wt% water based on Karl-Fischer titration. This corresponds to a Steam/C ratio of 0.46 which sets the lower limit of our experimental range. From Fig. 3.22, it's observed that without steam addition, the H_2 yield is very high in fact it's the highest in the range at a value of about 90%. With water added, the H_2 yield drops precipitously but increases thereafter with increased Steam/C ratio. However, it should be noted that the highest amount of carbon deposit was also recorded at this Steam/C ratio. The CO yield is also highest with no water addition but unlike the behavior of the H_2 yield, it remains almost constant as the Steam/C ratio increases. With steam addition, the H_2/CO ratio expectedly increases as the Steam/C ratio increases since the H_2 yield increases while the CO yield remains essentially flat.

Figure 3.23 shows the change in gas composition as the Steam/C ratio changes. The product gas composition on N_2-free basis is a good indication of how close the process is to attaining

equilibrium, since the H_2 or CO yield could be affected by other factors such as the loss of catalyst activity. The mole fraction of H_2 increases with increase in Steam/C ratio while a reverse behavior is observed for CO composition. These trends are as expected. For our process conditions, and the associated reactor configuration, a Steam/C ratio between 1.1 and 1.5 will provide a product with desired H_2/CO ratio of close to 2 while an operationally tolerable quantity of carbon deposit is produced.

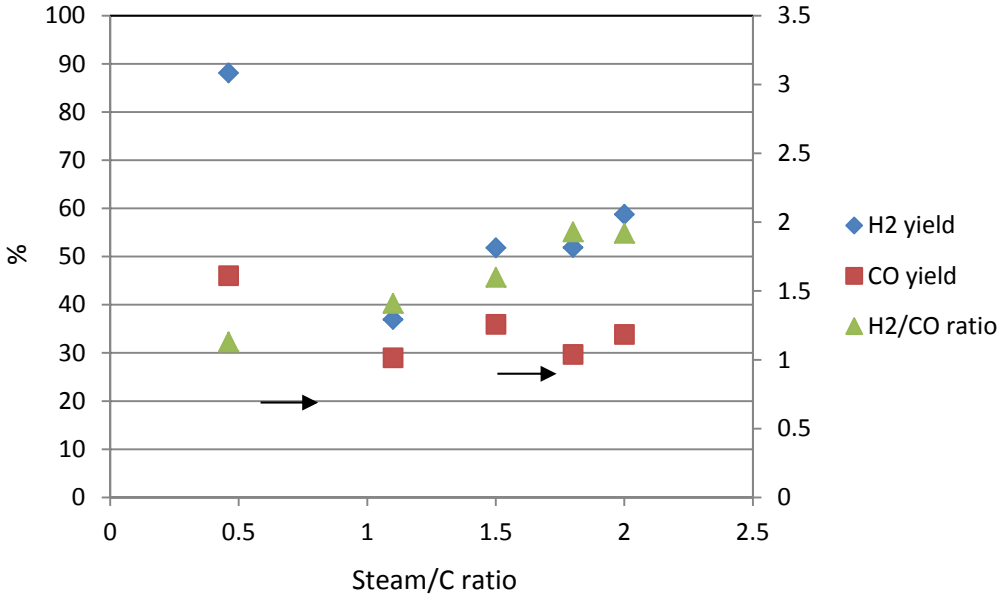

Figure 3.22: Effect of Steam/C ratio on H_2 yield, CO yield and H_2/CO ratio (Temperature=800°C, O_2/C=0.37, GHSV=8102 (1/h))

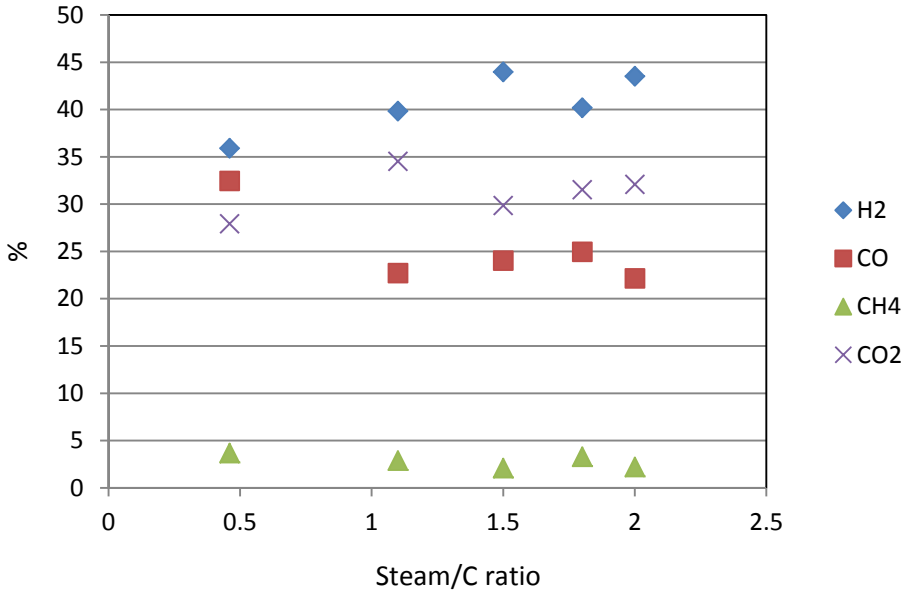

Figure 3.23: Effect of Steam/C ratio on product gas composition on N_2-free dry basis (Temperature=800°C, O_2/C=0.37, GHSV=8102 (1/h))

IV.4.4. Effect of GHSV

As a first step in the kinetic studies of ATR of pyrolysis oil, parametric studies (**see Task 4, sections III.4 & IV.**) of the effects of various processing conditions, including temperature, steam/C ratio, O_2/C ratio, and GHSV, on reactor performance were undertaken for two model compounds, namely acetic acid and glycerol. We also compared the experimental data with predictions from Aspen process simulation software, and we observed that for some values of GHSV, the equilibrium predictions were in satisfactory agreement, indicating approach to equilibrium. Kinetic studies are usually conducted under conditions of extremely high values of GHSV where the reactions are expectedly kinetically controlled, and far away from thermodynamic equilibrium. Hence one of the goals of the GHSV experiments was to identify such a regime. In the experiments conducted on ATR of acetic acid and glycerol, the GHSV was varied by keeping all process parameters constant (temperature, steam/C ratio, O_2/C ratio) and changing the feed flow rate. This was accomplished by changing the flow rate of N_2, an inert. For kinetic studies in gas phase reactions, this may not be the appropriate method for changing the GHSV because the partial pressures also change simultaneously, making it difficult to separate the two effects. Hence we decided to adopt another approach, which involved varying the length of the catalyst.

This new approach was applied to the ATR of PO. Six different lengths of catalysts were used, i.e., 1/3, 2/3, 1, 4/3, 5/6 and 2 with the unit length of catalyst being 2.75”. The experiments with 4/3, 5/3 and 2 lengths of catalyst were achieved by combining a unit length of catalyst with 1/3, 2/3 and 1 unit length of catalyst respectively, in the reactor. For these lengths of catalyst, a gap of about 0.25” was kept between the catalysts to prevent possible pressure drop increase that may be caused by the non-alignment of the monolith channels in the two units.

Figures 3.24 and 3.25 show the effect of GHSV on product gas yields, and composition on water and nitrogen-free basis. The highest GHSV corresponds to the shortest catalyst used. From Fig. 3.24, as the GHSV increases, the yields, except for that of CH_4, first increase and then decrease with the maximum occurring at about a GHSV of 9928, which corresponds to 1 unit of catalyst. The reason for one unit length of catalyst exhibiting the best performance could be attributed to a combined effect of the catalyst capacity and the recirculation of atomized PO droplets above the catalyst. With a shorter catalyst, the capacity of the catalyst was not sufficient for reforming the amount of PO being processed, therefore, part of the PO passes through the catalyst without being reformed resulting in poor yields of desired products. On the other hand, with the use of a catalyst longer than the unit length, the pressure drop across the catalyst increases, and the back-pressure leads to a less smooth flow through the catalyst thereby resulting in more intense recirculation of atomized PO droplets above the catalyst. The recirculation of PO droplets leads to a higher amount of coke formed around the nozzle tip, and the coke thus formed will further deteriorate the atomization as it creates a solid surface around which the PO droplets will coalesce. That explains the decrease in the amount of coke formed with increased GHSV, observed in Fig. 3.25. From Figures 3.24 and 3.25, it is clearly seen that the optimum result is achieved by using 1 unit length of catalyst. The GC readings of 1 unit length of catalyst at 30 minutes and 60 minutes are quite similar, indicating a stable running condition. The average H_2 and CO yields are respectively 79% and 41%, with an H_2/CO ratio of 2.1. Further validation of this observation will require increasing the unit length of catalyst from 2.75” to some higher value.

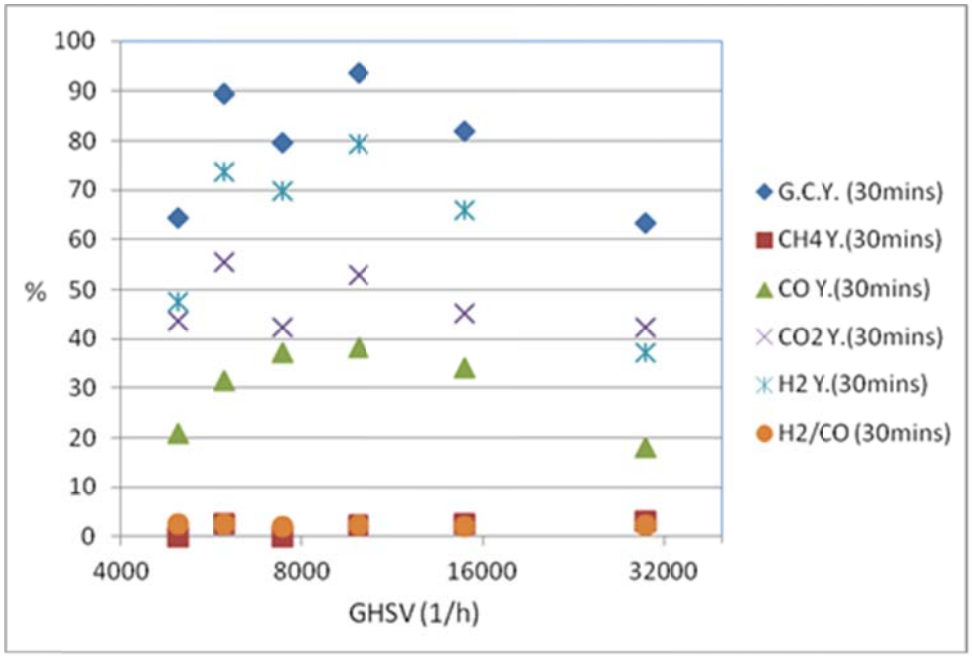

Figure 3.24a: Effect of GHSV on reactor performance for ATR of PO Conditions: $T_{reaction}$=750 ^{0}C, Steam/C=1.3, O_2/C=0.37, Catalyst length 2", GC reading taken at 30 minutes

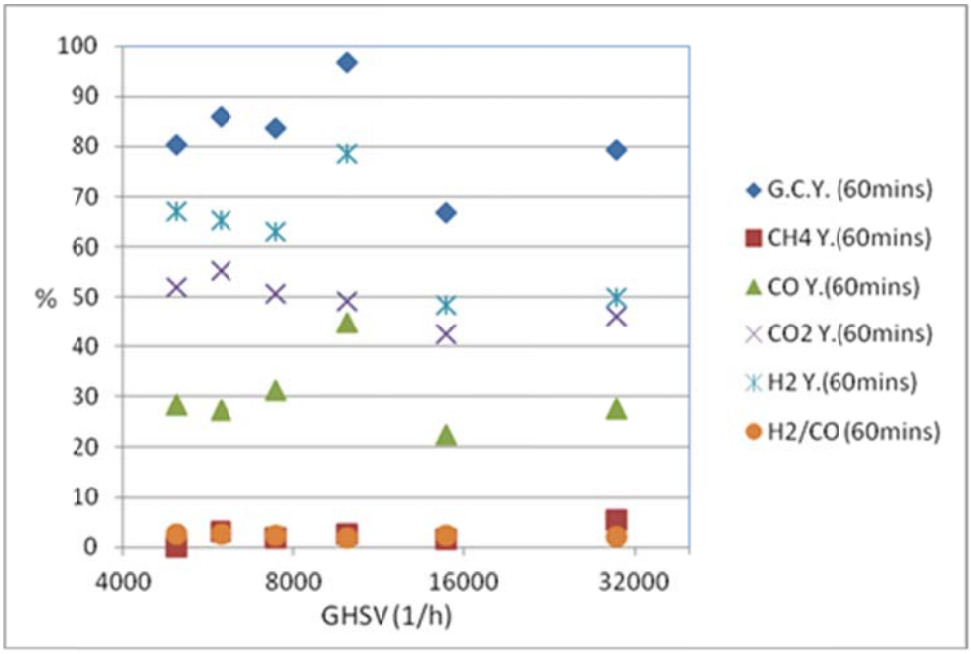

Figure 3.24b: Effect of GHSV on reactor performance for ATR of PO Conditions: $T_{reaction}$=750 ^{0}C, Steam/C=1.3, O_2/C=0.37, Catalyst length 2", GC reading taken at 60 minutes

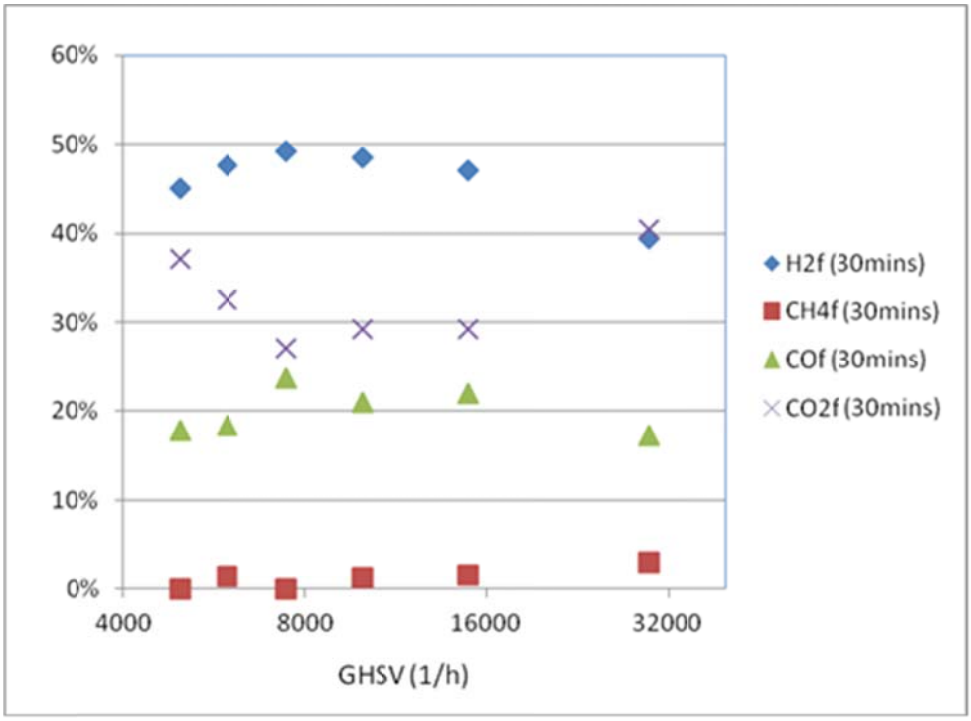

Figure 3.25a: Effect of GHSV on product gas composition for ATR of PO Conditions: $T_{reaction}$=750 ^{0}C, Steam/C=1.3, O_2/C=0.37, Catalyst length 2", GC reading taken at 30 minutes

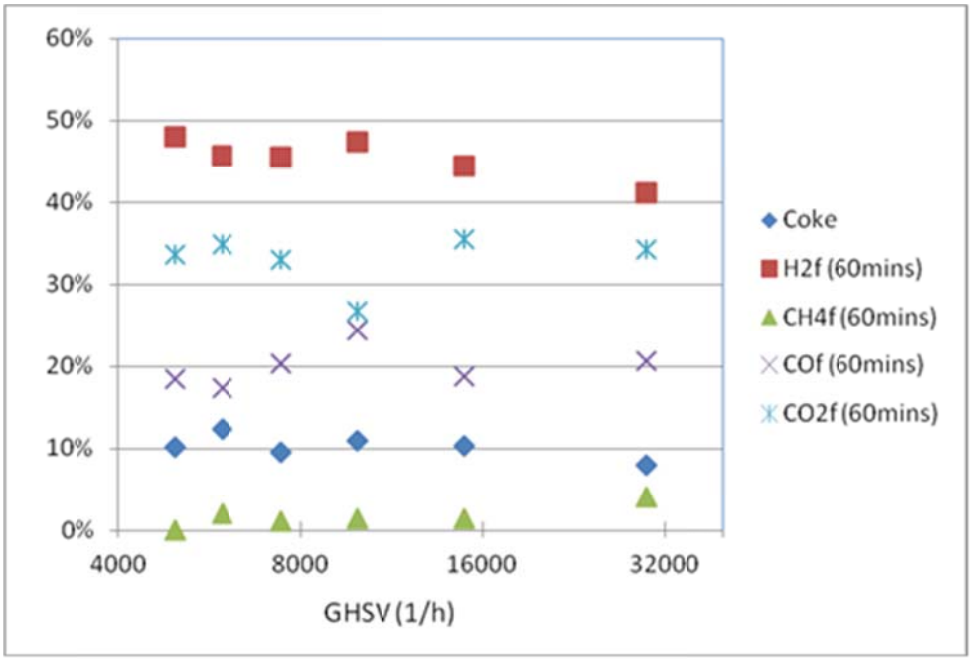

Figure 3.25b: Effect of GHSV on product gas composition for ATR of PO Conditions: $T_{reaction}$=750 ^{0}C, Steam/C=1.3, O_2/C=0.37, Catalyst length 2", GC reading taken at 60 minutes

V. References

Rennard, D.C., “Catalytic Partial Oxidation of Pyrolysis Oils,” Ph.D. thesis, University of Minnesota, Minnesota, 2009.

Simson, A., Waterman, E., Farrauto, R., and M. Castaldi, “Kinetic and Process Study for Ethanol Reforming using a Rh/Pt Washcoated Monolith Catalyst,” Applied Catalysis B: Environmental 2009, 89, 58-64

Van Rossum, G., “Steam Reforming and Gasification of Pyrolysis Oil,” Ph.D. thesis, University of Twente, Netherlands, 2009.

Task 4: Kinetic and Equilibrium Studies of ATR of Pyrolysis Oil

I. Summary

As a prelude to the kinetic study of ATR in the BASF dual layer monolith catalyst, thermodynamic equilibrium calculations were performed for acetic acid, glycerol and pyrolysis oil. The predictions based on the assumption of thermodynamic equilibrium were compared with actual experimental data to provide insight on how close the entire system was to thermodynamic equilibrium. For certain process conditions, the agreement was generally good while for others, there were indications that some of the component reactions of ATR did not attain equilibrium, thus warranting the development of appropriate kinetic equations. Pyrolysis oil is a complex mixture of a few hundred component species, hence there appears to be no systematic method for developing practically reliable kinetic equations for such a system. We therefore opted to use one of the model compounds, glycerol for this part of the task. The use of differential reactor kinetic data is the preferred choice for kinetic analysis, but for the ATR of glycerol it was not feasible to identify a practically relevant parameter space where the requirement of low conversion was met. Model equations based on the Langmuir- Hinshelwood approach were derived and the parameters evaluated by fitting these equations to the integral reactor kinetic data using non-linear regression analysis. One of the kinetic expressions seemed to provide the best fit. The kinetic data were also similarly fitted to the simple power-law expression for the kinetic constants.

II. Equilibrium Studies of ATR of Pyrolysis Oil

Thermodynamic equilibrium calculations provide guidance in the selection of optimum process conditions for desired reactor performance. Equilibrium studies are also essential in determining how close the experimental reactor performance is to thermodynamic equilibrium, if at all. Equilibrium calculations of ATR of whole PO, and 50wt% mixture of PO and methanol were therefore undertaken using the Aspen process simulation software based on Gibbs free energy minimization, but results are only presented here for whole PO. The effects of process parameters, namely reactor temperature, H_2O/C, and O_2/C ratio on the product composition were studied. The ranges of the process parameters considered are as follows: reactor temperature – 600 to 1000^oC; H_2O/C ratio – 0.0 to 2.0; and O_2/C ratio – 0.0 to 1.0. As each parameter was varied, the others were kept constant.

To study the effect of reactor temperature, the values of H_2O/C and O_2/C ratios were set to 1.6, and 0.1 respectively. For the range of temperature used in the study, the mole fraction of H_2 in the dry product gas remains fairly constant (Figure 4.1), varying between a minimum of 0.5 to a maximum of 0.53, with the minimum value occurring at the lower and upper temperature limits. As the temperature increases from 600^oC, the amount of H_2 increases, attaining its maximum value at about 700^oC, and thereafter decreasing to 0.5 at 1000^oC. The composition of CO increases as the temperature increases whereas CO_2 displays an opposite behavior. The minimum value of the mole fraction of CO is 0.1 while the maximum is 0.24. The corresponding values for CO_2 are 0.13 and 0.23 respectively. The ratio of H_2/CO varies between 5 at the lowest temperature to 2.2 at the highest temperature. In order to achieve an H_2/CO ratio of 2.1 required for Fischer-Tropsch (F-T) synthesis, there are several options one of which is the reduction of H_2O/C ratio as the results to follow will indicate. Very little methane is formed for all temperatures considered, with the maximum value of 0.03 occurring at the lowest temperature, and subsequently decreasing to an immeasurable value beyond 700^oC. The general behavior observed here is not unexpected, and is qualitatively similar for all other values of H_2O/C and O_2/C ratios. Also, the results for whole PO were strikingly similar to those of 50wt% PO/methanol mixture, both qualitatively and quantitatively.

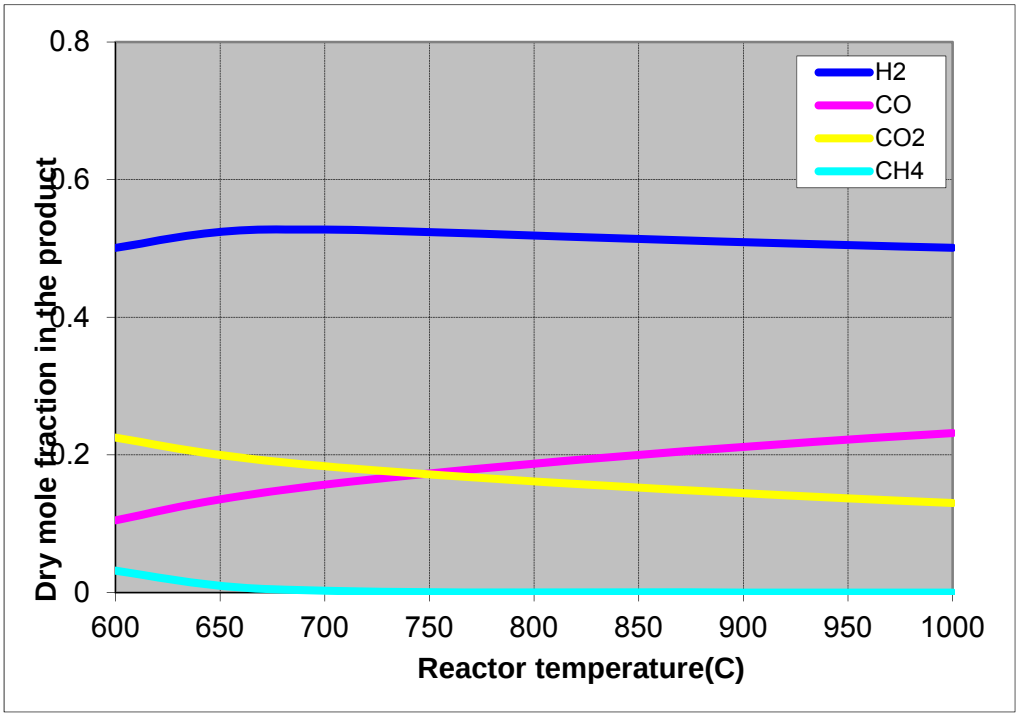

Figure 4.1: The effect of temperature on dry product composition for ATR of whole PO (sawdust) (H_2O/C = 1.6 and O_2/C = 0.1)

For the effect of H_2O/C ratio, the values of reactor temperature and O_2/C ratio were kept constant at 750°C and 0.1 respectively. The mole fraction of H_2 in the dry product gas monotonically increases as the H_2O/C ratio increases (Figure 4.2), ranging between 0.42 and 0.53. In contrast with the behavior of H_2, the mole fraction of CO reduces slowly as the H_2O/C ratio increases until the H_2O/C ratio reaches 0.5 after which it begins a rapid decrease. The CO mole fraction ranges between 0.15 and 0.35. In the range of H_2O/C ratio studied, the H_2/CO ratio varies from a minimum value of 1.2 to a maximum value of 3.5 which as expected occurs at the highest H_2O/C ratio. Increase in temperature, coupled with a low H_2O/C ratio will produce desired H_2/CO ratio of 2.1. The composition of methane in the dry product gas is negligible for all H_2 O/C ratios considered. The trend exhibited by CO_2 is similar to that of H_2, as it increases as the H_2O/C ratio increases for all values considered, ranging from 0.044 to 0.19. Also, the mole fraction of CO_2 is lower than that of CO for all values of H_2O/C ratio less than 1.75, thereafter, the behavior is reversed.

Finally, in order to study the effect of the ratio of O_2/C on the composition of the dry product gas, the values of temperature and H_2O/C ratio were kept constant at 750°C and 1.6 respectively. As the O_2/C ratio is increased from 0.0 to the maximum value of 1.0, the composition of H_2 decreases sharply from 0.62 to 0.03 (Figure 4.3). The composition of CO also decreases but less rapidly, starting at a maximum value of 0.21 and ending at 0.01. The amount of methane produced is very insignificant for all values of O_2/C ratio considered. The H_2/CO ratio remains fairly constant at about 3.0 for all O_2/C values. Similar to the other cases considered so far, the mole fraction of methane was very small, and will be experimentally immeasurable. In contrast to the behavior of these three components, the mole fraction of CO_2 remains almost constant, ranging between 0.17 and 0.19, and higher than that of CO except for O_2/C values less than 0.1.

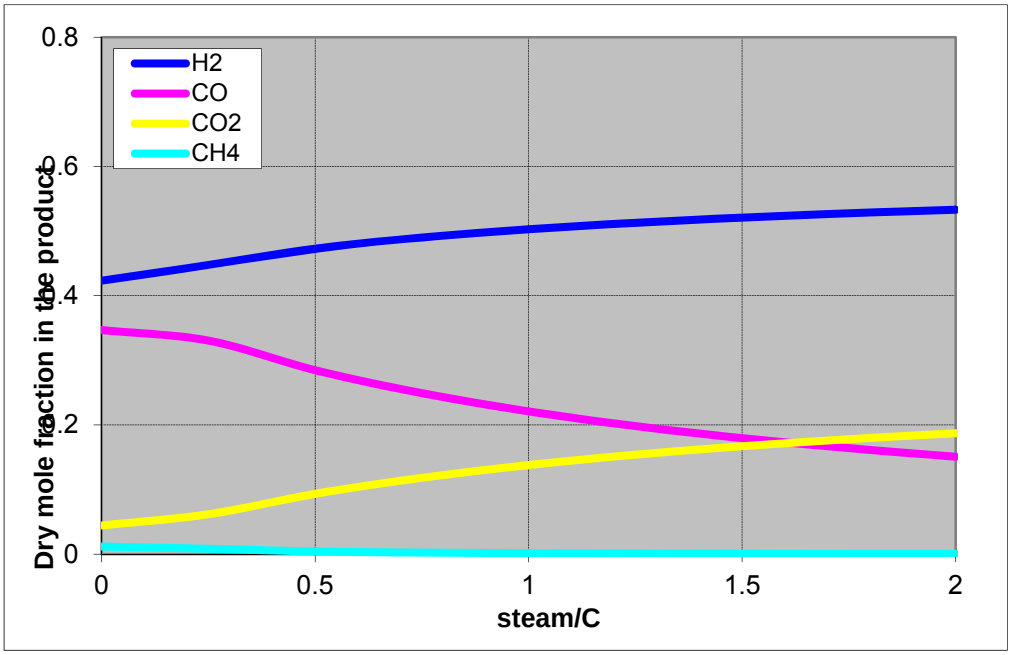

Figure 4.2: The effect of H_2O/C ratio on dry product composition for ATR of whole PO (sawdust) (Temperature = 750°C and O_2/C = 0.1)

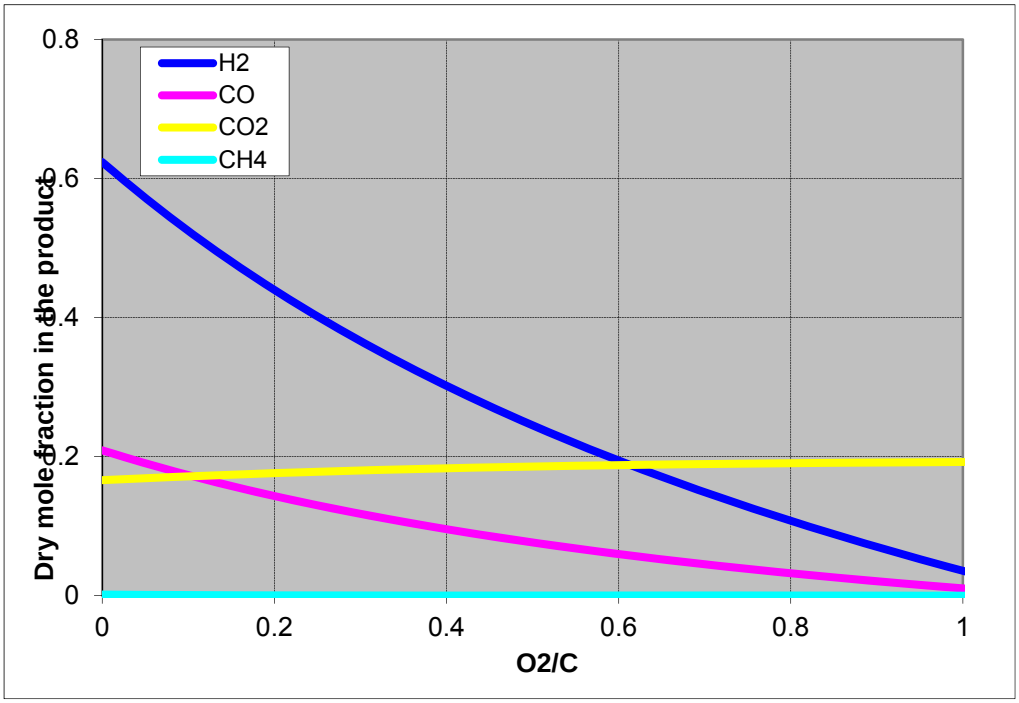

Figure 4.3: The effect of O_2/C ratio on dry product composition for ATR of whole PO (sawdust) (Temperature = 750°C and H_2O/C = 1.6)

II.1. Comparison of Experimental Data with Equilibrium Calculations

Some of the experimental data from the ATR of 50wt% PO (from sawdust)/methanol mixture were selected for comparison with the results from Aspen process simulation as shown in Figure 4.4. At low values of H_2O/C ratio, the agreement between the simulation results and the experimental data is indeed satisfactory, and the difference in H_2/CO ratio is well within experimental error. However, as the H_2O/C increases, the numerical results begin to deviate from the experimental data. It's obvious that for these experimental conditions, equilibrium was not attained. One possible explanation is that the GHSV is higher than required for attainment of equilibrium. Since our objective was ATR of whole pyrolysis oil, the experimental data from the performance studies on whole PO are next compared with process simulation results, providing further insight into residence time requirements for attainment of chemical equilibrium for the ATR of PO.

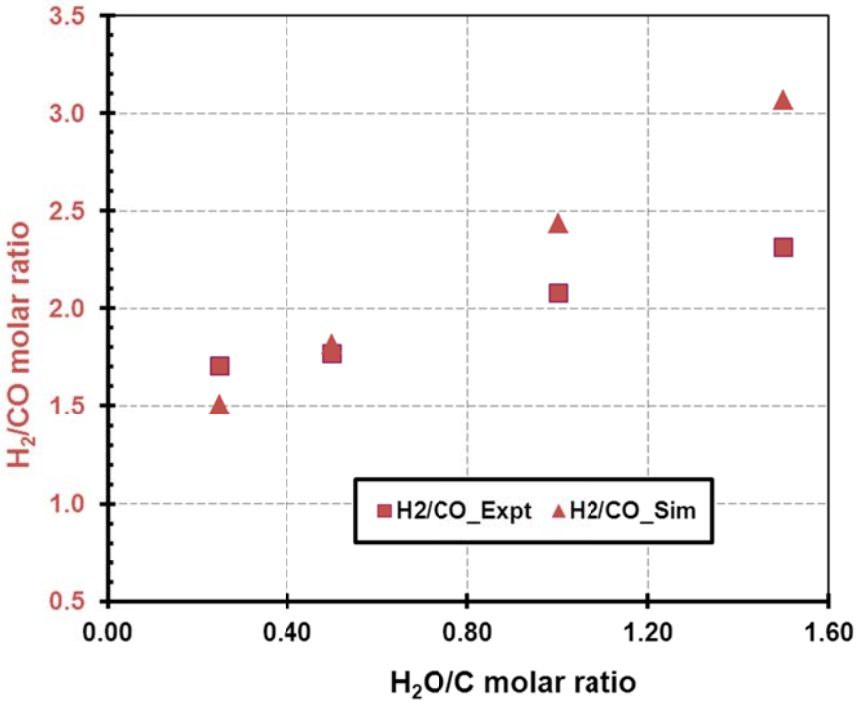

Figure 4.4: The plot of H_2/CO molar ratio as a function of H_2O/C molar ratio at $T_{rxtor\text{-}z2}$ = 750 ^{0}C and O_2/C = 0.45 (for both the simulation and experiment).

The experimental data showing the effect of O_2/C ratio on the ATR of whole PO were selected for comparison with the results from Aspen process simulation as shown in Figure 4.5. In general, for all values of O_2/C ratio, the agreement between the simulation results and the experimental data is indeed satisfactory, and the difference in H_2/CO ratio is well within experimental error. The deviation between the experimental data and predictions from equilibrium analysis is highest at low values of O_2/C ratio (0.1 & 0.2) where by coincidence, the amount of carbon deposit was also the highest. For values of O_2/C ratio ≥ 0.3, one can observe that there is very little difference between the experimental data and the equilibrium predictions. One can conclude that for the selected experimental conditions, and associated reactor configuration, equilibrium was attained, providing further confidence in the parametric study reported in Task 3, Section IV.4.

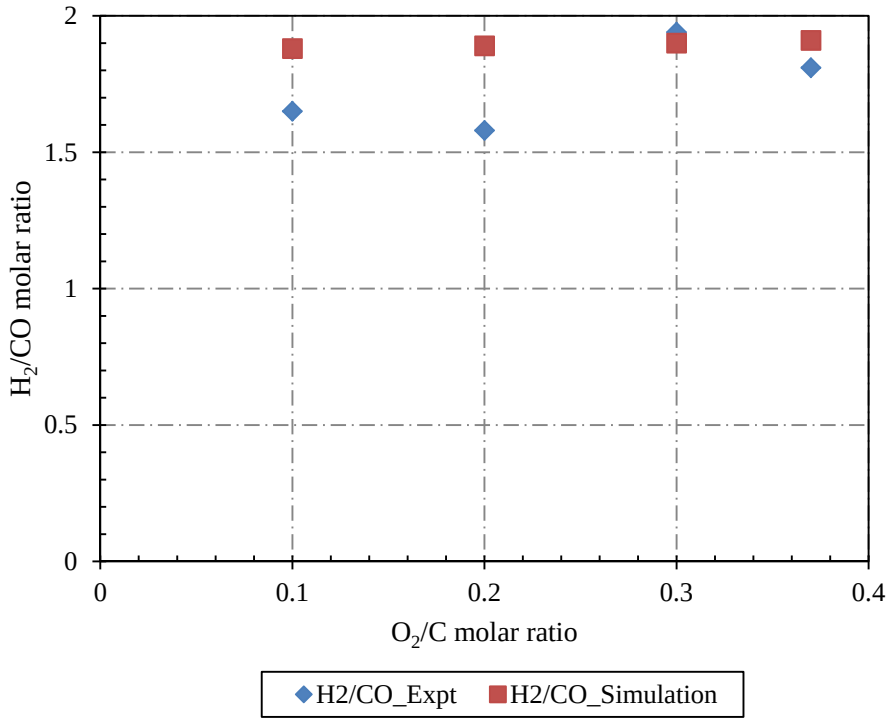

Figure 4.5: The plot of H_2/CO molar ratio as a function of O_2/C molar ratio at reactor temperature of 800^{0}C, H_2O/C = 1.1 and GHSV = 8102 (1/h) (for both simulation and experiment on whole PO).

III. Performance and Equilibrium Studies of ATR of Acetic Acid

Acetic acid (AA) has been used in a lot of studies as a model compound for pyrolysis oil since it is one of the major components in pyrolysis oil. This well-behaved oxygenate enables evaluation of a process or catalyst for pyrolysis oil upgrading. In what follows, a parametric study was carried out to evaluate the effectiveness of the dual layer catalyst for the auto-thermal reforming of oxygenates.

Before the study of the effect of different process parameters, several preliminary runs with blank monolith were carried out to evaluate the contribution of thermal decomposition to the ATR, and thus delineate the effect of the catalyst on the reactions. As shown in Fig. 4.6, at low temperature, the conversion of acetic acid is low. As the temperature increases, so does the conversion. At a temperature of 700°C, the conversion reaches ~43% with a CO yield of ~20%. From these runs with the blank monolith, we can see that the oxidation of AA, even without the catalyst, takes place at a high temperature. The oxidation could be purely thermal, or could be due to catalyzation by the ceramic material of the blank monolith. Either way, the data in Fig. 4.6 is used as a baseline against which to compare the runs with active catalyst to show the effect of the catalyst on the reforming of AA. Comparison of the result of blank monolith and that of active catalyst at 700°C clearly shows the role of the catalyst in the autothermal reforming of acetic acid (Table 4.1). The reason why the measured conversion is higher than 100% is attributed to the instrumental error of the GC.

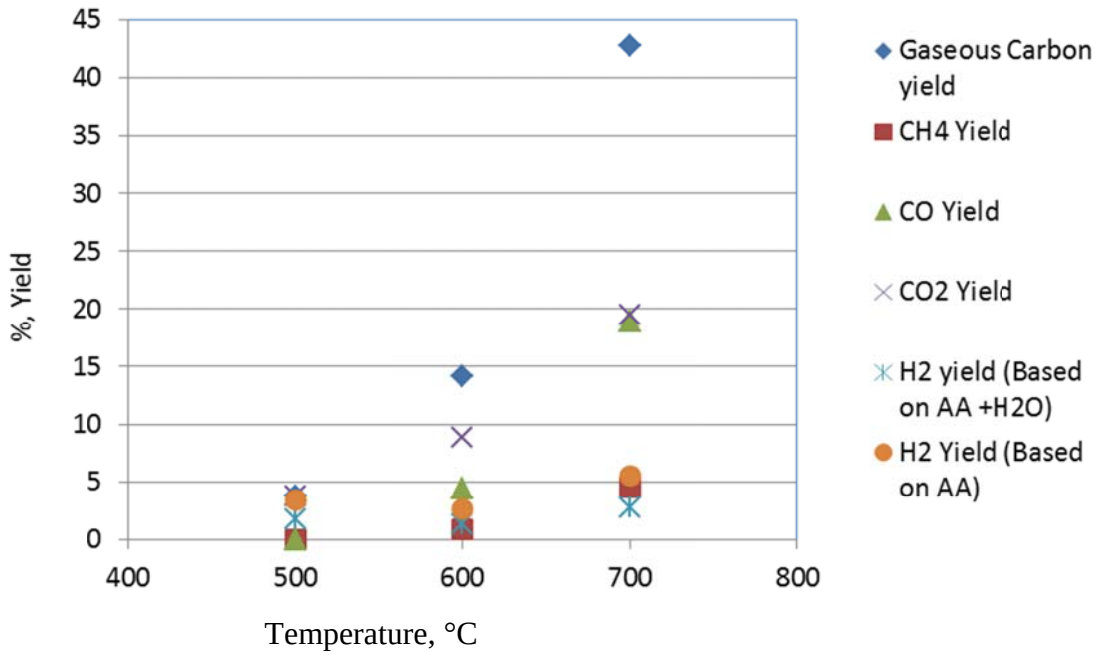

Figure 4.6: Effect of Temperature on Reaction Performance with Blank Monolith $H_2O/C=1$; $O_2/C=0.3$; GHSV=9061 (1/hr) @NTP; Monolith Length = 2.75"

Table 4.1: Comparison between blank monolith and catalyst loaded monolith at T=700 °C, S/C=1, O2/C=0.3, GHSV=9061 (1/hr)

	Conversion	H_2 yield (AA+H2O)	CO yield	CH_4 yield
Blank monolith	42.8%	2.7	18.9	4.5
Catalyst loaded	101.8%	46.4	42.2	1.06

III.1. Effect of temperature

Figure 4.7 shows the effect of temperature on product gas composition and conversion of acetic acid. At low temperature, the conversion is low due to the slow reaction rate. As the temperature increases, the percentage of H_2 increases and at 500°C, the H_2 composition attains its maximum value and remains unchanged thereafter. CO percentage remains around 20% throughout the temperature range. The observation indicates more or less that when the temperature changes from 300 °C to 500 °C, the temperature increase has a more significant effect on increasing the reaction rate of reactions producing H_2, which are mainly steam reforming and reverse water-gas shift reactions. After 500 °C, as the temperature increases, the increase of the reaction rate for all reactions involved seems to be almost the same. Although CO mole fraction shows a slight increase and that of CO_2 shows a slight decrease as the temperature is increased, the changes are not significant. The secondary axis shows the conversion of acetic acid versus temperature. As the temperature increases, the reaction rate increases, and at a temperature higher than 600 °C, the conversion reaches around 100%.

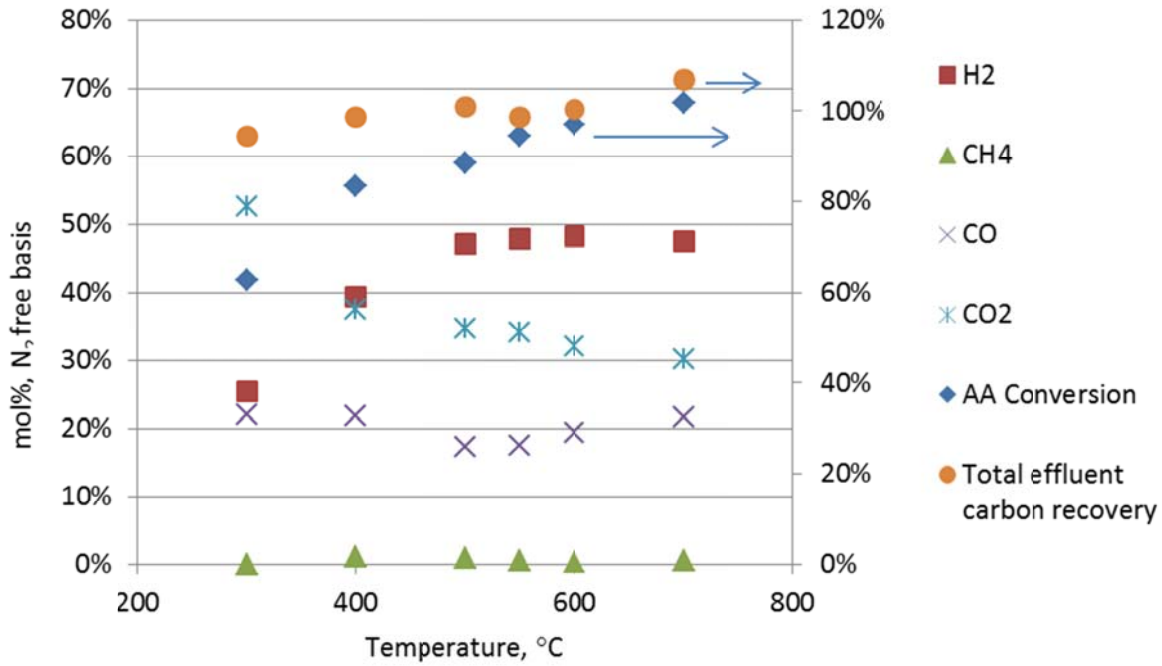

Figure 4.7: Effect of Temperature on Product Gas Composition GHSV=9061 (1/hr) @ NTP; Steam/C=1.0; O_2/C=0.3; Catalyst Length=2.75"

Figure 4.8 shows the comparison between experimental and equilibrium product gas yield. The equilibrium product gas was simulated using Aspen with the R-equilibrium block selected. Four main reactions used for the simulation are listed below:

Steam reforming: $C_2H_4O_2 + 2H_2O \rightarrow 2CO_2 + 4H_2$ (4.1)

Partial oxidation: $C_2H_4O_2 + O_2 \rightarrow 2CO + 2H_2O$ (4.2)

Water-gas shift: $CO + H_2O \leftrightarrow CO_2 + H_2$ (4.3)

Methanation reaction: $CO + 3H_2 \rightarrow CH_4 + H_2O$ (4.4)

From the comparison, it can be seen that at low temperature range, the experimental data are not in good agreement with the equilibrium prediction, however, as the temperature increases, the difference between the experimental data and equilibrium calculations narrows. At 700°C, good agreement between the experimental data and the prediction can be observed. The explanation is straightforward. The equilibrium prediction is simulated assuming an unlimited reaction time or in other words, extremely high reaction rates for all reactions involved. However, in the experiments, a finite residence time is imposed. The reason why the yields for H_2 and CO in Fig. 4.8 are still higher than equilibrium can be attributed to the relatively low methanation reaction rate (which consumes CO and H_2) compared to other reactions at low temperature. The extent of reaction of the methanation reaction which consumes CO and H_2 is far lower than other reactions, because there isn't enough residence time for produced CO and H_2 to go through methanation. That also explains why the CH_4 yield is far less than the predicted value. As the temperature increases, all reaction rates increase. Depending on the activation energy, different reactions will show different rate increases as the temperature is increased. The increase of CO and H_2 yields are understood to be the result of the rate increases of both steam reforming and partial oxidation reactions. At high temperature, all reactions rates, for the selected GHSV, are so high that equilibrium is more or less achieved. The auto-thermal reforming catalyst does not show any preference over any specific reaction at high temperature with the GHSV used. It catalyzes all the reactions thus resulting in product composition close to that at equilibrium.

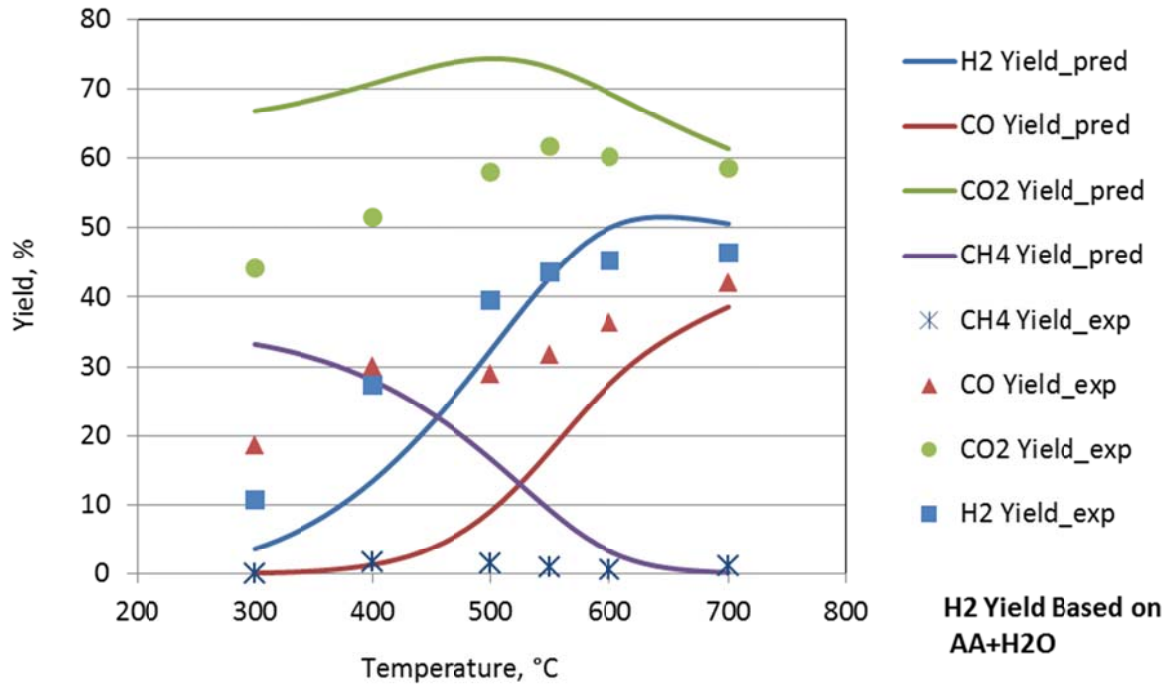

Figure 4.8: Comparison between Experimental and Equilibrium Product Gas Yield GHSV=9061 (1/hr) @ NTP; Steam/C=1.0; O_2/C=0.3; Catalyst Length=2.75"

III.2. Effect of O_2/C ratio

Figure 4.9 shows the effect of O_2/C ratio on product gas composition. From Fig.4.9, it can be seen that with the increase of O_2/C ratio, the conversion of acetic acid increases. At O_2/C ratio higher than 0.2, nearly 100% conversion is obtained. As for the auto-thermal reforming, catalytic partial oxidation is highly exothermic, emitting heat to sustain the highly endothermic steam reforming reaction. Figure 4.10 shows the comparison between experimental and equilibrium product gas yield. At O_2/C<0.2, the conversion is relatively low, all the yields are therefore as expected lower than predicted by equilibrium calculations. CO yield at O_2/C =0.15 approaches the equilibrium value, which shows that the partial oxidation reaction rate increases faster than other reactions as the O_2/C ratio increases. At O_2/C>0.2, the experimental CO yield is higher than the equilibrium, however, the H_2 yield is higher than predicted at O_2/C=0.25 and then lower than predicted when O_2/C is increased further to 0.3. The explanation of slow methanation reaction can also explain the observation. Higher CO yield results from the combined effect of slow methanation reaction and fast partial oxidation. However, as the O_2/C continues to increase, combustion of H_2 overrides the effect of slow methanation and results in a lower experimental H_2 yield than the equilibrium.

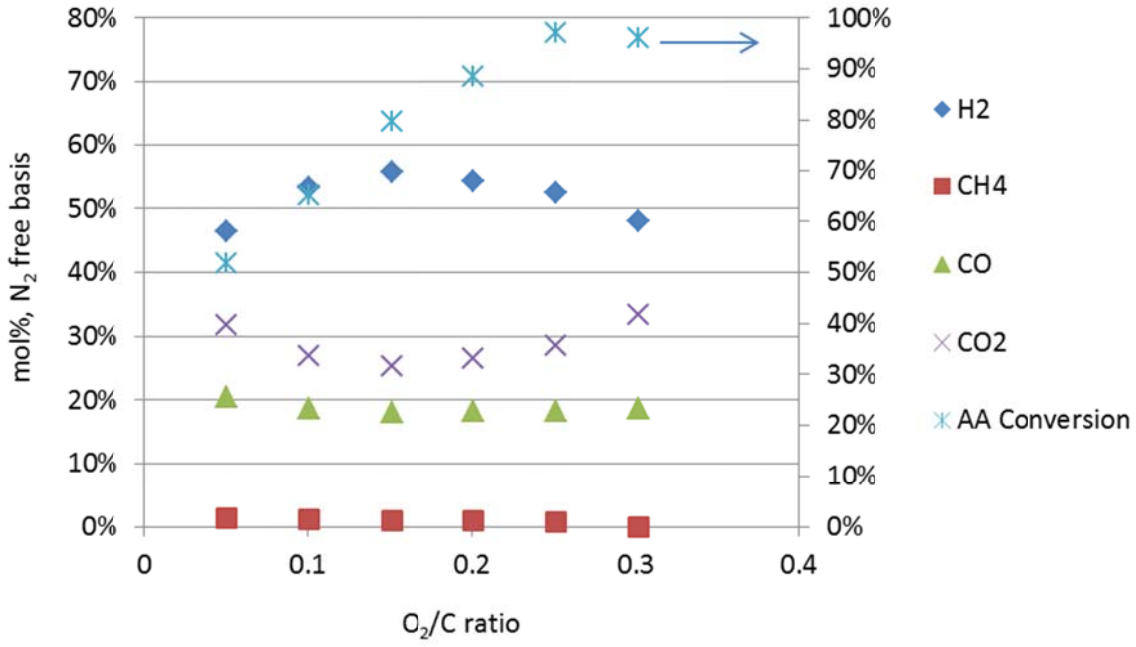

Figure 4.9: Effect of O_2/C on Product Gas Composition
GHSV=9061 (1/hr) @ NTP; T=700°C; Steam/C=1.0; Catalyst Length=2.75"

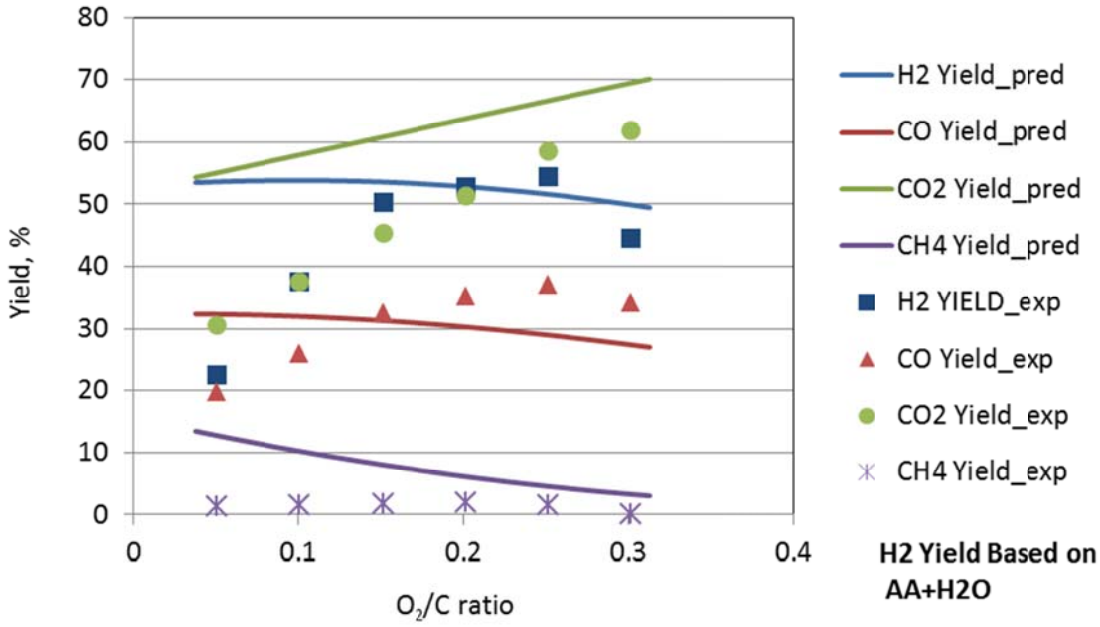

Figure 4.10: Comparison between Experimental and Equilibrium Product Gas Yield
GHSV=9061 (1/hr) @ NTP; T=700°C; Steam/C=1.0; Catalyst Length=2.75"

III.3. Effect of S/C ratio

Figure 4.11 shows the effect of S/C ratio on product gas composition. At 700 °C, O_2/C=0.3, GHSV=9061 (1/hr), and for the range of S/C ratio studied, the conversion of acetic acid is close

to 100%. Variance is attributed to the instrumental error of GC. As the S/C ratio increases, it is obvious that the CO percentage in the product gas decreases and H_2 increases. This observation can be explained by the water-gas shift reaction equilibrium. As the H_2O/C ratio increases, the reaction shifts to the right side, resulting in consumption of CO and production of H_2. Methane remains more or less constant throughout the change of S/C ratio from 0.5 to 2.

Figure 4.12 shows the comparison between experimental and equilibrium product gas yield. The experimental data agrees quite well with the predicted equilibrium values. From the effect of temperature, we know that at T=700 °C, O_2/C=0.3, the reaction rates of all competing reactions are so high value that under the finite residence time the equilibrium was more or less achieved. The good agreement of the experimental data and the predicted value for the studied range of S/C ratio supports the explanation by reaction rates. It is worth mentioning that as the S/C ratio increases, the H_2/CO ratio of the product gas increases accordingly, which enables the tuning of the H_2/CO ratio to a desired value, such as 2.1 for the Fischer-Tropsch reaction to produce diesel.

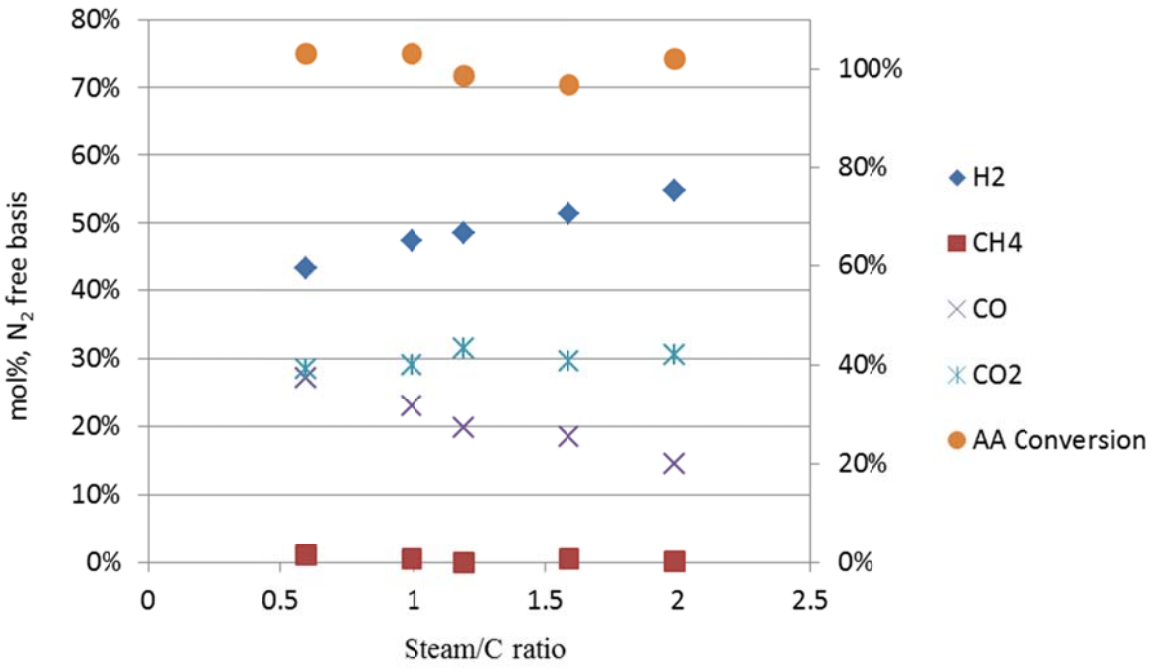

Figure 4.11: Effect of Steam/C Ratio on Product Gas Composition GHSV=9061 (1/hr) @ NTP; T=700°C; O_2/C=0.3; Catalyst Length=2.75"

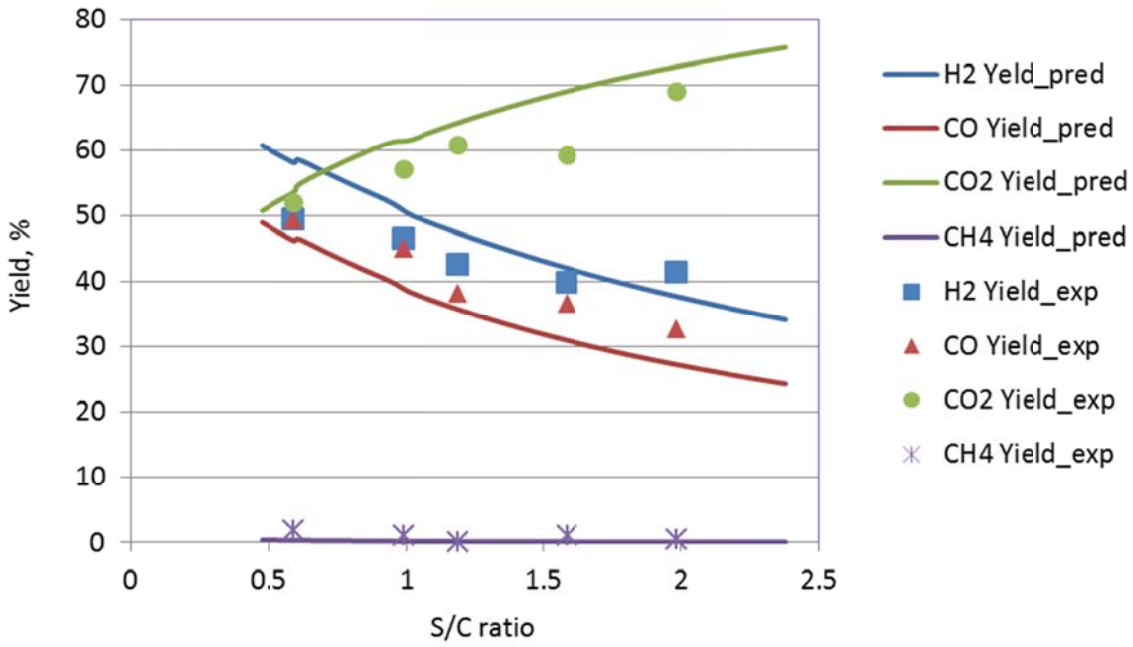

Figure 4.12: Comparison between Experimental and Equilibrium Product Gas Yield GHSV=9061 (1/hr) @ NTP; T=700°C; O_2/C=0.3; Catalyst Length=2.75"

III.4. Effect of GHSV

Figure 4.13 shows the effect of GHSV on product gas composition and conversion of acetic acid. The GHSV was varied by changing the flow rate of N_2 while keeping all the other process parameters constant, i.e., temperature, steam/C ratio, and O_2/C ratio. In this approach, for this gas-phase reaction, the partial pressures of the different components also change, thus making it difficult to isolate the effect of GHSV. However, it is easier to implement experimentally than the more rigorous approach which involves changing the length of the monolith catalyst. It was decided to apply the rigorous approach to whole pyrolysis oil, and the results are presented in **section IV.4.4 Task 3**.

From Fig. 4.13, we can see that at GHSV lower than 20,000 the conversion of acetic acid remains constant around 100% and the composition of the product gas is more or less unchanged, which indicates that with a GHSV lower than 20, 000 the residence time is high enough for the reactions to reach equilibrium. However, when the GHSV increases beyond 25,000, a sharp drop in conversion of acetic acid is detected, indicating insufficient time for the reactions. The change of the composition agrees with the reaction rate explanation. Partial oxidation has a high reaction rate while steam reforming has a relatively low rate. The decrease of residence time decreases the extent of the reaction of steam reforming resulting in less H_2 produced, while the effect of residence time has much less effect on the extent of reaction of partial oxidation. That explains why in the product gas composition, H_2 molar composition decreases and CO molar composition increases. Conversion of acetic acid higher than 100% is attributed to the calibration curve used for the GC.

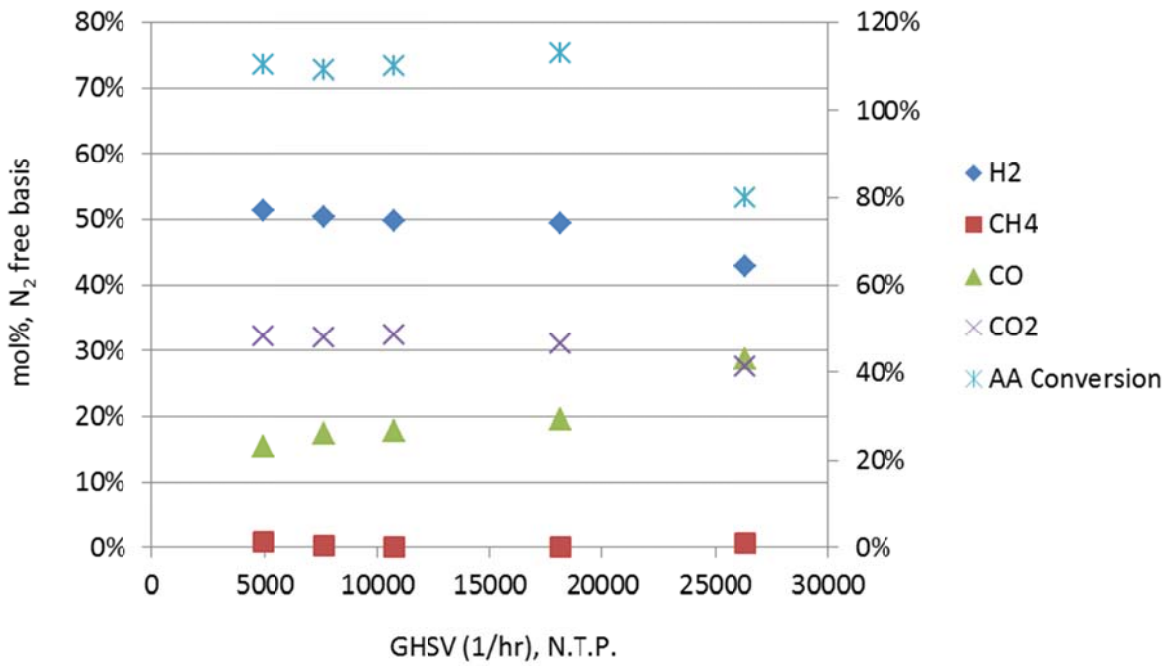

Figure 4.13: Effect of GHSV on Product Gas Composition
T=700°C; Steam/C=1.0; O_2/C=0.3; Catalyst Length=2.75"

IV. Performance & Kinetic Studies of ATR of Glycerol

IV.1. Performance Study of ATR of Glycerol

The performance and optimization studies of ATR of whole PO were conducted and the results are presented in **section IV.4 Task 3**. Also, some of the experimental data were selected for comparison with results predicted by Aspen process simulation software based on Gibbs free energy minimization, and the agreement was generally good. Based on this outcome, and previous comparisons between experimental data and equilibrium predictions for whole PO and acetic acid, we had been able to find ranges of process conditions (especially in terms of GHSV) for which the dual layer monolith ATR catalyst was able to provide reactor exit compositions close to equilibrium. In theory, attainment of equilibrium conditions will require the GHSV to be close to zero, however, such a process will obviously not be economically viable. So in practice, the objective will be to increase the GHSV as high as possible and still obtain desired exit gas composition, and H_2/CO ratio of ~ 2.1. This may necessitate operating the process at values of process parameters different from optimum. Kinetic studies provide the necessary tools to address this objective. If done correctly, kinetic studies can also shed light on the dominant reactions, as well as the associated reaction mechanisms.

There are two common approaches to conducting kinetic studies, namely the power law, and the Langmuir-Hinshelwood (L-H) approaches, each with its advantages and disadvantages. We prefer the L-H approach since it provides valuable insight into the reaction mechanisms. However, it is far more complicated and challenging than the power law approach, and it's not obvious how this approach can be applied to a complex mixture such as pyrolysis oil. For this reason, selection of a model compound that closely resembles the pyrolysis oil has been the alternative. Initially, we had proposed acetic acid for this purpose. However, further review of the literature on upgrading of pyrolysis oil indicated a need to rethink this choice. Therefore, we

replaced acetic acid with glycerol. Glycerol, just like acetic acid, is a component of pyrolysis oil. But in addition, its physical properties, e.g., viscosity and density, are closer to those of pyrolysis oil. Its heat content is also similar to that of pyrolysis oil.

The starting point for the kinetic studies is a parametric study of the effects of various process conditions on reactor performance. Therefore, the performance study of the ATR of glycerol was undertaken by varying the temperature, steam/C ratio, O_2/C ratio, and GHSV. Here we only present a few of the results as the study has been published in a journal article (Yujia et al., 2012). Figure 4.14 shows typical experimental data obtained, displaying the effect of temperature on product gas composition (on N_2–free dry basis), as well as H_2/CO ratio. Generally, within experimental error, the mole fraction of H_2 increases as the temperature increases while both the CO and CO_2 mole fractions remain essentially constant. The H_2/CO ratio is within the desired range. It is also noteworthy that the amount of methane produced is small, even at low temperatures, which is highly desirable since methane production implies loss of valuable carbon and hydrogen. It appears that the BASF catalyst, unlike other commercially available steam reforming catalysts, is very effective in suppressing the methanation reaction. We also observed minimal coke formation for the experimental ranges of all the process parameters.

Next, the experimental data on temperature effect were compared with the results from Aspen process simulation as shown in Figure 4.15. In general, for all values of temperature, the agreement between the simulation results and the experimental data is indeed satisfactory, and the difference in composition at lower temperature, especially for CO, can be explained by the generally low composition of methane in the product gas. The deviation between the experimental data and predictions from equilibrium analysis is highest at low values of temperature (500°C & 550°C) where the amount of methane produced is lower than predicted by equilibrium analysis. One can conclude that for the selected experimental conditions, close to equilibrium conditions were attained, providing further confidence in the parametric study.

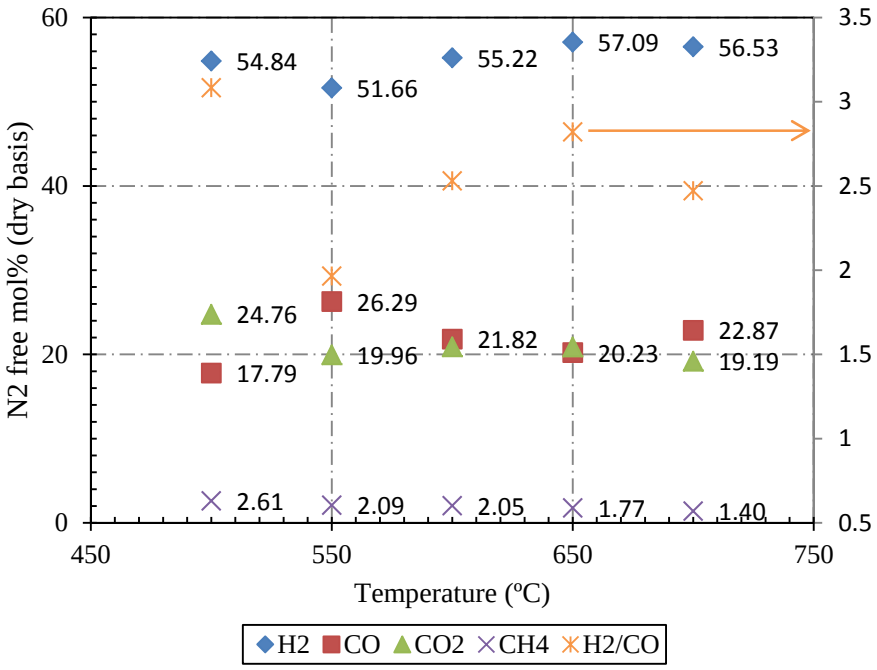

Figure 4.14: The plot of gas composition and H_2/CO molar ratio as a function of temperature for the ATR of glycerol

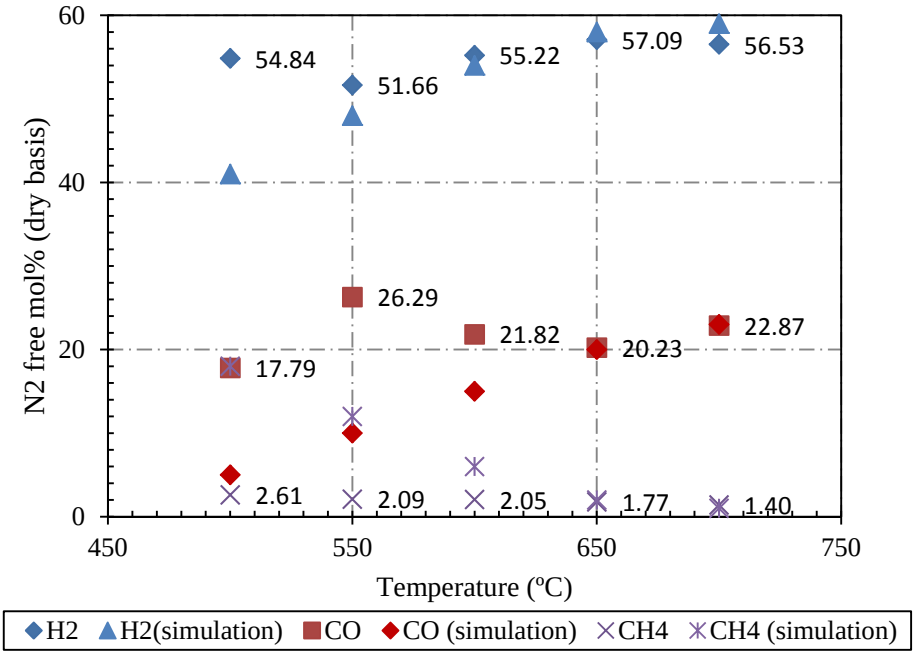

Figure 4.15: Comparison of experimental data with Aspen process simulation equilibrium results

IV.2. Kinetic Study of ATR of Glycerol

In order to obtain the intrinsic kinetics, the mass transfer and heat transfer resistances have to be minimized.

IV.2.1. Analysis of Mass & Heat Transfer Effects

IV.2.1.1. External mass transfer

For the monolithic reactor studied, the external mass transfer refers to the mass transfer from the gas bulk to the surface of the catalyst coating. The catalyst provided by BASF has 400 cells per square inch. The cells are square and each cell roughly has a side of 1.09mm. The typical gas flow rate through each channel for parametric study is around 0.012 SL/min. The calculated Re number is more than 76000, assuming the flow was all air (density and viscosity of air at 500°C were used for estimation). The flow is highly turbulent within the channels, indicating that the neglect of mass transfer resistance in gas phase is a safe assumption.

IV.2.1.2. Internal mass transfer

The dual-layer catalyst contains a 10 μm thickness coating consisting of one layer of steam reforming catalyst in contact with one layer of partial oxidation catalyst. The internal mass transfer refers to the mass transfer from the external surface of the catalyst coating to the interface between the catalyst coating and the support. The experimental study of the internal mass transfer limitation is not a practical option at this moment. The thickness of the catalyst coating is a design parameter for the catalyst to ensure sufficient active catalyst sites for both steam reforming and partial oxidation. For the case studied, we have to consider the effect of the internal mass transfer and account for the effect in the kinetic model using the estimated

effective diffusion factor. There are different ways to evaluate the effective diffusivities of different substances in the wash coat member, such as random pore model and parallel pore model.

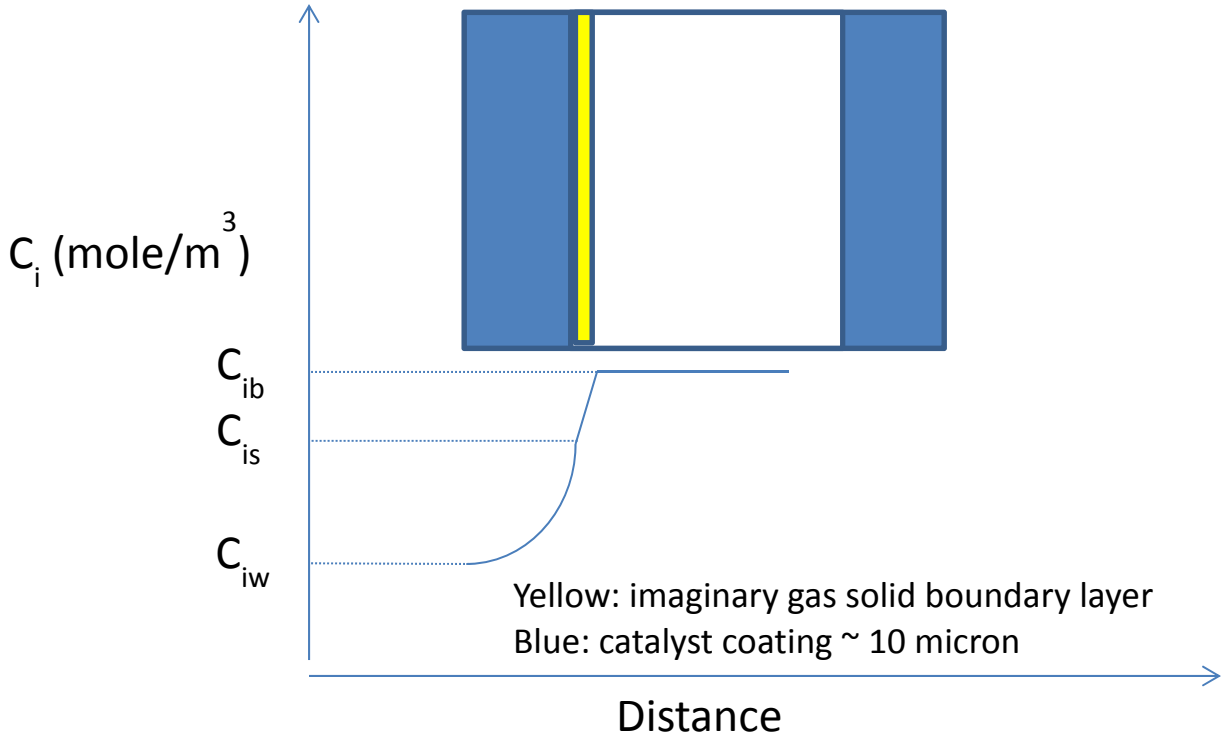

Figure 4.16: Schematic of concentration distribution in transverse dimension

The qualitative distribution of concentration of specie i could be schematically illustrated as in Figure 4.16. Accordingly, the reaction rate will show a similar distribution along the thickness of the catalyst coating. Assuming the reaction rate for a specific reaction is r_j, then the average reaction rate throughout the layer could be written as,

$$r_{j,avg} = \frac{\int_0^{th} r_j(x)dx}{th} \tag{4.5}$$

where "th" stands for the thickness of the catalyst coating layer and "x" stands for the relative distance from the location of the reaction to the surface of the coating. The mass conservation equation considering diffusion, convective transport and reaction is as follows:

$$D_{AB}\left[\frac{\partial^2 C_A}{\partial x^2}+\frac{\partial^2 C_A}{\partial y^2}+\frac{\partial^2 C_A}{\partial z^2}\right]-U_x\frac{\partial C_A}{\partial x}-U_y\frac{\partial C_A}{\partial y}-U_z\frac{\partial C_A}{\partial z}+r_A=\frac{\partial C_A}{\partial t} \tag{4.6}$$

Within the catalyst layer, the convective transport could be neglected due to extremely small velocity in all directions, and in steady state,

$$\frac{\partial C_A}{\partial t}=0 \tag{4.7}$$

The diffusion in z and y direction could be neglected after the order of magnitude analysis. Therefore, the equation could be simplified and the relation between concentration C_i (mol/m3) and location x inside the catalyst coating is as follows.

$$D_i \frac{d^2 c_i}{dx^2} = -\rho_{ca} \sum \nu_i r_j \tag{4.8}$$

where D_i is the diffusion coefficient of specie i in the catalyst layer, ν_i is the stoichiometric coefficient of specie i and ρ_{ca} is the density of the catalyst coating.

Theoretically, both transvers and axial dimensions should be considered, however, the computational process will be a bit overwhelming and it is also experimentally impractical to obtain required data for regression. In order to simplify the model, in this study, we neglect the axial concentration gradient and consider only the transverse direction gradient by evaluating the criteria proposed by Chinkui Cheng (2011) which is, when

$$\Phi_{\exp}^2 = \frac{(-r_{\exp}) d_p^2 \rho_b}{4 D_{eff} C_{As}} < 1 \tag{4.9}$$

is satisfied, less than 5% variance in the transverse direction is expected. Moreover, according to Creaser et al. (2010), the simplification is relatively safe here. In that study, they used a catalyst layer of ~35 microns and they neglected the internal mass transport resistance within the layer for the regression of kinetic parameters at a GHSV of ~ 15000 h^{-1}.

IV.2.1.3. Analysis of heat transfer effect

The novelty and the most important part of the patent for the dual-layer catalyst is the integration of the reaction heat provided by CPO and that required by steam reforming in a micron-size layer by layer reactor. The layer of CPO catalyst is in direct contact with the steam reforming catalyst and the heat produced by CPO reaction will be effectively absorbed and used to drive steam reforming reaction. The application of the dual-layer catalyst enables us to neglect the heat transport within the catalyst layer.

The criterion for determining whether there will be a temperature gradient in the studied region is given in Mears (1971):

$$D_a = \left| \frac{-\Delta H (-r_{obs})(1-\varepsilon) R_o^{\,2}}{\lambda T_w (1+b)} \right| < 0.4 \frac{R T_w}{E_a} \tag{4.10}$$

If the left hand side of the equation is smaller than the right hand side, the radial temperature gradients would be less than 5%. In the catalyst layer, the apparent heat of reaction is approximately zero since the heat produced by CPO reaction is consumed instantly by steam reforming. Therefore, the equation is satisfied and it can be concluded that the radial heat transfer resistance could be neglected. For the reaction system studied, the monolith catalyst is wrapped with an insulating material. The heat transfer from the furnace to the catalyst therefore could be neglected. For the gas bulk, heat transfer limitation will not be considered. The vibrant Brownian motion would eliminate any heat transfer limitation and make the temperature uniform in gas phase. Therefore, the system studied could be considered as an isothermal system.

IV.2.2. Kinetic Modeling

A relationship between the experimentally measurable values and the kinetic parameters should be established first. Considering only one cell of the monolithic catalyst, the mass balance

accounting for mass transport between the bulk gas and the catalyst wash coat surface is as follows:

$$dFi = A_c \times dZ \times S_v \times k_c (c_{is} - c_{ig}) = \rho_{ca} \times A_c \times dZ \times \sum v_i r_{j,avg} \tag{4.11}$$

where A_c is the cross-sectional area of the catalyst coating, S_v is the wash coat surface area per monolith volume. Since the concentration gradient across the catalyst layer is neglected, $r_{j,avg}$ could be substituted by the r_j at the surface of the catalyst layer. The equation could be written as.

$$\frac{dFi}{dz} = \rho_{ca} \times A_c \times \sum v_i r_j \tag{4.12}$$

Combined with GC analysis, the change of concentration of different species could be measured before and after the reaction and hence the left side of the equation could be calculated under the assumption that the reaction rate is constant throughout the catalyst. Reaction rate is a function of concentration of reactants, therefore in order for the assumption to be reasonable the concentration of reactants should not go through a significant change during the reaction. In other words, the conversion should be maintained relatively low.

For the study of the auto-thermal reforming of glycerol, there will be a number of reactions taking place. Including all possible reactions in a global kinetic model is not practical. In this model, only a few key overall reactions which will represent the experimental observations will be considered to yield the needed kinetic parameters. In the dual-layer catalyst, the main active component for partial oxidation is platinum while the active component for steam reforming is rhodium. No kinetic model has been published regarding the auto-thermal reforming of glycerol. Due to the lack of published kinetic data, only the general form of the rate expressions developed for other catalytic systems could be used as a guide.

The measurable quantities from current experimental setup are the reactant composition at the entrance and the product composition at the exit. In the rate expressions, "y_i" which is the mole fraction of specie i is actually a function of time (in a batch reactor) or for continuous reactor, the location relative to the entrance, $y_i=f(z)$. It is not practical to monitor the composition change along the monolith catalyst and derive the function in current setup. Therefore, in order to be able to integrate over the catalyst length under current experimental setup, the composition has to be considered constant throughout the reaction, which requires that the conversion of the reaction be as low as possible.

The kinetic modeling of the dual layer monolith ATR presents challenges because of the number of reactions involved as well as the fact that all the reactions occur in one reactor, instead of two sequential reactors as is common practice. Hence, the kinetics will be modeled based on the approach pioneered by Yang and Hougen (1950). Different rate expressions are derived from the Yang-Hougen model and the experimental kinetic rate data will be fitted to these expressions to determine the kinetic rate constants k_i and the equilibrium adsorption constants K_i. For acetic acid, it was possible to obtain all the kinetic data using a differential reactor whereas for glycerol, it was difficult to keep the conversion within <10%, hence the integral reactor method was applied. The individual rate equations as obtained from the Yang-Hougen model were incorporated into the material balance equations which were then subjected to a nonlinear regression analysis to obtain the kinetic constants. For the integral reactor, the material balance equations are non-linear ordinary differential equations.

IV.2.2.1. Development of Kinetic Models and Rate Expressions

We will now describe the approach for deriving the rate expressions for the different models based on different mechanisms and different rate limiting steps. The chemical species mainly involved in the ATR of glycerol are $C_3H_8O_3$, O_2, H_2O, H_2, CO, and CO_2. From our parametric study, the dual layer monolith ATR catalyst converts the reactants to products expected at equilibrium. Based on "atomic matrix", only three independent chemical reactions are needed to describe this 6-component, 3-atomic species system. The other combinations of reactions can be used to describe all possible products; however, reactions (1) to (3) below provide an appropriate set of reactions that can be combined to describe all possible reaction routes.

Steam reforming (SR): $C_3H_8O_3 + 3H_2O \leftrightarrow 7H_2 + 3CO_2$ (4.13)

Partial Oxidation: $C_3H_8O_3 + 2O_2 \leftrightarrow 4H_2O + 3CO$ (4.14)

Water-Gas Shift: $CO + H_2O \leftrightarrow H_2 + CO_2$ (4.15)

The Yang-Hougen rate model for heterogeneous catalytic reactions is generally expressed by a combination of three terms, namely, the kinetic factor, driving force group, and adsorption group;

$$\text{Rate}=\frac{(kinetic\ factor)(driving\ force\ group)}{adsorption\ group} \quad (4.16)$$

For example, the SR reaction $C_3H_8O_3 + 3H_2O \leftrightarrow 7H_2 + 3CO_2$ simplifies as:

$$G + 3S \leftrightarrow 7H + 3D \quad (4.17)$$

where G, S, H and D represent glycerol, steam, hydrogen and carbon dioxide respectively. For all the models, we assume that surface reaction is controlling, hence driving force, and adsorption group are given by:

Driving force: surface reaction controlling $(P_G P_S - \frac{P_H P_D}{K_1})$ (4.18)

Adsorption group: $(1 + K_G P_G + K_S P_S + K_H P_H + K_D P_D)^n$ (4.19)

The exponents for adsorption, the kinetic groups and the rate expressions for different mechanisms are given in Table 4.2 for the steam reforming reaction.

Table 4.2: Rate Expressions for SR of Glycerol based on Yang-Hougen Model

	Exponents of adsorption group	Kinetic group
Without dissociation	n=2	$k_{SR,1}K_G K_S$
Dissociation of G	n=3	$k_{SR,1}K_G K_S$
Dissociation of G (S not adsorbed)	n=2	$k_{SR,1}K_G$
No dissociation of G (S not adsorbed)	n=2	$k_{SR,1}K_G$

Adsorption group	Kinetic group	Rate expression
n=2 (no dissociation of G)	$k_{SR}K_GK_S$(without dissociation)	$\frac{(k_{SR,1}K_GK_S)(P_GP_S-\frac{P_HP_D}{K_1})}{(1+K_GP_G+K_SP_S+K_HP_H+K_DP_D)^2}$
n=2 (dissociation of G, S not adsorbed)	$k_{SR}K_G$ (dissociation of G, S not adsorbed)	$\frac{(k_{SR,1}K_G)(P_GP_S-\frac{P_HP_D}{K_1})}{(1+K_GP_G+K_SP_S+K_HP_H+K_DP_D)^2}$
n=3 (dissociation of G)	$k_{SR}K_GK_S$ (dissociation of G)	$\frac{(k_{SR,1}K_GK_S)(P_GP_S-\frac{P_HP_D}{K_1})}{(1+K_GP_G+K_SP_S+K_HP_H+K_DP_D)^3}$

Following the same approach, different rate expressions based on different mechanisms were derived for the other two reactions that comprise the ATR. These rate equations are listed in Table 4.3. The values for the kinetic constants obtained from these rate equations have to satisfy certain conditions, which are derived from the thermodynamic and optimization considerations. These constraints are:

1) $K_i, k_i > 0$ (4.20a)
2) E_a (Activation Energy) >0 (4.20b)
3) R^2 (optimization variable)>95% (4.20c)
4) The confidence intervals of the parameter values should be much less than the values of the parameters themselves. (4.20d)

Table 4.3: Different Rate Expressions Based on Yang-Hougen Model

Reaction		Rate Equation
SR: $C_3H_8O_3+3H_2O \leftrightarrow 7H_2+3CO_2$	no dissociation of G	$\frac{(k_{SR,1}K_GK_S)(P_GP_S-\frac{P_HP_D}{K_1})}{(1+K_GP_G+K_SP_S+K_HP_H+K_DP_D)^2}$
	dissociation of G, S not adsorbed	$\frac{(k_{SR,1}K_G)(P_GP_S-\frac{P_HP_D}{K_1})}{(1+K_GP_G+K_SP_S+K_HP_H+K_DP_D)^2}$
	dissociation of G	$\frac{(k_{SR,1}K_GK_S)(P_GP_S-\frac{P_HP_D}{K_1})}{(1+K_GP_G+K_SP_S+K_HP_H+K_DP_D)^3}$
CPO: $C_3H_8O_3+2O_2 \leftrightarrow 4H_2O+3CO$	no dissociation of G	$\frac{(k_{SR,2}K_GK_O)(P_GP_O-\frac{P_SP_M}{K_2})}{(1+K_GP_G+K_OP_O+K_SP_S+K_MP_M)^2}$

	dissociation of G, O not adsorbed	$\frac{(k_{SR,2}K_G)(P_GP_O - \frac{P_SP_M}{K_2})}{(1 + K_GP_G + K_OP_O + K_SP_S + K_MP_M)^2}$
	dissociation of G	$\frac{(k_{SR,2}K_GK_O)(P_GP_O - \frac{P_SP_M}{K_2})}{(1 + K_GP_G + K_OP_O + K_SP_S + K_MP_M)^3}$
WGS: $CO + H_2O \leftrightarrow H_2 + CO_2$	no dissociation of M	$\frac{(k_{SR,3}K_MK_S)(P_MP_S - \frac{P_HP_D}{K_3})}{(1 + K_MP_M + K_SP_S + K_HP_H + K_DP_D)^2}$
	dissociation of M, S not adsorbed	$\frac{(k_{SR,3}K_M)(P_MP_S - \frac{P_HP_D}{K_3})}{(1 + K_MP_M + K_SP_S + K_HP_H + K_DP_D)^2}$
	dissociation of M	$\frac{(k_{SR,3}K_MK_S)(P_MP_S - \frac{P_HP_D}{K_3})}{(1 + K_MP_M + K_SP_S + K_HP_H + K_DP_D)^3}$

The equilibrium constants K_1, K_2, and K_3 can be determined from thermodynamic data, and their values are presented in Table 4.4 below:

Steam Reforming: $C_3H_8O_3 + 3H_2O \rightarrow 7H_2 + 3CO_2$ K_1

Catalytic Partial Oxidation: $C_3H_8O_3 + 2O_2 \rightarrow 4H_2O + 3CO$ K_2

Water Gas Shift: $CO + H_2O \leftrightarrow H_2 + CO_2$ K_3

Table 4.4: Thermodynamic Equilibrium Constants

T (° C)	T (K)	K_1	K_2	K_3
500	773	3.5E+30	2.0E+128	5.19
550	823	7.8E+31	4.7E+122	3.67
600	873	1.4E+33	5.3E+117	2.71
650	923	1.9E+34	2.2E+113	2.08
700	973	2.2E+35	2.9E+109	1.64

The steam reforming reaction of glycerol can be obtained by combining the water-gas shift reaction (Eq. 4.15), and the glycerol decomposition reaction:

$$C_3H_8O_3 \rightarrow 3CO + 4H_2 \quad (4.21)$$

In the analysis that follows, we focus on the steam reforming reaction since it's assumed to be the slowest of all reactions. The catalytic partial oxidation reaction is extremely fast and as data will show, is completed within a short distance from the entrance of the reactor. There was no equivalent test for the decomposition reaction. A future study that incorporates the decomposition reaction is envisioned. For the SR reaction, the eight rate expressions tested for fit with the kinetic data are presented in Table 4.5.

Table 4.5: Fitted Model Equations and Associated Reaction Mechanisms

Model	Equation	Mechanism
1.	$r_G = \frac{k_{rxn} P_G P_W}{(1 + K_G P_G + K_W P_W)^2}$	Competitive Adsorption of Reactants; Non-dissociative Reactants
2.	$r_G = \frac{k_{rxn} P_G P_W}{(1 + K_G P_G)(1 + K_W P_W)}$	Non-Competitive Adsorption of Reactants; Non-Dissociative Reactants
3.	$r_G = \frac{k_{rxn} P_G P_W^{0.5}}{(1 + K_G P_G + (K_W P_W)^{0.5})^2}$	Competitive Adsorption of Reactants; Dissociative Steam
4.	$r_G = \frac{k_{rxn} P_G^{0.5} P_W}{(1 + (K_G P_G)^{0.5} + K_W P_W)^2}$	Competitive Adsorption of Reactants; Dissociative Glycerol
5.	$r_G = \frac{k_{rxn} P_G^{0.5} P_W^{0.5}}{(1 + (K_G P_G)^{0.5} + (K_W P_W)^{0.5})^2}$	Competitive Adsorption of Reactants; Dissociative Reactants
6.	$r_G = \frac{k_{rxn} P_G P_W^{0.5}}{(1 + K_G P_G)(1 + (K_W P_W)^{0.5})}$	Non-Competitive Adsorption of Reactants; Dissociative Steam
7.	$r_G = \frac{k_{rxn} P_G^{0.5} P_W}{(1 + (K_G P_G)^{0.5})(1 + K_W P_W)}$	Non-Competitive Adsorption of Reactants; Dissociative Glycerol
8.	$r_G = \frac{k_{rxn} P_G^{0.5} P_W^{0.5}}{(1 + (K_G P_G)^{0.5})(1 + (K_W P_W)^{0.5})}$	Non-Competitive Adsorption of Reactants; Dissociative Reactants

IV.2.2.2. Kinetic Data on ATR of Glycerol

The eight rate expressions for the ATR of glycerol for different kinetic models were developed based on the Yang-Hougen model, which is similar to the Langmuir-Hinshelwood approach. The objective would be to use the experimental rate data in combination with non-linear regression techniques to obtain the kinetics and adsorption parameters. It is preferred that such rate data come from differential reactor which requires that the conversion is kept below 10%. However, in the case of glycerol, it was extremely difficult to meet this criterion with practically relevant processing conditions. It would require processing temperatures lower than 300^{o}C to meet the requirement. Even at such low temperatures, we would need to search the operating parameter space which is a time-consuming exercise. We therefore decided to abandon the differential reactor approach and instead we switched to the integral reactor method. Regardless of the approach, the data must be obtained under kinetically controlled processing conditions. Adopting the integral reactor method necessitated the re-design of the kinetics experiments. Essentially, for the monolith reactor, this entailed performing the reaction under practically realistic conditions at different reactor lengths. Initially we planned to conduct the kinetics experiments with the following reactor lengths; 2.75", 2.5", 2.25", 2", 1.75", and 1.25". However, as the kinetic study progressed and the data were analyzed, we observed that shorter reactor lengths needed to be included to elucidate the ATR of glycerol in the entrance region of the reactor, especially the interplay amongst the reactions comprising the process. The reactor lengths selected for inclusion were 0.75", 0.5", and 0.25". The results presented here pertain to the six reactor lengths initially selected.

IV.2.2.2.1 Effect of Steam/C ratio

For each of the six reactor lengths, the temperature and the O_2/C ratio were kept constant at 650^{o}C and 0.15 respectively while the Steam/C (S/C) ratio was varied. Based on the

performance and optimization studies, three values of S/C ratios were selected, i.e., 0.4, 0.8, and 1.2. For each experimental run, the flow rate and the corresponding partial pressure of each component species were determined at the exit of each reactor length, and these data were then associated with the amount of catalyst contained in the entire reactor length. The reactor performance data when plotted against catalyst weight indirectly provides the composition profile along the length of the reactor which would otherwise have been difficult to obtain without sophisticated online monitoring probes installed along the length of the reactor. The only shortcoming of this approach is that end-effects are assumed negligible.

Figures 4.17a-c show the partial pressure of each of the reactants, oxygen, glycerol, and steam as a function of the catalyst weight (or reactor length). It is very striking that within a short distance from the entrance of the reactor, the oxygen (Fig. 4.17a) is rapidly consumed which suggests that the catalytic partial oxidation (CPO) reaction is restricted to the region close to the reactor entrance. This is not surprising since CPO is an extremely fast reaction when compared to the steam reforming or water-gas shift reaction. This behavior in oxygen partial pressure profile necessitated the inclusion of shorter reactor lengths so as to be able to better define the region where the CPO was active. It is reasonable to infer that for the reactor lengths used, the only reaction needed to be considered for kinetic analysis is the steam reforming (SR) reaction.

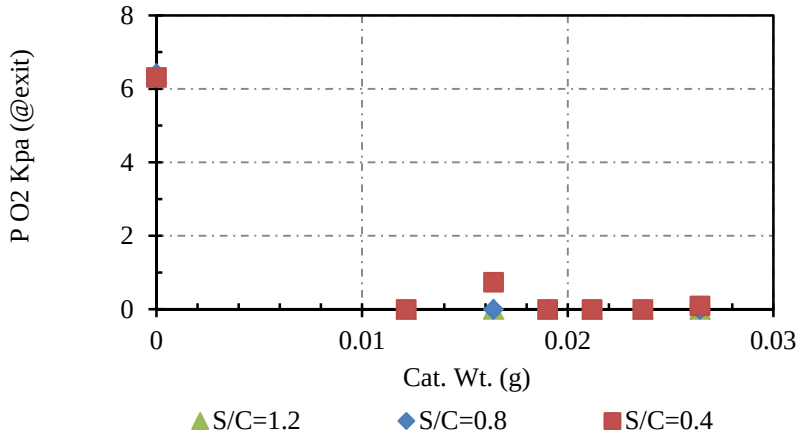

(a)

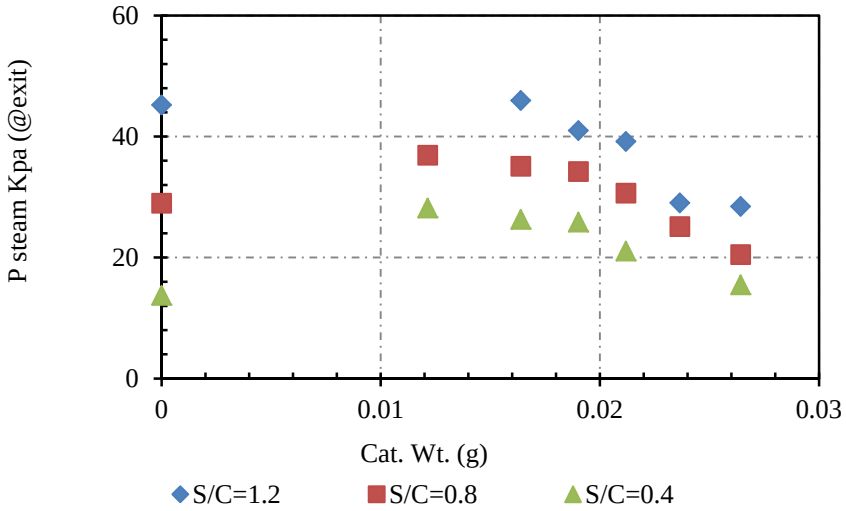

(b)

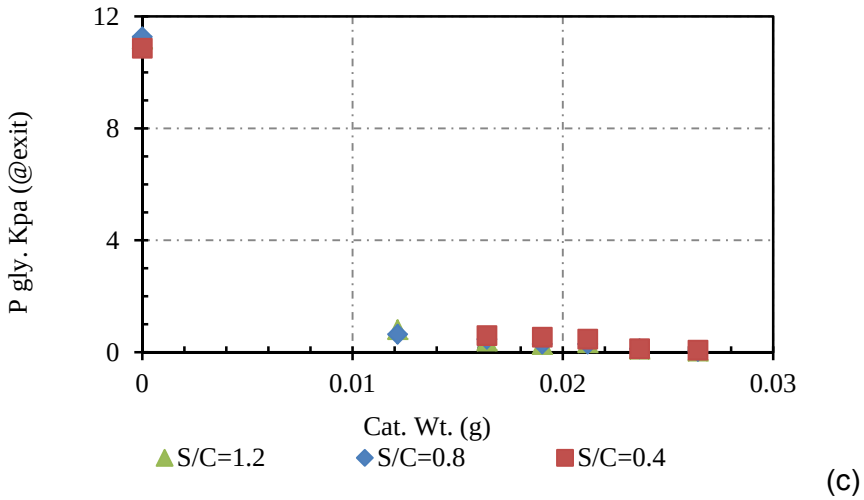

Figures 4.17a-c: Partial pressure profile of reactants (a) O_2 (b) Steam, and (c) glycerol along the reactor length for three different S/C ratios

The pressure profile for steam (Fig. 4.17b) also suggests that CPO predominates close to the entrance of the reactor as the amount of steam first increases and then begins to decrease. This could only be explained by the CPO generating more water in addition to the water in the feed. As soon as the CPO is completed, the SR and WGS reactions, both of which consume water, take over. The data from the short reactor lengths will enable us to determine, to a reasonable degree, where the switch occurs. We will also be able to ascertain whether SR occurs to any appreciable extent close to the entrance of the reactor. The pressure profile of the glycerol (Fig. 4.17c) indicates that the glycerol exhibits a behavior similar to that of oxygen as it is rapidly depleted. These observations taken together suggest that under the selected processing conditions only a short reactor length is required for almost complete conversion of the main reactant.

The pressure profiles for the main products, H_2, CO, and CO_2 are presented in Figures 4.18a-c for the three different values of S/C ratio. From Fig. 14.18a (S/C of 1.2), after the CPO reaction ceases, one would expect that the composition of CO will remain the same but the S/C ratio is so high that the WGS reaction continues to consume CO and steam (Fig. 14.18b) to produce more H_2 as evident from the H_2 profile. In contrast, at the low S/C ratio of 0.4, the composition of CO remains essentially constant after the initial production from the CPO. The concomitant decrease in steam (Fig. 14.18b) indicates that the SR reaction predominates in this region.

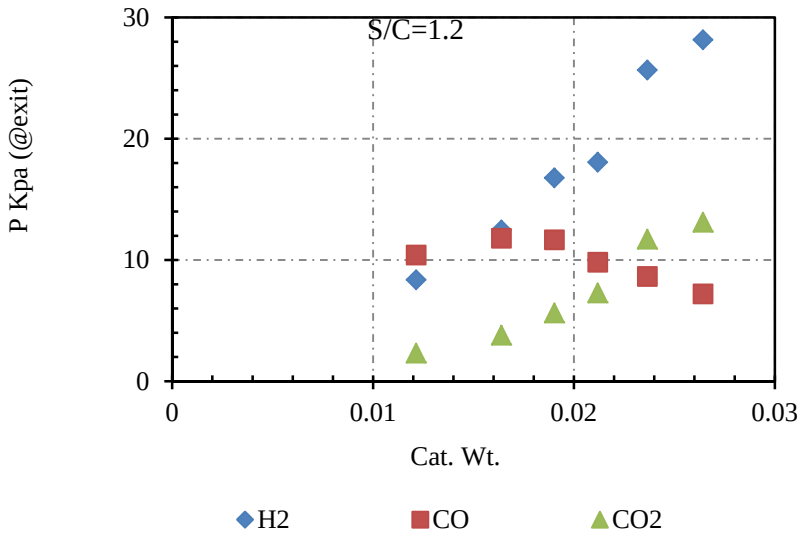
S/C=1.2
P Kpa (@exit)
30
20
10
0
0
0.01
0.02
0.03
Cat. Wt.
H2
CO
CO2

(a)

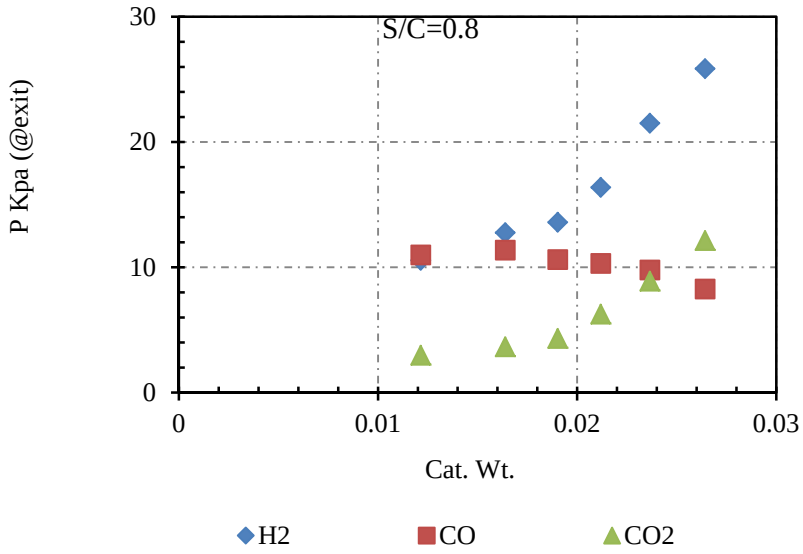
S/C=0.8
P Kpa (@exit)
30
20
10
0
0
0.01
0.02
0.03
Cat. Wt.
H2
CO
CO2

(b)

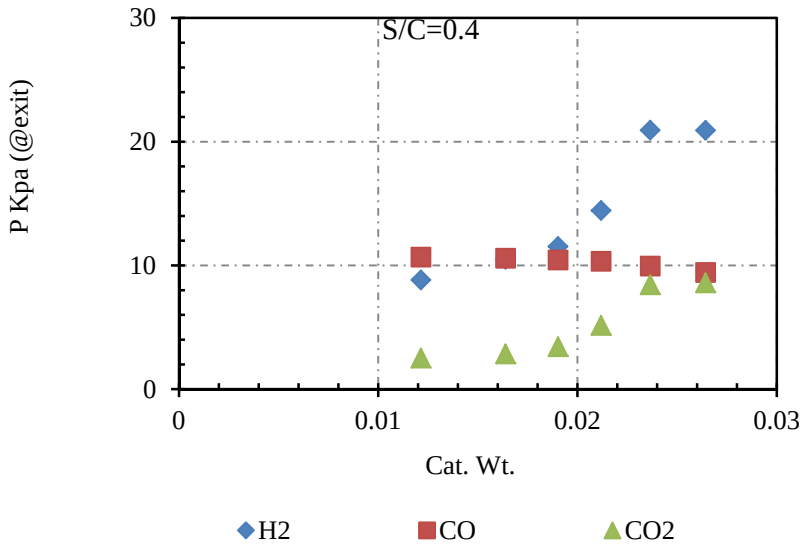

(c)

Figures 4.18a-c: Partial pressure profile of products H_2, CO, and CO_2 along the reactor length for three different S/C ratios (a) 1.2, (b) 0.8, and (c) 0.4

For the calculation of kinetics and adsorption parameters, the glycerol reaction rates need to be determined from the flow rate rather than the partial pressure, although the expressions for the rate are written in terms of partial pressures. Figures 14.19a-c show the flow rate profiles for the three values of S/C ratio and the data indicate an exponential decay with catalyst weight (or reactor length). *We have also indicated (using the red vertical line) on each figure the location where all the oxygen would have been consumed assuming that only CPO occurs in the entrance region. For all the experimental conditions, the location corresponds to approximately a reactor length of 0.25".* This provides a reasonable preliminary estimate which could be improved upon from the short reactor lengths. About one-third of the glycerol was consumed in the short CPO region.

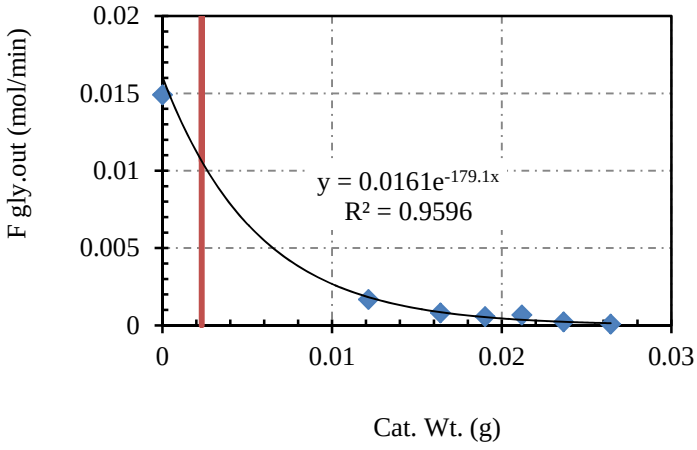

(a)

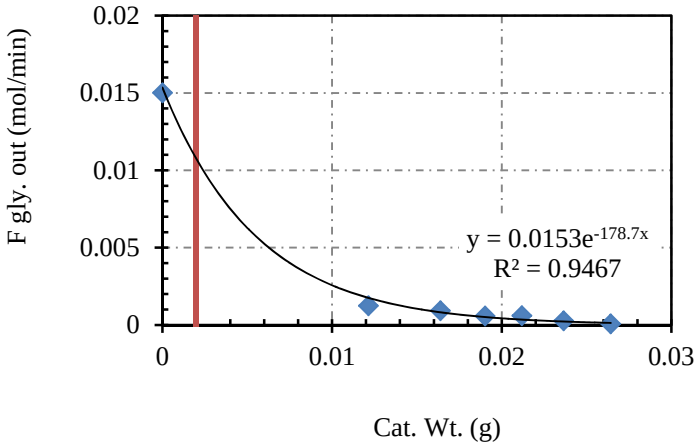

(b)

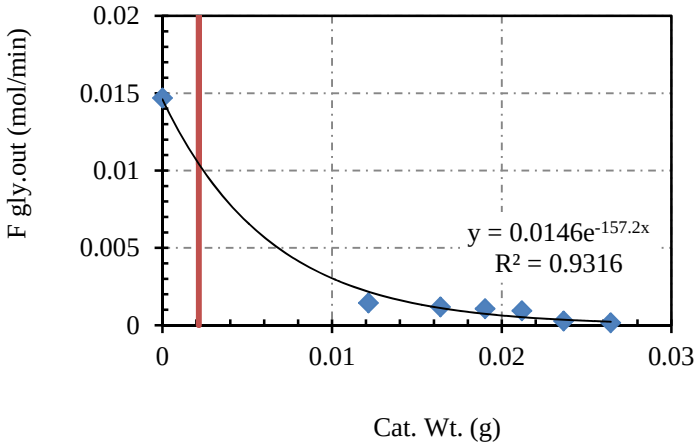

(c)

Figures 4.19a-c: Flow rate of glycerol along the reactor length for three different S/C ratios (a) 1.2, (b) 0.8, and (c) 0.4

IV.2.2.2.2. Effect of O_2/C ratio

The kinetic experiments to elucidate the effect of O_2/C ratio were similar to those conducted for S/C ratio except in this case we varied the O_2/C ratio instead of S/C ratio. For each of the six reactor lengths, the temperature and the S/C ratio were kept constant at 650°C and 0.8 respectively while the O_2/C ratio was varied. Based on the performance studies previously conducted and reported in section IV.1, three values of O_2/C ratio were considered, namely 0.1, 0.15, and 0.2, well below the stoichiometric requirements for possible CPO reactions.

Figure 4.20a shows the partial pressure profile for O_2 which again shows that CPO occurs, and is completed close to the entrance of the reactor. In Figure 4.20b, the O_2/C ratio does not appear to have any significant effect on the steam partial pressure. This is to be expected since the steam is in excess and O_2 and H_2O do not appear together as reactants in any of the reactions postulated for the ATR of glycerol. In Figure 4.20c, for high O_2/C ratio (0.2), a significant amount of glycerol is consumed in the entrance region, leaving a smaller amount for subsequent SR and WGS reactions when compared to the low O_2/C ratio (0.1). In any case, for all O_2/C ratios, only a relatively small amount of glycerol remains beyond the entrance region which is dominated by CPO.

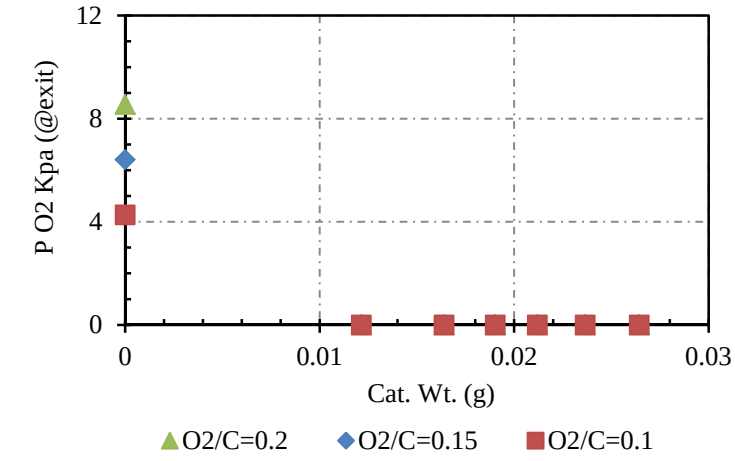

(a)

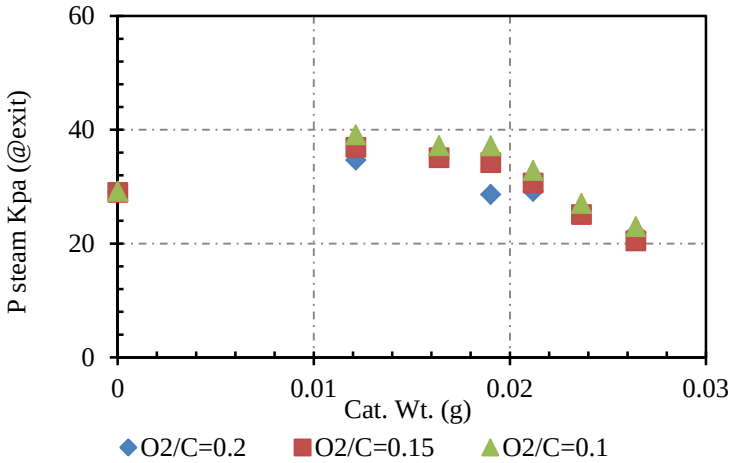

(b)

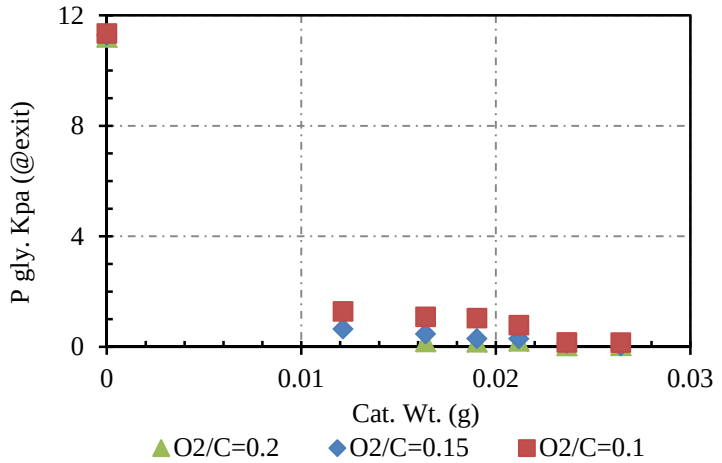

(c)

Figures 4.20a-c: Partial pressure profile of reactants (a) O_2 (b) Steam, and (c) glycerol along the reactor length for three different O_2/C ratios

The pressure profiles for the products, H_2, CO and CO_2 are presented in Figures 4.21a-c. At low O_2/C ratio, the amount of CO remains constant because in the axial location where the data were collected the CPO reaction is complete and the amount of CO produced is not sufficiently

high for the WGS reaction to affect CO composition. Essentially, only the SR reaction occurs. The amount of H_2 continues to increase sharply even though the amount of unreacted glycerol is relatively small. The reason is that for every mole of glycerol consumed in the SR reaction, seven moles of hydrogen are produced. At the intermediate O_2/C ratio, 0.15, we observe a slight decrease of CO with reactor location because more CO is produced when compared to the low O_2/C ratio. Therefore, more CO is available for the WGS reaction which consumes some of it to produce a little more H2. As the O_2/C ratio increases, the effect of WGS in this region becomes more pronounced. Although the amount of unreacted glycerol reduces as the O_2/C ratio increases however more CO is produced from the CPO region which is then available for the WGS reaction. For all ratios of O_2/C, the amount of CO_2 increases since it's a product of all the ATR reactions.

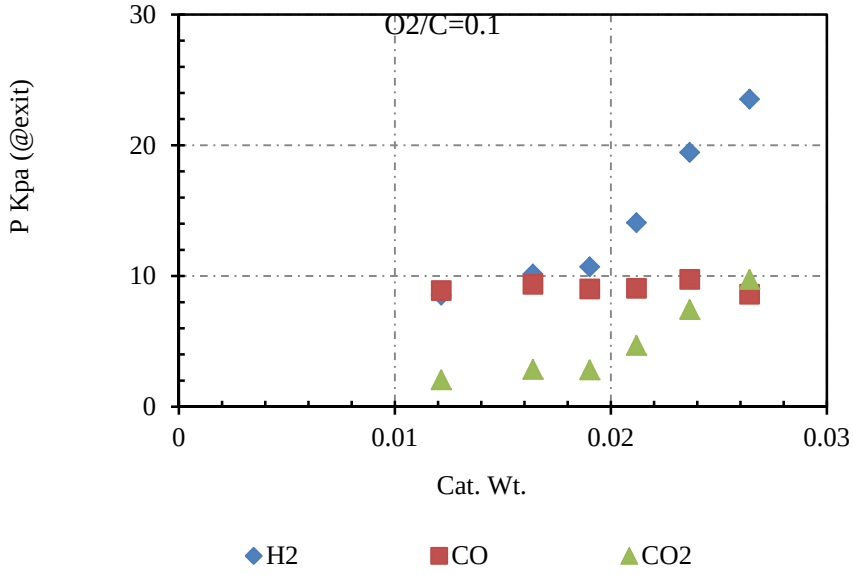

(a)

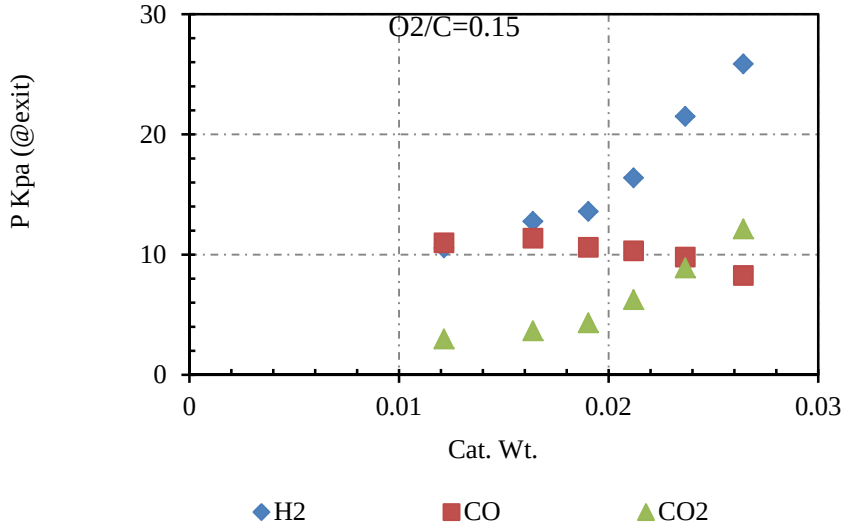

(b)

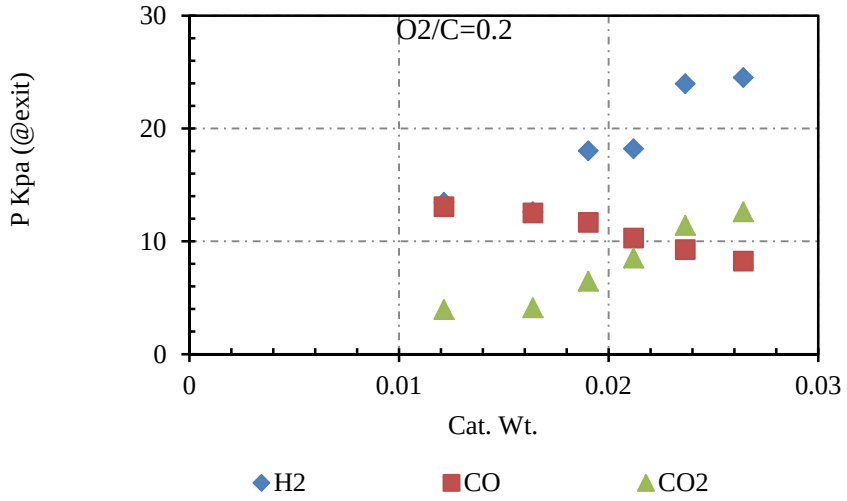

(c)

Figures 4.21a-c: Partial pressure profile of products H_2, CO, and CO_2 along the reactor length for three different O_2/C ratios (a) 0.1, (b) 0.15, and (c) 0.2

Figures 4.22a-c show the flow rate of glycerol as a function of catalyst weight for different values of O_2/C ratio. These data are regressed and fitted to exponential equations from which the reaction rate can be easily calculated.

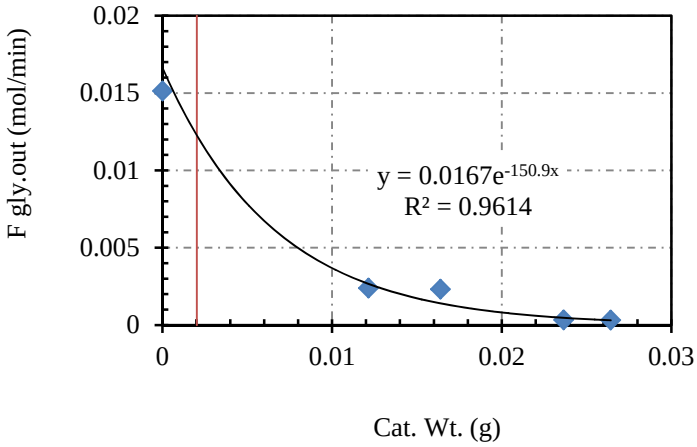

(a)

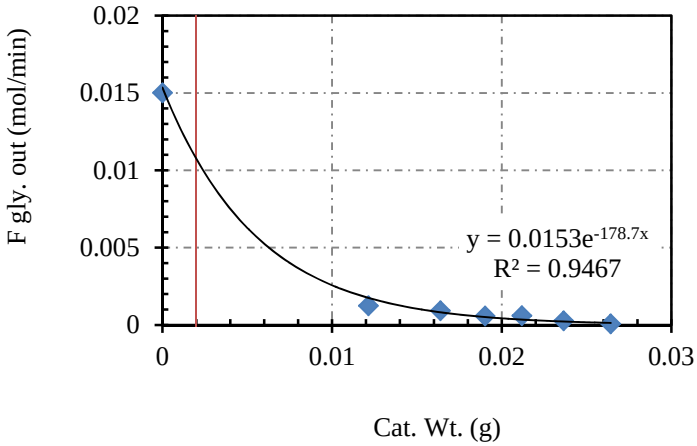

(b)

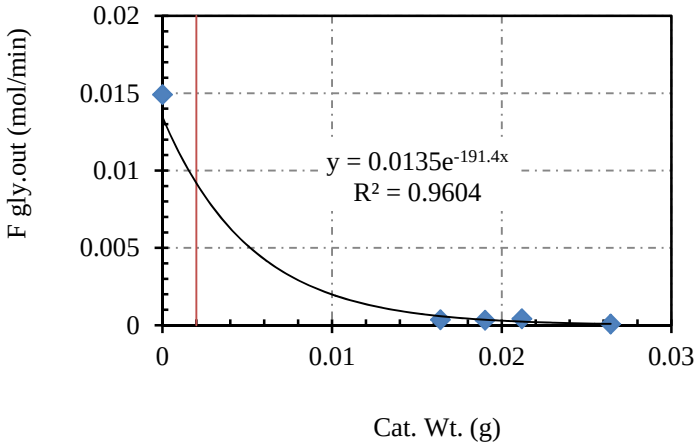

(c)

Figures 4.22a-c: Flow rate of glycerol along the reactor length for three different O_2/C ratios (a) 0.1, (b) 0.15, and (c) 0.2

IV.2.2.2.3. Effect of feed flow rate of glycerol

In addition to the S/C and O_2/C ratios, we also varied the amount of glycerol in the feed while keeping all the other parameters, i.e, S/C, O_2/C and temperature the same. The experimental results are qualitatively similar to those of other parameters and are presented in Figures 4.23-4.25.

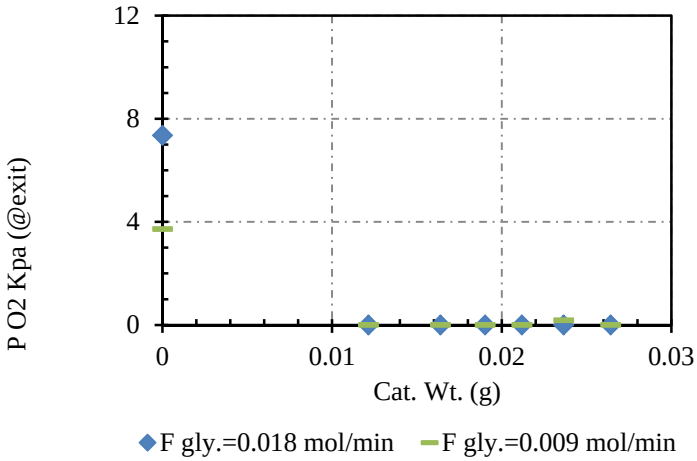

(a)

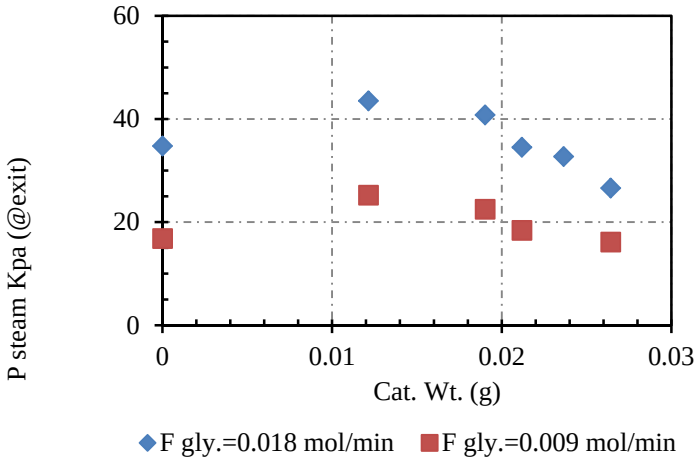

(b)

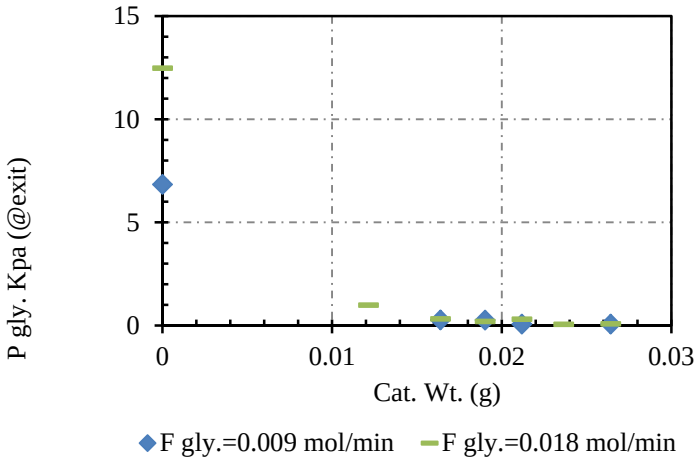

(c)

Figures 4.23a-c: Partial pressure profile of reactants (a) O_2 (b) Steam, and (c) glycerol along the reactor length for two different glycerol flow rate values

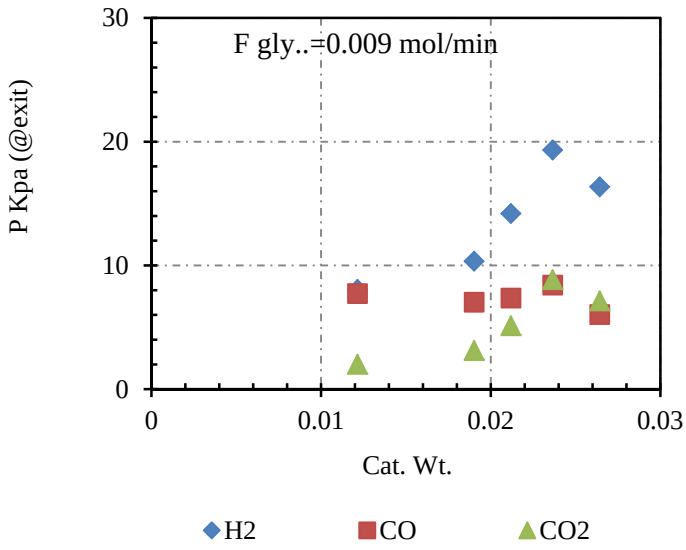

(a)

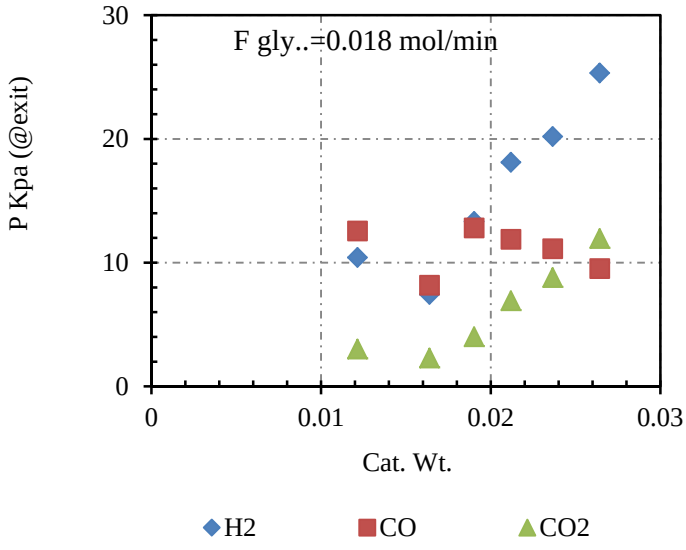

(b)

Figures 4.24a-b: Partial pressure profile of products H_2, CO, and CO_2 along the reactor length for two different flow rates of glycerol (a) 0.009 (b) 0.018 mol/min

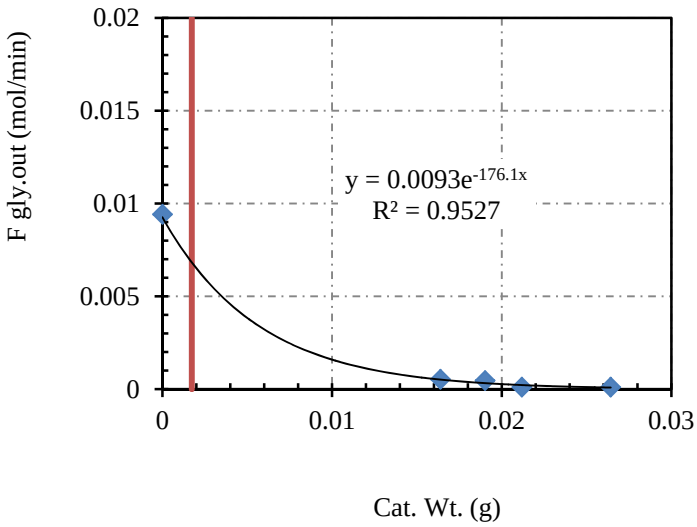

(a)

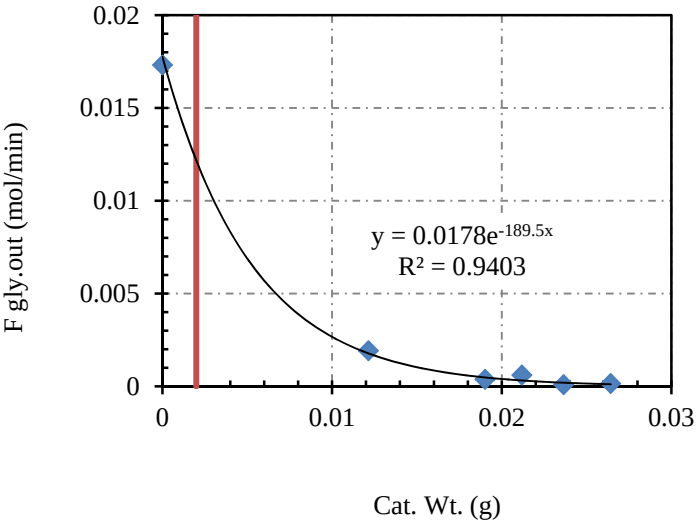

(b)

Figures 4.25a-b: Flow rate of glycerol along the reactor length for two different flow rates of glycerol (a) 0.009, (b) 0.018 mol/min

Altogether, we collected forty-two data points for the estimation of the kinetic parameters.

IV.2.2.3. Kinetic Parameters Evaluation

The reaction rate expression of Eq. 4.12 can be re-written as:

$$\text{Reaction rate} = dF/dW = f(P_G, P_W, P_O; k_{RXN}, K_G, K_W, K_O) \quad (4.12)$$

where

F = flow rate (mol/min)
W = catalyst weight (gm)
P_G = partial pressure of glycerol (kPa)
P_W = partial pressure of steam (kPa)

P_O = partial pressure of oxygen (kPa)
k_{RXN} = reaction rate coefficient
K_G = adsorption coefficient for glycerol (kPa^{-1})
K_W = adsorption coefficient for water (kPa^{-1})
K_O = adsorption coefficient for oxygen (kPa^{-1})

The unit of k_{RXN} will be determined by the form of the expression on the right hand side of Eq. 4.12. Based on the above equation, the reaction rate can be evaluated by taking the derivative of the flow rate (mol/min) vs. catalyst weight (gm) from the expressions fitted to the experimental data and presented in Figures 4.19a-c, 4.22a-c, and 4.25a-b. At selected axial locations on these figures (which correspond to actual experimental data), the values of the partial pressures of the reactants and associated derivatives needed in Eq. 4.12 are obtained. The kinetic parameters can then be determined using regression analysis. Since only the SR and WGS reactions occur in the region under consideration, we can ignore oxygen in the analysis.

IV.2.2.3.1. Power-law model

The glycerol reforming rate was fitted to the power-law equation in the form:

$$\text{(-Reaction rate of glycerol)} = (k_{RXN})\, P_G^{\alpha} P_W^{\beta} \qquad (4.22)$$

where α and β are the power-law parameters and k_{RXN} is the rate coefficient in units of (mol./g.min $kPa^{-(\alpha+\beta)}$). The non-linear regression of the experimental data gave the estimates in Table 4.6 while Figure 4.26 shows the difference between the experimental rate data and the rate data predicted by the power-law equation. The model discrimination parameters indicate that the rate expression provides a satisfactory fit for the kinetic data.

Table 4.6: Kinetics and model discrimination parameters for the power-law model

Nonlinear regression (L-M)

Model: rgly = K*(Pgly^a)*(Pw^b)

Variable	Ini guess	Value	95% confidence
K	1	0.0741479	0.0288206
a	1	0.8186801	0.0372347
b	0	0.3834204	0.1075464

Nonlinear regression settings
Max # iterations = 300

Precision
R^2 = 0.9890113
R^2adj = 0.9884478
Rmsd = 0.0016407
Variance = 1.218E-04

General
Sample size = 42
Model vars = 3
Indep vars = 2
Iterations = 17

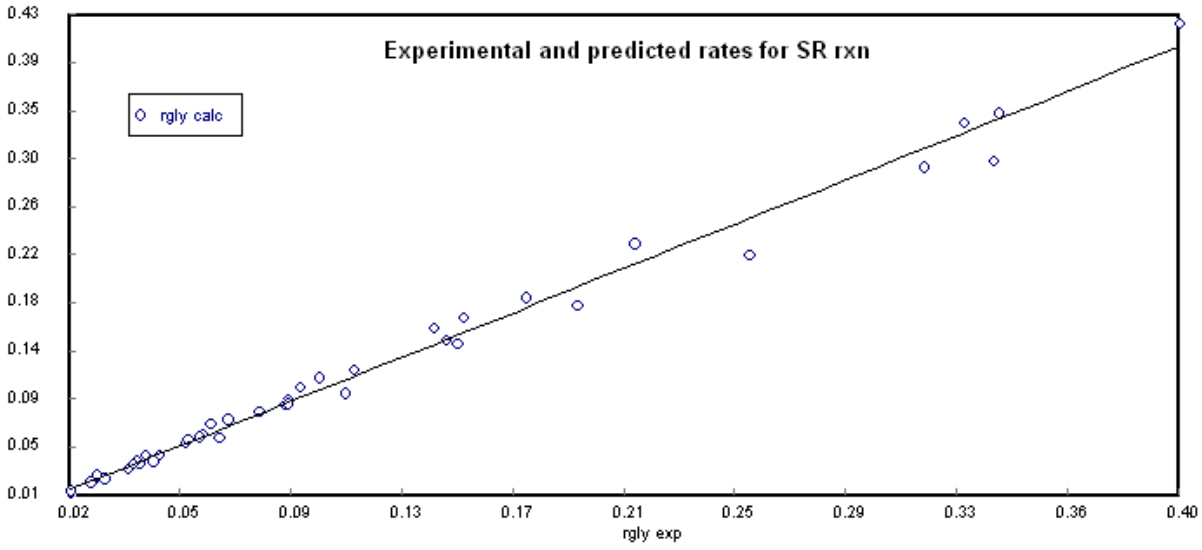

Figure 4.26: Comparison between experimental and predicted reaction rates for power-law model based on parameters in Table 4.6.

IV.2.2.3.2. L-H Type Rate Expressions

For the Langmuir-Hinshelwood type rate expressions, the eight different models of Table 4.5 were considered, and the experimental rate data were fitted to the models using non-linear regression. The results are presented in Table 4.7. The model discrimination parameters clearly indicate that a few of the models provide adequate fit while the others should be rejected. All the kinetic parameters were obtained from data at 650^{o}C.

Table 4.7: Reaction parameters estimation from LH-type rate expressions

Model	Equation	Variables	Model Discrimination		
			95% confidence	R^2	Variance
1.	$r_G = \frac{k_{rxn} P_G P_W}{(1 + K_G P_G + K_W P_W)^2}$	k_{rxn}=0.0287 mol $g^{-1}min^{-1}kPa^{-2}$	0.0055	0.99	1.118E-04
		K_G =0.2368kPa^{-1}	0.0561		
		K_w =0.0171kPa^{-1}	0.0042		
2.	$r_G = \frac{k_{rxn} P_G P_W}{(1 + K_G P_G)(1 + K_W P_W)}$	k_{rxn}=0.0334 mol $g^{-1}min^{-1}kPa^{-2}$	0.0098	0.99	1.133E-04
		K_G =0.3395 kPa^{-1}	0.0879		
		K_w =0.0552 kPa^{-1}	0.0252		
3.	$r_G = \frac{k_{rxn} P_G P_W^{0.5}}{(1 + K_G P_G + (K_W P_W)^{0.5})^2}$	k_{rxn}=0.0971 mol $g^{-1}min^{-1}kPa^{-1.5}$	0.0269	0.99	0.0001
		K_G =0.1791kPa^{-1}	0.0438		
		K_w =0.0013 $kPa^{-0.5}$	0.0021		
4.	$r_G = \frac{k_{rxn} P_G^{0.5} P_W}{(1 + (K_G P_G)^{0.5} + K_W P_W)^2}$	k_{rxn}=0.03945 mol $g^{-1}min^{-1}kPa^{-1.5}$	2.009E-06	0.68	0.0035
		K_G =4.621E-13 $kPa^{-0.5}$	1.084E-10		
		K_w =0.0483 kPa^{-1}	2.009E-06		
5.	$r_G = \frac{k_{rxn} P_G^{0.5} P_W^{0.5}}{(1 + (K_G P_G)^{0.5} + (K_W P_W)^{0.5})^2}$	k_{rxn}=0.1022 mol $g^{-1}min^{-1}kPa^{-1}$	2.714E-06	0.85	0.0017
		K_G =2.166E-15 $kPa^{-0.5}$	2.223E-12		
		K_w =0.0081$kPa^{-0.5}$	6.232E-07		
6.	$r_G = \frac{k_{rxn} P_G P_W^{0.5}}{(1 + K_G P_G)(1 + (K_W P_W)^{0.5})}$	k_{rxn}=0.0957 mol $g^{-1}min^{-1}kPa^{-1.5}$	0.0280	0.99	0.0001
		K_G =0.3380 kPa^{-1}	0.0873		
		K_w =0.0054 $kPa^{-0.5}$	0.0105		
7.	$r_G = \frac{k_{rxn} P_G^{0.5} P_W}{(1 + (K_G P_G)^{0.5})(1 + K_W P_W)}$	k_{rxn}=49.5375 mol $g^{-1}min^{-1}kPa^{-1.5}$	0.0014	0.82	0.0020
		K_G =1.776E-14$kPa^{-0.5}$	9.13E-12		
		K_w =195.1229 kPa^{-1}	0.0057		

8. $r_G = \frac{k_{rxn} P_G^{0.5} P_W^{0.5}}{(1+(K_G P_G)^{0.5})(1+(K_W P_W)^{0.5})}$	k_{rxn}=0.0707 mol $g^{-1}min^{-1}kPa^{-1}$	1.748E-06	0.87	0.0015
	K_G =4.426E-15$kPa^{-0.5}$	3.816E-12		
	K_w =0.0109 $kPa^{-0.5}$	1.415E-06		

Figure 4.27 shows the comparison between the experimental and predicted rate data for model 2. The fit is quite satisfactory.

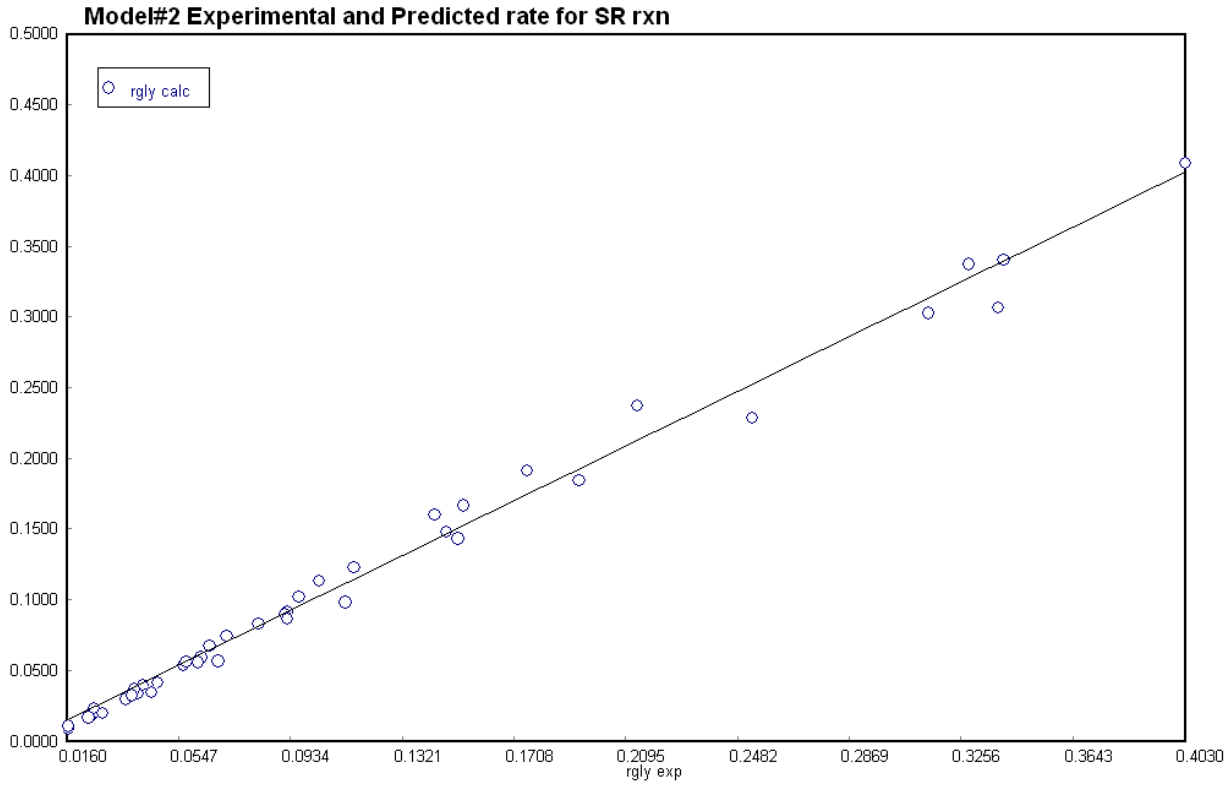

Figure 4.27: Comparison between experimental and predicted reaction rates for L-H type model 2 based on parameters in Table 2.

V. References

Cheng, C. K., S. Y. Foo, and A. A. Adesina, "Steam Reforming of Glycerol over Ni/Al_2O_3 Catalyst," Catalysis Today, 2011, 178, 25-33.

Creaser, D., M. Nilsson, L. J. Pettersson and J. Dawody, "Kinetic Modeling of Autothermal Reforming of Dimethyl Ether," Ind. Eng. Chem. Res., 2010, 49, 9712-9719.

Mears, D. E., "Tests for Transport Limitations in Experimental Catalytic Reactors," Industrial Eng. Chem. Process Development," 1971, 10, 541-547

Yang, K. H., and O. A. Hougen, "Determination of mechanism of catalyzed gaseous reactions," Chemical Engineering Progress, 1950, pgs. 146-157.

Yujia, L., R. Farrauto, and A. Lawal, "Autothermal Reforming of Glycerol in a Dual Layer Monolith Catalyst," Chemical Engineering Science, 2013, 89, 31-39.

Task 5: Catalyst Chemistry, Deactivation & Regeneration Strategy

I. Summary

The objective of this task was to identify the main causes of catalyst deactivation during the ATR of PO, develop and implement a regeneration strategy, and evaluate the effectiveness of the regeneration strategy. During the catalyst life study, we focused not only on the effect of time-on-stream on the activity of the catalyst but also on the reproducibility of the performance data, in terms of coke formation as well as the product gas composition. For this purpose, the deactivation of the catalyst was studied and an explanation of the deactivation mechanisms was proposed based on catalyst characterization before and after reaction, as well as visual observation. Characterization techniques implemented included XRD, SEM, and TEM. Based on the understanding of the deactivation mechanisms, a catalyst regeneration process was implemented to explore the restoration of the activity of the catalyst, and its effectiveness was also studied. By implementing a cyclic operation comprising auto-thermal reforming and catalyst regeneration, a practically feasible production process was demonstrated. However, the loss of catalyst activity was found to be caused by more than one factor, hence different modes of deactivation seemed to be involved. Depending on the nature of the catalyst deactivation, the loss of activity could be divided into two main categories, reversible loss and irreversible loss. The regeneration process implemented was able to restore the activity loss caused by physical covering of the active sites, however, it was found to be ineffective for irreversible loss caused by temperature or chemical reactions. Other strategies were proposed, some of which were evaluated and found to mitigate thermal deactivation. Future effort in the ATR of PO should be devoted to the prevention of chemisorption of high molecular weight oxygenates on catalytic sites, which causes irreversible loss of activity with the objective of prolonging the catalyst life thus enhancing the commercial viability of the process.

II. Catalyst Deactivation Modes

Catalyst deactivation takes different forms, and could affect either the active component or the support on which it's deposited or both. Catalyst deactivation can occur by a number of different mechanisms, some reversible and others irreversible depending on the nature of the deactivation, physical or chemical. Generally the deactivation modes can be divided into four main classes, namely poisoning, coking, sintering of support and active metal, and phase transformation. Temperature is a very important causal factor in catalyst deactivation Thermal deactivation occurs due to prolonged exposure to very high temperature, usually in excess of $950^{o}C$. In both the active metal and the support it can manifest as sintering, causing a reduction in the surface area of the active metal, and in the case of the support, a reduction in total pore volume. The effect in either of the two cases is a vitiation of the activity of the catalyst. High temperature can also cause a change in the crystal structure of the catalyst support. For example, in the presence of impurities and temperatures greater than $900^{o}C$, γ–alumina can be transformed to α–alumina which has about 1-2% surface area of the γ–alumina.

Catalysts can also suffer deactivation due to chemical interaction between the active metal and the support forming a product that is catalytically inactive for the particular reaction. Poisoning is another form of catalyst deactivation and it could be selective such as the chemisorption of SO_2 onto Pd or non-selective, the commonest form being coke deposition. In addition to all these forms of catalyst deactivation, for wash-coated catalysts such as the dual layer monolith which we used in this project, a loss in wash-coat can also occur resulting in a loss of active material as well as catalyst support. The characterization technique for identifying causes of deactivation

in a monolith catalyst, when done properly, is pain-staking and time consuming since it involves scraping the catalyst layers from the monolith channels one by one.

Coke formation is the easiest cause of catalyst deactivation to detect since it can be visually observed. Our initial study on catalyst deactivation therefore focused on coking. Unlike coke formation in hydrocarbon processing which involves several consecutive steps, among which the formation of unsaturated molecules and cyclo-alkene is the rate determining step, for pyrolysis oil, coke formation is facilitated by unsaturated oxygenated molecules already present in the PO, and thus proceeds much faster.

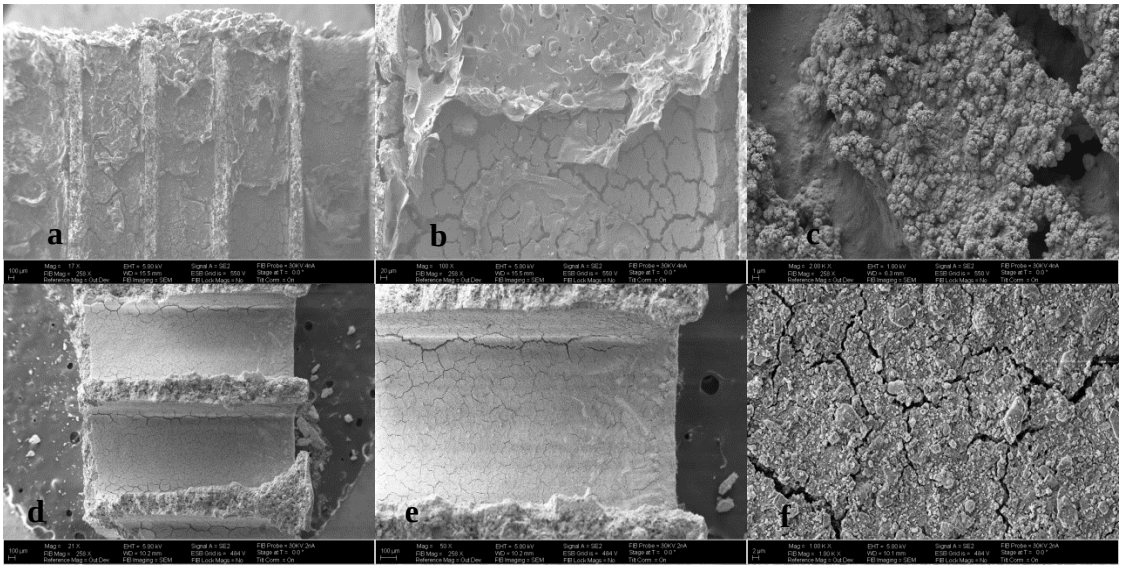

Figure 5.1: SEM images of the aged catalyst (a) to (c) and fresh catalyst (d) to (e)

Coking, which was visually observed was imaged using scanning electron microscopy (SEM) (Zeiss Auriga FIB-SEM, Zeiss NTS, Peabody, MA). Figure 5.1 shows the SEM images of both the aged (20 hours on-stream time) and fresh catalyst. Figures 5.1a and 5.1d have the same amplification while Figures 5.1c and 5.1f also have the same amplification. Figures 5.1b and 5.1e are both showing one single axially-cut channel therefore they have similar amplification though not exactly the same. The difference between the aged catalyst and fresh catalyst is significant at the entrance of the monolith channels (top portion of Fig. 5.1a). Comparing the images of the aged and fresh catalysts, coke deposition can be easily observed.

Figure 5.1a shows the cross section of the monolith channels axially cut exposing the inner surfaces with which the reactants first make contact. The top part of the catalyst which is significantly covered by coke deposit is the entrance to the monolith. Along the channel, coke deposition decreases from top to bottom. The coke deposition at the entrance appears to be a thick blanket covering almost the entire surface, including both the Al_2O_3 support and the active catalytic metal sites, leaving no active sites for absorption of the chemical species for catalytic reaction either CPO or SR. Coke formation inside the channels shows a pattern of inverted triangle. As you go down the channel, the coke becomes thinner and thinner and eventually it becomes so thin that it is not able to fully prevent the contact between the active sites and the reactants. It's obvious that complete blockage of the entrance to the channels will occur if the auto-thermal reforming reaction is allowed to continue for a long time without appropriate removal of the coke deposited on the catalyst surface. Removal of the coke deposit is

necessary for restoring catalytic activity and maintaining continuous operation. By closely monitoring the time-on-stream effect on the catalyst performance, we devised a cyclic operation (see Section III.4.3 below) in which the reforming process and the catalyst regeneration process (coke removal) were run alternately. The regeneration process was successful in restoring the loss of activity due to coke formation, but it appeared that in addition to this physical adsorption of coke molecules on the catalyst, there was also another cause of deactivation, the irreversible chemical adsorption of high molecular weight oxygenates which could not be removed by the simple regeneration method of combustion. The result will be discussed further in section III.

Other than catalyst deactivation by poisoning (coking and chemical adsorption of high molecular weight oxygenates), we also suspected thermal deactivation. Therefore, the next step in our investigation of catalyst deactivation focused on thermal deactivation since one of the two reactions comprising ATR is the exothermic catalytic partial oxidation (CPO) which in combination with high feed temperature at the catalyst inlet may lead to temperatures that exceed the limit for thermal deactivation.

Active metal sintering can be evaluated using XRD (X-ray diffraction) or high resolution TEM (Transmission Electron Microscope) techniques by measuring the particle size of the used catalyst and comparing it to that of the fresh catalyst. Chemisorption can also give an indication of the change in pore size or volume. The pore size and pore size distribution of the support can be measured by BET, and XRD. XRD can also be used to detect phase transformation of the catalyst support. To complement these microscopy techniques, monitoring of the axial temperature distribution along the catalyst length can be used to evaluate the progression of thermal deactivation along the catalyst length.

Structural characterization by powder X-ray diffraction (XRD, Rigaku Ultima IV XRD system with Cu Kα radiation at λ = 1.5418 Angstrom) was performed at Stevens on a sample of a used catalyst that had been on-stream for more than 50 hours. The sample was taken from the entrance section of the catalyst since this is the section that is most susceptible to thermal deactivation. Figure 5.2 shows the XRD spectrum of the aged monolithic catalyst. The X-ray diffraction patterns show the presence of the α-alumina structure which indicates a transformation from the original γ crystalline structure to the lower surface area α-structure. The characteristic peaks marked by green lines identify corundum, normally referred to as α-Al_2O_3, and comprises colorless hexagonal crystals with a specific area of about 5 m^2/ gm. However, the crystalline form of the alumina support used in catalyst preparation is γ-Al_2O_3, comprising minute colorless cubic crystals with a specific area of about 100 m^2/ gm. The sharp decrease of the support surface area will definitely cause a significant loss in catalyst activity. With the growth of the alumina particle size, it is expected that some of the active metal sites will be enclosed and thus become inaccessible to the reactants.

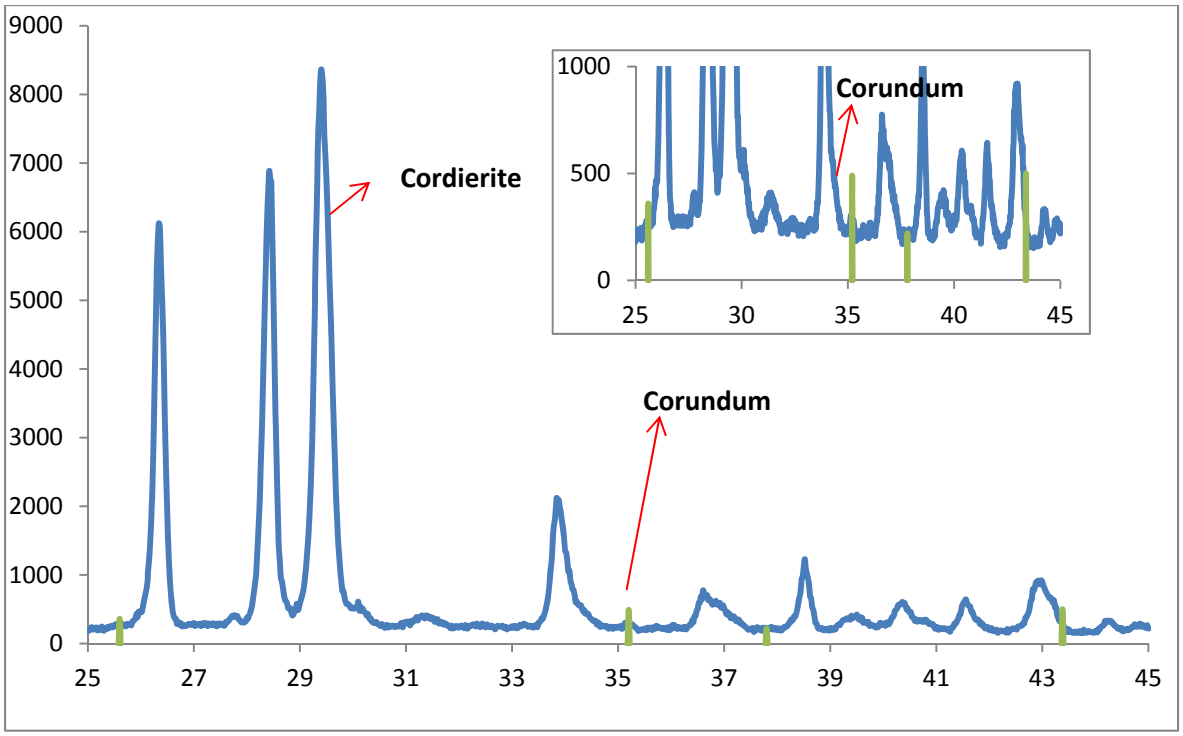

Figure 5.2: XRD spectrum of the used monolithic catalyst.

The XRD measurements performed at Stevens were confirmed by BASF which reported diffraction patterns that showed predominantly α-alumina in the aged catalysts. The other morphologies of alumina, namely $\delta-$and θ-alumina were also present but not the original γ-alumina. Of all the morphologies, the α-alumina has the lowest surface area, and the morphology change, occurs at temperatures higher than 1000°C for this dual layer monolith catalyst. While the catalytic activity loss caused by coke deposition is reversible, the loss caused by phase transformation of the support is irreversible. The only effective way to prevent the catalyst from undergoing this type of activity loss is to prevent phase transformation of the support in the first place.

For further confirmation of the occurrence of excessively high temperature in the catalyst, temperature was monitored along the center of the catalyst and it was established that the catalyst experienced temperatures in excess of 1000°C due to a combination of the high feed temperature and the highly exothermic catalytic partial oxidation (CPO). The CPO takes place close to the entrance of the monolith which is where the highest temperature was expected, and observed. Temperature was measured by a thermocouple threaded through a small hole at the center of the monolith.

Both metal and catalyst support sintering could also have taken place due to this excessively high temperature (>1000°C). The size of the active metal could not be accurately determined from the XRD patterns because of the low concentration of this component in the catalyst. Since TEM would be expected to be more suitable for such measurements, TEM analysis (CM20, FEI Oregon) was undertaken, and a large number of images were taken for both fresh and aged catalysts. However, at the end, the data were inconclusive hence not included in this report. As an alternative approach, we used the SEM in conjunction with Energy Dispersive Spectroscopy (SEM-EDS) on both fresh and used catalysts. However, the results were also inconclusive. At

every selected location of the catalyst sample, whether fresh or used, in addition to the active metal components, additives which act as thermal stabilizers also appeared on the micrographs (Figure 5.3), making it difficult to estimate particle size. The stabilizers are in general much bigger than the active metal components. In order to make any valid comparisons of particle size between used and fresh catalysts, ideally only known active components should be present which will render particle size determination easy. This option will of course lead to a practically unrealistic situation because the removal of the stabilizer will further vitiate the thermal resistance of the catalyst, thus bringing about rapid thermal deactivation of the catalyst.

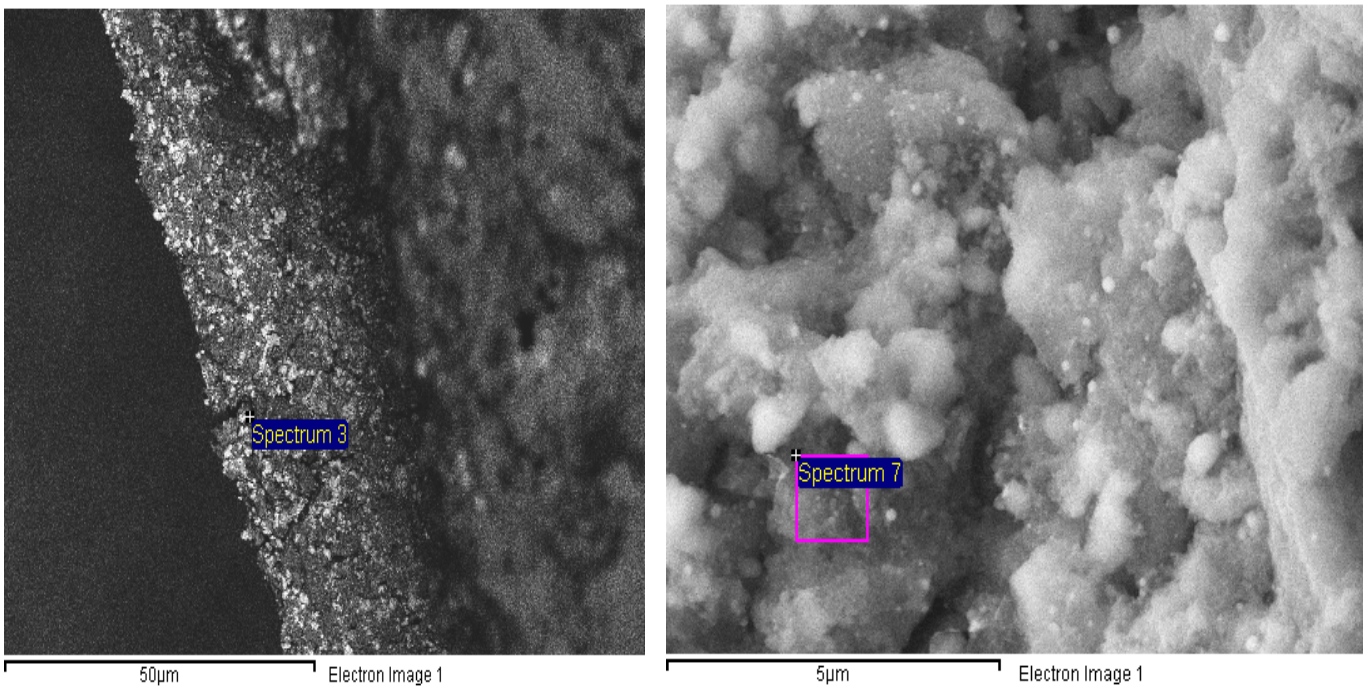

Figure 5.3: SEM-EDS Micrographs of (a) Fresh (b) Used catalysts

In industrial practice, catalyst/catalyst support sintering has been identified as an important contributory factor to catalyst deactivation therefore we intend to explore other techniques to evaluate it in a future study.

In concluding this section, we identified the two main factors that were responsible for irreversible loss of catalyst activity. The first factor was the chemical adsorption of high molecular weight oxygenates which could not be removed by the simple regeneration method of combustion. The second mode of irreversible deactivation was phase transformation of catalyst support and possibly sintering due to thermal effects. In order to preserve the catalyst activity, we have to remove the factors responsible for the deactivation. In this project (see next section), we proposed some modifications to the process that could alleviate the conditions that lead to permanent catalyst deactivation. The effectiveness of these modifications was evaluated.

III. Catalyst Deactivation Studies

III.1. Data Reproducibility

Experimental data reproducibility was given serious consideration at each step of our study of ATR of PO, more so for the long-term catalyst life study. In order to reproduce a selected reactor performance result, in addition to the main reaction processing conditions, other

operational conditions should be closely monitored and maintained. For example, the HPLC pump for pyrolysis oil had a built-in filter which had to be cleaned regularly otherwise the actual flow rate of the pyrolysis oil might deviate appreciably from the set value, thus giving rise to inconsistency in the data from one run to another. The operational conditions that could cause data inconsistency also included the performance of the steam generator, and the pressure drop across the nozzle. All these operational conditions are believed to affect either the degree of atomization of the pyrolysis oil or the heat transfer from the furnace to the reactor or both. Any change in one of the operational conditions could lead to inconsistency in the experimental data.

III.2. Experimental

Before performing the ATR of PO, methanol was used to evaluate the operational state of the system as well as the catalyst activity. After the GC reading was taken for methanol, the 3-way valve was switched to PO and the ATR of PO commenced. Depending on the objective of each run, the experimental run-time might change. Some runs were made for 2 hours while the duration of others was 1 hour. After the reaction, for those runs aimed at studying the effect of a certain parameter on carbon formation, the reactor was taken down, the carbon deposit was removed and its weight recorded. For certain experimental runs, the amount of carbon deposited was not required, and an in-situ combustion process was applied to combust the formed coke inside the reactor without taking the system apart.

Due to coke formation, the ATR of PO could not be operated continuously using one reactor. A de-coking procedure was therefore required to keep the reactor tubing from blockage and also to keep the active sites of the catalyst from being blocked by coke deposition, causing the catalyst to lose activity. Two different de-coking procedures were evaluated. In the first approach, which we practiced for quite a long time, the reactor was disconnected from the setup, and as much of the coke as possible was removed. Then the reactor with the catalyst still inside it, was placed back in the furnace and air was used to combust the remaining carbon that was left adhering to the tube or deposited on the catalyst with the reactor heated at an elevated temperature for a certain period of time. In the other approach, the de-coking was done in-situ without bringing down the reactor from the setup. After the reaction, the air was fed into the reactor through the steam feed port and the combustion of the coke performed at elevated temperature for a certain period of time. However, for the second approach, the ash that accumulated upstream still needed to be cleaned out before running the next experiment. For an industrial operation, the process design would incorporate an easy to implement back-flush step which would resolve this problem. But in the laboratory case, the quartz reactor still needed to be disconnected from the setup and the ash cleaned out offline. The successful demonstration of the second approach provided confirmation of the practical realization of the continuous operation of the ATR of PO. Our catalyst life study began with a short-term evaluation of catalyst activity, followed by long-term catalyst life evaluation. In what follows, we will present for comparison and discussion the results associated with the effect of the life of the catalyst on reactor performance, both short- and long-terms.

III.3. Start-up and Shut-down Procedure for Catalyst Regeneration

Based on the information from BASF, catalyst reduction was only required the first time a fresh catalyst was used. The fresh catalyst was reduced at 500°C in flowing 10% H_2/N_2 at 250 sccm for 45 minutes. For normal startup, the furnace was heated to the desired reaction temperature before the methanol pump was switched on. Fifteen minutes after the set temperature was reached, the first GC reading was taken to evaluate the activity of the catalyst by comparing it to

a baseline obtained from fresh catalyst for methanol. The pyrolysis oil pump was then switched on. After the set run-time of the reaction was attained, the furnace, pyrolysis oil pump, air and steam pump were all shut off instantly to ensure no further reactions were occurring, and thus the reactor system was preserved for analysis. For example, if the air flow were to be continued during furnace cooling, the deposited coke would continue to be combusted, thus providing misleading information on the actual amount of coke formed during the reaction. The regeneration process for the monolithic catalyst was performed with the aim of removing the coke deposited on the catalyst and restoring its activity by flowing air through the monolith at a high temperature for 2 hours.

III.4. Short-term Catalyst Life Evaluation

III.4.1. Effect of the age of the catalyst on ATR of PO

In Fig. 5.4, the results of the runs with aged (20 hours on-stream time) and fresh catalysts are compared, and the effect of the age of the catalyst on the performance of ATR of pyrolysis oil can be clearly seen especially for the results at 60 minutes. With the fresh catalyst, H_2 yield is more than double that at 60 minutes. The CO yield as well as the gaseous carbon yield is also greatly increased indicating that the decreased performance and the lack of reproducibility of experimental data could be related to the deactivation of the catalyst, possibly caused by coke deposition. The percentage of the coke formation for the fresh catalyst is also much smaller than that for aged catalyst. Although the coke normally formed above and away from the catalyst, the results seemed to suggest a relationship between the catalyst activity and the amount of coke deposit. It could be that with the deactivation of the catalyst close to the entrance of the monolith, fine deposit of coke formed at the entrance and hence hindered the flow of reactants into the monolith channels. The decrease of the opening of the monolith channels at the entrance created a back-pressure that could possibly increase the recirculation of the pyrolysis oil mist, thus increasing the amount of coke formed upstream. Moreover, the loss of activity of the CPO catalyst close to the entrance of the monolith also decreased the reaction temperature and increased coke formation.

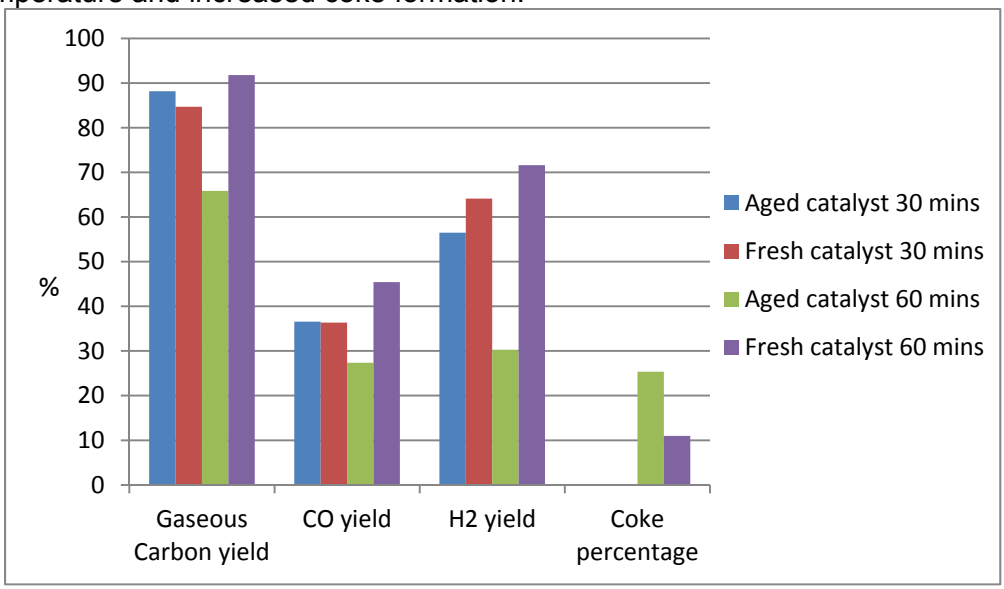

Figure 5.4: Effect of the age of the catalyst on the performance of ATR of pyrolysis oil at Steam/C=1.1, O_2/C=0.37 and GHSV=8102 (1/h)

III.4.2. Effect of duration of experimental run on catalyst activity

As can be observed from Fig. 5.5, after one hour of running the experiment, except for CO_2 yield, all yields show an abrupt decrease, which thereafter remain essentially constant. This was attributed to formation of coke which partially blocked the opening of the channels or covered part of the catalytic sites dispersed on the inner surface of the channels. H_2 and CO yields in the first hour were relatively high reflecting good catalyst activity and selectivity. However, after one hour, due to coke formation, the activity and selectivity were reduced. The reason why the yields after one hour did not continue to decrease may be due to a steady state being attained between the rate of coke production and the rate of coke removal by gasifying agents (e.g. H_2, H_2O and O_2). The yields after one hour even showed a slight trend towards an increase. The explanation could be that the coke that accumulated in the reactor above the catalyst underwent thermal cracking or partial combustion in the presence of O_2, thus increasing the yields and decreasing overall coke formation. Nevertheless, due to the accumulation of coke, the auto-thermal reforming of pyrolysis oil could not be run continuously without removing the coke formed. The long duration experimental run indicated that it was necessary to add a catalyst regeneration step in a cyclic operation to make the ATR of pyrolysis oil practically feasible.

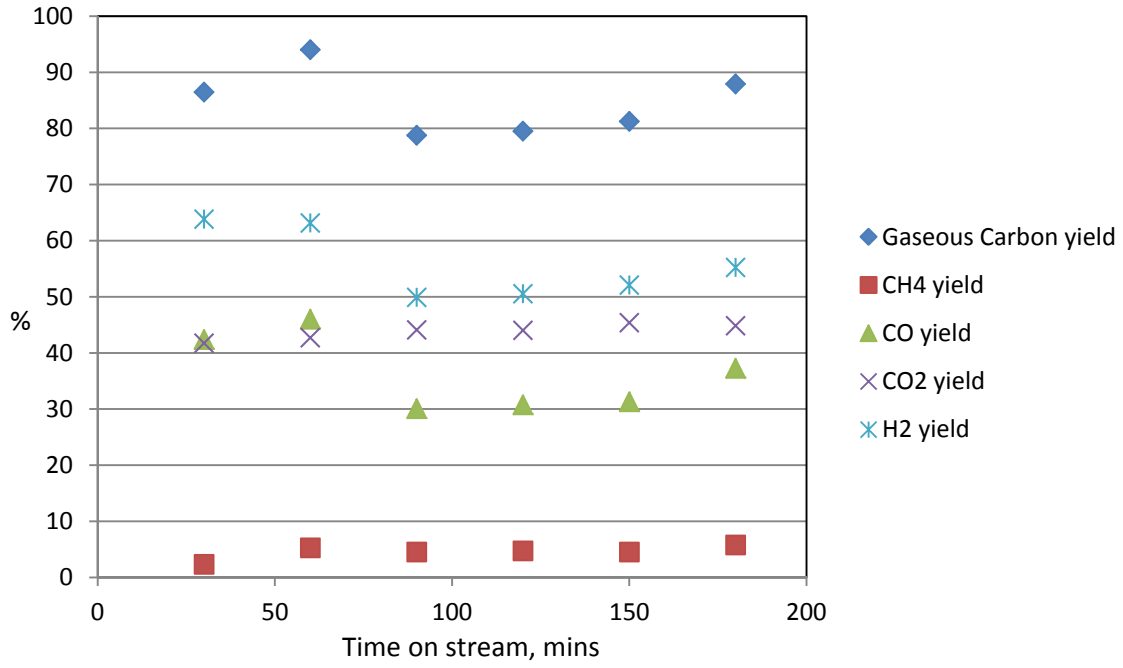

Figure 5.5: Performance of the ATR of PO versus duration of run

III.4.3. Evaluation of a Reaction Cycle Comprising ATR and Regeneration

It was always visually confirmed that coking played an important role in catalyst deactivation for our auto-thermal reforming of pyrolysis oil. Typically, a small amount of coke was observed on the catalyst surface close to the entrance after about one hour of running the ATR reaction. In order to restore the catalyst activity, the reaction had to be interrupted for the coke to be

removed and the ATR reaction resumed. A regeneration process, which involved the combustion of the coke under continuous air flow, proved to be substantially effective in removing the coke deposition and restoring the catalyst activity.

As shown in Fig. 5.6, unlike in the long duration run (section III.4.2. above) where the catalyst activity decreased abruptly after 60 minutes, the performance of the catalyst between 60 minutes and 90 minutes did not show much of a difference. It appeared that the regeneration process was able to restore some of the catalyst activity by combusting off the coke film covering the catalytically active sites. However, the subsequent decrease of yields at 120 minutes might indicate that the regeneration step would require some modification for it to be fully effective (see section III.6 below). The flow rate of the air used for combustion was not controlled. Thin layers of coke (possibly graphitic carbon) might still remain, and while they might not have totally blocked the active sites, they could still grow into thick layers with time and block some active sites, thus vitiating the catalyst performance.

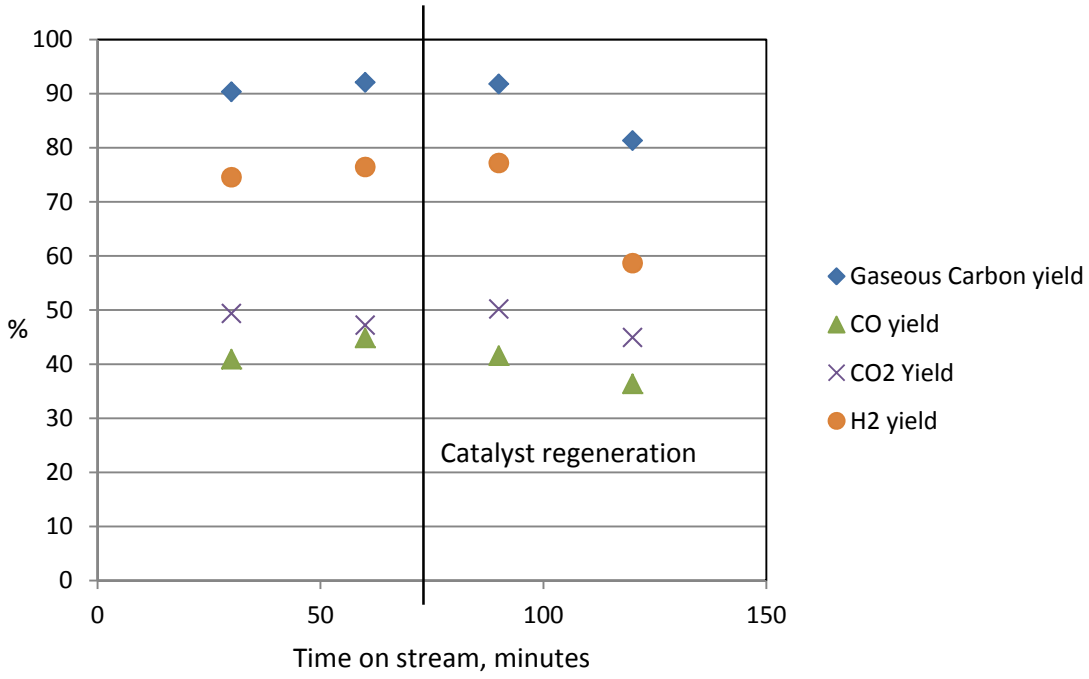

Figure 5.6: Performance of the catalyst in a cycle comprising ATR and catalyst regeneration. The line in the center indicates the catalyst regeneration.

III.5. Long-term Catalyst Life Evaluation

The long-term catalyst life evaluation did not present any major technical challenges. However due to the fragile nature of monoliths, in combination with repeated handling, during the evaluation of the catalyst life, the catalyst broke and its length was reduced from 2.75" to 2". At that point, the catalyst had been on-stream for 28 hours. A decision was made to continue the catalyst evaluation with the remaining 2" catalyst, since we could always use a 2" fresh catalyst to compare with the 2" catalyst and evaluate the run-time effect on the performance. Our main objective was to find out at which point a sharp decline in catalyst efficiency occurred and the deactivation became irreversible. Therefore, the long-term study of the catalyst life occurred in

two phases. In phase 1, the runs were carried out with the 2.75" catalyst while in phase 2 the runs were conducted with the 2" catalyst recovered from the original broken 2.75" catalyst. The findings are reported here.

III.5.2. Results and Discussion

The experiments were all carried out using the same reaction conditions, which are: Steam/C=1.3, O_2/C=0.37, and reaction temperature of 750 ºC. For the catalyst life evaluation, we monitored the change in the values of the yields of selected gases with respect to the catalyst on-stream time, independent of the de-coking method (refer to section III.2. above) applied. Both coke combustion processes proved satisfactory for removing coke from both the reactor tube and the catalyst surface. As shown in Fig. 5.7 and Fig. 5.8, the methanol reforming results for the two de-coking procedures are remarkably quite similar. The slight difference is in all cases within the relative error of the GC equipment (<5%).

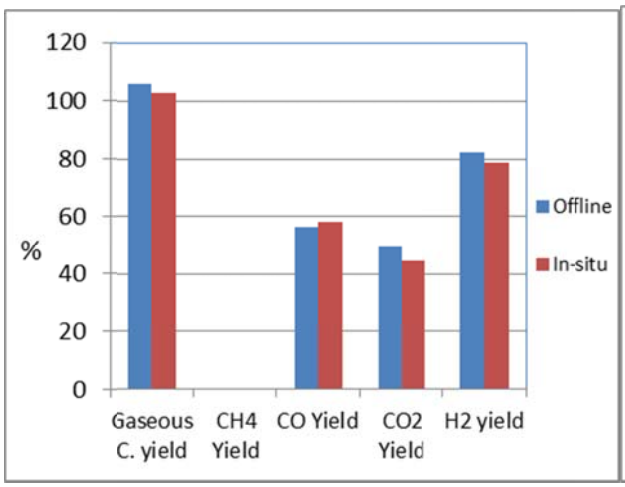

Figure 5.7: Product gas yield of ATR of Methanol for two different de-coking methods

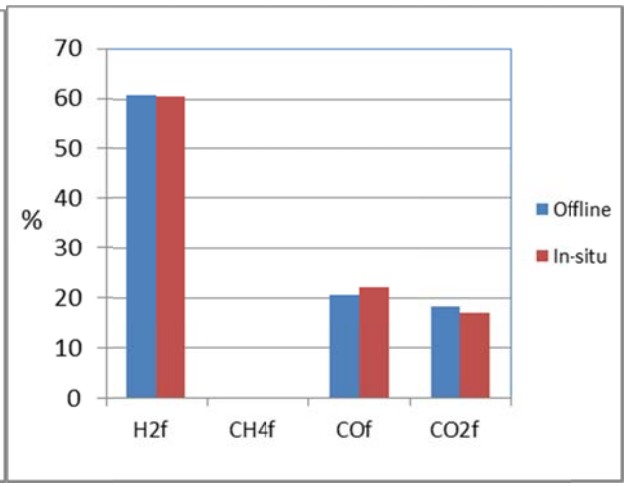

Figure 5.8: Product gas composition of ATR of Methanol for two different de-coking methods

As mentioned, the catalyst evaluation study was divided into two phases. The first 28 hours of operation were carried out with 2.75" catalyst while the last 27 hours were carried out with the 2" catalyst (recovered from the 2.75" catalyst that broke) for a total on-stream time of 55 hours. Figure 5.9 shows the performance of the catalyst versus time on-stream in the first evaluation stage. As can be observed, the CH_4 yield is increasing as the catalyst on-stream time increases and the H_2 yield shows a decrease after 5 hours of run-time, probably indicating a fast deactivation of steam reforming component of the dual layer monolith catalyst. The combustion and catalyst regeneration process (in-situ or offline at elevated temperature) was applied after each experimental run with the purpose of recovering the activity lost due to coke deposition. After on-stream time of 28 hours, the H_2 yield decreased from around 80% to around 50%. However, the CO yield and gaseous carbon yield only showed a slight decrease with run-time, fluctuating around 40% and 85% respectively. The obvious decrease in the H_2 yield and the relatively stable CO yield with increase in catalyst on-stream time indicates that for the dual layer monolith catalyst, the steam reforming active sites appear to experience far more thermal deactivation than the CPO component, either during the reaction as a result of the high reaction temperature or during the regeneration step, a high temperature combustion process.

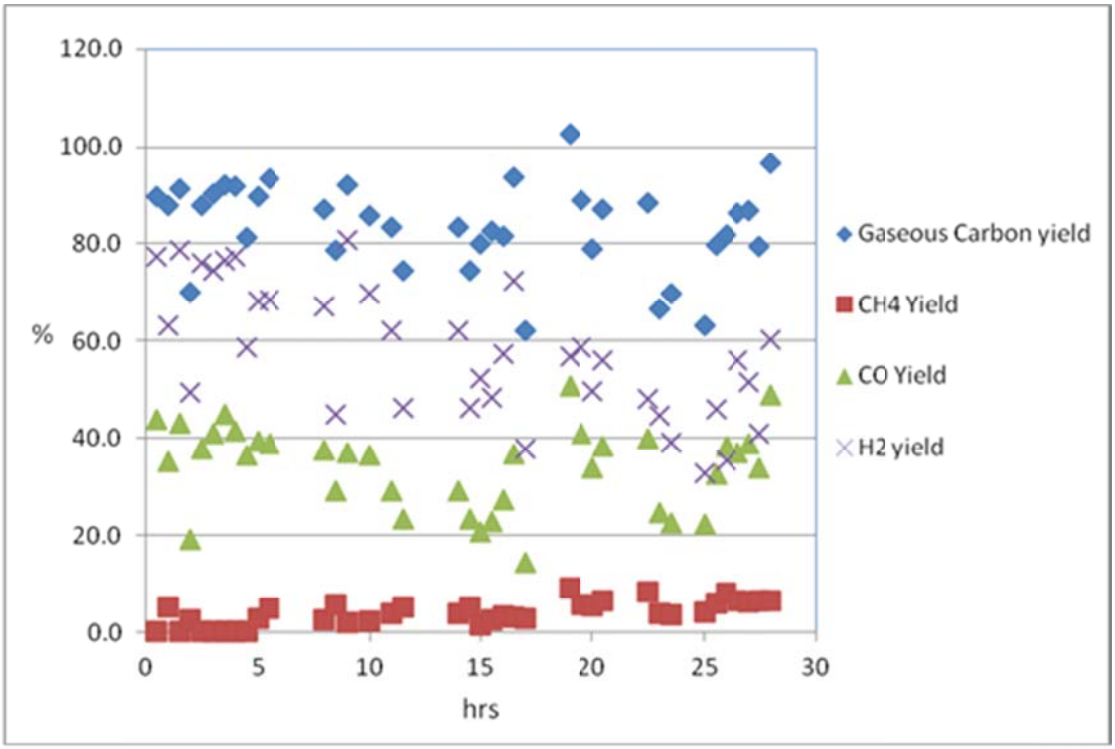

Figure 5.9: Performance of catalyst during first stage of evaluation. Typical conditions: $T_{reaction}$=750 ^{o}C, Steam/C=1.3, O_2/C=0.37, Catalyst

In the second stage, of catalyst evaluation, after the catalyst broke, a decision was made to continue the test runs with the remaining 2" catalyst since the focus of the test was to find out at what point a dramatic change in the experimental data would occur, and we can always compare the data with those from a fresh 2" catalyst if necessary. The results are shown in Fig. 5.10. Except for CH_4 yield, all other yields including gaseous carbon, CO and H_2 decreased greatly compared to 2.75" results. Gaseous carbon yield averaged around 70% compared to 85% for the 2.75" catalyst. The CO yield averaged around 30% dropping from 40%, and H_2 yield decreased to around 25%. The comparison of the results for these two catalysts, i.e., 2.75" and 2" catalyst may not be tenable for evaluating catalyst deactivation since the results reflect a combined effect of both the amount of catalyst as well as deactivation. The comparison between the results of runs made with 2" catalyst will be more valid for determining catalyst deactivation. The GC readings for stage 2 of the deactivation study show more scatter than those of stage 1, and all the yields do not follow any consistent trends with catalyst on-stream time. There is no apparent dependency of catalyst performance on run-time in stage 2 study. Figure 5.11 shows the result of experiments conducted with a fresh 2" catalyst, under process conditions the same as those used for the 2" used catalyst. After comparing the results with Fig.5.10, we can see that for CO yield, the average is about 30% for both fresh and used catalysts. Gaseous carbon yields are also similar, around 70-75% for both catalysts. However, the H_2 yields are significantly different with the H_2 yield of fresh 2" catalyst averaging around 60% while for the used 2" catalyst, the value was around 20%. The explanation of the sharp decrease of H_2 yield is similar to that of the 1st stage. For the dual layer monolithic catalyst, steam reforming component of the catalyst appears to be deactivated and the de-coking combustion process was not effective in regenerating the catalyst. However, the catalytic partial oxidization catalyst appears better able to withstand the high temperature processing conditions and shows more or less the same level of catalytic activity after a combination of 55 hours of auto-thermal reforming and around 110 hours of combustion in the presence of excess air for catalyst de-coking.

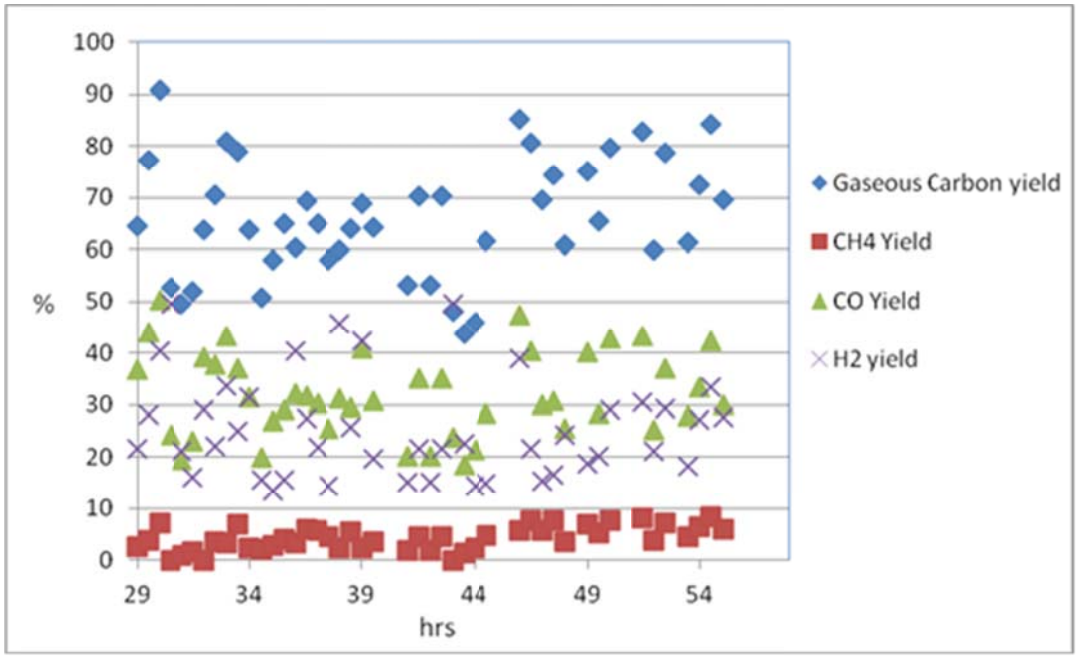

Figure 5.10: Performance of catalyst during second stage of evaluation. Typical condition: $T_{reaction}$=750 ^{o}C, Steam/C=1.3, O_2/C=0.37, Catalyst length 2”

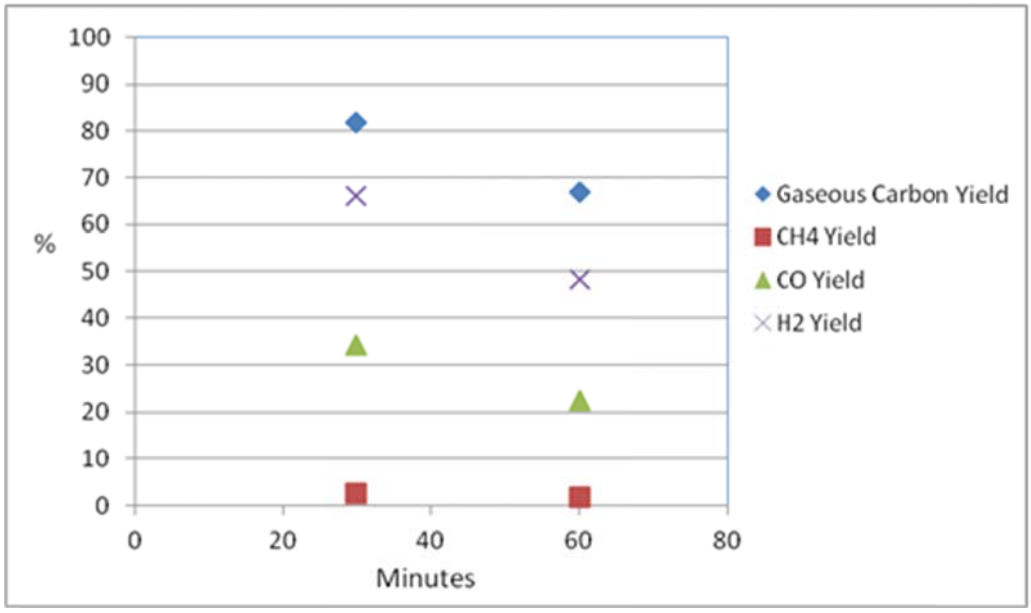

Figure 5.11: Performance of fresh 2” catalyst. Typical condition: $T_{reaction}$=750 ^{o}C, Steam/C=1.3, O_2/C=0.37

III.6. Catalyst Preservation Strategy

In order to preserve the catalyst activity, the factors responsible for the deactivation, especially those pertaining to irreversible deactivation, must be removed. We proposed and implemented the following strategy in our bench-scale system: (1) re-designed the ATR reactor configuration such that the catalyst was prevented from exposure to temperatures that led to thermal deactivation, and (2) altered the temperature profile within the reactor configuration. These modifications to the process should mitigate the conditions that lead to irreversible thermal deactivation.

With the new reactor configuration, the ATR experiments were conducted over a period of weeks. The center cell of the monolith catalyst was drilled-out to a size big enough for insertion of a 1/16" thermocouple. During each experimental run, the thermocouple was positioned along the axis of the drilled-out cell to continuously monitor the temperature. This location was changed with each experiment by moving it along the axis of the hole, beginning at the entrance of the monolith and ending at the exit. For all the experimental runs, we were able to confirm that the temperature along the center of the reactor did not approach the temperature at which the phase transformation from γ-Al2O3 to α-Al2O3 is initiated. It should also be stated that the performance of the ATR reactor in terms of product gas composition remained unchanged with the re-design of the reactor system. Also, the amount of carbon deposit was not adversely affected. Temperature measurements along the center of the catalyst indicated that the temperature experienced by the monolith was moderated by about 200^{o}C with the implementation of the first modification alone.

Although we successfully implemented a strategy that prevented thermal deactivation, we continued to observe significant catalyst deactivation. We attributed this deactivation to two possible sources: (1) presence of difficult-to-crack high molecular weight oxygenates in a complex mixture such as pyrolysis oil which are chemisorbed on the catalyst support as well as the active metal, leading to the loss of catalyst activity and (2) irreversible formation of graphitic carbon on catalyst. These deactivation modes had been observed with mixtures of gasoline and ethanol (Simson et al. (2011)). In order to confirm the second source of deactivation, fresh and aged catalyst samples were analyzed using Raman spectroscopy, and presence of graphitic carbon was confirmed on the aged sample. Since both sources of catalyst deactivation are irreversible, they have to be prevented. We proposed that the catalyst regeneration strategy be modified by reducing the time between regeneration and controlling the regeneration temperature by using O_2 lean air, but increasing the duration of regeneration. The frequent cyclic regeneration will prevent prolonged exposure of catalyst to excessively high temperature, and formation of graphitic carbon or high-molecular weight oxygenates that may chemisorb irreversibly on catalyst active sites. This approach had been used successfully by BASF with the steam reforming of mixtures of gasoline and ethanol (Simson et al. (2011)). We began the implementation of this regeneration strategy towards the project end-date but it could not be completed because of lack of funds. Our request for additional funding to complete the evaluation of this new strategy was declined. Future work should focus on the implementation and evaluation of this strategy for extending the catalyst life for the BASF dual layer monolith ATR of pyrolysis oil.

III.7. Future Work on Catalyst Life Preservation

The objectives of future work on catalyst life preservation should include (1) further confirmation of the postulated catalyst deactivation modes (2) evaluation of the effectiveness of the proposed catalyst regeneration strategy, and more importantly (3) extension of the catalyst total on-stream time to at least 500 hours. Catalyst should be subjected to exhaustive characterization after extended duration use in the dual layer monolith ATR reactor to observe changes in catalyst

properties. The sample preparation method that we adopted at Stevens which involved simply grinding the monolith was inadequate. Because of the small amount of wash-coat, ~10 μm thickness the sample was mainly cordierite, the monolith material, the intensity of which swamped that of the catalytic support, the alumina. The BASF procedure which involves the tedious and pain-staking process of scraping the wash-coat off the walls of the monolith should be implemented. Scanning electron microscopy (SEM), transmission electron microscopy (TEM), and X-ray diffraction should be used to follow changes in pore size, morphology, active metal size, and film thickness. TPO experiments in conjunction with TG-DTA should be used for quantification of deposits of carbon and high molecular weight oxygenates. For confirmation of graphitic carbon, Raman spectroscopy could be deployed. The successful demonstration of an extended (> 500 on-stream hours) catalyst life would affirm the commercial viability of the process.

IV. Reference

Simson, A., R. Farrauto, and M. Castaldi,“Steam Reformig of Ethanol/Gasoline Mixtures: Deactivation, Regeneration and Stable Performance,“ Applied Catalysis B: Environmental, 2011, 106, 295 – 303.

TASK 6: Process Analysis and Design of ATR System for Pyrolysis Oil

The research effort under Task 6 has been reported in two publications, the contents of which are presented in what follows.

I. Summary

An energy balance in broad outline is presented for the production of a high quality liquid transportation fuel from, primarily, residual crop biomass. The particular process considered is comprised of: (1) harvesting surplus biomass such as crop residue, (2) locally pyrolyzing the biomass into pyrolysis oil (PO), char, and non-condensable gas (NCG), (3) transporting the PO to a remote central processing facility, (4) converting the PO at this facility by autothermal reforming (ATR) into synthesis gas (CO and H2), followed by, at the same facility, (5) Fischer Tropsch (FT) synthesis of the syngas into diesel fuel. The process considered is outlined in Figure 6.1 below.

In carrying out our calculations we have made a number of assumptions about the values of the process parameters. These parameters can of course be modified as better input data becomes available. The overall material and energy balance has been incorporated into an Excel© spreadsheet, see Table 6.1. The scope and our approach to the energy budget using a widely available spreadsheet hopefully provide greater transparency as well as ease of scenario manipulation than has generally been found in the literature. The estimated energy efficiencies computed with the spreadsheet are comparable to those obtained with Aspen©. The spreadsheet of Table 6.1 is offered as a tool for further analysis of the energy budget of this and related processes. The Excel spreadsheet can be used as a nimble scouting tool to indicate promising avenues of study in advance of using more comprehensive analysis such as afforded by Aspen.

The process considered, in which a portion of the char and non-condensable gas are used to supply heat to the drying and pyrolysis step and under the assumptions made, was found to have energy efficiency to liquid fuel on the order of 40%. That is, 40% of the initial energy in the biomass will be found in the final liquid fuel after subtracting out external energy supplied for complete processing including transportation as well as material losses. This is our definition of the term “energy efficiency” (see Appendix A, II.7). Our energy efficiency calculation does not include energy required to make and assemble the metal and non-metal parts of equipment such as trucks, process equipment, etc, to perform the process. It is believed that this would be a small contributor to the energy balance. If the energy of the remaining char and NCG is added to that in the product diesel oil the total recovered energy is estimated to be about 50% of the initial energy content of the biomass. If char and NCG are not used as a heat source in the process, the energy efficiency of the produced diesel drops from 40% to 15%. It must be realized that the distribution of energy content among the fast pyrolysis products PO, char, and NCG is approximately 69%, 27% and 4%, respectively (see Table 6.7). Therefore, using char and NCG to provide fuel for the drying and pyrolysis steps is very critical in maintaining high energy efficiency of the product fuel.

The weight of diesel fuel produced is estimated to be about 13% of the initial weight of biomass, implying that 1 metric ton of biomass (30% moisture) will produce 1.0 barrels of diesel oil. Pyrolysis of biomass to PO, char and NCG is estimated to have an intrinsic energy efficiency of about 90%. For the model considered, trucking biomass to a central facility without first converting it to PO is estimated to reduce energy efficiency by ~ 1%.

An economic analysis of producing Fischer-Tropsch (FT) liquid fuel such as diesel from crop residue is presented. The process is thermochemical based involving fast pyrolysis and autothermal reforming (ATR) followed by FT synthesis. A spreadsheet for estimating economics is presented which is simple to use and transparent in its input parameters and its output. Plant sizes of 2 000, 10 000, and 35 000 dry metric tons per day were calculated at 8% return on capital to require sales prices (exclusive of tax) of $3.30, $2.40 and $2.06 per gallon, respectively. US tax would add another ~ $0.50/gallon. A biomass feed stock cost of $61.20/dry metric ton was assumed. Capital cost for the 2 000 dry T/day plant is estimated to be $M231. These estimates, of course, must be regarded as rough, but suggest that even without the benefit of imposed regulations liquid fuel derived from biomass could be competitive at current price levels. Sale of char produced in the pyrolysis step for soil amendment as a by-product at $500/ton, had a significantly favorable impact on the economics, reducing diesel price by $0.35/gal. Like the heavy influence of the cost of crude oil on current fuel price, the cost of biomass is the largest single contributor to the final price of biomass derived fuel, and becomes more so as plant capacity increases. This suggests the need to improve methods of biomass gathering and delivery. For each $10 per dry ton increase in the price of biomass the sales price of the FT fuel is estimated to increase by $0.20 per gallon. It is estimated that pyrolyzer collectives 25 miles square on a side would reduce diesel price by $0.12/gal as compared to those 14 miles on a side.

II. Conversion of Residual Biomass into Liquid Transportation Fuel: An Energy Analysis (published in Energy & Fuels 2011, 25, 2711-2720)

II.1. Introduction

The question is often asked about liquid transportation fuels derived from biomass: “Are you putting more energy into making the fuel than is present in the produced fuel?” An answer in the affirmative would imply that the only redeeming feature of such a process would be the fact that US dollars are not being put into foreign hands since about 60% of our petroleum is imported. This paper seeks to probe this question in broad terms for a specific model system. Although dependent on the energy balance, economics is a separate issue and is not addressed in this paper.

When we use the unmodified term “biomass” we mean that it contains 30% moisture as distinguished from the term “dry biomass” which contains 10% moisture, which is further differentiated from “bone dry biomass” which contains 0% moisture. Also, in Table 6.1 we use “crop residue” interchangeably with “biomass”.

About 85% of the total energy consumed in the US comes from CO_2 emitting fossil fuels (oil, gas and coal). Indeed, fully 40% of total energy is derived from oil and is primarily consumed as transportation fuel. To be specific, the US consumption rate is about 20 million barrels of oil a day[1].

With respect to transportation, a liquid fuel has several important advantages at present over pure electric power. These are: (1) high energy density (the useable energy per unit weight of gasoline or diesel oil is about 60 times greater than that of a Ni-hydride battery and about 30 times greater than the developing Li-ion battery), (2) liquid fuel is easy to store, handle and rapidly recharge a fuel tank, and (3) fits into the existing infrastructure. It is for these reasons and, additionally, a degree of CO_2 neutrality, that liquid biofuels have lured current alternative energy research effort. These estimates account for the efficiency differences in the gas engine (30% efficient) and electric motor (90-95% efficient). However, the 30% value for the gas engine

doesn't account for idling and non-optimum operation. So, more realistic comparison values might be something like 40X and 20X, respectively. For this reason, few are the number of electric airplanes and trucks (!).

An introduction to the potential role of biomass as a renewable fuel has been discussed[2]. Studies of the global energy budget for fast pyrolysis of biomass followed by hydrotreating of the resulting pyrolysis oil are outlined in[3,4]. In these references it was noted that about 1% of the sun's incident energy to produce biomass can be converted to liquid fuel in conventional fast pyrolysis to PO. These studies also explored what they referred to as "augmented" processes in which a portion of the land area is used to produce H_2, e.g., by solar or wind or gasification of biomass. This H_2 can then be incorporated by hydrogenation into the liquid biofuel to measurably enhance the sun-to-liquid fuel yield. The economics of biomass conversion to liquid fuel has been explored in the literature[5-7]. A detailed study by Laser[8,9] et al utilizing Aspen of numerous biomass processing scenarios (some including FT liquids) with regard to economics, efficiency, greenhouse gas emissions and water usage has been reported. A techno-economic study of the conversion of biomass into liquid transportation fuel via fast pyrolysis and hdrotreating-hydrocracking is given in[10]. An energy balance and economic study[11] has been made of biomass gasification followed by FT synthesis into diesel along with co-production of electricity[12,13]. An economic analysis[12] with Aspen software of 16 possible designs involving coal and biomass feeds and was reported.

II.2. The Model

Our model has two major components: (1) gathering biomass, converting it to pyrolysis oil and then transporting the PO to a central processing facility, and (2) at the central processing facility, converting the PO into diesel fuel. A schematic of the process is shown in Figure 6.1.

Figure 6.1: Process for the Conversion of Biomass into Liquid Transportation Fuel

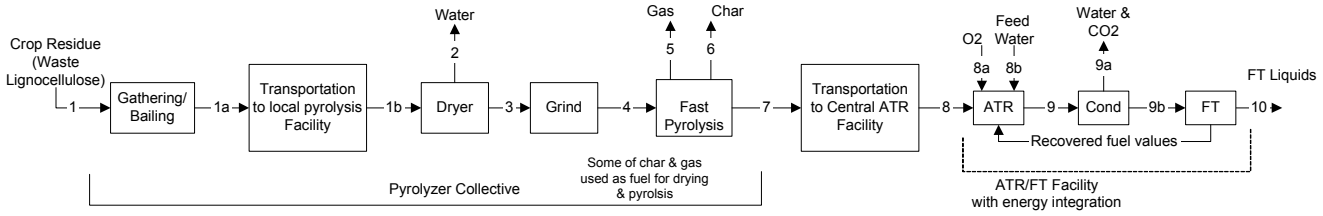

The fuel, resulting ultimately from Fisher Tropsch synthesis, is expected to be of a higher quality compared to common diesel due to its low sulfur, soot, nitrogen, nickel, vanadium, and other contaminants and its high cetane number[11]. By incorporating the components of this model into a readily available Excel spreadsheet we hope that this will make available a tool for scouting scenarios and promising concepts for process optimization.

II.2.1. Biomass Gathering, Conversion to PO, and Transportation

We have focused on crop residue as biomass raw material feed as it is low cost and plentiful. Since crops are harvested at specific and limited times during the year, the resulting crop residue will be baled and stored as inventory on the field to be collected throughout the year to feed the biofuel process in a steady stream. It may be possible to gather crop residue, for example corn stover, in a single pass as the food crop is harvested[14]. Collection is necessarily from a large geographic area, such as from farms in a state the size of Iowa. Therefore, transportation cost both in energy and dollars is a consideration.

Referring to Figure 6.1, crop residue is baled and placed on the field. Bales are then collected and transported by truck to a relatively local pyrolysis facility. At this facility the crop residue is dried if necessary, comminuted, and pyrolyzed by fast pyrolysis which favors liquid rather than gas or char production[15,16]. Combining the steps of drying, grinding and pyrolysis in one location would allow use of the non-condensable gases and char from pyrolysis to provide heat for drying and pyrolysis which greatly improves energy efficiency. The pyrolysis step converts the biomass into an easily transportable oil (pyrolysis oil), char, and NCG. The weight of PO is ~65% of the weight of the original biomass and is substantially increased in bulk density rendering it more efficiently transportable. This permits a savings in transportation cost and fuel consumption to a remote large central processing facility. However, an energy penalty is incurred in the need to re-vaporize the PO.

II.2.2. Converting PO to Diesel Fuel at the Central Processing Facility

Pyrolysis oil is a complex mixture of over 400 oxygenated organic compounds and contains from 15 to 30% water. It has a heating value of less than one-half that of crude oil and can be unstable, difficult to use directly, and is corrosive. It is these reasons that motivate upgrading of PO to diesel. At the central processing facility PO will be transformed by ATR into synthesis gas (H_2 and CO in a 2:1 mole ratio) followed by Fischer Tropsch synthesis into diesel oil.

II.3. Scale of Process

The Biomass R&D Technical Advisory Committee to the US Congress[17] stated a goal of 30% of US petroleum consumption to be replaced by biofuel by the year 2030. To do this, about 1 billion dry (i.e., 10% moisture) tons of biomass needs to be available or about 1.3 billion tons of biomass with 30% moisture. It is estimated[14] that, 250 million dry tons per year is available from corn stover alone. Reference[17] has shown that 1 billion dry tons a year could be made available.

Table 6.1: Material and Energy Balance for Figure 6.1

Energy balance on conversion of waste lignocellulose to transportation fuel use F9 to calculate in manual mode

Feed Rate of Crop Residue. kg/h	500,000	Trucking distance to pyrolyzer, miles	7		Syn gas temp to FT step, C	250	
Moisture content of crop residue, wt%	30	Trucking dist of PO to ATR/FT facility, miles	70		FT synthesis op pressure, psia	225	
Moisture content of DCR, wt%	10	Truck payload limit, **lb**	43,000		FT Synthesis carbon efficiency	90	
% by wt of DCR to PO	65	Truck volume capacity limit, ft^3	4,013		Energy content of DCR(w/ 10%H2O), MJ/kg	17.0	LHV
% by wt of DCR to Char	20	Truck gas mileage, gal/mile	0.125		Energy content of BDCR, MJ/kg	19.1	LHV
% by wt of DCR to non-cond gas	15	PO oil bone dry: C wt %	56.4		Energy content of diesel oil, MJ/kg	42.8	LHV
Energy content of: PO, MJ/kg	18	H wt %	6.5		Energy content of diesel oil, MJ/gal	137.9	LHV
Char, MJ/kg	23	O wt %	37.1		Energy content of CO, MJ/kg	10.9	LHV
Non-cond Gas, MJ/kg	5	water content of PO, wt %	25		Energy content of H2, MJ/kg	120	LHV
Frac of eng rec'd from NCG & char for **drying step**	0.23	Steam reforming ht of rxn (endothermic), MJ/kg-mol o	200		Energy content of PO, MJ/kg	17.5	LHV
Frac of eng rec'd from NCG & char (**pyr step**)	0.58	Exit temp of ATR reactor, C	650		Eng input for pryolysis step, MJ/kg	1.56	
Pyrolysis temperature, C	500	Eng (thermal) req'd for O2 gas production, MJ/kg of O	2.38		Production Rate of Diesel Oil, bbl/day	11,481	
Heat of pyrolysis rxn (+ means endo), MJ/kg	0.3	Temp of syngas exiting heat recovery HEX, C	200		Production, bbl per metric ton of biomass feed	1.0	
Energy required to bail crop residue, MJ/kg	0.054	Total H20 to carbon in PO mole ratio for ATR	0.9		Number of PO trucks per hour to ATR/FT facility	13	
Energy required to grind crop residue, MJ/kg	0.18	Mole ratio of O2 in air to carbon in PO for ATR	0.17		% of original biomass energy in diesel fuel	42.1	
Heat of water evaporation, MJ/kg	2.2	% carbon lost in ATR due to coking	0	<--not used	% of original biomass energy in char	5.1	
Heat of vaporization of PO, MJ/kg	1.21	Carbon efficiency of ATR step, %	**61.1**		% of original biomass energy in NCG	0.8	
Heat released by F-T rxn, MJ/kg-mol CO	170	Mole Ratio of H2 to CO in Syn Gas	**2.0**		Total % original biomass energy recovered=	48.0	
					Heat release rate by FT, MJ/h	832,400	
					Compressor size for FT step, HP	65,448	

	Mol Wt		Crop Res. 1	Gather/ Bale in field 1a	Transport Crop Res. 1b	Water 2	Dry Crop Res. (DCR) 3	Ground DCR 4	Gas (NCG) 5	Char 6	PO 7	Trans-ported PO 8	O2 8a	Fresh water 8b	ATR Syn Gas 9	H2O & CO2 removal 9a	Dry ATR Syn Gas 9b	FT liquids diesel oil 10
BDCR		kg/h	350,000	350,000	350,000		350,000	350,000										
H2O	18	kg/h	150,000	150,000	150,000	111,111	38,889	38,889						81,154	4,350	4,350		
PO as is		kg/h									252,778	252,778						
Char		kg/h								14,100								
NCG gas		kg/h							10,575									
CO	28	kg/h													152,335		152,335	
H2	2	kg/h													22,154		22,154	
O2	32	kg/h											48,473					
CO2	44	kg/h													203,567	203,567		
Diesel oil		kg/h																68,551
Waxes		kg/h																
Total		kg/h	*500,000*	*500,000*	*500,000*	*111,111*	*388,889*	*388,889*	*10,575*	*14,100*	*252,778*	*252,778*	*48,473*	*81,154*	*382,405*	*207,917*	*174,488*	*68,551*
Cum Wt Yield		**%**	**100**	**100**	**100**	-	**77.8**	**77.8**	**2.1**	**2.8**	**50.6**	**50.6**			-			**13.7**
Energy content		MJ/kg	12.7	12.7	12.7		17.0	17.0	5	23	18	18			11		25	42.8
Gross energy available		MJ/h	6,366,667	6,366,667	6,366,667		6,611,111	6,611,111	**52,874**	**324,293**	4,550,000	4,550,000			4,318,872		4,318,872	2,933,966
Net eng available		*MJ/h*	*6,366,667*	*6,339,667*	*6,329,166*		*6,573,610*	*6,503,610*			*4,442,499*	*4,411,286*			*4,064,793*		*4,064,793*	*2,679,887*
Energy eff of step		%	-				50	-	-	-	50				-			-
Ext Eng input for step		MJ/h	0	27,000	10,501		0	70,000			0	31,213	115,365		0		0	0
Cum external eng input		MJ/h	0	27,000	37,501		37,501	107,501	107,501	107,501	107,501	138,714	254,079		254,079		254,079	254,079
Cum energy eff.		**%**	**100**	**99.6**	**99.4**	-	**103.3**	**102.2**	-	-	**69.8**	**69.3**			**63.8**		**63.8**	**42.1**
Bulk density		lb/ft^3	8	8	6.3		10	10			68	68						56.2
Heat Capacity		**kJ/kg/K**						1.00			2.00	2.00	1.0		1.8			

CR=crop residue (contains 30% moisture) DCR=dry crop residue (contains 10% moisture) BDCR=bone dry crop residue (contains 0% moisture)

Net energy= energy available minus cum energy input from prior steps 1 kW-hr = 3.6 MJ 1 kJ/kg/K = 0.24 BTU/lb/F 1 kcal = 4.18 kJ

1kJ = 0.948 BTU 42 gal in bbl of oil 1 watt-hr= 3600 Joules energy content of diesel, MJ/lb= 19.5 1 HP = 2.68 MJ/h

Strm 9 composition	vol %(wet)	vol %(dry)
H2O	13	-
CO	24	27
H2	48	55
CO2	15	17

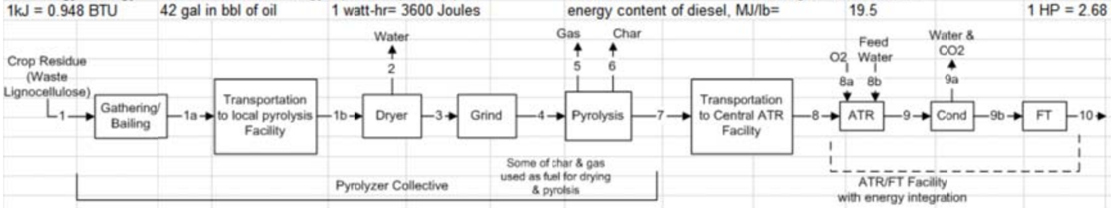

We assume, as a starting point, that there are 8 states (e.g., Illinois, Iowa, Indiana, Minnesota, Missouri, Nebraska, North Dakota, and Texas) each with a single central facility to perform the ATR and FT. Let's say that half of the 30% petroleum consumption goal is to be replaced by the model process of Figure 6.1. This means that each state would handle about 1.3E+9/2/8 = 8.0 E+7 tons of biomass per year. We represent a state as a square about 240 miles on a side (a rough approximation for the size of Iowa, for example) and assume that a single central ATR/FT facility is located in the geometric center of the state. Under this conception, it is estimated that the average distance from a local pyrolyzer to the central ATR/FT conversion facility would be on the order of 70 miles. The average distance from a farm to a local pyrolyzer is assumed to be about 7 miles. This might be idealized as defining a square 14 miles on a side (with an area of 196 sq miles) feeding a single pyrolyzer. Such a collection of farms and a single pyrolyzer we have termed a "pyrolyzer collective".

It is essential to leave a certain amount of crop residue on the field to limit erosion, maintain soil organic carbon, and for nutrient amendment[18]. After leaving 50% on the field the net yield of crop residue is expected to be ~ 2.5 tons (at 30% moisture) per acre per year[19]. Using 2.5 T/ac/y, then each square 14 miles on a side with its single pyrolyzer (pyrolyzer collective) would handle about $2.5*14^2*640$ = 3.1E+5 T/yr. This translates to a pyrolyzer rate of 44 T/h (for 300 days in the year at 24 hours per day). The number of pyrolyzer collectives required to feed the ATR/FT central facility is 258 (= 8.0E+7/3.1E+5). The area of these pyrolyzer collectives is $258*14^2$ = 50,600 square miles, which is about 90% the area of a state the size of a square 240 miles on a side (e.g., Iowa).

Assuming that half of the 1.3 billion tons of biomass feeds the type of process of Figure 6.1, and that 8 central facilities perform ATR and FT, this means that each complex of pyrolyzer collectives and a central ATR/FT facility would be handling the equivalent of (8E+7/300/24 =) ~11,000 tons per stream hour of biomass. This, of course, is prodigious in scale (indeed, a 1000 MW coal fired power plant handles only 375 T/h of coal). For our initial calculations, however, we have taken a scale of only 500 tons/h in Excel spreadsheet of Table 6.1. Such a rate would involve about 10 pyrolyzer collectives.

II.4. Material and Energy Balance

Stream numbers in the material and energy balance spreadsheet of Table 6.1 refer to the diagram of Figure 6.1. Input parameters are in cells filled green. Abbreviations are given in the sheet. The "cumulative energy efficiency" at each relevant step is reported in the Table. At the drying step the "cum energy eff." jumps to 103.1%. This is an artifact of the calculation as char and NCG are burned to perform the drying operation (shifting energy from char and NCG to the liquid fuel) and is rectified in the pyrolysis step of the process.

II.4.1. Assumptions and Comments

1. Biomass is envisioned to come primarily from crop residue.
2. Starting moisture content in biomass is 30%.
3. Char and NCG are burned (at 50% thermal efficiency) to fuel the drying and pyrolysis steps without the use of external energy
4. The small parasitic energy losses that would occur from pumps, etc., have been ignored.
5. A cryogenic plant to produce high purity gaseous oxygen to minimize the compression requirement in the FT step and minimize equipment size. Although we haven't considered it here, use of liquid oxygen instead of gaseous opens the possibility of completely eliminating compression in the FT step if the ATR step is run at elevated pressure using all liquid feeds.

6. Our calculations suggest that the carbon efficiency to CO in the ATR step is about 60%.
7. Loss of carbon by coking in the ATR step is ignored.
8. Energy required to condense water and remove CO_2 from the exit gas of the ATR has not been accounted for.
9. The carbon yield from CO to diesel within the FT step is assumed to be 90%.
10. The heat released by the FT step is used to run a steam turbine which generates more than enough electricity to run the compressor for the FT reactor.

II.4.2. Gathering and Baling

Gathering and baling is the first part of what the USDA refers to as CHST (cut, harvest, store and transport). Baled crop residue is temporarily stored in the field thereby being exposed to weather, i.e., retting, allowing a portion of the more water soluble nutrients such as potassium and sugars to be leached back into the ground; less so for the less water soluble phosphorus, for example. Removal of biomass with the removal of macro and micronutrients from the soil is a consideration. Some of this can be ameliorated or eliminated by returning char from pyrolysis or the ash from burning of the char back to the soil. Allowing crop residue to just decompose in the soil would recycle macro and micronutrients but would release CO_2 to the atmosphere without producing useful energy.

The energy used for harvesting perennial grass which consists of mowing, raking and baling is estimated as 1 gallon of diesel per 800 lb bale. This converts to 0.054 MJ/kg and is taken to also apply to harvesting crop residue.

II.4.3. Transportation to Pyrolysis Facility

We assume that trucks are being used to transport biomass in the form of bales to the pyrolyzer of the pyrolyzer collective. The maximum allowable gross weight for a tractor-trailer combination is 80,000 lb (40T). Depending on the construction of the rig, payloads might range from 43,000 to 55,000 lb. The volumetric capacity of a trailer is about 4,013 ft^3. The bulk density of baled biomass is about 8 lb/ft^3, however, when packed into the volume of a trailer the effective bulk density is about 6.3 lb/ft^3. This would mean the payload of biomass in the tractor-trailer is about 25,000 lb which is well under the payload weight limit of 43,000 to 55,000 lb.

For transportation of a liquid, a tank truck or tanker is used. This type of truck can have capacities from 5,500 to 9,000 gallons. Because of its much higher density (68 lb/ft^3 or 9.1 lb/gal) pyrolysis oil can be transported at a higher payload than baled crop residue. The transportation costs (external energy input) of biomass and PO, streams (1b) and (8), were calculated for payloads of 25,300 and 43,000 lb, respectively. An interesting estimate of transporting liquid fuel in a tank truck of say 5,500 gallons capacity over a distance of 1,000 at 8 miles per gallon is that the fuel penalty is ~ 2.3%.

II.4.4. Drying

It is assumed that the biomass delivered to the pyrolyzer has to be dried from 30% moisture to 10% moisture. A 50% drying efficiency is assumed. It is also assumed that some of the char and non-condensable gas can be used for drying. If 23% of the char and NCG are used for the drying step, then there is essentially no consumption of “external” energy.

II.4.5. Grinding

Based on grinding maize[20], an energy requirement of 0.18 MJ/kg is used for grinding biomass in this step.

II.4.6. Pyrolysis

The energy input for the pyrolysis step is calculated from (1) the sensible heat to heat the biomass from ambient to reaction temperature, (2) the heat of vaporization of the PO, and (3) heat of the pyrolysis reaction (which is said to be slightly endothermic for fast pyrolysis), see equation (6.1).

$$E_P = c_p(T\text{-}25) + f\Delta H_v + \Delta H_r \qquad (6.1)$$

Given the non-uniform nature of the materials being studied, the literature reports a range of property values. Here, we state the values selected for our calculations realizing that they are open to improvement in the light of further data (see also Appendix). The heat capacity[15] of the biomass was taken as 1.0 kJ/kg/K. From Figure 13 of reference[21], the heat of vaporization of PO was taken as 1.21 MJ/kg. The heat of reaction[15], ΔH_r, was taken to be 0.3 MJ/kg. Pyrolysis operating temperature, T, is taken to be 500° C. Thus, for the assumed parameters, the energy requirement for the pyrolysis step is E_P = 1.56 MJ/kg. For these parameters and assuming a pyrolysis thermal efficiency of 50%, the pyrolysis step can be run without external energy input by consuming 58% of the NCG gas and char. If energy for drying and pyrolysis were totally supplied by char and NCG, then 100 – 23 – 58 = 19% of the produced char and NCG would be left. Further economizing might be possible from recovering some of the heat from cooling pyrolysis vapors. The mass stream rates for 'gas' and 'char', streams 5 and 6 of Table 6.1, reflect material loss due to their use in the drying and pyrolysis steps as a heat source.

II.4.7. Transportation to the Central ATR/FT Facility

The discussion given in "Transportation to Pyrolysis Facility" applies here. As mentioned, since PO is much denser than biomass, advantage could be taken of tanker trucks with higher payloads. Alternatively, if the infrastructure permits, use could be made of existing rail lines.

The effect of trucking biomass directly to a central facility and doing the pyrolysis directly at the central facility without first producing PO can be obtained by changing "Trucking distance to the pyrolyzer" to 70 miles (instead of 7 miles) and changing "Trucking distance of PO to ATR/FT facility" from 70 miles to zero. This results in a calculated reduction of energy efficiency of 1.0%, i.e., the energy efficiency goes from 42.1% to 41.1%. However, this simple calculation doesn't account for two other relevant factors, namely, (a) the cost of trucking in maintenance and salaries would be appreciably greater, but (b) if the biomass were pyrolyzed at the central facility a significant heat saving (item 3 in Table 6.2) in the ATR step would be possible. Thus, a case could be made (with no local pyrolyzer) in which biomass is received pyrolyzed, reformed, and converted into diesel at the single site in each state. Wright, Brown and Boateng[6] have examined in detail the capital and operating costs of distributed processing of biomass to PO followed by shipping PO to a central facility vs. direct shipping of the biomass to a central facility.

II.4.8. ATR Step

With the autothermal reforming step (ATR) we arrive at a critical point in the process and the one which embodies currently developing technology. It is in this step that the diverse and multitudinous oxygenated organics comprising PO are converted, i.e., reformed, into syngas (H_2 and CO in an approximate 2:1 ratio). The ATR step along with the Fischer-Tropsch step is located at the central processing facility. The BASF Catalyst LLC dual layer monolith ATR reactor couples catalytic partial oxidation (CPO) which is exothermic with endothermic steam reforming. This approach or a variant thereof has been called adiabatic oxidative reforming[22] by Haldor Topsoe Inc. Bartholomew and Farrauto[23] discuss the advantages of ATR which include a more compact reactor, better heat management, mechanical integrity and lower pressure drop than conventional reactors. This step represents an area of high capital cost[24,25].

Since ATR of PO is in its initial stages of investigation, what we say here is based on what is known about ATR for feeds such as CH_4 and methanol. Particularizing the analysis to PO feed awaits further data. The ATR step, shift reactors, and the FT step followed by hydrocracking of waxes and product separtion are diagrammatically shown in Figure 6.2. Pressure swing adsorption is used to obtain hydrogen for hydrocracking[25]. Use of oxygen is indicated which will reduce the ATR heat requirement and downstream capital and operating costs in the Fischer Tropsch step which requires compression of the syngas to elevated pressures. The electrical energy required for cryogenic production of 95% purity gaseous O_2 is taken as 220 kWh/metric ton of oxygen[26]. Converting this to thermal energy (~3X the electrical requirement) and changing units we have 2.38 MJ/kg O_2. For purposes of calculation the O_2 purity was assumed 100%.

Figure 6.2: ATR and FT Steps (with integrated energy recovery)

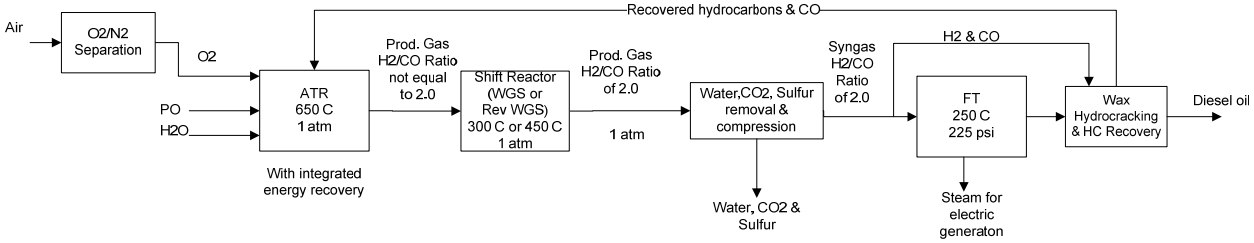

A syngas purification step utilizing, for example, the Lurgi Rectisol™ process, removes CO2 and sulfur. Although it is not expected that crop residue will have much sulfur it can have more than wood residue. For example, Mullen and Boateng[27] report alfalfa as having a sulfur content of 0.09 – 0.22%. This compares to forestry residue which is reported by Oassma[28] et al in the range of 0.04% sulfur. The sulfur content of PO resulting from alfalfa is reported as 0.05 – 0.07%. However, the purity requirements for syngas are strict being on the order of < 0.1 ppm total sulfur. The ATR step can be designed to accommodate a higher sulfur loading.

Since FT produces waxes as well as diesel, the waxes need to be converted to useable diesel, using for example a UOP hydrocracking catalyst. Hydrogen in the syngas is used in the cracking step. Residual fuel values from the FT step may be recycled back to the ATR step. A shift reactor may not be necessary if the H_2/CO ratio can be sufficiently controlled at 2:1 in the ATR step.

Figure 6.3 gives the ATR reactor in more detail and shows preheating of the feeds for energy economy. The ATR reactor can be a plug flow monolithic honeycomb reactor in which the gases enter at about 400° C. Near the reactor inlet an exothermic spike to about 850° C occurs due to the partial oxidation reaction. As the gases move toward the exit the endothermic reforming reactions take over and cooling occurs resulting in an exit gas temperature of about 650° C. The exit gas passes through a heat recovery exchanger to preheat the feeds to the ATR reactor. It is noted that metal dusting corrosion issues can occur with CO at elevated temperature in this exchanger[29].

Figure 6.3: ATR Reactor with Integrated Energy Recovery

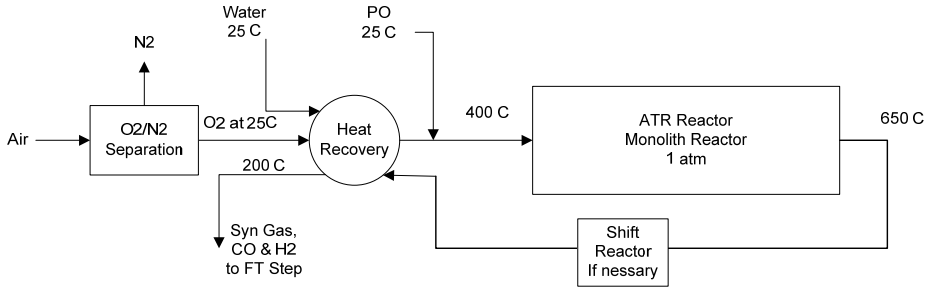

In the autothermal reforming step, PO is reacted with water vapor and sub-stoichiometric oxygen to produce a gas which contains H_2 and CO in the mole ratio near or at 2:1. The reactions that could occur in ATR of pyrolysis oil of the general empirical formula $C_nH_mO_k$ are represented below:

$$C_nH_mO_k + (2n-k)H_2O = nCO_2 + (2n+0.5m - k)H_2 \quad (6.2)$$

$$C_nH_mO_k + (n-k)H_2O = nCO + (n+0.5m - k)H_2 \quad (6.3)$$

$$C_nH_mO_k + (0.5n +0.25m - 0.5k)O_2 = nCO + 0.5mH_2O \quad (6.4)$$

$$C_nH_mO_k + 0.5(n-k)O_2 = nCO + 0.5mH_2 \quad (6.5)$$

$$CO + 0.5O_2 = CO_2 \quad (6.6)$$

$$CO + H_2O = CO_2 + H_2 \quad (6.7)$$

This step is operated at an exit temperature of 650°C over a catalyst[23] at 1 atm. The pyrolysis oil that we are using in our lab has an empirical formula (carbon taken as 1.0) on a *bone dry basis* of $CH_{1.4}O_{0.5}$.

The reforming reaction is endothermic. An idea of the magnitude of the heat requirement for reforming can be obtained from a few example reactions:

$$CH_4 + H_2O = CO + 3H_2 \qquad \Delta H_{298} = 206 \text{ MJ/kg-mol} \quad (6.8)$$

$$CH_4 + 2H_2O = 2CO_2 + 4H_2O \qquad \Delta H_{298} = 164.9 \text{ MJ/kg-mol} \quad (6.9)$$

$$C_2H_5OH + H_2O = 2CO_2 + 4H_2 \qquad \Delta H_{298} = 238 \text{ MJ/kg-mol} \quad (6.10)$$

The calculations of Table 6.1 use an endothermic heat of reaction for the reforming reaction of 200 MJ//kg-mol of carbon in the PO. The heat capacity[30] of PO was taken as ~ 2 kJ/kg/K.

Equations (6.2) – (6.10) are given for reference and are not directly used in the calculations. For the parameters of Table 6.1, an energy balance around the ATR is made without the use of equations (6.2) – (6.10) to give estimates of the amounts of CO, CO_2, H_2O and H_2 formed. The energy balance is as follows:

Table 6.2: Energy Balance around ATR Step shown in Fig. 6.3 for Table 6.1 Parameters

		MJ/h
1	Eng needed to heat oxygen (or air, if used)	30,295
2	Eng needed to heat & evap fresh H2O	292,156
3	Eng needed to heat & evap PO	621,833
4	Eng needed for endothermic reforming rxn*	1,088,105
5	Total energy required =	2,032,389
6	Energy given up by exit gases & recovered	309,748
7	Energy required by combustion of PO	1,722,641
8	Am't of PO burned to provide energy, kg/h	98,437
9	Am't of PO left to be converted into CO, kg/h	154,341
10	Carbon efficiency into CO of ATR step, %	61
	* the PO which is burned is not included in the endothermic heat of rxn	

*The PO which is burned is not included in the endothermic reaction (This produces a circular reference (trial and error) which necessitates putting the spreadsheet into manual mode).

It is seen from Table 6.2 that the endothermic reforming reaction absorbs about 54% of the heat requirement for this step. The energy recovered by the preheat heat exchange is about 15% of that needed for the step. Bear in mind that the endotherm of the reaction is not lost energy but is in essence transferred to the products, CO and H_2, as higher energy materials than the feed. Carbon is lost in this step by two routes: (1) oxidation to CO_2 to provide heat for the reaction and (2) coking. Laboratory studies indicate a carbon loss from coking can be on the order of 5%. Our calculation ignores coking for the present.

The calculations for the ATR step are as follows: the energy required by combustion of PO gives the amount of PO consumed and therefore defines the carbon efficiency. The amount of CO_2 produced is determined by the amount of PO burned. The remaining carbon values are assumed to go to CO. The carbon efficiency to useable CO, in the case shown in Table 6.2, is calculated to be ~60%. Knowing the moles of CO_2 and CO produced, the remaining oxygen is assigned to water in the exit gas. A hydrogen elemental balance then gives the free H_2 in the exit gas.

Our recent laboratory work indicates that control of the H_2 to CO ratio is quite possible at the ATR reactor by manipulating the flow rates of water and O_2 in proportion to the PO. However, if the H_2/CO ratio is < 2.0 in the reformer exit gas then the water gas shift reaction (WGS) may be used to correct it, see eq. (6.11). If the ratio is > 2.0 then the reverse WGS may be used, eq. (6.12).

WGS	$CO + H_2O \rightarrow CO_2 + H_2$	300°C & 1 atm	ΔH = - 41.1 kJ/mol	(6.11)
RWGS	$CO_2 + H_2 \rightarrow CO + H_2O$	450°C & 1 atm	ΔH = + 41.1 kJ/mol	(6.12)

It has been pointed out[3,4] that H_2 produced from renewable sources such as solar or wind could be used to convert the CO_2 into useable CO which would improve the overall energy efficiency of this process. Also solar heating might be usable in the ATR step. Owing its critical importance and its nascent state of development, ATR of PO should be the object of vigorous research.

II.4.9. FT Step

In the FT step syngas produced in the ATR step is converted to diesel oil. Carbon efficiency of the FT step is assumed to be 90%. The generic, strongly exothermic, FT reaction along with operating conditions is[25]:

$$(2n+1)H_2 + nCO \rightarrow C_nH_{(2n+2)} + n\ H2O\ 250°C\ \&\ 225\ psi\ \ \Delta H = -170\ kJ/mol\ of\ CO \qquad (6.13)$$

In the production of diesel fuel "n" in the equation above can be in the range of 12 to 25. Therefore, a H_2 to CO mole ratio very close to 2:1 is required. Iron based catalysts and an operating temperature of 330 – 350° C will produce mostly gasoline, while cobalt based catalysts at an operating temperature of 200° C will produce mostly diesel oil[31].

The energy input for compressing syngas from the ATR step to operating pressure for the Fischer Tropsch synthesis step is calculated for two-stage isothermal compression and included in the spreadsheet of Table 6.1. The following equation for multistage compression with inter-cooling[32] was used to estimate the compressor horsepower requirement, hp:

$$hp = \frac{0.00436 N p_1 q_1}{\alpha \eta}\left[\left(\frac{p_2}{p_1}\right)^{\frac{\alpha}{N}} - 1\right] \qquad (6.14)$$

Where, N = number of stages (we use 2); p_1 = inlet pressure, psia; p_2 = outlet pressure, psia; q_1 = flow rate at intake conditions, ACFM; α=(k - 1)/k; k = ratio of heat capacities (we use 1.4); η = efficiency as fraction (we use 0.8). The compressor hp requirement for the balance of Table 6.1 is estimated to be 65,153 hp. This converts to 2.68(MJ/h/hp)*65,153 = 174,600 MJ/h this means that about 3 times as much heat energy would be needed to produce that amount of electricity, or 523,800 MJ/h. However, the heat release rate from FT is 863,400 MJ/h. So, if as outlined in[12], steam is raised in cooling the FT reactor and then superheated by exchange with the exit of the ATR reactor and run through a steam turbine to generate electricity, it appears that this amount of electricity could be sufficient to run the compressor for the FT step. An alternative concept would be to use liquid oxygen and pump liquid water and liquid PO into the ATR reactor which could be run at the pressure needed for FT. Thus, eliminating the need for a compressor for FT.

The production rate for the material balance of Table 6.1 is about 11,000 barrels of diesel per day. Therefore, a plant of this size would produce about 0.06% of the US consumption need. Sasol utilizes natural gas and coal to run a FT process. The Sasol plant in Qatar, SASOLI, produces FT diesel at a rate of 34,000 bbl/day. This would be about three times the rate of the material balance of Table 6.1, or a feed rate of about 1,500 T/h of biomass.

II.5. Results

II.5.1. Energy Efficiency and the Internal Use of Char and NCG

The spreadsheet of Table 6.1 contains a row labeled "Cum. Eng. Eff., %" which traces the energy efficiency of the final fuel or its intermediate stages. It is seen that when char and NCG are used in the drying and pyrolysis steps the cumulative energy efficiency in the final diesel fuel is 42.1%. If char and NCG are not used to fuel the drying and pyrolysis steps the cumulative energy efficiency drops to 15.3%. A comparison of the cumulative energy efficiency with and without char and NCG combustion at several points in the process is shown in Table 6.3. However, the total energy to be found in the final products of diesel fuel, char and NCG remains the same, see Table 6.4.

Table 6.3: Comparison of Cumulative Energy Efficiency with and without Burning of Char & NCG

Stream no.	*Description*	*Cum. Eng. Eff., %*	
		with burning Char & NCG	*without burning Char & NCG*
1	Crop Residue	100	100
3	Dry crop residue	103.3	95.6
4	Ground DCR	102.2	94.5
7	PO	69.8	43.1
9b	Dry ATR Syn Gas	63.8	37.1
10	FT liquids diesel oil	42.1	15.3

Note: as already mentioned the efficiencies > 100% are an artifact of the calculation and are compensated for at the pyrolysis step.

Table 6.4: **Comparison of the Final Distribution of energy in the Products**

Product	*% of Original biomass energy in Product*	
	with burning Char & NCG	*without burning Char & NCG*
Diesel fuel	42.1	15.3
Char	5.1	28.1
NCG	0.8	4.6
Total	48.0	48.0

Using char and NCG to provide energy for the drying and pyrolysis steps will be important in operating an efficient process. These energy efficiencies are comparable to prior detailed literature estimates utilizing Aspen[9,13].

II.5.2. Diesel Yield

Table 6.1 shows that the weight yield of diesel oil is about 13.7% of the initial weight of the biomass (30% moisture) or about 1 barrel per metric ton of biomass (30% moisture).

II.5.3. Effect of Moisture Content in the Biomass

Table 6.5A shows the effect of moisture content in the biomass on energy efficiency. Provided that char and NCG are used as fuel in the drying and pyrolysis steps, moisture content in the biomass essentially does not affect the energy efficiency to liquid fuel although it will affect the total energy recovered. The mild decrease in calculated energy efficiency to diesel with decreased moisture when char and & NCG are used is due to the larger energy content initially in the biomass. If char and NCG are not used in the drying and pyrolysis steps then moisture content does have an effect on the efficiency to diesel due to the increased external energy needed.

Table 6.5A: Effect of Biomass Moisture Content on Energy Efficiency

Biomass Moisture Content wt %	Energy Efficiency to Diesel %		Total Energy Recovery in Diesel + Char + NCG, %
	Using* char & NCG	Not using* char & NCG	
30	42.1	15.3	48.0
20	41.3	19.4	51.4
10	40.7	22.3	53.8

*to fuel the drying and pyrolysis steps

The effect of biomass moisture content on weight yield of diesel is shown in Table 6.5B. Of course as the moisture content decreases weight yield increases.

Table 6.5B: Effect of Biomass Moisture Content on Weight Yield of Diesel

Biomass Moisture Content wt %	Weight Yield of Diesel, % of initial biomass	Barrels of Diesel per metric ton of biomass
30	13.7	1.0
20	15.7	1.1
10	17.6	1.2

II.6. Conclusions and Recommendations

1. A transparent material and energy analysis of each component of a specific model of a biomass route to FT fuel has been presented. Also, a widely available tool (an Excel spreadsheet as opposed to Aspen which is of limited availability and more difficult to use) for use by any investigator is provided which can serve as a facile approach for scouting alternatives prior to comprehensive energy and economic analysis by more powerful tools such as Aspen.
2. The process of Figure 6.1, in which a portion of the char, and non-condensable gas (NCG) are used to supply heat to the drying and pyrolysis step and externally supplied energy is accounted for, is estimated to have an energy efficiency on the order of 40%. If the energy of the remaining char and NCG is added to that in the product diesel oil the total recovered energy is estimated to be 50% of the initial energy content of the biomass. These estimates agree with more detailed Aspen calculations.
3. If char and NCG are <u>not</u> used to fuel the drying and pyrolysis steps then the energy efficiency drops to 15%. However, the final total of energy in the product diesel, char and NCG remains constant at ~50% of the initial energy content of the biomass.
4. Clearly, effort should be given to finding an effective means of using the energy values of char and NCG in the conversion process to liquid fuel.
5. The weight of diesel fuel produced is about 13% of the initial weight of biomass or about 1 metric ton of biomass (30% moisture) will produce 1.0 barrels of diesel oil.
6. Our estimate indicates that the autothermal reforming step results in a carbon yield of ~ 60% as useable CO.
7. Pyrolysis of biomass to PO is estimated to have an intrinsic energy efficiency of about 90%.
8. Trucking biomass to a central facility without first converting it to PO decreases the calculated energy efficiency by 1.0%. However, the additional trucks and labor and also the re-evaporation of PO would factor into an economic analysis.
9. Reduced moisture content in the biomass does not affect the energy efficiency to diesel provided that char and NCG are used to fuel the drying and pyrolysis steps.
10. Using the process of Figure 6.1, to replace ~ 15% of current petroleum consumption in the US, will require gathering biomass from a substantial portion of the land area of the major crop producing states.
11. Clearly, there are many, many conceptual variations and refinements to be explored, not to mention an experimental terra incognita.

II.7. Appendix A

Energy efficiency is defined as:

$$\begin{pmatrix}\text{Energy Eff. of}\\ \text{converting}\\ \text{biomass to fuel, \%}\end{pmatrix} = \frac{\left(\begin{pmatrix}\text{LHV of fuel}\\ \text{produced from 1 lb}\\ \text{of biomass}\end{pmatrix} - \begin{pmatrix}\text{External Eng. input}\\ \text{to process 1 lb of}\\ \text{biomass to fuel}\end{pmatrix}\right)*100}{\begin{pmatrix}\text{LHV of orginal}\\ \text{1 lb of biomass}\end{pmatrix}}$$

II.7.1. Comments on Energy Content of Biomass Components

Comparisons of energy densities are given in Table 6.6.

Table 6.6: Some Relevant Energy Densities

Component	*Energy (LHV) Density, MJ/kg*	*Symbol*
Biomass (bone dry, 0% moisture)	19.1	E_{bd}
Biomass (10% moisture)	17.0	E_1
Biomass (30% moisture)	12.7	E_3
PO	18.0	E_{PO}
Char	23	E_C
NCG	5	E_{NGC}
Compare above to below:		
Cellulose	17.3	
Lignin	25.4	
Wood (bone dry)	20.0	
Diesel oil	42.8	

It is seen that

$$E_1 = 0.65E_{PO} + 0.2E_C + 0.15E_{NGC} \qquad (A.1)$$

where the coefficients on the energy densities on the right hand side are the weight fractions typically generated by the biomass (10% moisture) pyrolyzing to its respective products, see input parameters of Table 6.1. Also note

$$E_1 = 0.9E_{bd} - 0.1*2.2 \qquad (A.2)$$

$$E_3 = 0.7E_{bd} - 0.3*2.2 \qquad (A.3)$$

where, we have calculated the energy available from the fuel by subtracting out the energy required to vaporize the water content. Note that the energy density of bone-dry biomass of 19.1 MJ/kg lies between that of cellulose, 17.3 MJ/kg, and that of lignin, 25.4 MJ/kg. Also note that the energy density of bone-dry wood (20 MJ/kg) is close to that of bone-dry biomass (19.1 MJ/kg). These energy contents, due to the presence of oxygenated compounds, are well below that of diesel oil, which is 42.8 MJ/kg.

II.7.2. Energy Loss on Pyrolysis

An estimate can be made of the energy lost in pyrolysis of 10% moisture biomass ("dry biomass"). As noted in eq. (A.1) the energy content of dry biomass is equal to the sum of the energy contents

of its products of PO, char, and NCG. Now, from eq. (6.1) it was estimated that the energy required to produce the pyrolysis products was 1.56 MJ/kg at 100% thermal efficiency. Thus the loss of energy in pyrolysis of dry biomass to PO, char and NCG is estimated at 1.56/17=9.2%, or the "intrinsic" energy efficiency (ie, at100% thermal efficiency) of pyrolysis is 91%

The distribution of energy into the products of pyrolysis is estimated in Table 6.7. Thus, upon pyrolysis about 70% of the energy in dry biomass ends up in the PO and close to 30% in the char, with only a small portion going to NCG.

Table 6.7: Distribution of Energy Content Among Pyrolysis Products

Fraction	*% Energy of Original Dry Biomass in Given Fraction*
PO	69
Char	27
NGC	4

Some Property Values used in the Calculations

Heat capacity of biomass, kJ/kg/K	1.0
Heat capacity of pyrolysis oil, kJ/kg/K	2.0
Heat capacity of NCG, kJ/kg/K	1.8
Heat capacity of water (liquid), kJ/kg/K	4.2
Heat capacity of water vapor, kJ/kg/K	2.0
Heat of vaporization of PO, MJ/kg	1.21
Heat of pyrolysis reaction, MJ/kg	0.3
Heat of reaction for reforming PO (endothermic), MJ/kg-mol of C in PO	200
Heat of reaction for FT synthesis (exothermic), MJ/kg-mol of CO	170

Empirical formula of bone dry PO taking C=1: $CH_{1.4}O_{0.5}$ (mol. wt. = 21)

II.8. Nomenclature

c_p heat capacity of biomass, MJ/kg/°C
f fraction of biomass converted to PO
E_P Energy requirement for pyrolysis, MJ/kg
ΔH_v heat of vaporization of PO, MJ/kg
ΔH_r heat of reaction of pyrolysis, MJ/kg

II.9. References

1. http://oil.com, 2009.
2. Lynd, L., E Larson, N Greene, M Laser, J Sheehan, BE Dale, S McLaughlin, M Wang, *The role of biomass in American's energy future: framing the analysis.* Biofuels Bioproducts & Biorefining, 2009. 3: p. 113-123.
3. Singh, N., WN Delgass, FH Ribeiro, R Agrawal, *Estimation of liquid fuel yields from biomass.* Environ. Sci. Technol., 2010. 44: p. 5298-5305.
4. Agrawal, R., NR Singh, FH Ribeiro, WN Delgass, *Sustainable fuel for the transportation sector.* Proc. Natl. Acad. Sci. U.S.A., 2007. 104(12): p. 4828-4833.
5. Cottam, M., A Bridgewater, *A techno-economic modelling of biomass flash pyrolysis and upgrading systems.* Biomass & Bioenergy, 1994. 7(1): p. 267-273.

6. Wright, M., RC Brown, AA Boating, *Distributed processing of biomass to bio-oil for subseqent production of Fischer-Tropsch liquids.* Biofels, Bioprod. & Bioref., 2008. 2: p. 229.
7. Jones, S., C Valkenburg, C Walton, DC Elliott, JE Holladay, DJ Stevens, C Kinchin, S Czernik, *Production of gasoline and diesel from biomass via fast pyrolysis, hydrotreating and hydrocracking: a design case*. 2009, Pacific Northwest National Laboratory: Richland, Washington. February 2009
8. Laser, M., H Jin, K Jayawardhana, BE Dale, LR Lynd, *Projected mature technology senarios for conversion of cellulosic biomass to ethanol with coproduction of thermochemical fuels, power, and/or animal feed protein.* Biofels, Bioprod. & Bioref., 2009. 3: p. 231-246.
9. Laser, M., E Larson, B Dale, M Wang, N Greene, LR Lynd, *Comparative analysis of efficiency, environmental impact, and process economics for mature biomass refining scenarios.* Biofuels, Bioprod. Bioref., 2009. 3: p. 247-270.
10. Wright, M., DE Daugaard, JA Satrio, RC Brown, *Techno-economic analysis of biomass fast pyrolysis to transportation fuels.* Fuel Processing Technolgy, 2010. 89: p. S2-S10.
11. Tijmensen, M., APC Faaij, CN Hamelinck, MRM van Hardeveld, *Exploration of the possiblities for production of Fischer Tropsch liquids and power via biomass gasification.* Biomass & Bioenergy, 2002. 23: p. 129.
12. Lui, G., ED Larson, RH Williams, TG Kreutz, X Guo, *Making Fischer-Tropsch fuels and electricity from coal and biomass: performance and cost analysis.* Energy & Fuels, 2011. 25: p. 415-437.
13. Larson, E., J Haiming. *Biomass conversion to Fischer-Tropsch liquids: preliminary energy balances*. in *4th Biomass conference of the Americas*. 1999. Oakland, CA Aug. 29- Sept. 2, 1999: Elsevier Science, Ltd.
14. Atchison, J., JR Hettenhaus, *Innovative Methods for Corn Stover Collecting, Handling, Storing and TRansporting Rpt. NREL/SR-510-33893*. March 2003, NREL Golden Colorado.
15. van de Velden, M., J Baeyens, A Brems, B Janssens, R Dewil, *Fundamentals, kinetics and endothermicity of the biomass pyrolysis reaction.* Renewable Energy, 2010. 35: p. 232-242.
16. Bridgewater, A., *The status of biomass fast pyrolysis*, in *Fast Pyrolysis of Biomass: A Handbook Volume 1*, A. Bridgewater, Editor. 1999, CPL Press.
17. Perlack, R., LL Wright, AF Turhollow,RL Graham, BJ Stokes, DC Erbach, *Biomass as feedstock for a bioenergy and bioproducts industry: The technical feasiblity of a billion-ton annual supply ORNL/TM-2005/66*. 2005, Oak Ridge National laboratory: Oak Ridge, TN.
18. Wilhelm, W., FMF Johnson, DL Karlen, DT Lightle, *Corn stover to sustain soil organic carbon further constrains biomass supply.* Agronomy Journal, 2007. 99(Nov Dec): p. 1665-1667.
19. Sawyer, J., A Mallarino, *Nutrient removal when harvesting corn stover.* Integrated Crop Management, 2007. August 6, 2007: p. 251-253.
20. Velu, e., J of Food Eng, 2006. 77: p. 30-36.
21. Shidhadeh, A., S Hochgreb, *Impact of biomass pyrolysis oil process conditions on ignition delay in compression ignition engines.* Energy and Fuels, 2002. 16: p. 552-561.
22. KAasberg-Petersen, e.a., *Synthesis gass production for FT synthesis.* Studies in Surface Science and Catalysis, 2004. 152: p. 258.
23. Bartholomew, C., RJ Farrauto, *Fundamentals of Industrial Catalytic Processes*. 2nd ed. 2006: J Wiley.
24. Aasberg-Petersen, K., TS Christensen, CS Nielse, I Dybkjaer, *Recent developments in autothermal reforming and pre-reforming for synthesis gas production in GTL applications.* Fuel Processing Technolgy, 2003. 83: p. 253-261.
25. Steynberg, A., M Dry, *Fischer-Tropsch Technology, Vol. 152*. Studies in Surface Science and Catalysis, ed. G. Centi. 2004: Elsevier.

26. Christie, M., R Victor, BA van Hassel, N Nagabushana, JLi, J Corpus, J Wilson, *Advanced oxyfuel boilers and process heaters for cost effective CO2 capture and sequestration. Report DOE Awards no. DE-FC26-01NT41147*. 2007, Praxair Inc: Tonawanda, NY. Dec. 17, 2007
27. Mullen, C., AA Boateng, *Chemical composition of bio-oils produced by fast pyrolysis of two energy crops.* Energy and Fuels, 2008. 22: p. 2104-2109.
28. Oasmaa, A., E Kuoppala, Y Solantausta, *Fast pyrolysis of forestry residue. 2. Physicochemical composition of product liquid.* Energy and Fuels, 2003. 17: p. 433.
29. Dybkjaer, I., *Synthesis gas technology.* Hydrocarbon Engineering, 2006. 11(July): p. 33-36.
30. van Rossum, G., BM Guell, RPB Ramachandra, KS Lefferts, L Lefferts, WPM van Swaaij, SRA Kersten, *Evaporation of pyrolysis oil: product distribution and residue char analysis.* AIChE Journal, 2010. 56(8): p. 2200-2210.
31. Scherb, J., *The Fischer-Tropsch (FT) Process:Production of synthetic fuels.* [Internet]. Version 68. Knol. 2010 Mar 4. Available from: http://knol.google.com/k/jean-scherb/the-fischer-tropsch-ft-process/3opar7xno0682/9, 2010.
32. Peters, M., KD Timmerhaus, *Plant Design and Economics for Chemical Engineers, 3rd Ed.* 1980: McGraw-Hill.

III. Conversion of Residual Biomass into Liquid Transportation Fuel: Techno-Economic Analysis (published in Energy & Fuels 2012, 26, 2442-2453)

III.1. Introduction

The matter of ensuring a reliable supply of liquid fuel, which is used primarily for transportation, represents a particularly thorny conundrum to the governing bodies of the world. Liquid fuel is a major commodity central to the wellbeing of any advanced nation. Given their extremely high energy density and ease of handling and storage, liquid transportation fuels such as gasoline, diesel, JP-1, biodiesel, ethanol, etc., bid fair to be in demand at a significant level well into the foreseeable future.

However, over the past 3 to 5 decades, the distressing themes of renewable resources, CO2 emission and national defense implications have reoccurred with, what can only be regarded as, wearisome frequency. To address these concerns, production of a liquid hydrocarbon fuel, not ethanol, from renewable resource biomass (be it waste or specifically grown as an energy crop) has received much theoretical and experimental attention in the US and worldwide [1-8].

The “billion ton” report [9] and its update [10] investigated currently available and projected biomass potential supply from forest, agricultural residues, and energy crops. These reports indicate that it is not unreasonable to expect biomass availability of a magnitude sufficient to achieve a replacement of approximately 30% of current petroleum consumption. A penultimate aim is to meet the Energy Independence and Security Act of 2007 (EISA) to produce 36 billion gallons per year (about 12% of current US consumption) of renewable fuels by 2022 [11]. Of course, developing the infrastructure for such a scale of biomass collection constitutes a major task.

The problem of comparing the “true” economics of liquid fuel produced from renewable biomass versus that produced from conventional crude oil or from coal or natural gas is, to say the least, an interesting and non-trivial one. In comparing the economics of the various routes to liquid fuels it is necessary, as is done in thermodynamics, to define the system under consideration. Usually the system considered is not ‘global’ but restricted to production alone. Such ‘externalities’ as the

cost of military protection of the raw material supply or the cost of flood or hurricane repair due to global warming are not included in the sales price at the pump. Unfortunately, however, these costs are still real and are paid for by the inhabitants of the world, whether or not they buy the product. It is the reality of 'externalities' that make the matter of a decision on a production process not strictly an economic one (in a 'local' sense) but also a *policy* one. This paper, however, like the majority of economic studies, addresses only the economics of the production process.

Economic studies have been made of many variations of the biomass feedstock theme. Here we examine the specific case of crop residue to Fischer-Tropsch liquid (FTL) fuel. For capital cost, the literature often reports capital cost estimates based on Aspen model design and Icarus cost estimates. Our approach to capital cost has been to use reported estimates based on actual plants, such as a Bechtel-Syncrude estimate [12], to which we have applied the 0.6 factor. This is coupled with the usual sensitivity analysis of capital cost.

It must be borne in mind in comparing the economics of the nascent biomass to liquid fuel processes to the "mature", century old, processes of crude oil or FT of natural gas or coal, that the biomass processes are on a learning curve and, over time, assuming commercial implementation, will more rapidly improve in economics relative to the mature processes [13]. This also implies that early entrants into the field of biomass derived fuel would establish a competitive advantage. It then becomes a question of whether and when to enter the bio-derived fuel field in a committed way [14].

From this preliminary analysis of FT liquids derived from biomass, even without policy intervention, could be competitive at current prices at a sufficiently large production scale.

III.2. Process Description

The integrated process for conversion of biomass into liquid transportation fuel, such as diesel is being investigated experimentally and theoretically by the Lawal group at Stevens Institute of Technology. This process is comprised of: (1) harvesting surplus biomass such as crop residue, (2) locally pyrolyzing the biomass into pyrolysis oil (PO), char, and non-condensable gas (NCG), (3) transporting the produced PO to a remote central processing facility, (4) converting the PO at this facility by autothermal reforming (ATR) into synthesis gas (CO and H2), followed by, at the same facility, (5) Fischer Tropsch (FT) synthesis of the syngas into diesel fuel. Steps (1) and (2) are embodied in what we call the "*pyrolyzer collective*" (PC). The integrated enterprise of all steps 1-5 we term a "*biorefinery collective*" (BRC). A block diagram of the process considered is given in Figure 6..

Figure 6.4: Block Diagram of the Process

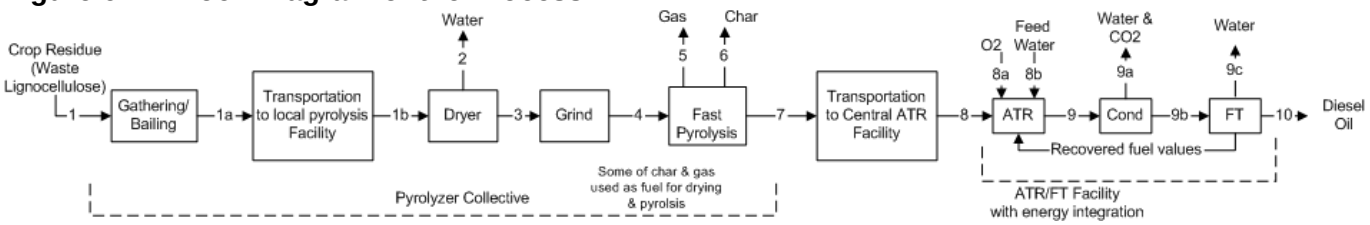

Pyrolysis of biomass has an advantage over gasification in that, by virtue of the higher density of PO compared to baled biomass it allows reduced transport cost to a central ATR/FT processing plant. This aspect has been explored in detail by Wright, et al [15]. Producing a liquid intermediate such as PO also opens the possibility of pipe line transport. In this paper we undertake an

economic analysis of the process outlined in the block diagram of **Figure 6.** which is described in more detail in our prior paper [16]. That paper also presented a material and energy balance for the process.

III.2.1. Pyrolyzer Collective and BioRefinery Collective

To be more specific about a pyrolyzer collective (PC): it is defined as a collection of farms contained within a land area of arbitrary size in which each farm sends its crop residue to a single centrally located pyrolyzer within the land area where the biomass is converted to pyrolysis oil. An example of 4 square PCs each with its pyrolyzer and each sending pyrolysis oil to a central ATR/FT plant is depicted in

Figure . Such a group of PCs and a single central ATR/FT plant is, as mentioned, called a *biorefinery collective* (BRC).

Figure 6.5: Biorefinery Collective

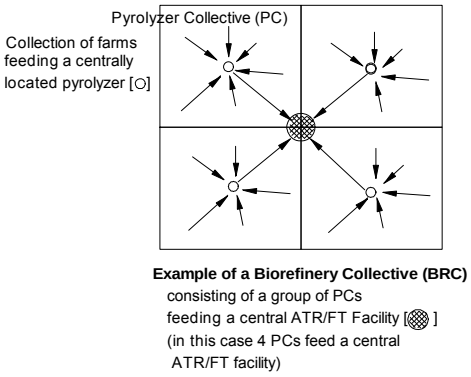

III.2.2. Average Distance to a Central Point

In the pyrolyzer collective, biomass is gathered from a farm area, here idealized as a square, and trucked to a central pyrolyzer. From the various pyrolyzing points, PO is trucked or shipped to a central ATR/FT facility. We consider the problem of calculating the average distance to a central point for the simplified model of a *unit square* which has N^2 points uniformly distributed within it. The average distance, d_{ave}, to the center of the unit square is calculated from equation(6.15) in which N is a large number.

$$d_{ave} = \frac{\sum_{j=1}^{N}\sum_{i=1}^{N}\left\{\left[\left(\frac{1}{1+N}\right)i-0.5\right]^2+\left[\left(\frac{1}{1+N}\right)j-0.5\right]^2\right\}^{0.5}}{N^2} = 0.382 \qquad (6.15)$$

If the square is “S” miles on a side the average distance to the center point is estimated to be 0.382*S. Thus, if a pyrolyzer collective is idealized as a square 14 miles on a side, the average distance to the center of the square is estimated to be 0.382*14 = 5.35 miles. Iowa is an example of a state in which crops are grown on an overwhelming portion of the land area. It has a land area of ~56,000 square miles and can be idealized roughly into the shape of a square 240 miles on a side and would have an average distance from uniformly distributed PC’s to a single central ATR/FT processing facility of 0.382*240 = ~92 miles.

III.3. Scale Required for Measurable Impact

Current consumption of petroleum in the US is about 20 million barrels per day. For biomass to FTL to have a measurable impact we should examine a scale on the order of 10% of that or 2 million bbl/day. If we say about 10 states are the major contributors of residual biomass then we could possibly view each state as a biorefinery collective each with a single central ATR/FT facility. Therefore, each BRC would produce about 200,000 bbl/day and handle about 200,000 T/day of biomass. Using a land productivity of 5.8 bbl per day per square mile (see Table 6.16), a land area about 60% the size of the state of Iowa would be required to produce 200,000 bbl/day.

III.4. Base Case Design Basis and Material & Energy Balance

In implementing this technology, the U.S. DOE regards biomass feed rates of ~1 dry T/day as pilot scale, 50 – 70 dry T/day as demonstration, and > 700 dry T/day as commercial scale [17]. Our analysis starts with a base case of a dry biomass feed rate of ~2,000 ton/day. This is in keeping with prior studies [18]. Such a scale, ~2,000 T/day, in our view, is boarder line commercially competitive and would serve to demonstrate process operability, work out the kinks, and provide a decision gate for advancing further. The effect of production scale on economics will be explored latter. To begin our material balance calculations we use that developed in [16] as customized for ~ 2,000 dry metric T/day. A design basis to produce FT diesel fuel along with some calculated values is shown in **Table 6.8**

Table 6.8: A Design Basis Note: db = daily barrel, i.e., barrels per day; 1 db = 0.067 MW_{th}

Biomass Rate, dry T/stream day	**2,000**
On-stream factor, %	**95.6**
Production Rate of diesel, millions of gallons per calendar year	**36**
Biomass Stream rate, dry T/stream hr	83
Biomass Stream rate, (30% moisture) T/stream hr	107
Biomass Rate, (30% moisture) T/stream day	2,571
Biomass Rate, (30% moisture) T/calendar year	900,000
Biomass Capacity, dry T per calander year	700,000
Production Rate, gallons per stream day	103,331
Production Rate, barrels per stream day	2,460
Density of diesel, lb/gal	6.94
Energy rate of biomass input, MW_{th}	379
Energy rate of diesel production, MW_{th}	165

Note: db = daily barrel, i.e., barrels per day; 1 db =0.067 MW_{th}

The material and energy balance is shown in the spreadsheet of **Table 6.9** wherein the stream numbers refer to **Figure 6.**. When we use the unmodified term “biomass” we mean that it contains 30% moisture, as distinguished from the term “dry biomass” which contains 10% moisture. Also, the symbol “T” for ton refers to metric ton. The moisture content of the biomass as collected from the field is taken to be 30% and therefore the feed to the dryer is at the rate of 2,568 T/day. But after drying, the feed rate to the pyrolyzer is 2,000 dry T/day. For a feed rate of 2,000 dry T per day of biomass, it is estimated that the production rate of diesel fuel will be about 36 million gallons per year for a 95.9% on-stream factor or 350 operating days in a year. This is admittedly an overly optimistic value for on-stream time, but variation away from this value will be explored in the ‘Sensitivity Analysis’ section.

Regarding amounts, 1 ton of 30% moisture biomass will yield about 0.96 barrel of diesel, while 1 ton of dry (10% moisture) biomass will yield about 1.22 barrels of diesel. Letting x = the weight %

moisture content of the biomass, a general formula obtained from the mass balance of Table 6.9 for the diesel yield is:

$$(\text{barrel of diesel})/(\text{metric ton of biomass}) = 1.36\text{-}0.0135x \quad (6.16)$$

Also note that 1.0 T of dry (10% moisture) is equivalent to 1.29 T of 30% moisture biomass on a bone dry or yield of diesel basis.

Table 6.9: Material and Energy Balance

Energy balance on conversion of waste lignocellulose to transportation fuel					**use F9 to calculate in manual mode**						Syn gas temp to FT step, C			250					
Feed Rate of Crop Residue. kg/stream h			107,000		Trucking distance to pyrolyzer, miles			5.35			FT synthesis op pressure, psia			225					
Moisture content of crop residue, wt%			30		Trucking dist of PO to ATR/FT facility, miles			92			FT Synthesis carbon efficiency			90					
Moisture content of DCR, wt%			10		Truck payload limit, **lb**			43,000			Energy content of DCR(w/ 10%H2O), MJ/kg			17.0	LHV				
% by wt of DCR to PO			65		Truck volume capacity limit, ft^3			4,013			Energy content of BDCR, MJ/kg			19.1	LHV				
% by wt of DCR to Char			20		Truck gas mileage, gal/mile			0.125			Energy content of diesel oil, MJ/kg			42.8	LHV				
% by wt of DCR to non-cond gas			15		PO oil bone dry: C wt %			56.4			Energy content of diesel oil, MJ/gal			137.9	LHV				
Energy content of: PO, MJ/kg			18		H wt %			6.5			Energy content of CO, MJ/kg			10.9	LHV				
Char, MJ/kg			23		O wt %			37.1			Energy content of H2, MJ/kg			120	LHV				
Non-cond Gas, MJ/kg			5		water content of PO, wt %			25			Energy content of PO, MJ/kg			17.5	LHV				
Frac of eng rec'd from NCG & char for **drying step**			0.23		Steam reforming ht of rxn (endothm), MJ/kg-mol of C			200			Eng input for pryolysis step, MJ/kg			1.56					
Frac of eng rec'd from NCG & char (**pyr step**)			0.58		Exit temp of ATR reactor, C			650			Production Rate of Diesel Oil, bbl/stream day			2,457					
Pyrolysis temperature, C			500		Eng (thermal) req'd for O2 gas production, MJ/kg of O2			2.38			Production, bbl per metric ton of biomass feed			0.96					
Heat of pyrolysis rxn (+ means endo), MJ/kg			0.3		Temp of syngas exiting heat recovery HEX, C			200			Production rate (300 day/y), Mgal/yr			31					
Energy required to bail crop residue, MJ/kg			0.054		Total H2O to carbon in PO mole ratio for ATR			**0.9**			Number of PO trucks per hour to ATR/FT facility			3					
Energy required to grind crop residue, MJ/kg			0.18		Mole ratio of O2 in air to carbon in PO for ATR			**0.17**			% of original biomass energy in diesel fuel			42.0					
Heat of water evaporation, MJ/kg			2.2		% carbon lost in ATR due to coking			0	<--not used		% of original biomass energy in char			5.1					
Heat of vaporization of PO, MJ/kg			1.21		Carbon efficiency of ATR step, %			**61.1**			% of original biomass energy in NCG			0.8					
Heat released by F-T rxn, MJ/kg-mol CO			170		Mole Ratio of H2 to CO in Syn Gas			**2.0**			Total % original biomass energy recovered=			47.9					
Energy rate of biomass input, MWth			378		Consumption of ("dry", 10% h2o)crop residue, mton/d			1,997			Heat release rate by FT, MJ/h			178,134					
Energy rate of diesel production, MWth			165		Consumption of ("dry")crop residue, mT/hr			83.2			Compressor size for FT step, HP			14,006					
Dry metric tons per day fed to pyrolyzer			1,997		Oxygen requirement, mT O2/mT of dry biomass			0.125			Overall Carbon efficiency to FT liquid fuel, %			38.4					
				Gather/	Transport														
			Crop	Bale	Crop	Water	Dry Crop	Ground	Gas			Trans-			ATR	H2O	Dry ATR		
			Res.	in field	Res.	Evap'd	Res. (DCR)	DCR	(NCG)	Char	PO	ported PO	O2	Fresh water	Syn Gas	& CO2 removal	Syn Gas	FT liquids	diesel oil
	Mol Wt		1	1a	1b	2	3	4	5	6	7	8	8a	8b	9	9a	9b	10	
BDCR		kg/h	74,900	74,900	74,900		74,900	74,900											
H2O	18	kg/h	32,100	32,100	32,100	23,778	8,322	8,322						17,367	931	931			
PO as is		kg/h									54,094	54,094							
Char		kg/h								3,017									
NCG gas		kg/h							2,263										
CO	28	kg/h													32,600		32,600		
H2	2	kg/h													4,741		4,741		
O2	32	kg/h											10,373						
CO2	44	kg/h													43,563	43,563			
Diesel oil		kg/h																14,670	
Waxes		kg/h																	
Total		kg/h	*107,000*	*107,000*	*107,000*	*23,778*	*83,222*	*83,222*	*2,263*	*3,017*	*54,094*	*54,094*	*10,373*	*17,367*	*81,835*	*44,494*	*37,340*	*14,670*	
Cum Wt Yield		**%**	**100**	**100**	**100**	**-**	**77.8**	**77.8**	**2.1**	**2.8**	**50.6**	**50.6**			**-**			**13.7**	
Energy content		MJ/kg	12.7	12.7	12.7		17.0	17.0	5	23	18	18			11		25	42.8	
Gross energy available		MJ/h	1,362,467	1,362,467	1,362,467		1,414,778	1,414,778	**11,315**	**69,399**	973,700	973,700			924,239		924,239	627,869	
Net eng available		*MJ/h*	*1,362,467*	*1,356,689*	*1,354,971*		*1,407,282*	*1,392,302*			*951,225*	*942,446*			*868,296*		*868,296*	*571,926*	
Energy eff of step		%	-				50	-	-	-	50				-			-	
Ext Eng input for step		MJ/h	0	5,778	1,717		0	14,980			0	8,779	24,688		0		0	0	
Cum external eng input		MJ/h	0	5,778	7,495		7,495	22,475	22,475	22,475	22,475	31,254	55,943		55,943		55,943	55,943	
Cum energy eff.		**%**	**100**	**99.6**	**99.4**	**-**	**103.3**	**102.2**	**-**	**-**	**69.8**	**69.2**			**63.7**		**63.7**	**42.0**	
Bulk density		lb/ft^3	8	8	6.3		10	10			68	68						56.2	
Heat Capacity		**kJ**/kg/K						1.00			2.00	2.00	1.0		1.8				
CR=crop residue (contains 30% moisture)				DCR=dry crop residue (contains 10% moisture)					BDCR=bone dry crop residue (contains 0% moisture)										
Net energy= energy available minus cum energy input from prior steps							1 kW-hr = 3.6 MJ		1 kJ/kg/K = 0.24 BTU/lb/F			1 kcal = 4.18 kJ							
1kJ = 0.948 BTU		42 gal in bbl of oil		1 watt-hr= 3600 Joules			energy content of diesel, MJ/lb=		19.5		1 HP = 2.68 MJ/h		1 db = 0.0671 MWth						

Table 6.9 also shows that the produced FT fuel, after deducting any external energy input, contains a net positive of 42% of the original energy content of the biomass. Additionally, the carbon efficiency from biomass to FT fuel is seen to be 38.4%. A Fischer-Tropsch carbon efficiency to fuel of 90% has been assumed.

III.5. Economic Analysis

Before estimating of the economics of liquid fuel production from biomass, let us first examine the current retail price composition of diesel fuel. This will serve as something of a guide to our thinking. The current retail price components of diesel fuel in the United States are shown in Table 6.10 for the early 2011 time frame [19]. Return on capital invested for distribution and marketing, refining and crude oil are factored into the numbers quoted.

Table 6.10

Retail Price of Diesel Fuel				
			$/gal	% of Tot.
Tax (50/50 state & federal)			0.49	12
Distribution & Mkting			0.45	11
Refining			0.53	13
Crude Oil			2.60	64
		Total Cost	4.07	

It is seen that crude oil is the major contributor accounting for 64% of the total retail price, at this particular point in time. As the price of crude oil fluctuates the sales price will be strongly affected, a phenomenon known only too well. Thus, the raw material, crude oil, is the major factor in US diesel price. We will see that the cost of biomass will also be a major component of biomass derived fuel. Average state tax and federal tax are equal at ~ 25 cents/gal each.

When “plant gate price” is quoted in the literature for a gallon of diesel, it appears ordinarily not to include tax and distribution and marketing. This, as seen from Table 6.10, can increase the price of the fuel by as much as $1 per gallon.

III.5.1. Assumptions and Comments

The primary assumptions are:

1. Design is on the basis of current technology.
2. Capital cost for the entire process includes:
   a. Pyrolyzer(s), grinder, dryer
   b. Steam or ATR reforming plant
   c. Fischer-Tropsch plant
   d. All off-sites, e.g., utilities, storage, and infrastructure included.
3. Capital and operating cost estimates assume technology to be more mature than pioneer, but of course, nowhere nearly as mature as petroleum refining.
4. Raw material cost of biomass (30% moisture) delivered (i.e., including transportation) to pyrolyzer is fixed at $61.20 per dry T based on Table B-2 of ref. [20]. Biomass price is on the basis of “dry ton”. In reality biomass cost will be a function of transportation distance. Examination of this important feature is deferred to later studies.
5. No utility requirement other than electricity for compression to produce O2. Steam cost is assumed to be zero as explained in the “Utility Requirement” section. Also no allowance for cooling cost was made.

6. Char, not burned as a fuel from the pyrolysis step is used as a product for soil amendment. Char contains macro and micro nutrients as well as a pore structure conducive to soil health. As such, it is valued at $500 per ton. This credit contributes measurably to the economics, reducing the price of diesel by $0.35/gal. Determination of the credit, of course, awaits the market's valuation. For example, ref. [15] assumes $50/T for char.
7. Federal, state or local tax on final product diesel fuel is generally not included in the stated sale price.
8. Fill out for the plant is 50%, 75% and 100% for the first 3 years, respectively, and remains at 100% thereafter.
9. A discount factor of 8% is used.
10. The parameters of **Table 6.11** generally apply.

III.5.2. Spreadsheet used for Economics Calculations

The spreadsheet used for the economic calculations is shown in Table 6.11. The case shown is for the case of 1,909 dry metric tons per day of biomass and for a specific selection of parameters. Use of the value of "1,909 dry T/day" corresponds to two PCs 14 miles on a side with a reasonable biomass yield of 2.5 T/ac/yr (see Table 6.16). The parameters used are of course open to correction as better data become available. Variations from this case will made later in the paper. Parameters such as construction period, R&D cost, startup expense, escalation rates, etc. are also available as adjustable parameters.

Table 6.11: Economics of Biomass to Diesel Fuel (~2,000 T/day of biomass feed)

Economic Analysis of Biorefinery Collective Operation (Biomass to Diesel Fuel)						
Biomass Feed Rate, dry T/stream day				1,909		
Production Rate, millions of gallons per calendar year				33.7		
On-stream factor, %				95.9		
Biomass Stream rate, dry T/stream hr				80		
Biomass Stream rate, (30% moisture) T/stream hr				102		
Biomass Rate, (30% moisture) T/stream day				2,455		
Biomass Capacity, dry T per calander year				668,275		
Production Rate, barrels per stream day				2,291		
Production Rate, gallons per stream day				96,222		
Density of diesel, lb/gal				6.94		
Capital cost, million $				249		
VARIABLE COSTS						
		Act. Usage	Price	Cost	% of Eqiv	
Raw Materials & Other Costs	Units	Unit/gal	$/Unit	$/gal	Sales Pr	k$/yr
Dry biomass (10% water)	T	0.020	61.2	1.21		40,898
Catalyst	-	-	-	0.05		1,684
				0.00		0
TOTAL Raw Mat Cost				1.26	39.8	42,582
		Act. Usage	Price	Cost		
Utilities & other	Units	unit/gal	$/unit	$/gal		
Electricity (combustion air)	KWH	0.53	0.08	0.04		1,432
Steam	k lb	0.000	8.00	0.00		0
External eng costed at the price of diesel	KWH	0.00	0	0.00		0
Transportation of diesel fuel	gal	1.000	0.2	0.20		6,736
Transportation of char	T	0.00070	15.7	0.01		370
TOTAL Utilities Cost				0.25	8.0	8,538
		Act. Usage	Price	Cost		
Credits	Units	unit/gal	$/Unit	$/gal		
Char	T	-0.00070	500	-0.35		-11,788
			0	0.00		0
TOTAL Credits				-0.35	-11.0	-11,788
TOTAL Variable Cost				1.17	36.8	39,333

FIXED COSTS		Cost, $K/				
A. Labor (incl PAC)	Shift-man	shft-man/y	$K/y			
Operating	20.0	320	6,400			
Oper Superv	6.0	480	2,880			
Lab'tory	5.0	280	1,400			
Yard	5.0	200	1,000			
Packaging	5.0	320	1,600		Total people =	164
Maintenance (1.5% of capital)			3,735			
B. Supplies						
Operating (10% of total operating labor)			1,702			
Maintenance (1.5% of capital)			3,735			
C. Indirect						
Admin (Tech,acc,safety: 40%of tot labor)			6,806			
Taxes & Ins (1.1% of capital)			2,739			
TOTAL Fixed Cost ($K/y)			31,998			
TOTAL Fixed Cost ($/gal)				0.95	29.9	
CASH COST (Var + Fixed, ex depr), $/gal				2.12		
					(Sales Pr - Cash Cst)*gal/y	
SALES PRICE (ex tax), $/gal				3.18	M$/yr =	36

ROR VALUE	8.00%
NET PRESENT VALUE,K$	0
DISCOUNTED PAYBACK PERIOD, YRS	16.50

PRESTARTUP VALUES	
FIRST YEAR OF PROJECT	2011
CAPITAL COST,M$	249
CONST PERIOD,YRS(3 MAX)	2
FIRST YEAR OF SALES	2013
TOTAL YEARS OF SALES	15
R & D EXPENSES,K$	3,000
CAPITAL AS M & E,% OF TOT	90%
CAPITAL AS BLDGS,% OF TOT	9%
CAPITAL EXPENSE,% OF TOT	1%

INITIAL VALUES	
SALES VOLUME,million gal per year	33.68
SALES PRICE,$/gal	3.18
VARIABLE PLC,$/gal	1.17
FIXED PLC,K$/YEAR	31,998
STARTUP EXPENSE,K$	1,000
ADS&R COSTS,K$/YEAR	1,000
WORKING CAPITAL,% SALES	16%
DEPL ALLOWANCE,% OF SALES	0%
DEPL LIMIT,% OF PROFIT	0%

ESCALATION--	RATES	BASE YR
SALES PRICE	2.40%	2011
VARIABLE PLC	2.40%	2011
FIXED PLC	2.40%	2011
ADS&R COSTS	2.40%	2011
CAPITAL	2.40%	2011
DISCOUNT FACTOR		**8.00%**
*CAPACITY FILLOUTS	1ST YR.	50%
AS PERCENT	2ND YR.	75%
OF VOLUME	3RD YR.	100%
(4 YRS. MAX.)	4TH YR.	100%

III.5.3. Operating Costs

III.5.3.1. Feed Stock Transportation Cost

As mentioned, the cost of $61.20 per dry T of biomass includes the cost of transportation and is fixed.

III.5.3.2. Product Transportation Cost

With regard to product diesel fuel, it is assumed that the cost of operating a tank truck (capital, labor, insurance, etc.) is $2/mile. If the average delivery distance is about 500 miles and the average amount of petroleum hauled is 5,000 gal, the transportation cost is about $0.20 per gallon of diesel oil. For the product char, it is assumed that truck pay load is 25,300 lb or 12.7 tons. If we say the average transport distance is 100 miles, then the cost of trucking the char to various farms is ~$15.70/ton.

III.5.3.3. Catalyst Replacement for ATR and FT

This was estimated based on ref.[21] which considered 2000 T/day biomass plant for hydrotreating pyrolysis oil. The estimated cost from this reference was $1.8 million per year. As a first estimate we assume that this cost holds for the process of **Figure 6.** for 2000 T/day which translates to about 36 million gal per year giving a catalyst cost of $0.05/gallon.

III.5.3.4. Utility Requirements

For purposes of this initial estimate, as mentioned above, we assume that there is no requirement for externally supplied heating- all the heat requirement being provided by char and NCG. Some char (for sale as a soil amendment) and NCG are left over. Also we initially assume no water requirement. The only externally supplied electrical is that for producing 95% pure gaseous oxygen. To produce a metric ton of O_2 requires 220 kWh ref. [22]. From the material balance, Table 6.9, it is seen that 0.125 mT of O_2 is needed per mT of dry biomass. This results in an electrical usage of 27.5 kWh per T of dry biomass. Since the energy requirement is already built into the ATR step (stream 8b of **Table 6.9**), steam usage is estimated to be at or near zero. If stream 8b was included as a steam requirement this would be 0.0089 klb/gal of diesel. At $8/klb for steam cost this would add $0.07/gal to the final price of diesel. Clean-up of syngas prior to being sent to the Fischer Tropsch process often requires cooling to condense tars and absorb CO2 and sulfur or other impurities. However, the cost of cooling has not been accounted for in our analysis.

III.4.3.5. Labor

For a 1,909 dry ton/day operation the labor was estimated at 41 shift-man or 164 people total (see **Table 6.11**). This includes the labor for operating the pyrolyzers. The 2 pyrolyzer collectives, which are 14 miles squares each, have to deal with a total of ~ 400 square miles, so it is possible that such a large (or larger) number of people may be required. The effect of scale of operation on the labor force requirement was assumed to vary in the way capital does, i.e., with the 0.6 factor. So, an operation twice the size, viz., 3,818 ton/day the labor force is estimated as 164*(2^0.6) = 249 people. The labor wage rates include “overhead” which encompasses general plant maintenance, secretarial services, plant security and janitorial services and are based on those given in p. 38 of the NREL report [23].

III.5.4. Capital Cost

Capital cost is a very difficult parameter to estimate for any new large scale process which does not have the benefit of prior construction on a commercial scale. The literature reports numerous capital cost estimates for manifold configurations, see **Table 6.12**. The last column in

the table attempts to normalize the cost to the year 2011 using a 3% inflation rate and takes a biomass feed rate of 2,000 dry tons per day.

Table 6.12: Capital Cost Reported in the Literature

Author	Ref. no.	Process to produce liquid fuel	Size	Capital Cost[1], M_{2011}	Specific Cap. Cost, $$_{2011}$/db	Capital cost computed[2] to 2000 dT/day biomass feed rate, M_{2011}
Tijmensen, et al	[24]	Biomass, grinding, drying, gasification, reforming, FT, power[3] turbine	367 MW_{th} Input	380	146,000	380 (similar to us)
Islam, et al	[25]	Rice husks, grinding, drying, fast fluid bed pyrolysis (produces pyrolysis oil only)	24 T/d biomass	0.54	-	8 (PO only)
Wright, et al	[21]	Corn stover, grinding, drying, fast pyrolysis, hydrotreating	2,000 dT/d, 35 Mgal/y	295	120,000	295 (hydrotreating)
Lui, et al	[26]	Coal, grinding gasification, WGS, FT & power generation (CTL)	50,000 bbl/day FTL	5,460	109,200	756 (estimated without electric gen., but with coal grinding)
Vosloo	[27]	Nat. gas to FT liquid (GTL)	30,000 bbl/day	806	26,880	216 (this is a low no. because CH4 vs biomass feeds)
Choi, et al	[12]	Nat. gas to FT liquid (GTL)	8,820 bbl/day	628	71,200	292 (this is a low no. because CH4 vs biomass feeds)
Laser, et al	[6]	Switchgrass gasified, sent to FT, cogeneration of electricity (scenario 10)	4,535 T/day biomass	703	?	430 (this is for a gasifier and cogeneration of electricity)
ETSAP	[28]	Coal to FT (CTL)	50,000 db	4,753	95,000	780 (coal handling)

Note 1: This capital cost is for the size of the plant given in prior column and is inflation adjusted to 2011 using an average inflation rate of 3.0% (see www.inflationdata.com).
Note 2: A biomass feed rate of 2000 dry Tons/day corresponds to a production rate of 2,460 bbl/day of diesel (see Table 6.8). Capital cost for the 2000 dT/d biomass or 2,460 bbl/d is calculated based on the 0.6 exponential factor.
Note 3: Capital cost without power generation.
db = Daily barrels

In the coal to liquid fuel (CTL) plants, it is noted that [28] coal preparation and gasification accounts for 50% of the capital. The main sections of a biomass (eg, crop residue) to FTL plant is comprised of: (a) pyrolyzers, (b) an ATR unit, and (c) a FT unit.

III.5.4.1 Pyrolyzer Capital Cost

Pyrolyzer capital cost estimates have been given by Dynamotive p.35 in ref [29] and are shown in **Table 6.13**. The capital cost has been updated from the year 2002 to 2011 using a 3% inflation rate. According to ref [29] the capital cost includes all equipment including feed

preparation, planning, and construction. The cost does not include the cost of land or site preparation. It must be mentioned that pyrolyzer cost has been given in ref. [15] as $M47.8 for 550 T/day. We note here that the capital costs quoted in Table 6.13 may be low as Evergent Technologies [30], a joint venture between UOP and Ensyn, estimates that for a 400 bone dry metric tons per day pyrolyzer capital cost as being $M38 +/-40% excluding preparation equipment, off-sites and land. This is more than double the capital cost we have used. It is estimated that a pyrolyzer capital cost of $M45 for 400 T/day pyrolyzer would result in a ~$0.50/gal increase over the price from use of $M18.7 for 400 T/day (Table 6.13) at a production rate of 2,291 db. In any event, the effect of capital cost will be explored later.

Table 6.13: Capital Cost of Pyrolyzer vs. Capacity (ref. Dynamotive [29])

Biomass Capacity, T/d	M$$_{2002}$$	M$$_{2011}$$
100	6.6	8.6
200	8.8	11.5
400	14.3	18.7

III.5.4.2. ATR/FT Plant Capital Cost based on Bechtel-Syncrude Estimate

The capital cost of the central ATR/FT plant is based on a report by Bechtel Corp. and Syncrude Technology Inc. [12]. This reference discusses a natural gas to FT liquid transportation fuel plant designed to produce 8,820 db and 84 MW of electric power. Assume a favorable situation in which the 84 MW_{el} is convertible to liquid fuel. Now 84 MW_{el} = 3*84 = 252 MW_{th} = 3,600*252 = 9.07E+5 MJ/h. But, a barrel of diesel oil contains 6,120 MJ/bbl, so that we have that 84 MW is equivalent to the production of (9.07E5 MJ/h)/(6,120 MJ/bbl) = 148 bbl/h or 3,552 db. Thus, if we say of the 3,552 db only 2,500 db is realizable, and if all the energy of methane was directed to liquid fuel, then the total fuel production is 8,820 + 2,500 = 11,320 db. Table 2 of reference [12] gives the capital cost distribution, see Table 6.14. From this table, it is seen that:

1. Offsite cost is 56% of inside battery limits (ISBL)
2. Home office service/fees & contingency is 24% of (ISBL + Offsite)

Table 6.14: Capital Cost for Plant to Produce 8,820 db and 84 MW of Power from Methane Reforming & Once Through FT (From Choi, et al in the year 1997 [12])

Plant	Description	Cost, $M	%ISBL
101	Air compression & separation	70.4	32.7
102	Autothermal reforming	22.8	10.6
103	CO2 removal & recycle	13.4	6.2
201	Fischer-Tropsch synthesis	35.8	16.6
202	H2 recovery	3.6	1.7
203	Product fractionation	3.2	1.5
204	Wax hydrocracking	11.8	5.5
301	Combined cycle plant	54.5	25.3
	Total ISBL	215.5	
	Offsite	120.3	
	Subtotal:	335.8	
	Home office/Fees & Contingency	79.4	
	Total Cost	415.2	

If we (a) update this table to 2011 figures using a 3% inflation rate, (b) remove the "combined cycle plant" which generates electricity, and (c) use the percentages for offsites and home office, we have Table 6.15 for a methane to FTL plant of 11,320 db capacity.

Table 6.15: Capital Costs For Reforming and FT Sections from [12] (Updated to 2011)

Reforming Section		1997	2011
Air compression & separation		70.4	110
ATR		22.8	36
CO2 removal & recycle		13.4	21
	total	**106.6**	**166**
FT Section			
FT synthesis		35.8	56
H2 recovery		3.6	6
Production fractionation		3.2	5
Wax hydrocracking		11.8	18
	total	**54.4**	**85**
	Total ISBL		**251**
	Offsite (56% of ISBL)		**140**
HO service/fees & contingency (24% of ISBL+Offsite)			**94**
	Total Cost		**485**
Plant Capacity = 11,320 db			

This capital cost doesn't include the (1) pyrolyzer(s) and equipment for drying and grinding, (2) costs for transloading and storage of PO, and (3) the added cost of the ATR and FT plants to process the added fuel that would have gone to the combined cycle power plant. The estimated total capital cost in Table 6.15 is relatively in good agreement with the ORYX GTL project published [31] capital cost of $B1.0 (2007) for the 34,000 db gas to liquid plant in Qatar.

III.5.4.3. Effect of Scale on Capital Cost of BRC

Using Table 6.15 for the base capital and capacity information for the ATR/FT portion and adding the estimated cost for pyrolyzers from Table 6.13 and employing the 0.6 scale factor rule to both the ATR/FT and pyrolyzer sections, an estimate of the capital cost for an integrated enterprise handling 1,909 T/d of dry (10% moisture) biomass is made in Table 6.16. Input parameters are in the green shaded cells. From this table it is seen that the estimated total capital cost for this enterprise which is to consume 1,909 dry ton/day and produce 2,291 db is $M 249 or a specific capital cost of $109,000/db. This estimated capital cost of $M 249 for a biomass feed rate of ~2000 dry tons per day is somewhere in the middle of the normalized costs (last column) given in Table 6.12.

Table 6.16

BRC Capital Cost Estimates	Single pyrolyzer per PC
On-stream factor	0.9
Size of pyrolyzer collective (PC) (square), length of side, miles	**14**
Number of pyrolyzer collectives feeding enerprise ATR/FT facility	**2.0**
Usuable biomass production rate, T/ac/y	2.5
Payload capacity of tanker truck for PO, lb	43,000
Moisture content of biomass, wt %	10
Base size of single pyrolyzer, T/d	400
Base capital cost of single pyrolyzer, $M	18.7
Base size of combined ATR/FT facility, db	11,320
Base capital cost of combined ATR/FT facility, $M	485
Rate of biomass consumed in PC, T/stream d	955
Rate of PO generated in PC, T/stream d	621
Total Rate of biomass consumed by enterprise, T/stream d	**1,909**
Total Rate of PO feeding ATR/FT facility, T/stream d	1,241
Number of trucks bringing PO to central ATR/FT facility, trucks/day	58
Time between trucks, minutes	24.9
Specific rate of diesel production, barrels/ton of biomass	1.2
Area production,(db diesel)/sq mile	5.8
Enterprise rate of production of diesel oil, db	**2,291**
Enterprise rate of production of diesel oil, Mgal/cal yr	**32**
Estimated capital cost (in $M): Pyrolyzer(s)	**63**
Combined ATR/FT facility	**186**
Provision for scope uncertaintiy (0% of ATR/FT facility)	**0**
Total enerprise capital cost, $M	**249**
Specific capital cost, $k/db	**109**
Enterprise=consists of several pyrolzer collectives and a central ATR/FT facility	
PC= pyrolyzer collective	
db= daily barrel (ie, barrels per day)	

The effect of production size on the specific capital ($k/db) of a biorefinery collective (BRC) as influenced by the number of PC's and the size of a PC is illustrated in Figure 6.6 for PCs having a square size of 14 miles on a side and 25 miles on a side. The total capital cost of the BRC includes the capital cost of the pyrolyzer facilities and the capital cost of the central ATR/FT facility.

It is seen that capacities much beyond 60,000 db and 80,000 db for 14 mile and 25 mile square PCs, respectively, encounter diminishing returns due to the fact that although the capital cost economics of the central ATR/FT facility benefits from increased scale, the PCs are modular and do not. In any event, a state or BRC would probably not be producing more than 200,000 db.

Figure 6.6

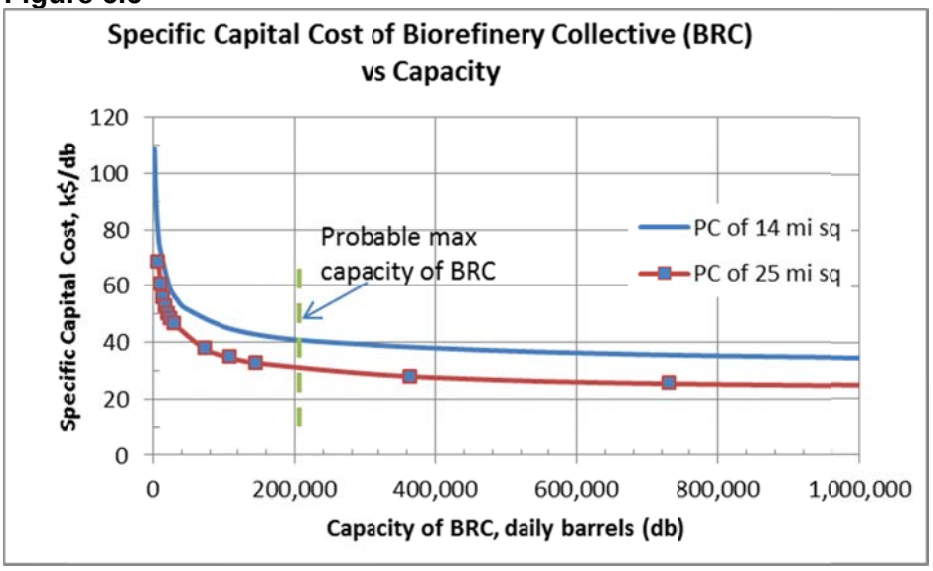

The data upon which Figure 6.6 is constructed is shown in Table 6.17 for 14 and 25 mile square PCs. For a BRC which produces ~200,000 db, it is seen that for PCs that are 14 miles on a side, nearly 200 PCs would be required to feed the central ATR/FT plant. For PCs which are 25 miles on a side, about 55 PCs would be necessary. For a BRC capacity of 200,000 db, the specific capital cost would be $k40/db vs $k30/db for the 14 mile vs. the 25 mile square PC, respectively. These specific capital costs are well below the $110,000/db calculated for the ~2,000 db capacity. Estimated capital cost of the biorefinery collective vs. capacity taken from Table 6.17 is plotted in Figure 6.7.

Table 6.17: Summary of Biorefinery Collective Capital Cost Estimates

Capital Cost of Biorefinery Collective for PCs 14 miles square				Capital Cost of Biorefinery Collective for PCs 25 miles square			
No. of PCs	Capacity db	Total Cap. Cost $M	Spec. Cap. Cost k$/db	No. of PCs	Capacity db	Total Cap. Cost $M	Spec. Cap. Cost k$/db
2	2,291	249	108.7	2	7,306	499	68.3
4	4,582	408	89.0	4	14,612	818	56.0
6	6,873	549	79.8	6	21,918	1,100	50.2
8	9,165	679	74.1	8	29,224	1,362	46.6
20	22,911	1,371	59.8	20	73,059	2,749	37.6
40	45,823	2,383	52.0	40	146,119	4,778	32.7
100	114,557	5,096	44.5	100	365,297	10,219	28.0
200	229,114	9,250	40.4	200	730,594	18,550	25.4
500	572,785	20,865	36.4	500	1,826,484	41,840	22.9
1000	1,145,571	39,256	34.3	1000	3,652,968	78,720	21.5

Figure 6.7

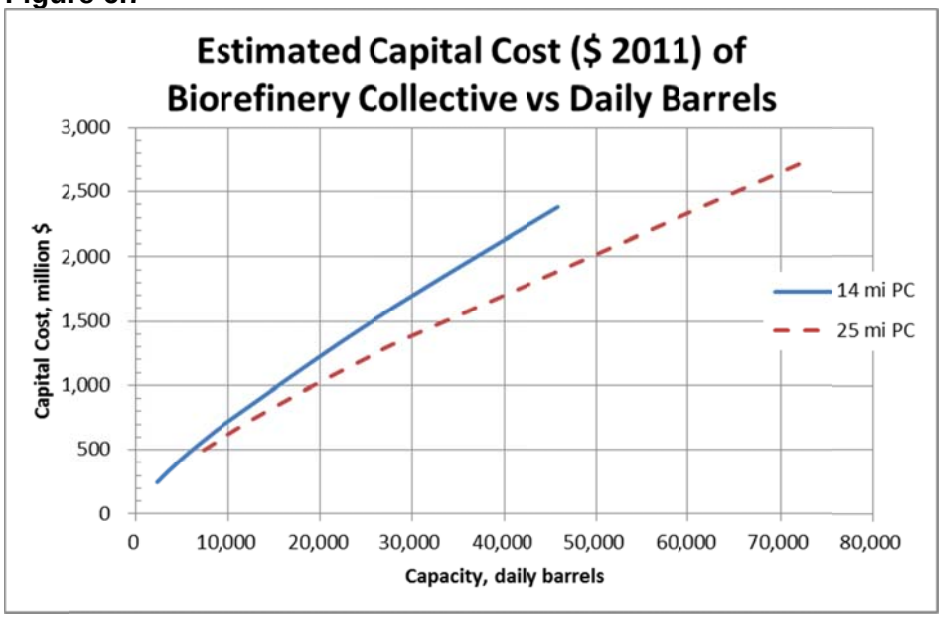

III.5.5. Estimated Sales Price of Product Diesel

In this section we estimate the sale price of diesel produced from the route of Figure 6.4. First we turn attention to a relatively small scale operation of ~ 2,000 dry tons per day of biomass and then consider the effect of scale.

Base Case: Biorefinery Collective of 1,909 dry T/day Capacity

Consider a BRC consisting of 2 pyrolyzer collectives 14 miles square consuming a total of 1,909 dry metric tons per day of biomass. This would produce 2,291 barrels of diesel per day.

The capital cost of $249 million for a 1,909 dry ton/day BRC is inputted into Table 6.11. Referring to Table 6.11, it seen that, for the specific parameters chosen, the sales price for a 8% discount factor is $3.18/gal. This does not include tax (local, state or federal) or marketing. With tax (at total of $0.50/gal) we would be looking at ~ $3.68/gal which is not far removed from prices that occurred in the last year or two.

III.5.6. Sensitivity Analysis

In this section the effect on sales price of capital cost, scale, and other factors are examined.

III.5.6.1. Effect of Capital Cost for1,909 dry T/day BRC

Using the base case in Table 6.11 we can plot selling price of diesel fuel for a 1,909 dry ton per day biomass capacity (2,291 db or on the order of 33Mgal/yr) vs capital cost of the biofuel enterprise for several rates of return on investment (ROI). This is shown in Figure 6.8.

Figure 6.8: Selling Price of Diesel Fuel vs Capital Investment

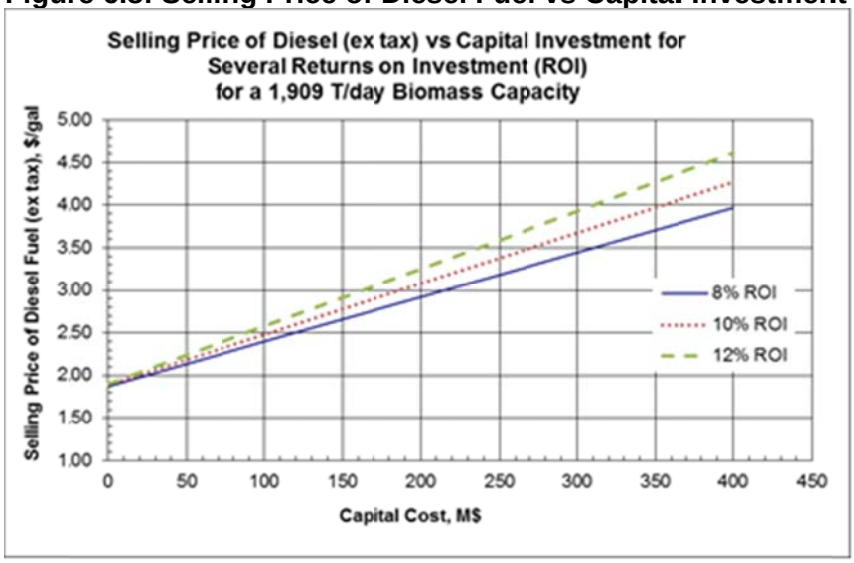

Observing the linear functionality of sales price on capital for this production scale of ~2,000 dry ton per day, an increase in capital cost of $100 million would raise the required sales price of the diesel by $0.52/gal for 8% ROI. Also, it is seen that if the capital cost were zero (but there still were costs for raw materials, maintenance, etc.) the cost of diesel would be ~ $1.90/gal (the y-intercept of Figure 6.8). An increase in ROI from 8% to 10% to 12% increases sales price by ~ $0.20/gal for each 2% increment at the given capacity and estimated capital cost of $249M.

III.5.6.2. Effect of Scale

Inputting the capital cost estimates shown in Figure 6.7 for biorefinery collectives with PCs of 14 and 25 miles on a side as a function of capacity, into the spreadsheet of Table 6.11, the sales price of diesel as a function of capacity is calculated. The result of such a calculation is shown in Figure 6.9.

Figure 6.9

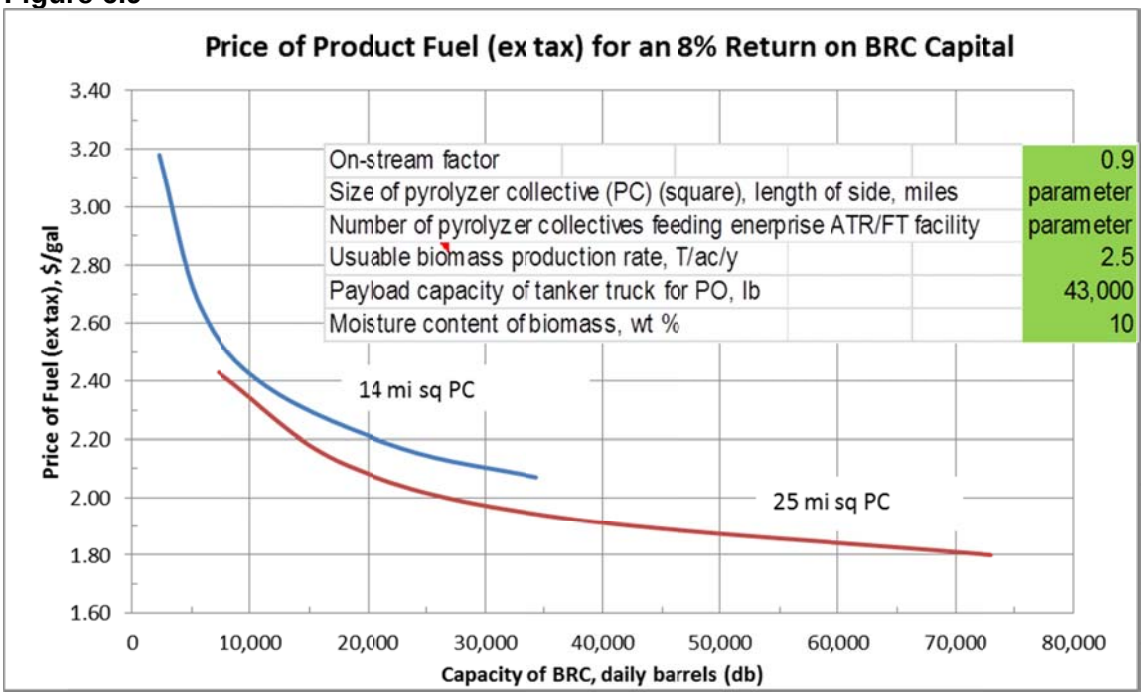

Table 6.18 shows the data on which Figure 6.9 is based.

Table 6.18: Calculated Fuel Price as a Function of Number of PCs and Size of PC

For PC 14 miles square				Spec.	Fuel Price		*For PC 25 miles square*				Spec.	Fuel Price
No. of	dry Tons			Cap.	(ex tax)		No. of	dry Tons			Cap.	(ex tax)
PCs	per day	db	$M	k$/db	$/gal		PCs	per day	db	$M	k$/db	$/gal
2	1,909	2,291	249	108.7	3.18		2	6,088	7,306	499	68.3	2.43
5	4,773	5,728	480	83.8	2.66		5	15,221	18,265	962	52.7	2.11
10	9,546	11,456	804	70.2	2.38		10	30,441	36,530	1,611	44.1	1.93
20	19,093	22,911	1,371	59.8	2.17		20	60,883	73,059	2,749	37.6	1.80
30	28,639	34,367	1,890	55.0	2.07							

It is seen that there appears to be on the order of a 12 cent/gal benefit in using a 25 mile square PC rather than a 14 mile square due to the benefit of pyrolyzer scale. It appears that a BRC of on the order of 10,000 db capacity would be competitive with a sales price of ~$2.35 + 0.50 (tax) = $2.85/gal.

From Figure 6.9 it is seen that biorefinery collective using PCs of 14 mile square and having a capacity of 35,000 barrels per day would generate a price of diesel fuel of ~ $2.08 per gallon, not including taxes. With taxes the price would be about $2.58 gallon, this would include distribution but not marketing. About 31 PCs of 14 mile square would be needed to produce 35,000 barrels per day. The estimated total capital for 31 PCs (14 mile square) and an ATR/FT central facility to handle the biomass is about $ 1.9 billion. Table 6.19 summarizes the effect of scale for 14 and 25 mile square PCs for the process of Figure 6.4.

Ref. [15] shows that a centralized gasification plant (not using distributed pyrolysis oil) by virtue of the opposing balance between economics of scale and increased cost of biomass collection will have an optimum size in which the sales price of fuel will be a minimum. Their calculation indicated that the optimum size for a gasification plant is 550 million gge per year (roughly 32,300 db) which will produce FT fuel at a minimum price of $1.56/gal (ex tax). For a distributed

system utilizing pyrolyzers ref. [15] estimates that an optimum production size of 2,500 million gge (roughly 147,000 db) will produce an FT liquid price of $1.43/gal (ex tax) where "gge" is gasoline gallon equivalent; diesel being ~0.9 gge. The distributed processing (i.e., pyrolyzer) curves of Figure 4 of ref. [15] are similar in shape and value to those of Figure 6.9.

Table 6.19: Summary of Estimated Diesel Price as a Function of Capacity and PC size

Capacity		*14 mile PC*			*25 mile PC*		
db	*Dry T/day*	*Cap. Cost, $M*	*Sale Price $/gal (ex tax)*	*Sale Price $/gal (w/ tax)*	*Cap. Cost, $M*	*Sale Price $/gal (ex tax)*	*Sale Price $/gal (w/ tax)*
2,000	1700	231	3.30	3.80	207	3.15	3.65
10,000	8,400	700	2.40	2.90	625	2.31	2.81
35,000	29,200	1,900	2.06	2.56	1563	1.94	2.44

It is seen that a very substantial reduction in sale price is possible in going from 2,000 to 35,000 db; a reduction of on the order of $1.20 per gallon. These estimated sales prices of FT liquid fuel appear to be quite in the range of being competitive at current prices.

III.5.6.3. Effect of Capital Cost for 35,000 db Capacity

The capital cost used in Figure 6.9 may be too low, especially for pioneer plants. Figure 6.10 plots the calculated fuel price as a function of capital for a plant capacity of ~35,000 db. It is seen from Figure 6.10, for a 35,000 db scale that the price of diesel derived from crop residue with *no expense for capital* is $1.41/gal. It is also seen that if the capital cost went from $2 billion to say $4 billion dollars the price of diesel would increase by ~ $0.70/gal, that is, from 2.09 to $2.78/gal (ex tax), still within competitive range.

Figure 6.10

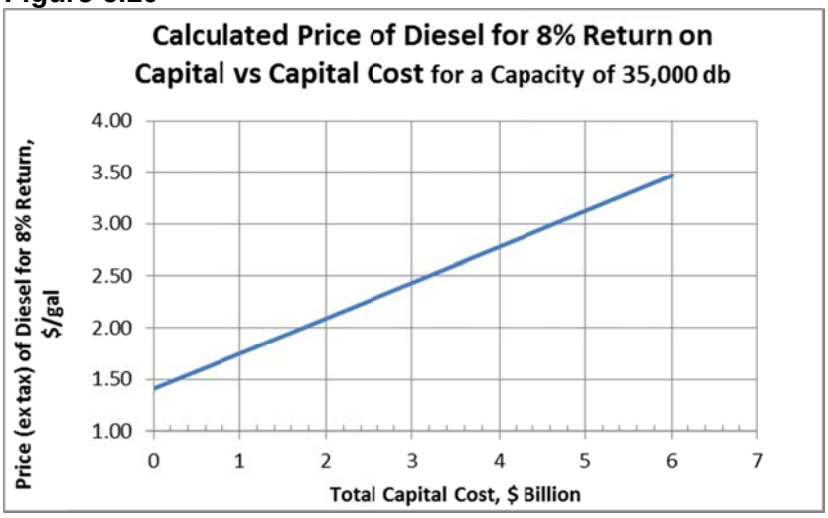

III.5.6.4. Effect of Biomass Cost

From Table 6.11 it is clear that a $10 per dry metric ton increment in the cost of biomass will result in a $0.20 per gallon increment in the sales price of FT liquid, e.g., diesel.

III.5.6.5. Sensitivity of Sales Price to Economic Factors

Table 6.20 shows the effect of changing a factor from the base case value, all other factors being held constant. The effect as a delta is shown in the 4th column of the table.

Table 6.20: Sensitivity of Sale Price to Some Factors

Factor	*Base Value*	*New Value*	*Delta Effect, $/gal*	*New Sale Price (ex tax), $/gal*
Capacity* Capacity**	35,000 db	30,000 db	+ 0.12* + 0.04**	2.18* 2.10**
Biomass cost, $/dry T	61.20	67.32	+ 0.12	2.18
Capital cost	$M 1,900	$M 3,000	+ 0.38	2.44
Size of PC	14 miles	25 miles	- 0.12	1.94
On-stream factor	95.9%	85%	+ 0.11	2.17
Discount factor	8%	10%	+ 0.10	2.16
Char price	$500/T	$100/T	+0.28	2.34
Price of diesel (ex tax)	$2.06/gal	-	-	-

*****For this case of capacity effect only capacity was changed other factors remained fixed.

** For this case of capacity effect, capacity was changed and also the capital cost was changed to account for the lower capacity.

Using the column "Base Value" in Table 6.20 as the origin, we construct the spider plot shown in Figure 6.11. This figure plots the effect on diesel price as a % change of the base price ($2.06/gal) vs. a % change in the parameters away from their base case values. The capacity case shown is that for which the capital changes reflecting the capacity change. It is seen that the biomass cost plays a major role in affecting the final fuel product price. A 30% increase in biomass price causes an 18% increase in diesel selling price. This suggests the need for exploring ways of reducing the cost of biomass gathering and delivery. The effect of moisture content on the sales price was not investigated as it was assumed that the biomass price was on the basis of 'dry', i.e., 10% moisture. Obviously, in reality there would be an effect due to shipping cost. From Figure 6.11 it is seen that capital cost is the next most significant economic factor. An increase of capital cost of 30% over the base value will increase the sales price of fuel by ~ 10%.

Figure 6.11: Sensitivity Plot for the Base Case Values shown in Table 6.20

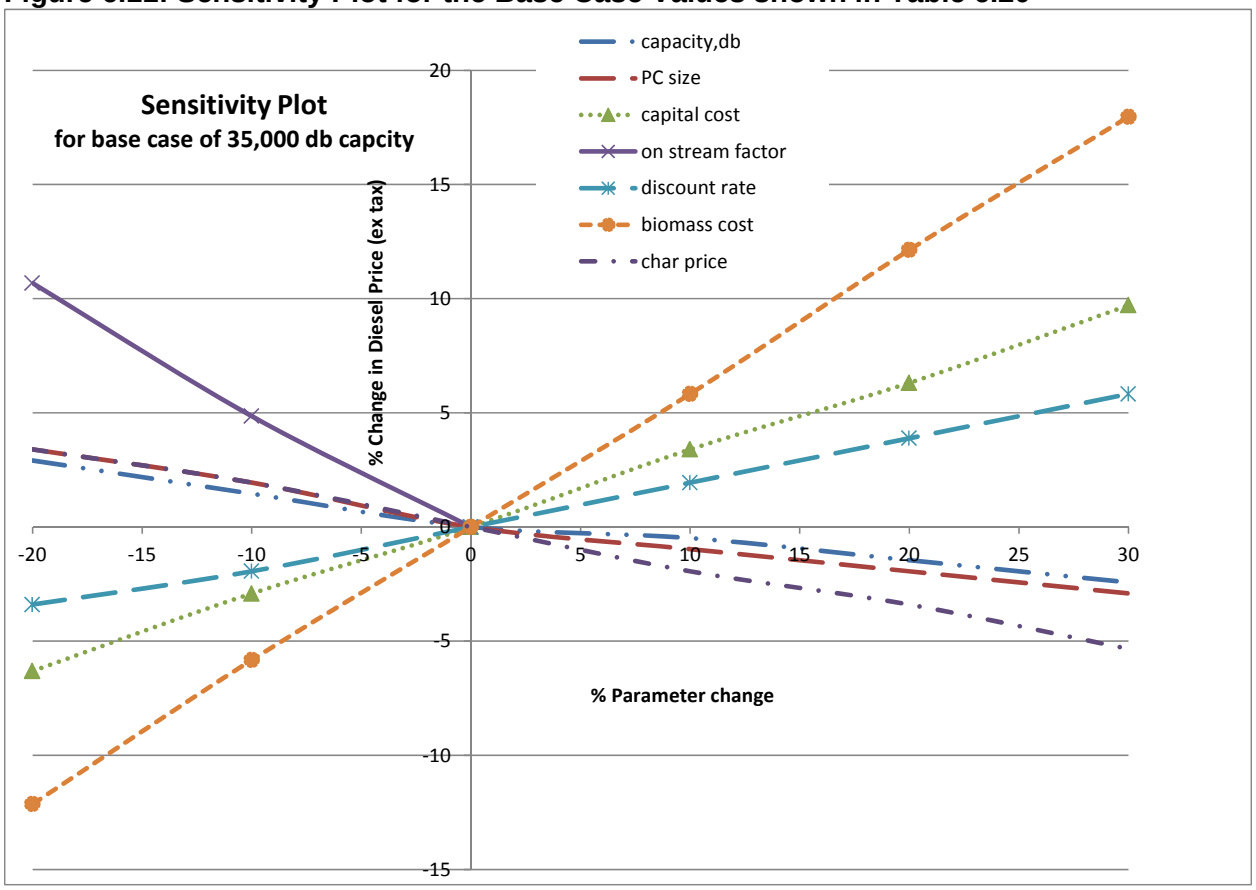

Table 6.21 shows the components of the sales price (ex tax) of the fuel for plant capacities of 2,000 db and for 35,000 db.

Table 6.21: Contributors to Fuel Price (2000 dry ton/day biomass feed)

Component of Product Fuel Price	*% of Product Fuel Price*	
	2,000 db	*35,000 db*
Biomass	37	59
Catalyst	2	2
Utilities	7	12
Fixed (payroll, benefits, maintenance & supplies)	31	18
Debt service at 8% discount factor	34	25
Credit for char sales	-11	-17

Thus, as in the case of crude oil, the major contributor to the price of the product fuel is the cost of the feed stock biomass, even more so when the scale of the plant increases. It is also seen that sale of char can have a substantially favorable impact on sales price.

III.6. Conclusions

Table 6.22 compares some characteristics and consequences of liquid fuel production routes. The cost considerations in the table assume a free market environment, which in reality may be purely delusional. It would appear that the primary advantages of biomass derived liquid transportation fuel are that it has a degree of CO2 neutrality and is renewable. If a dollar value can be placed on the benefit of reducing the cost resulting from hurricanes, floods, droughts, power outages, or other variety of climate calamities stemming from global warming and the military cost of protecting a reliable oil supply, then an appropriate incentive for the biomass to FT liquid route can be estimated. Policy has a role in deciding which production route to choose.

Under the Energy Independence and Security Act (EISA) of 2007, the Renewable Fuels Standard (RFS) program calls for*: an increased volume of renewable fuel required to be blended into transportation fuel from 9 billion gallons in 2008 to 36 billion gallons (99 million gallons/day) by 2022.* Recalling that U.S. consumption is 800 million gallons per day, this would represent a maximum of ~12% of present U.S. consumption.

Table 6.22: Assessment (from U.S. perspective) of Production Routes of Liquid Transportation Fuel

Production Route	Characteristics	Consequence
Conventional oil drilling or tar sands	Low cost. Requires significant importing.	Low petroleum price. Encourages consumption. Increased foreign dependence. Military expense.
Gas or Coal to FT Liquids	Medium cost. Less importing.	Somewhat higher petroleum price. Improved balance of payment. Reduced need for military protection. Less consumption by military. Lower prices of general goods.
Crop residue to FT Liquids	Higher cost. Less importing. ***More CO2 neutral.*** ***Renewable resource.***	Higher petroleum price. Improved balance of payment. Reduced need for military protection. Less consumption by military. Lower prices of general goods. More local economy & jobs ***Lower impact of global warming.*** ***Non-depleteable raw material***

In summary,

- Although, greater accuracy in input numbers is needed, this theoretical analysis of producing FT liquid fuel from crop residue biomass indicates that at a sufficiently large scale the economics of such a process could be competitive at current price levels.
- Like the heavy influence of the cost of crude oil on current fuel price, the cost of biomass is the largest single contributor to the final price of biomass derived fuel. This suggests the need to improve methods of biomass gathering and delivery or looking into growth of energy crops such as bamboo.
- An increase of $10 per dry metric ton in the price of biomass will result in an increase of ~ $0.20/gallon in the sales price of the FT diesel fuel.

- For the “demonstration” size biomass to FT liquid plant of ~2,000 db (~2,000 dry ton/day biomass) it was estimated that the capital cost is ~231 million and the price of the diesel fuel produced is $3.30 (ex tax) for a 8% discount factor. Tax would add ~$0.50/gal.
- A BRC capacity of 10,000 db resulted in an estimated diesel price of ~ $2.40/gal (ex tax). This price is commercially competitive.
- For a plant producing ~35,000 db, capital cost was estimate at $2 billion and sales price at $2.06/gal (ex tax). At this production scale, an additional $1 billion in capital cost will raise the price of diesel by $0.34/gal.
- Char is a by-product of the biomass process and when sold at $500/ton contributes very measurably to the economics, reducing the price of diesel by $0.35/gal.
- There appears to be on the order of a 12 cent/gal benefit in using a 25 mile square PC rather than a 14 mile square PC due to the economy of scale of the pyrolyzer plant.
- In order to make a measurable impact on reduction of fossil petroleum consumption in the U.S., one possible scenario calls for 10 BRCs producing 200,000 db each.
- Future economic analyses, rather than taking a fixed price of biomass, should include refinement of economic input data as well as accounting for the cost of (collecting) biomass as a function of the geographic land area, e.g., ref. [15].
- Viewed in broad perspective, policy making has a role to play in encouraging specific production routes to liquid fuels.
- If a square is “S” miles on a side the average distance to the center point is estimated to be 0.382*S

III.7. References

1. Boateng, A., DE Daugaard, NM Goldberg, KB Hicks, *Bench-scale fluidized-bed pyrolysis of switchgrass for bio-oil production.* Ind. Eng. Chem. Res., 2007. **46**: p. 1891.
2. Brown, R.C., *Thermochemical processing of biomass: conversion into fuels, chemicals and power*. Wiley Series in Renewable Resource. 2011, Hoboken, NJ: John Wiley & Sons. xiv, 330 p.
3. Dutta, A., M. Talmadge, J. Hensley, M. Worley, D. Dudgeon, D. Barton, P. Groenendijk, D. Ferrari, B. Stears, D. Barton, P. Groenendijk, D. Ferrari, B. Stears, *Process Design and Economics for Conversion of Lignocellulosic Biomass to Ethanol NREL/TP-5100-51400, 2011.*
4. Elliot, D., *Historical developments in hydroprocessing bio-oils.* Energy and Fuels, 2007. **21**: p. 1792.
5. Larson, E., J Haiming. *Biomass conversion to Fischer-Tropsch liquids: preliminary energy balances*. in *4th Biomass conference of the Americas*. 1999. Oakland, CA Aug. 29-Sept. 2, 1999: Elsevier Science, Ltd.
6. Laser, M., E Larson, B Dale, M Wang, N Greene, LR Lynd, *Comparative analysis of efficiency, environmental impact, and process economics for mature biomass refining scenarios.* Biofuels, Bioprod. Bioref., 2009. **3**: p. 247-270.
7. Laser, M., H Jin, K Jayawardhana, BE Dale, LR Lynd, *Projected mature technology senarios for conversion of cellulosic biomass to ethanol with coproduction of thermochemical fuels, power, and/or animal feed protein.* Biofels, Bioprod. & Bioref., 2009. **3**: p. 231-246.
8. Mullen, C., AA Boateng, *Chemical composition of bio-oils produced by fast pyrolysis of two energy crops.* Energy and Fuels, 2008. **22**: p. 2104-2109.
9. Perlack, R., LL Wright, AF Turhollow,RL Graham, BJ Stokes, DC Erbach, *Biomass as feedstock for a bioenergy and bioproducts industry: The technical feasiblity of a billion-ton annual supply ORNL/TM-2005/66*. 2005, Oak Ridge National laboratory: Oak Ridge, TN.
10. Perlack, R., BJ Stokes, *US Billion-Ton Update: Bionmass Supply for a Bioenergy and Bioproducts Industry* 2011, ORNL: Oak Ridge.

11. Langholtz, M.R.G., L Eaton, R Perlack, C Hellwinkel, D Ugarte, *Price projections of feedstocks for biofuels and biopower in the U.S.* Energy Policy, 2011. doi: 10.1016/j.enpol.2011.11.009.
12. Choi, G., SJ Kramer, SS Tam, JM Fox, NL Carr, Geoffrey, R Wilson. *Design/Economics of a once-through natural gas Fischer-Tropsch plant with power co-production*. in *DOE Conf. Proc. Coal Conference*. 1997.
13. Spence, A., *The learning curve and competition.* The Bell Journal of Economics, 1981. **12**(1): p. 49-70.
14. Dixit, A.K., RS Pindyck, *Investment under uncertainty*. 1994: Princeton University Press.
15. Wright, M., RC Brown, AA Boating, *Distributed processing of biomass to bio-oil for subseqent production of Fischer-Tropsch liquids.* Biofels, Bioprod. & Bioref., 2008. **2**: p. 229.
16. Manganaro, J., B Chen, J Adeosun, S Lakhapatri, D Favetta, A Lawal, R Farrauto, L Dorazio, DJ Rosse, *Conversion of residual biomass into liquid transportation fuel: an energy analysis.* Energy & Fuels, 2011. **25**: p. 2711-2720.
17. Bryan, B., *Activities in DOE's Biomass Program*. 2011, Biological and Environmental Research Advisory Committee Meeting March 9, 2011.
18. Phillips, S., JK Tarud, MJ Biddy, A Dutta, *Gasoline from Woody Biomass via Thermochemical Gasification, Methanol Synthesis, and Methanol-to-Gasoline Technologies: A Technoeconomic Analysis.* Industrial & Engineering Chemistry Research, 2011. **50**(20): p. 11734-11745.
19. http://www.andersontalkzone.com/2011/05/06/price-components-of-gasoline-and-diesel-fuel/.
20. DOE, *US DOE Energy Efficiency and Renewable Energy: Biomass multi-year program plan*. Nov. 2010, US Dept. of Energy.
21. Wright, M., J Satrio, R Brown, D Daugaard, D Hsu, *Techno-Economic Analysis of Biomass Fast Pyrolysis to Transportation Fuels NREL/TP-6A20-46586*. 2010, NREL.
22. Christie, M., R Victor, BA van Hassel, N Nagabushana, JLi, J Corpus, J Wilson, *Advanced oxyfuel boilers and process heaters for cost effective CO2 capture and sequestration. Report DOE Awards no. DE-FC26-01NT41147*. 2007, Praxair Inc: Tonawanda, NY.
23. Phillips, S., JK. Tarud, MJ Biddy, A Dutta, *Gasoline from Wood via Integrated Gasification, Synthesis, and Methanol-to-Gasoline Technologies Rpt NREL/TP-5100-47594*. 2011, NREL.
24. Tijmensen, M., APC Faaij, CN Hamelinck, MRM van Hardeveld, *Exploration of the possiblities for production of Fischer Tropsch liquids and power via biomass gasification.* Biomass & Bioenergy, 2002. **23**: p. 129.
25. Islam, M., FN Ani, *Techno-economics of rice husk pyrolysis, conversion with catalytic treatment to produce liquid fuel.* Bioresource Technology, 2000. **73**: p. 67-75.
26. Lui, G., ED Larson, RH Williams, TG Kreutz, X Guo, *Making Fischer-Tropsch fuels and electricity from coal and biomass: performance and cost analysis.* Energy & Fuels, 2011. **25**: p. 415-437.
27. Vosloo, A., *Fischer Tropsch: a futuristic view.* Fuel Processing Technolgy, 2001. **71**: p. 149-155.
28. ETSAP, *Liquid Fuels Production from Coal & Gas*, in *Energy Technology Systems Analysis Programme*. May 2010.
29. Mullaney, H., IH Farag, *Final Report Technical, environomental and economic feasibility of bio-oil in New Hampshire's North Country UNH Project Numbers: 14B316 UDKEIF or ABAN-URI-BO43*. Aug. 31, 2002.
30. *www.evergenttech.com*.
31. *http://www.oryxgtl.com.qa/ORYX-GTL-pioneering-new-gtl-markets-broadening-customer-base.html*.

6. Products Developed and Technology Transfer Activities

a. Publications

Manganaro, J., B. Chen, J. Adeosun, S. Lakhapatri, D. Favetta, A. Lawal, R. Farrauto, L. Dorazio, and D. J. Rosse, "Conversion of Residual Biomass into Liquid Transportation Fuel: An Energy Analysis," Energy & Fuels, 2011. 25, 2711-2720.

Manganaro, J., and A. Lawal, "Economics of Thermochemical Conversion of Crop Residue to Liquid Transportation Fuel," Energy & Fuels, 2012, 26, 2442-2453

Yujia, L., R. Farrauto, and A. Lawal, "Autothermal Reforming of Glycerol in a Dual Layer Monolith Catalyst," Chemical Engineering Science, 2013, 89, 31-39.

Yujia, L. and A. Lawal, "Kinetic Study of Autothermal Reforming of Glycerol in a Dual Layer Monolith Catalyst,' in preparation, 2012

b. Web site or other Internet sites that reflect the results of this project

Not Applicable

c. Networks or collaborations fostered

The first sample of pyrolysis oil evaluated during the course of the project was supplied to us by ARS, USDA, in Pennsylvania. It was made from switch-grass. Subsequently, we jointly explored funding opportunities by submitting proposals on projects of mutual research interest on thermochemical conversion of biomass waste to liquid transportation fuel. Columbia University (Prof. Marco Castaldi, now at City College) was also involved in one of these proposals. Stevens and City College of New York have also discussed potential areas of collaboration on the extension of catalyst life for the ATR of pyrolysis oil.

Dynamotive Corporation, and Ensyn Corporation also supplied us significant quantities of pyrolysis oil derived from sawdust and hardwood/softwood respectively which made it possible for us to evaluate the developed technology on different biomass feedstocks. Several discussions with Ensyn Corporation on the technical but non-confidential aspects of the project were beneficial. We will explore possible future collaboration.

d. Technologies/Techniques

Synthesis Gas Production from Autothermal Reforming of Pyrolysis Oil, and Glycerol

e. Inventions/Patent Applications, licensing agreements

Not Applicable

f. Other products –

Not Applicable